

11-25-77
12542
P246

**DEVELOPMENT OF A GRID-INDEPENDENT
APPROXIMATE RIEMANN SOLVER**

by

Christopher Lockwood Rumsey

A dissertation submitted in partial fulfillment
of the requirements for the degree of
Doctor of Philosophy
(Aerospace Engineering)
in The University of Michigan
1991

Doctoral Committee:

Professor Bram van Leer, Chairman
Assistant Professor Smadar Karni
Assistant Professor Kenneth G. Powell
Professor Philip L. Roe
James L. Thomas, Research Scientist, NASA Langley Research Center

(NASA-TM-104746) DEVELOPMENT OF A
GRID-INDEPENDENT APPROXIMATE RIEMANN SOLVER
PH.D. Thesis - Michigan Univ. (NASA) 246 p
CSCL 01A

N91-22090

Unclas
33/02 0012242

To Kim: my love always

ACKNOWLEDGEMENTS

I would like to thank my wife and family, first and foremost, for supporting me and enduring me throughout my studies. My chairperson, Dr. Bram van Leer, deserves special thanks for his technical support and ability to maintain a "long-distance" relationship. Thanks also to George Allison for keeping Financial Operations at the University of Michigan on their toes, to members of my committee for their assistance, and to Jerry South and NASA for allowing me to attain this goal.

TABLE OF CONTENTS

DEDICATION	ii
ACKNOWLEDGEMENTS	iii
LIST OF FIGURES	vi
LIST OF APPENDICES	xii
CHAPTER	
1. INTRODUCTION	1
2. GOVERNING EQUATIONS	7
2.1 Two-Dimensional Navier-Stokes Equations	7
2.2 Traveling-Wave Form of the Euler Equations	11
3. SPATIAL AND TEMPORAL DISCRETIZATION	15
3.1 Finite-Volume Formulaton	15
3.2 Explicit Time-Marching	17
3.3 Implicit Time-Marching	18
4. GRID-ALIGNED FLUX FUNCTION	21
5. GRID-INDEPENDENT FLUX FUNCTION	32
5.1 Wave Propagation Direction	33
5.2 Wave Decomposition	36
5.3 Flux Formulation	46
5.3.1 Standard Formula	46
5.3.2 Rotated Riemann Solver	49
5.4 Recovering the Grid-Aligned Scheme	53
6. STABILITY ANALYSIS	59
6.1 Explicit Time-Marching	59
6.2 Implicit Time-Marching	66
7. MONOTONICITY ANALYSIS	80

7.1	Scalar Wave Equation	80
7.2	Euler Equations	81
8.	TWO-DIMENSIONAL RESULTS	94
8.1	Euler Computations	94
8.1.1	Shock Reflection	94
8.1.2	Ramp Flow in a Channel	107
8.1.3	Oblique Supersonic Shear	110
8.1.4	Supersonic Flow Over an Airfoil	116
8.1.5	Subsonic Flow Over an Airfoil	127
8.2	Navier-Stokes Computations	136
8.2.1	Shock / Boundary-Layer Interaction	136
8.2.2	Subsonic Separated Flow Over an Airfoil	143
9.	EXTENSION TO THREE DIMENSIONS	152
9.1	Governing Equations	152
9.2	Spatial and Temporal Discretization	154
9.3	Grid-Aligned Flux Function	156
9.4	Grid-Independent Flux Function	160
9.5	Stability Analysis	167
9.6	Monotonicity Analysis	175
10.	THREE-DIMENSIONAL EULER RESULTS	182
10.1	Ramp Flow in a Channel	182
10.2	Oblique Supersonic Shear	193
10.3	Transonic Flow Over a Wing	202
11.	CONCLUSIONS	211
	APPENDICES	218
	BIBLIOGRAPHY	231

LIST OF FIGURES

Figure

4.1	The Riemann Problem	25
4.2	Grid-Aligned Acoustic Waves	25
4.3	Grid-Aligned Shear Wave	27
4.4	Grid-Aligned Wave Decomposition	27
4.5	Grid-Aligned Wave Model Interpretation of a Single Shock Wave ...	29
4.6	Grid-Aligned Wave Model Interpretation of an Oblique Shear Wave	30
5.1	Velocity-Difference Vector	34
5.2	Components of \vec{V}_L and \vec{V}_R in the θ_d -Frame	34
5.3	Interpretations of Velocity Difference	35
5.4	$(\theta_d + \frac{\pi}{2})$ Shear Wave	37
5.5	$\pm\theta_d$ Acoustic Waves	37
5.6	Minimum-Pathlength Model Wave Decomposition (Entropy Wave Not Pictured)	40
5.7	Minimum-Area Model Wave Decomposition (Entropy Wave Not Pictured)	41
5.8	Inviscid Computation of Supersonic Flow Over an Airfoil With θ_d Computed Each Iteration	43
5.9	5-Wave Model Wave Decomposition (Entropy Wave Not Pictured)	44
5.10	Inviscid Computation of Supersonic Flow Over an Airfoil With θ'_d Frozen	45
5.11	Graphical Representation of State-Determined Model	52
5.12	Typical Plots of Difference Between Standard Flux Formula and State-Determined Model	52

5.13	Example of 5-Wave Model Interpretation of Difference in States When $\theta'_d = \theta_g$	55
5.14	Pressure Contours Near Leading Edge of NACA 0012 Airfoil, $M = 0.3$, $\alpha = 1^\circ$, 5-Wave Model	57
6.1	Stability Boundary of 4-Stage Time-Marching Scheme, and “Worst-Case” Fourier Footprint of First-Order Spatial Differencing Scheme for $\nu = 1.75$	65
6.2	Stability Boundary of 4-Stage Time-Marching Scheme, and “Worst-Case” Fourier Footprint of Second-Order Spatial Differencing Scheme for $\nu = 0.87$	65
6.3	Eigenvalues as Function of CFL Number for Implicit Scheme, First-Order, $M = 100$, $\alpha = 90^\circ$, $\theta'_d = 22.5^\circ$, $\theta_g = 0^\circ$, $\beta = 0$	70
6.4	Eigenvalues as Function of CFL Number for Implicit Scheme, First-Order, $M = 100$, $\alpha = 45^\circ$, $\theta'_d = 45^\circ$, $\theta_g = 0^\circ$	71
6.5	Eigenvalues as Function of CFL Number for Implicit Scheme, Second-Order, $M = 100$, $\alpha = 90^\circ$, $\theta'_d = 22.5^\circ$, $\theta_g = 0^\circ$, $\beta = 0$	72
6.6	Eigenvalues as Function of CFL Number for Implicit Scheme, Second-Order, $M = 100$, $\alpha = 45^\circ$, $\theta'_d = 45^\circ$, $\theta_g = 0^\circ$	74
6.7	Same as Figure 6.5, Except Approximate Jacobians (6.28) and (6.29) Used on Left-Hand Side	78
6.8	Convergence Histories for Implicit A-F Scheme Applied to Second-Order Accurate Euler Computation Using 5-Wave Model	78
7.1	Monotonicity for $M = 3$, $\beta = 0.95$	86
7.2	Monotonicity Regions	87
7.3	Empirically-Determined Monotonicity Regions	91
8.1	Shock Reflection, First-Order, Grid-aligned, 49×17	96
8.2	Shock Reflection, First-Order, Grid-aligned, 97×33	97
8.3	Shock Reflection, First-Order, 5-Wave (θ'_d -Unlimited), 49×17	98
8.4	Shock Reflection, First-Order, 5-Wave (θ'_d -Limited), 49×17	99
8.5	Shock Reflection, First-Order, 5-Wave (θ'_d -Limited), 97×33	100
8.6	Shock Reflection, Second-Order, Grid-aligned, 49×17	102
8.7	Shock Reflection, Second-Order, Grid-aligned, 97×33	103
8.8	Shock Reflection, Second-Order, 5-Wave (θ'_d -Unlimited), 49×17 ...	104
8.9	Shock Reflection, Second-Order, 5-Wave (θ'_d -Limited), 49×17	105

8.10	Shock Reflection, Second-Order, 5-Wave (θ'_d -Limited), 97×33	106
8.11	Ramp Flow 49×17 Grid	108
8.12	Ramp Flow, First-Order, Grid-aligned	108
8.13	Ramp Flow, First-Order, 5-Wave (θ'_d -Unlimited)	109
8.14	Ramp Flow, First-Order, 5-Wave (θ'_d -Limited)	109
8.15	Ramp Flow, Second-Order, Grid-aligned	111
8.16	Ramp Flow, Second-Order, 5-Wave (θ'_d -Unlimited)	111
8.17	Ramp Flow, Second-Order, 5-Wave (θ'_d -Limited)	112
8.18	Oblique Shear, Exact Solution	112
8.19	Oblique Shear, First-Order, Grid-Aligned	114
8.20	Oblique Shear, First-Order, 5-Wave	114
8.21	Oblique Shear, Second-Order, Grid-Aligned	115
8.22	Oblique Shear, Second-Order, 5-Wave	115
8.23	NACA 0012 257×73 O-Grid	117
8.24	Supersonic Airfoil-Flow, First-Order, Grid-Aligned, 65×19	117
8.25	Supersonic Airfoil-Flow, First-Order, Grid-Aligned, 129×37	118
8.26	Supersonic Airfoil-Flow, First-Order, Grid-Aligned, 257×73	118
8.27	Supersonic Airfoil-Flow, Location of $j = \text{Constant}$ Line	120
8.28	Supersonic Airfoil-Flow, First-Order, 5-Wave, 65×19	120
8.29	Supersonic Airfoil-Flow, First-Order, 5-Wave, 129×37	121
8.30	Supersonic Airfoil-Flow, First-Order, 5-Wave, 257×73	121
8.31	Grid-Convergence Study for Supersonic Airfoil-Flow, First- Order	122
8.32	Supersonic Airfoil-Flow, Second-Order, Grid-Aligned, 65×19	122
8.33	Supersonic Airfoil-Flow, Second-Order, Grid-Aligned, 129×37	123
8.34	Supersonic Airfoil-Flow, Second-Order, Grid-Aligned, 257×73	123
8.35	Supersonic Airfoil-Flow, Second-Order, 5-Wave, 65×19	124
8.36	Supersonic Airfoil-Flow, Second-Order, 5-Wave, 129×37	124
8.37	Supersonic Airfoil-Flow, Second-Order, 5-Wave, 257×73	125

8.38	Grid-Convergence Study for Supersonic Airfoil-Flow, Second-Order	125
8.39	Supersonic Airfoil-Flow, Second-Order, 5-Wave, 257×73 , Min-Mod Limiter Employed	128
8.40	Grid-Convergence Study for Subsonic Airfoil-Flow, First-Order	128
8.41	Subsonic Airfoil-Flow, Entropy Contours, First-Order, Grid-Aligned	130
8.42	Subsonic Airfoil-Flow, Entropy Contours, First-Order, 5-Wave	130
8.43	Subsonic Airfoil-Flow, Upper Surface Total Pressure Loss, First-Order	131
8.44	Grid-Convergence Study for Subsonic Airfoil-Flow, Second-Order	133
8.45	Subsonic Airfoil-Flow, Entropy Contours, Second-Order, Grid-Aligned	133
8.46	Subsonic Airfoil-Flow, Entropy Contours, Second-Order, 5-Wave	134
8.47	Subsonic Airfoil-Flow, Upper Surface Total Pressure Loss, Second-Order	134
8.48	Subsonic Airfoil-Flow, Pressure Contours, Second-Order, 257×73	135
8.49	Shock/Boundary-Layer Interaction 93×141 Grid	137
8.50	Shock/Boundary-Layer Interaction, Pressure Contours, Grid-Aligned	139
8.51	Shock/Boundary-Layer Interaction, Pressure Contours, 5-Wave	140
8.52	Shock/Boundary-Layer Interaction, Skin Friction	141
8.53	Shock/Boundary-Layer Interaction, Boundary-Layer Profiles, 24×36	142
8.54	NACA 0012 257×97 C-Grid	144
8.55	Viscous Airfoil-Flow, Pressure Contours, Grid-Aligned	146
8.56	Viscous Airfoil-Flow, Pressure Contours, 5-Wave	147
8.57	Lift-Coefficient Grid-Convergence Study for Viscous Airfoil-Flow	148
8.58	Viscous Airfoil-Flow, Surface Pressure Coefficients, 65×25	148

8.59	Drag-Coefficient Grid-Convergence Study for Viscous Airfoil-Flow	149
8.60	Viscous Airfoil-Flow, Pressure Contours, 5-Wave (θ'_d -Unlimited), 129 \times 49	150
9.1	Grid Face Normal Angles	159
9.2	Effect of Acoustic Waves	159
9.3	Effect of Two Perpendicular Shear Waves	163
9.4	Wave Decomposition, Including Combined Shear Wave	163
9.5	Effect of $(\bar{n}'_d + \frac{\pi}{2})$ Shear Wave	163
9.6	Illustration of Possible Shear Wave Interpretations	164
9.7	Steady Oblique Shear With Rotation Through the Wave	171
9.8	Stability Boundary of 4-Stage Time-Marching Scheme, and “Worst-Case” Fourier Footprint of First-Order Spatial Differencing Scheme for $\nu = 1.55$	171
9.9	Stability Boundary of 4-Stage Time-Marching Scheme, and “Worst-Case” Fourier Footprint of Second-Order Spatial Differencing Scheme for $\nu = 0.77$	173
9.10	Eigenvalues as Function of CFL Number for Implicit Scheme, First-Order, “Worst-Case” Parameters	173
9.11	Eigenvalues as Function of CFL Number for Implicit Scheme, Second-Order, “Worst-Case” Parameters	174
9.12	Monotonicity Regions, $M = 3, \beta = 1$	179
9.13	Monotonicity for $M = 3, \beta = 1$; Allowable \bar{n}'_d for $ \bar{n}'_g - \bar{n}'_f = 75^\circ$...	180
9.14	Monotonicity Region, $M = 0.3, \beta = 1, \phi_p = 0^\circ$	181
10.1	Geometry for Ramp Flow in Channel	183
10.2	2-D Sections of 41 \times 17 \times 17 Grid	184
10.3	Ramp Flow, Pressure Contours, First-Order, Grid-Aligned	185
10.4	Ramp Flow, Pressure Contours, First-Order, 5-Wave	187
10.5	Ramp Flow, Pressure Contours, Second-Order, Grid-Aligned	189
10.6	Ramp Flow, Pressure Contours, Second-Order, 5-Wave	191
10.7	Shear Layer Orientation Within Cube	195
10.8	Oblique Shear, Exact Solution, $i = 9$ Plane	195

10.9	Oblique Shear, Exact Solution, $j = 9$ Plane	196
10.10	Oblique Shear, Exact Solution, $k = 9$ Plane	196
10.11	Oblique Shear, First-Order, Grid-Aligned, $i = 9$ Plane	197
10.12	Oblique Shear, First-Order, Grid-Aligned, $j = 9$ Plane	197
10.13	Oblique Shear, First-Order, Grid-Aligned, $k = 9$ Plane	198
10.14	Oblique Shear, First-Order, 5-Wave, $i = 9$ Plane	198
10.15	Oblique Shear, First-Order, 5-Wave, $j = 9$ Plane	199
10.16	Oblique Shear, First-Order, 5-Wave, $k = 9$ Plane	199
10.17	Oblique Shear, In-Plane Mach Contours, Second-Order, Grid- Aligned	200
10.18	Oblique Shear, In-Plane Mach Contours, Second-Order, 5-Wave ...	201
10.19	Cut-a-Way View of F-5 Wing $97 \times 17 \times 17$ C-H Grid	204
10.20	F-5 Wing, Pressure Contours, First-Order, Grid-Aligned	205
10.21	F-5 Wing, Entropy Contours, First-Order, Grid-Aligned	207
10.22	F-5 Wing, Pressure Contours, First-Order, 5-Wave	208
10.23	F-5 Wing, Entropy Contours, First-Order, 5-Wave	210
A.1	Wave Patterns for Minimum-Pathlength Model	223
A.2	Minimum-Area Model	223
A.3	Geometry of Minimum-Area Model	227
A.4	Wave Patterns for Minimum-Area Model	227

LIST OF APPENDICES

Appendix

- A. Derivation of β for the Minimum-Pathlength and Minimum-Area Models 219
- B. Derivation of the Combined Shear-Wave Vector for the 3-D Euler Equations 228

CHAPTER 1

INTRODUCTION

Among today's flow-solvers for the Euler and Navier-Stokes equations, many are based on upwind differencing. Prominent in use are Godunov-type schemes [1], in which the upwind bias is achieved by using the solution to the Riemann problem defined at each cell face. Riemann's initial-value problem, which is a mathematical representation of the shock-tube problem [2], is well-understood and easy to model. A membrane separating a gas at two different states is ruptured, and shock, contact, and expansion waves are emitted when the two states interact. In a Godunov-type scheme this event is supposed to happen at any cell face and any time level.

The Riemann problem can be solved exactly with an iterative method, as Godunov [3] did, or approximately, as Roe [4] did, leading to the concept of the "approximate Riemann solver." In Roe's method the Euler equations are linearized about an average state and then solved exactly. Eigenvectors of the averaged flux Jacobian, which represent different types of waves, are allowed to propagate with speeds equal to their corresponding eigenvalues. These waves describe the difference in states across each cell face.

The "upwind" direction for each wave is clear in one-dimensional flow: it is either forward or backward, according to the sign of each eigenvalue. In two or three dimensions the direction of wave propagation is not so straightforward: the

waves can travel in infinitely many directions. In most current multidimensional upwind flow-solvers, however, the upwinding direction is taken normal to the cell faces. Thus the schemes are strongly coupled to the grid on which they are implemented. Consequently, high resolution of flowfield discontinuities such as shock or shear waves can be achieved only when the discontinuities are aligned with grid lines. The Riemann solver interprets such waves incorrectly when they lie oblique to the grid; this improper interpretation can lead to smearing in the numerical solution.

In recent years, in an attempt to improve the accuracy of flow solutions, a number of researchers have developed multidimensional upwind methods where information is obtained from or propagated in directions other than the grid contravariant directions. Initial investigations focused on upwind finite-difference schemes for advection-dominated flows, *e.g.* Raithby [5], Hassan *et al.* [6], and Lillington [7]. In these schemes, attempts were made to convect information in the streamwise direction, independent of the grid orientation. Jameson [8,9] developed a rotated difference scheme for the transonic potential equation. The equation is written in a system of coordinates aligned with and normal to the local streamwise direction. When the local flowfield is supersonic, grid-aligned derivatives that are used to form derivatives in the streamwise direction are upwind-differenced, while all other derivatives are centrally-differenced.

Moretti [10], and later Verhoff and O'Neil [11], developed nonconservative characteristic-based schemes for the Euler equations. These schemes define Riemann variables, and employ grid-decoupled computational stencils determined from the directions of the characteristics. The multidimensional Euler equations reduce to a set of ordinary differential equations, coupled only through the source terms due to entropy variation, which are typically small. Each ordinary differential equation describes the propagation of an individual wave along its characteris-

tic. Because the schemes are nonconservative, conservation errors are introduced when shock waves are present in the solution. These errors can be eliminated by applying a shock correction after each iteration.

Goorjian [12] extended the method of Jameson for use with the Euler and Navier-Stokes equations. This method was later improved by Obayashi and Goorjian [13]. In the latter method, grid-aligned input states are used to solve Riemann problems in both the local streamwise and normal directions. In the normal direction the Riemann problem involves two acoustic waves only.

Colella [14] designed a predictor-corrector algorithm for systems of hyperbolic conservation laws in which the left and right states at each grid face are modified by waves traveling parallel to the interface. A standard grid-aligned Riemann solver is then used to obtain the flux across the face. This is still a direction-split approach, in which an oblique wave would be represented by two grid-aligned waves. A similar multidimensional method was developed independently by van Leer [15].

Davis [16] developed a finite-volume method for the Euler equations in which the difference formula and computational stencil vary with angle of assumed wave propagation. The angle at each cell face is determined by the *velocity-difference* direction, which is normal to a hypothetical steady shock wave that exists between the given states bordering the cell face. Derivatives in the grid-aligned frame are written in terms of derivatives in the rotated frame. Fluxes normal to the assumed frame are calculated using flux-vector splitting. The flux function *along* the assumed shock is a central-difference flux with an arbitrary parameter that insures stability. Davis' method locates steady shock waves very accurately, but is unable to locate steady contact discontinuities.

Roe [17] designed a multidimensional method based on the decomposition of

local gradients. The number and type of waves present is chosen, then angles, strengths, and speeds are determined from the local data. One model uses four acoustic waves with orientation ninety degrees apart, one entropy wave with arbitrary orientation, and a shear wave represented by a uniform vorticity. Initial efforts to implement this model have been made by Kroner [18] and Struijs *et al.* [19].

Hirsch and Lacor [20] decouple the numerical solution from the grid-direction by seeking an approximate diagonalization of the Euler equations. The equations are written in terms of entropy, a component of velocity, and two acoustic-like variables. In general, the Euler equations are not diagonalizable because the two Jacobian matrices (in two dimensions) are not simultaneously diagonalizable. In [20], however, the similarity transformation is based on derivatives of the solution, allowing more freedom. Still, a source term may arise, which can be minimized. Two physical directions play a crucial role in the definition of flow variables and characteristic directions. One is aligned with the local pressure gradient, and the second is related to the strain-rate tensor. In practice these two directions are frozen to improve convergence. A variation of Raithby's [5] streamline-upwinding scheme is used to interpolate the flowfield variables, since standard grid-direction interpolation was found to produce no advantage over grid-aligned methods.

Powell and van Leer [21] and Powell [22] implemented a cell-vertex scheme for quadrilateral grids consisting of two basic steps: a residual calculation and a residual distribution. In the first step the residual is calculated based on a flux integral, and in the second step the residual is sent in a weighted manner only to the nodes that define the "downwind" face. The convection directions and corresponding characteristic quantities chosen are the same as those derived by Hirsch and Lacor [20]. These directions can be frozen to help the convergence of the scheme. A similar cell-vertex scheme was instituted by Giles *et al.* [23]. This

method differs from Powell's primarily in that the computations are performed on triangular grids using a trapezoidal rule integration for the residual calculation, and the local flow direction (rather than characteristic directions) is used to define the "downwind" face.

Levy *et al.* [24] developed a method which expands upon the work of Davis [16]. A dominant-direction angle is chosen, either in the direction of the local pressure gradient or the flow velocity, and two sets of left and right states are obtained at each cell face via interpolation from the surrounding flowfield data. One of these sets of left and right states is aligned with the dominant-direction, while the other set is aligned normal to the first. Then, two Riemann-type solvers are used to obtain fluxes in the rotated frame. The components of these fluxes in the grid direction are added to obtain the flux at the face.

Parpia and Michalek [25] independently derived a grid-independent upwind finite-volume method for the Euler equations very similar to the method proposed in this thesis. Left and right states at an interface are still interpolated along grid lines, but a multidimensional four-wave pattern made up of two acoustics, a shear, and an entropy wave is assumed to describe the difference in states. The strengths of these waves are chosen such that the sum of the jumps in the flow properties across the waves is minimized.

Finally, Dadone and Grossman [26] developed a rotated upwind scheme for the Euler equations in which flux-difference splitting is applied along two orthogonal directions for each cell face. The directions are determined from the pressure gradient, and the left and right states are selected from appropriately chosen cells near to the face where the flux is being computed.

One of the common features of many of the upwind methods described above is that information needed at special points because of physical considerations

must be interpolated from surrounding data points. Since this adds an extra level of complexity to any method, particularly for non-Cartesian meshes, it was decided early in the development of the present scheme to only use information obtained by interpolation along grid lines as the input to the approximate Riemann solver. It would then be the job of the solver to make “intelligent” use out of information gleaned from these left and right states. This constraint puts some limits on the ability of the solver to recognize what is going on in the flowfield, but the resulting simplicity and low expense of the method seem to outweigh its drawbacks.

The current method uses five waves to describe the difference in states at a grid face. Four of these are acoustic, shear, and entropy waves which act in the velocity-difference direction (the same dominant-direction chosen by Davis [16]), while the fifth is a shear wave that propagates at a right angle to the other four (also used by Parpia and Michalek [25]). This fifth wave allows the method to capture oblique steady shear waves sharply. The propagation directions can be frozen to improve convergence. The method also makes use of the linearizations of the Euler equations due to Roe [4] in order to maintain as simple and inexpensive a scheme as possible.

This thesis is organized as follows. Chapter 2 briefly describes the two-dimensional Euler and Navier-Stokes equations in Cartesian and generalized coordinates, as well as the traveling wave form of the Euler equations. The spatial and temporal discretization for both explicit and implicit time-marching schemes are described in Chapter 3. Chapter 4 outlines the grid-aligned flux function of Roe [4], while Chapter 5 details the derivation of the 5-wave grid-independent flux function. Chapters 6 and 7 contain stability and monotonicity analyses of the 5-wave model, respectively. Two-dimensional results are provided in Chapter 8. The extension to three dimensions is made in Chapter 9, with corresponding results given in Chapter 10. Finally, Chapter 11 gives conclusions.

CHAPTER 2

GOVERNING EQUATIONS

2.1 Two-Dimensional Navier-Stokes Equations

The two-dimensional Navier-Stokes equations in Cartesian coordinates can be written in conservation form as

$$\frac{\partial \tilde{U}}{\partial \tilde{t}} + \frac{\partial \tilde{F}}{\partial \tilde{x}} + \frac{\partial \tilde{G}}{\partial \tilde{y}} = \frac{\partial \tilde{F}_v}{\partial \tilde{x}} + \frac{\partial \tilde{G}_v}{\partial \tilde{y}}, \quad (2.1)$$

where the \sim indicates dimensional variables. The conserved variables are $\tilde{U} = [\tilde{\rho}, \tilde{\rho}\tilde{u}, \tilde{\rho}\tilde{v}, \tilde{\rho}\tilde{E}]^T$, where $\tilde{\rho}$ is the density, \tilde{u} and \tilde{v} are the components of velocity in the \tilde{x} and \tilde{y} directions, and \tilde{E} is the specific total energy. The inviscid flux vectors are

$$\tilde{F} = \begin{bmatrix} \tilde{\rho}\tilde{u} \\ \tilde{\rho}\tilde{u}^2 + \tilde{p} \\ \tilde{\rho}\tilde{u}\tilde{v} \\ \tilde{\rho}\tilde{u}\tilde{H} \end{bmatrix} \quad \tilde{G} = \begin{bmatrix} \tilde{\rho}\tilde{v} \\ \tilde{\rho}\tilde{u}\tilde{v} \\ \tilde{\rho}\tilde{v}^2 + \tilde{p} \\ \tilde{\rho}\tilde{v}\tilde{H} \end{bmatrix}, \quad (2.2)$$

where the specific total enthalpy $\tilde{H} = \tilde{E} + \tilde{p}/\tilde{\rho}$. The viscous fluxes are

$$\tilde{F}_v = \begin{bmatrix} 0 \\ \tilde{\tau}_{11} \\ \tilde{\tau}_{21} \\ \tilde{V}_j \tilde{\tau}_{1j} + \tilde{k} \frac{\partial \tilde{T}}{\partial \tilde{x}} \end{bmatrix} \quad \tilde{G}_v = \begin{bmatrix} 0 \\ \tilde{\tau}_{12} \\ \tilde{\tau}_{22} \\ \tilde{V}_j \tilde{\tau}_{2j} + \tilde{k} \frac{\partial \tilde{T}}{\partial \tilde{y}} \end{bmatrix}, \quad (2.3)$$

where

$$\tilde{\tau}_{ij} = \tilde{\mu} \left(\frac{\partial \tilde{V}_i}{\partial \tilde{X}_j} + \frac{\partial \tilde{V}_j}{\partial \tilde{X}_i} \right) + \tilde{\lambda} \frac{\partial \tilde{V}_k}{\partial \tilde{X}_k} \delta_{ij}. \quad (2.4)$$

In equations (2.3) and (2.4), summation convention is implied and $\bar{V}_1 = \bar{u}$, $\bar{V}_2 = \bar{v}$, $\bar{X}_1 = \bar{x}$, and $\bar{X}_2 = \bar{y}$.

The ideal-gas equation-of-state closes the set of equations:

$$\bar{p} = (\gamma - 1)\bar{\rho} \left(\bar{E} - \frac{\bar{u}^2 + \bar{v}^2}{2} \right). \quad (2.5)$$

The above equations can be nondimensionalized as follows. First the Prandtl number, Reynolds number, and freestream Mach number are defined by

$$\text{Pr} = \frac{\bar{\mu}\bar{c}_p}{\bar{k}} \quad \text{Re} = \frac{\bar{\rho}_\infty\bar{q}_\infty\bar{\ell}}{\bar{\mu}_\infty} \quad \text{M}_\infty = \frac{\bar{q}_\infty}{\bar{a}_\infty}, \quad (2.6)$$

where $\bar{q}_\infty = \sqrt{\bar{u}_\infty^2 + \bar{v}_\infty^2}$ is the freestream velocity and $\bar{\ell}$ is some characteristic length, specific to the problem considered. Then each of the variables is nondimensionalized via:

$$t = \frac{\bar{t}\bar{a}_\infty}{\bar{\ell}} \quad \rho = \frac{\bar{\rho}}{\bar{\rho}_\infty} \quad V_i = \frac{\bar{V}_i}{\bar{a}_\infty} \quad \mu = \frac{\bar{\mu}}{\bar{\mu}_\infty} \quad (2.7)$$

$$\lambda = \frac{\bar{\lambda}}{\bar{\mu}_\infty} \quad X_i = \frac{\bar{X}_i}{\bar{\ell}} \quad p = \frac{\bar{p}}{\bar{\rho}_\infty\bar{a}_\infty^2} \quad E = \frac{\bar{E}}{\bar{a}_\infty^2}. \quad (2.8)$$

Assuming a calorically perfect gas, \bar{T} is replaced by the expression

$$\bar{T} = \frac{\bar{a}^2}{(\gamma - 1)\bar{c}_p}, \quad (2.9)$$

and \bar{a} is nondimensionalized by \bar{a}_∞ .

After substitution, the nondimensional Navier-Stokes equations can be written

$$\frac{\partial \mathbf{U}}{\partial t} + \frac{\partial \mathbf{F}}{\partial x} + \frac{\partial \mathbf{G}}{\partial y} = \frac{\partial \mathbf{F}_v}{\partial x} + \frac{\partial \mathbf{G}_v}{\partial y}, \quad (2.10)$$

where

$$\mathbf{U} = \begin{bmatrix} \rho \\ \rho u \\ \rho v \\ \rho E \end{bmatrix} \quad (2.11)$$

$$\mathbf{F} = \begin{bmatrix} \rho u \\ \rho u^2 + p \\ \rho uv \\ \rho uH \end{bmatrix} \quad \mathbf{G} = \begin{bmatrix} \rho v \\ \rho uv \\ \rho v^2 + p \\ \rho vH \end{bmatrix} \quad (2.12)$$

$$\mathbf{F}_v = \begin{bmatrix} 0 \\ \tau_{11} \\ \tau_{21} \\ V_j \tau_{1j} - \dot{Q}_1 \end{bmatrix} \quad \mathbf{G}_v = \begin{bmatrix} 0 \\ \tau_{12} \\ \tau_{22} \\ V_j \tau_{2j} - \dot{Q}_2 \end{bmatrix}. \quad (2.13)$$

The nondimensional shear-stress and heat-flux terms are given by

$$\tau_{ij} = \frac{M_\infty}{\text{Re}} \left\{ \mu \left(\frac{\partial V_i}{\partial X_j} + \frac{\partial V_j}{\partial X_i} \right) + \lambda \frac{\partial V_k}{\partial X_k} \delta_{ij} \right\} \quad (2.14)$$

$$\dot{Q}_i = -\frac{M_\infty \mu}{\text{RePr}(\gamma - 1)} \frac{\partial(a^2)}{\partial X_i}. \quad (2.15)$$

Again $V_1 = u$, $V_2 = v$, $X_1 = x$, and $X_2 = y$. The equation-of-state is

$$p = (\gamma - 1)\rho \left(E - \frac{u^2 + v^2}{2} \right). \quad (2.16)$$

The Navier-Stokes equations can also be written in generalized curvilinear coordinates, where the coordinate directions are defined by

$$\xi = \xi(x, y) \quad (2.17)$$

$$\eta = \eta(x, y).$$

Using the chain rule, the derivatives in curvilinear coordinates are written in terms of the derivatives in Cartesian coordinates:

$$\begin{bmatrix} \frac{\partial}{\partial \xi} \\ \frac{\partial}{\partial \eta} \end{bmatrix} = \begin{bmatrix} x_\xi & y_\xi \\ x_\eta & y_\eta \end{bmatrix} \begin{bmatrix} \frac{\partial}{\partial x} \\ \frac{\partial}{\partial y} \end{bmatrix}. \quad (2.18)$$

The determinant of the 2×2 matrix in (2.18) is defined as the inverse of the metric Jacobian J :

$$J^{-1} = x_\xi y_\eta - x_\eta y_\xi. \quad (2.19)$$

Inverting (2.18), one can obtain the following equations for the metric terms:

$$\begin{aligned} \xi_x &= J y_\eta & \xi_y &= -J x_\eta \\ \eta_x &= -J y_\xi & \eta_y &= J x_\xi. \end{aligned} \quad (2.20)$$

The nondimensional Navier-Stokes equations (2.10) can be written in terms of the curvilinear coordinates:

$$\begin{aligned} \frac{\partial \mathbf{U}}{\partial t} + \frac{\partial}{\partial \xi} (\xi_x \mathbf{F} + \xi_y \mathbf{G}) + \frac{\partial}{\partial \eta} (\eta_x \mathbf{F} + \eta_y \mathbf{G}) = \\ \frac{\partial}{\partial \xi} (\xi_x \mathbf{F}_v + \xi_y \mathbf{G}_v) + \frac{\partial}{\partial \eta} (\eta_x \mathbf{F}_v + \eta_y \mathbf{G}_v). \end{aligned} \quad (2.21)$$

Multiplying (2.21) by J^{-1} , applying the chain rule, and combining and cancelling terms, the two-dimensional Navier-Stokes equations in curvilinear coordinates and conservation form become:

$$\frac{\partial \mathbf{U}^*}{\partial t} + \frac{\partial \mathbf{F}^*}{\partial \xi} + \frac{\partial \mathbf{G}^*}{\partial \eta} = \frac{\partial \mathbf{F}_v^*}{\partial \xi} + \frac{\partial \mathbf{G}_v^*}{\partial \eta}, \quad (2.22)$$

where

$$\mathbf{U}^* = \frac{1}{J} \begin{bmatrix} \rho \\ \rho u \\ \rho v \\ \rho E \end{bmatrix} \quad (2.23)$$

$$\mathbf{F}^* = \frac{1}{J} \begin{bmatrix} \rho u^* \\ \rho u^* u + \xi_x p \\ \rho u^* v + \xi_y p \\ \rho u^* H \end{bmatrix} \quad \mathbf{G}^* = \frac{1}{J} \begin{bmatrix} \rho v^* \\ \rho v^* u + \eta_x p \\ \rho v^* v + \eta_y p \\ \rho v^* H \end{bmatrix} \quad (2.24)$$

$$\mathbf{F}_v^* = \frac{1}{J} \begin{bmatrix} 0 \\ \xi_x \tau_{11} + \xi_y \tau_{12} \\ \xi_x \tau_{21} + \xi_y \tau_{22} \\ \xi_x (V_j \tau_{1j} - \dot{Q}_1) + \xi_y (V_j \tau_{2j} - \dot{Q}_2) \end{bmatrix} \quad (2.25)$$

$$\mathbf{G}_v^* = \frac{1}{J} \begin{bmatrix} 0 \\ \eta_x \tau_{11} + \eta_y \tau_{12} \\ \eta_x \tau_{21} + \eta_y \tau_{22} \\ \eta_x (V_j \tau_{1j} - \dot{Q}_1) + \eta_y (V_j \tau_{2j} - \dot{Q}_2) \end{bmatrix} \quad (2.26)$$

$$u^* = \xi_x u + \xi_y v \quad (2.27)$$

$$v^* = \eta_x u + \eta_y v.$$

The terms u^* and v^* are the contravariant velocity components, and V_1 and V_2 represent u and v , respectively. τ_{ij} and \dot{Q}_i are still given by (2.14) and (2.15), but

now

$$\begin{aligned} \frac{\partial}{\partial X_1} &= \xi_x \frac{\partial}{\partial \xi} + \eta_x \frac{\partial}{\partial \eta} \\ \frac{\partial}{\partial X_2} &= \xi_y \frac{\partial}{\partial \xi} + \eta_y \frac{\partial}{\partial \eta}. \end{aligned} \quad (2.28)$$

Therefore, the shear stress and heat flux terms are

$$\tau_{11} = \frac{M_\infty}{\text{Re}} \{(\lambda + 2\mu)(\xi_x u_\xi + \eta_x u_\eta) + \lambda(\xi_y v_\xi + \eta_y v_\eta)\} \quad (2.29)$$

$$\tau_{22} = \frac{M_\infty}{\text{Re}} \{(\lambda + 2\mu)(\xi_y v_\xi + \eta_y v_\eta) + \lambda(\xi_x u_\xi + \eta_x u_\eta)\} \quad (2.30)$$

$$\tau_{12} = \tau_{21} = \frac{M_\infty \mu}{\text{Re}} (\xi_y u_\xi + \eta_y u_\eta + \xi_x v_\xi + \eta_x v_\eta) \quad (2.31)$$

$$\dot{Q}_1 = -\frac{M_\infty \mu}{\text{RePr}(\gamma - 1)} \{ \xi_x (a^2)_\xi + \eta_x (a^2)_\eta \} \quad (2.32)$$

$$\dot{Q}_2 = -\frac{M_\infty \mu}{\text{RePr}(\gamma - 1)} \{ \xi_y (a^2)_\xi + \eta_y (a^2)_\eta \}. \quad (2.33)$$

The ideal gas equation of state is still given by (2.16).

In the Navier-Stokes equations, Stokes' hypothesis, $\lambda + (2/3)\mu = 0$, is used for bulk viscosity. Also, γ is taken as 1.4 and Pr is taken as 0.72. Sutherland's law for molecular viscosity,

$$\mu = \frac{\tilde{\mu}}{\tilde{\mu}_\infty} = \left(\frac{\tilde{T}}{\tilde{T}_\infty} \right)^{3/2} \left(\frac{\tilde{T}_\infty + \tilde{c}}{\tilde{T} + \tilde{c}} \right) \quad (2.34)$$

is employed, with $\tilde{T}_\infty = 460^\circ\text{R}$ and $\tilde{c} = \text{Sutherland's constant} = 198.6^\circ\text{R}$.

2.2 Traveling-Wave Form of the Euler Equations

Many numerical methods for the Euler equations, including those discussed in Chapters 4 and 5, are based upon the knowledge that certain types of waves are emitted when two fluid parcels at different states interact. The directions and strengths of these waves define the way in which information is propagated through the domain.

In the upwind-differencing method, care is taken that numerical information is propagated similarly. It is therefore instructive to look at traveling-wave solutions

to the Euler equations. Upwind-differencing also applies to the convective and pressure terms of the Navier-Stokes equations. The viscous terms of the Navier-Stokes equations are always centrally-differenced.

The Euler equations are the same as the Navier-Stokes equations (2.1), (2.10), or (2.22), except that the viscous terms \mathbf{F}_v and \mathbf{G}_v (or \mathbf{F}_v^* and \mathbf{G}_v^*) are taken as zero. Starting with equation (2.10), the nondimensional Euler equations in two dimensions are written as

$$\frac{\partial \mathbf{U}}{\partial t} + \frac{\partial \mathbf{F}}{\partial x} + \frac{\partial \mathbf{G}}{\partial y} = 0, \quad (2.35)$$

where \mathbf{U} is given by (2.11) and \mathbf{F} and \mathbf{G} are given by (2.12). These equations can also be written in quasilinear form:

$$\frac{\partial \mathbf{W}}{\partial t} + \mathbf{A} \frac{\partial \mathbf{W}}{\partial x} + \mathbf{B} \frac{\partial \mathbf{W}}{\partial y} = 0, \quad (2.36)$$

where \mathbf{W} is the vector of primitive variables, $\mathbf{W} = [\rho, u, v, p]^T$, and \mathbf{A} and \mathbf{B} are the matrices

$$\mathbf{A} = \begin{bmatrix} u & \rho & 0 & 0 \\ 0 & u & 0 & 1/\rho \\ 0 & 0 & u & 0 \\ 0 & \rho a^2 & 0 & u \end{bmatrix} \quad (2.37)$$

$$\mathbf{B} = \begin{bmatrix} v & 0 & \rho & 0 \\ 0 & v & 0 & 0 \\ 0 & 0 & v & 1/\rho \\ 0 & 0 & \rho a^2 & v \end{bmatrix}. \quad (2.38)$$

Traveling-wave solutions to (2.36) are of the form

$$\mathbf{W}(x, y, t) = \mathbf{W}(x \cos \theta + y \sin \theta - \lambda t), \quad (2.39)$$

where θ is the angle that defines the direction of wave propagation. Insertion of (2.39) into (2.36) results in the eigenvalue problem

$$(\mathbf{A} \cos \theta + \mathbf{B} \sin \theta) \delta \mathbf{W} = \lambda \delta \mathbf{W}, \quad (2.40)$$

where δW is the amplitude of the traveling wave. The four eigenvalues and corresponding right eigenvectors yielded by (2.40) are:

$$\begin{aligned}\lambda_1 &= u\cos\theta + v\sin\theta + a \\ \lambda_2 &= u\cos\theta + v\sin\theta - a \\ \lambda_3 &= u\cos\theta + v\sin\theta \\ \lambda_4 &= u\cos\theta + v\sin\theta\end{aligned}\tag{2.41}$$

$$\begin{aligned}\mathbf{P}_1 &= \left[1, \frac{a}{\rho}\cos\theta, \frac{a}{\rho}\sin\theta, a^2\right]^T \\ \mathbf{P}_2 &= \left[1, -\frac{a}{\rho}\cos\theta, -\frac{a}{\rho}\sin\theta, a^2\right]^T \\ \mathbf{P}_3 &= \left[0, -\frac{a}{\rho}\sin\theta, \frac{a}{\rho}\cos\theta, 0\right]^T \\ \mathbf{P}_4 &= [1, 0, 0, 0]^T.\end{aligned}\tag{2.42}$$

These eigenvectors represent: (1) an acoustic disturbance that propagates with speed λ_1 , (2) an acoustic disturbance that propagates with speed λ_2 , (3) a shear wave, and (4) an entropy wave. The latter two waves travel with speed $\lambda_3 = \lambda_4$, the projection of the fluid velocity in the direction of wave propagation. Together the four eigenvectors form the matrix \mathbf{P} .

The characteristic variables for the quasilinear form of the Euler equations can be computed from

$$\delta W^* = \mathbf{P}^{-1}\delta W,\tag{2.43}$$

where

$$\mathbf{P}^{-1} = \begin{bmatrix} 0 & \frac{\rho\cos\theta}{2a} & \frac{\rho\sin\theta}{2a} & \frac{1}{2a^2} \\ 0 & -\frac{\rho\cos\theta}{2a} & -\frac{\rho\sin\theta}{2a} & \frac{1}{2a^2} \\ 0 & -\frac{\rho\sin\theta}{a} & \frac{\rho\cos\theta}{a} & 0 \\ 1 & 0 & 0 & -\frac{1}{a^2} \end{bmatrix}.\tag{2.44}$$

This gives

$$\delta W^* = \begin{bmatrix} \frac{1}{2} \left\{ \frac{\delta p}{a^2} + (\cos\theta \frac{\rho}{a} \delta u + \sin\theta \frac{\rho}{a} \delta v) \right\} \\ \frac{1}{2} \left\{ \frac{\delta p}{a^2} - (\cos\theta \frac{\rho}{a} \delta u + \sin\theta \frac{\rho}{a} \delta v) \right\} \\ -\frac{\rho}{a} \sin\theta \delta u + \frac{\rho}{a} \cos\theta \delta v \\ \delta \rho - \frac{\delta p}{a^2} \end{bmatrix}.\tag{2.45}$$

Rewriting the Euler equations in terms of the characteristic variables yields

$$\frac{\partial \mathbf{W}^*}{\partial t} + \mathbf{P}^{-1} \mathbf{A} \mathbf{P} \frac{\partial \mathbf{W}^*}{\partial x} + \mathbf{P}^{-1} \mathbf{B} \mathbf{P} \frac{\partial \mathbf{W}^*}{\partial y} = 0. \quad (2.46)$$

In general, \mathbf{A} and \mathbf{B} do not commute, so a single θ that simultaneously diagonalizes both matrices cannot be found. This is indicative of the fact that in multidimensional flow the waves propagate in infinitely many directions. As numerical schemes are limited to modeling the flow with a finite number of waves, the choice of wave type and direction of propagation is not trivial. The more “physically relevant” the wave types and directions of propagation are, the more likely the model will be able to resolve a wide variety of flow features accurately. As will be discussed in Chapter 4, grid-aligned wave models choose the grid-normal direction as the direction of wave propagation. The grid-independent model derived in Chapter 5 allows waves to travel in directions dictated by the physics of the local flowfield.

CHAPTER 3

SPATIAL AND TEMPORAL DISCRETIZATION

3.1 Finite Volume Formulation

The Navier-Stokes equations are cast in finite-volume form, which is a discretization of the integral form of the equations. Equation (2.22) is integrated over a computational cell of area A :

$$\iint_A \frac{\partial \mathbf{U}^*}{\partial t} dA + \iint_A \{(\mathbf{F}^* - \mathbf{F}_v^*)_\xi + (\mathbf{G}^* - \mathbf{G}_v^*)_\eta\} = 0. \quad (3.1)$$

The second integral is converted to a line integral over the boundary S of the cell using Gauss' Theorem,

$$\iint_A \frac{\partial \mathbf{U}^*}{\partial t} dA + \oint_S \{(\mathbf{F}^* - \mathbf{F}_v^*) d\eta - (\mathbf{G}^* - \mathbf{G}_v^*) d\xi\} = 0. \quad (3.2)$$

The first integral can be interpreted as the rate of change of the vector of *averaged* conserved quantities (2.23) within each cell. The factor $1/J$ can be taken outside of the time derivative when the computational grid is fixed with respect to time. The line integral is discretized over the four faces of each cell; in the present formulation it is assumed that each cell is a quadrilateral. The final result is the finite-volume form of the Navier-Stokes equations:

$$\begin{aligned} \frac{1}{J} \frac{\partial \mathbf{U}_{i,j}}{\partial t} &= -(\delta_\xi \mathbf{F}^* + \delta_\eta \mathbf{G}^*)_{i,j} + (\delta_\xi \mathbf{F}_v^* + \delta_\eta \mathbf{G}_v^*)_{i,j} \\ &\equiv \mathbf{S}_{i,j}, \end{aligned} \quad (3.3)$$

where the right-hand side residual term \mathbf{S} is made up of an inviscid and a viscous part: $\mathbf{S} = \mathbf{S}_i + \mathbf{S}_v$, and

$$\begin{aligned}\{\delta_\xi(\cdot)\}_{i,j} &= (\cdot)_{i+\frac{1}{2},j} - (\cdot)_{i-\frac{1}{2},j} \\ \{\delta_\eta(\cdot)\}_{i,j} &= (\cdot)_{i,j+\frac{1}{2}} - (\cdot)_{i,j-\frac{1}{2}}.\end{aligned}\quad (3.4)$$

The terms $(\mathbf{F}^*)_{i\pm 1/2,j}$ and $(\mathbf{G}^*)_{i,j\pm 1/2}$ represent the inviscid fluxes normal to the cell faces. These fluxes are evaluated at the cell faces through the use of a *flux function*, which is the primary concern of the present study. A grid-aligned flux function is discussed in Chapter 4, and a grid-independent flux function is derived and discussed in Chapter 5. The second parenthetical expression in (3.3) consists of viscous fluxes at the cell faces, which are determined via central differencing.

The following relationships exist between the Jacobian J , the metric derivatives, and the cell areas and cell face lengths in the finite-volume formulation:

$$1/J = \text{Cell area } A$$

$$\xi_i/(J\Delta s_\xi) = i \text{ component } (i = x \text{ or } y) \text{ of unit normal to } \xi=\text{constant cell face} \\ \text{of length } \Delta s_\xi$$

$$\eta_i/(J\Delta s_\eta) = i \text{ component } (i = x \text{ or } y) \text{ of unit normal to } \eta=\text{constant cell face} \\ \text{of length } \Delta s_\eta.$$

Using these relations, it is sometimes convenient to write (3.3) in a different form:

$$\frac{\partial \mathbf{U}_{i,j}}{\partial t} = -\frac{1}{A_{i,j}} \left\{ \sum_{\ell=1}^4 \Phi_\ell \Delta s_\ell - \sum_{\ell=1}^4 (\Phi_v)_\ell \Delta s_\ell \right\}_{i,j} \quad (3.5)$$

$$\Phi = \begin{bmatrix} \rho q_g \\ \rho q_g u + p \cos \theta_g \\ \rho q_g v + p \sin \theta_g \\ \rho q_g H \end{bmatrix} \quad (3.6)$$

$$\Phi_v = \begin{bmatrix} 0 \\ \tau_{11} \cos \theta_g + \tau_{12} \sin \theta_g \\ \tau_{21} \cos \theta_g + \tau_{22} \sin \theta_g \\ (V_j \tau_{1j} - \dot{Q}_1) \cos \theta_g + (V_j \tau_{2j} - \dot{Q}_2) \sin \theta_g \end{bmatrix}, \quad (3.7)$$

where θ_g is the angle that the outward-pointing cell face normal makes with the x -axis, and q_g is the outward velocity normal to the cell face, given by

$$q_g = u \cos \theta_g + v \sin \theta_g. \quad (3.8)$$

Furthermore, $\Phi_\ell \Delta s_\ell$ is the inviscid normal flux at cell face ℓ , evaluated through the use of a flux function. The term $(\Phi_v)_\ell \Delta s_\ell$ is the viscous normal flux at cell face ℓ , evaluated using central differencing.

3.2 Explicit Time-Marching

The solution for the vector of averaged conserved variables can be advanced explicitly in time using an m -stage time-stepping scheme. Using the definition of \mathbf{S} from (3.3), the scheme is:

$$\begin{aligned} \mathbf{U}^{(1)} &= \mathbf{U}^{(n)} + \eta_1 J \Delta t \mathbf{S}^{(n)} \\ \mathbf{U}^{(2)} &= \mathbf{U}^{(n)} + \eta_2 J \Delta t \mathbf{S}^{(1)} \\ &\vdots \\ \mathbf{U}^{(m-1)} &= \mathbf{U}^{(n)} + \eta_{m-1} J \Delta t \mathbf{S}^{(m-2)} \\ \mathbf{U}^{(n+1)} &= \mathbf{U}^{(n)} + J \Delta t \mathbf{S}^{(m-1)}, \end{aligned} \quad (3.9)$$

where the superscript n denotes the current time level and $n+1$ denotes the next time level. The superscripts $1, 2, \dots, m-1$ denote intermediate time levels or stages. The coefficients $\eta_1, \eta_2, \dots, \eta_{m-1}$ are chosen to give desirable damping and stability properties for the scheme. When $m=1$ the scheme reduces to the one-step forward-Euler time-stepping scheme

$$\mathbf{U}^{(n+1)} = \mathbf{U}^{(n)} + J \Delta t \mathbf{S}^{(n)}. \quad (3.10)$$

3.3 Implicit Time-Marching

The solution can also be advanced implicitly in time. Starting with (3.3), the left-hand side is discretized to first-order in time and the right-hand side terms are taken at time level $n + 1$:

$$\frac{1}{J} \frac{\Delta_t \mathbf{U}^{(n)}}{\Delta t} = -(\delta_\xi \mathbf{F}^* + \delta_\eta \mathbf{G}^*)^{(n+1)} + (\delta_\xi \mathbf{F}_v^* + \delta_\eta \mathbf{G}_v^*)^{(n+1)}, \quad (3.11)$$

where $\Delta_t \mathbf{U}^{(n)} = \mathbf{U}^{(n+1)} - \mathbf{U}^{(n)}$. The right-hand side terms are linearized about time level n :

$$\begin{aligned} \mathbf{F}^{*(n+1)} &= \mathbf{F}^{*(n)} + \frac{\partial \mathbf{F}^*}{\partial \mathbf{U}} \Delta_t \mathbf{U}^{(n)} \\ \mathbf{G}^{*(n+1)} &= \mathbf{G}^{*(n)} + \frac{\partial \mathbf{G}^*}{\partial \mathbf{U}} \Delta_t \mathbf{U}^{(n)} \end{aligned} \quad (3.12)$$

$$\begin{aligned} \mathbf{F}_v^{*(n+1)} &= \mathbf{F}_v^{*(n)} + \left\{ \frac{\partial \mathbf{F}_v^*}{\partial \mathbf{U}}(\xi) + \frac{\partial \mathbf{F}_v^*}{\partial \mathbf{U}}(\eta) \right\} \Delta_t \mathbf{U}^{(n)} \\ \mathbf{G}_v^{*(n+1)} &= \mathbf{G}_v^{*(n)} + \left\{ \frac{\partial \mathbf{G}_v^*}{\partial \mathbf{U}}(\xi) + \frac{\partial \mathbf{G}_v^*}{\partial \mathbf{U}}(\eta) \right\} \Delta_t \mathbf{U}^{(n)}. \end{aligned} \quad (3.13)$$

Notice that in (3.13) the viscous matrix Jacobian terms are split in two parts: a matrix with derivatives that are a function of ξ only and a matrix with derivatives a function of η only.

The spatial cross-derivative terms $\delta_\xi[\mathbf{F}_v^*]_{\mathbf{U}}(\eta)$ and $\delta_\eta[\mathbf{G}_v^*]_{\mathbf{U}}(\xi)$ are treated explicitly, lagged in time, while $\delta_\xi[\mathbf{F}_v^*]_{\mathbf{U}}(\xi)$ and $\delta_\eta[\mathbf{G}_v^*]_{\mathbf{U}}(\eta)$ as well as the inviscid matrix Jacobian terms are treated implicitly. Equation (3.11) becomes:

$$\begin{aligned} & \left[\frac{\mathbf{I}}{J \Delta t} + \delta_\xi \left(\frac{\partial \mathbf{F}^*}{\partial \mathbf{U}} - \frac{\partial \mathbf{F}_v^*}{\partial \mathbf{U}}(\xi) \right) + \delta_\eta \left(\frac{\partial \mathbf{G}^*}{\partial \mathbf{U}} - \frac{\partial \mathbf{G}_v^*}{\partial \mathbf{U}}(\eta) \right) \right] \Delta_t \mathbf{U}^{(n)} \\ &= - \left(\delta_\xi (\mathbf{F}^* - \mathbf{F}_v^*) + \delta_\eta (\mathbf{G}^* - \mathbf{G}_v^*) \right) \\ & \quad + \left(\delta_\xi \frac{\partial \mathbf{F}_v^*}{\partial \mathbf{U}}(\eta) + \delta_\eta \frac{\partial \mathbf{G}_v^*}{\partial \mathbf{U}}(\xi) \right) \Delta_t \mathbf{U}^{(n-1)} \\ & \equiv \mathbf{T}. \end{aligned} \quad (3.14)$$

The equations are approximately factored and solved for $\Delta_t \mathbf{U}^{(n)}$ in two sweeps

$$\begin{aligned} \left[\frac{\mathbf{I}}{J\Delta t} + \delta_\xi \left(\frac{\partial \mathbf{F}^*}{\partial \mathbf{U}} - \frac{\partial \mathbf{F}_v^*}{\partial \mathbf{U}}(\xi) \right) \right] \Delta_t \mathbf{U}' &= \mathbf{T} \\ \left[\frac{\mathbf{I}}{J\Delta t} + \delta_\eta \left(\frac{\partial \mathbf{G}^*}{\partial \mathbf{U}} - \frac{\partial \mathbf{G}_v^*}{\partial \mathbf{U}}(\eta) \right) \right] \Delta_t \mathbf{U}^{(n)} &= \frac{\mathbf{I}}{J\Delta t} \Delta_t \mathbf{U}', \end{aligned} \quad (3.15)$$

where the term $\Delta_t \mathbf{U}'$ is an intermediate result. The conserved variables then are updated at the cell centers using

$$\mathbf{U}^{(n+1)} = \mathbf{U}^{(n)} + \Delta_t \mathbf{U}^{(n)}. \quad (3.16)$$

The implicit spatial derivatives of the convective and pressure terms are spatially first-order accurate, resulting in block tridiagonal inversions for each sweep. For example, the left-hand side of the first sweep in (3.15) is a block banded matrix with the following structure for the i th row:

$$\left[\dots, 0, -\mathbf{A}_{i-\frac{1}{2}}^+, (\mathbf{A}_{i+\frac{1}{2}}^+ - \mathbf{A}_{i-\frac{1}{2}}^- + \mathbf{I}/(J\Delta t)), \mathbf{A}_{i+\frac{1}{2}}^-, 0, \dots \right], \quad (3.17)$$

where $\mathbf{A}_{i+1/2}^+$ represents the portion of $(\partial \mathbf{F}^*/\partial \mathbf{U} - \partial \mathbf{F}_v^*/\partial \mathbf{U}(\xi))$ at cell face $i + \frac{1}{2}$ contributed from the left (the i th cell), and $\mathbf{A}_{i+1/2}^-$ represents the portion contributed from the right (the $(i + 1)$ st cell). Each of these terms can be divided into inviscid and viscous parts:

$$\begin{aligned} \mathbf{A}_{i+\frac{1}{2}}^+ &= (\mathbf{A}_i)^+ + (\mathbf{A}_v)^+_{i+\frac{1}{2}} \\ \mathbf{A}_{i+\frac{1}{2}}^- &= (\mathbf{A}_i)^- + (\mathbf{A}_v)^-_{i+\frac{1}{2}}. \end{aligned} \quad (3.18)$$

Since the viscous terms are centrally differenced, the viscous Jacobians are given by

$$\begin{aligned} (\mathbf{A}_v)^+_{i+\frac{1}{2}} &= \frac{1}{2} \left(\frac{\partial \mathbf{F}_v^*}{\partial \mathbf{U}}(\xi) \right)_i \\ (\mathbf{A}_v)^-_{i+\frac{1}{2}} &= \frac{1}{2} \left(\frac{\partial \mathbf{F}_v^*}{\partial \mathbf{U}}(\xi) \right)_{i+1}. \end{aligned} \quad (3.19)$$

However, using the flux functions discussed in Chapters 4 and 5, it is very difficult and computationally tedious to obtain exact expressions for the inviscid flux Jacobians. Instead the following approximations are used:

$$\begin{aligned} (\mathbf{A}_i)^+_{i+\frac{1}{2}} &= \frac{1}{2} \left\{ \left(\frac{\partial \mathbf{F}^*}{\partial \mathbf{U}} \right)_i + \left| \frac{\partial \hat{\mathbf{F}}^*}{\partial \mathbf{U}} \right|_{i+\frac{1}{2}} \right\} \\ (\mathbf{A}_i)^-_{i+\frac{1}{2}} &= \frac{1}{2} \left\{ \left(\frac{\partial \mathbf{F}^*}{\partial \mathbf{U}} \right)_{i+1} - \left| \frac{\partial \hat{\mathbf{F}}^*}{\partial \mathbf{U}} \right|_{i+\frac{1}{2}} \right\}. \end{aligned} \quad (3.20)$$

The second terms within the braces are Roe-averaged terms at the interfaces, equal to

$$\left| \frac{\partial \hat{\mathbf{F}}^*}{\partial \mathbf{U}} \right| = \hat{\mathbf{R}} \left| \hat{\mathbf{A}} \right| \hat{\mathbf{R}}^{-1}, \quad (3.21)$$

where $\hat{\mathbf{R}}$ and $\hat{\mathbf{A}}$ are defined in Chapter 4, along with the Roe-averaged (hatted) variables.

The left-hand side of the second sweep of (3.15) is of similar form to (3.17). However, the \mathbf{A} 's are replaced by \mathbf{B} 's, which are functions of derivatives of \mathbf{G}^* and \mathbf{G}_v^* . The approximate inviscid Jacobians for the second sweep are given by

$$\begin{aligned} (\mathbf{B}_i)^+_{j+\frac{1}{2}} &= \frac{1}{2} \left\{ \left(\frac{\partial \mathbf{G}^*}{\partial \mathbf{U}} \right)_j + \left| \frac{\partial \hat{\mathbf{G}}^*}{\partial \mathbf{U}} \right|_{j+\frac{1}{2}} \right\} \\ (\mathbf{B}_i)^-_{j+\frac{1}{2}} &= \frac{1}{2} \left\{ \left(\frac{\partial \mathbf{G}^*}{\partial \mathbf{U}} \right)_{j+1} - \left| \frac{\partial \hat{\mathbf{G}}^*}{\partial \mathbf{U}} \right|_{j+\frac{1}{2}} \right\}. \end{aligned} \quad (3.22)$$

The appropriateness of using (3.20) and (3.22) for the left-hand side inviscid Jacobians when the grid-independent model is employed on the right-hand side is discussed within the context of stability in Chapter 6.

CHAPTER 4

GRID-ALIGNED FLUX FUNCTION

Most flux computations have two distinct stages: a projection stage and an evolution stage. In the projection stage of a finite-volume scheme, left and right states are obtained at interfaces via interpolation along grid lines from surrounding cell-center values. For first-order spatial differencing, the state variables (normally the primitive variables) are extrapolated to a cell face $k + \frac{1}{2}$ (where k represents the grid index i or j of a structured 2-D grid) using

$$\begin{aligned}\mathbf{W}_L &= \mathbf{W}_k \\ \mathbf{W}_R &= \mathbf{W}_{k+1}.\end{aligned}\tag{4.1}$$

For higher-order spatial differencing,

$$\begin{aligned}\mathbf{W}_L &= \mathbf{W}_k + \frac{1}{4}[(1 - \kappa)\Delta_- + (1 + \kappa)\Delta_+]_k \\ \mathbf{W}_R &= \mathbf{W}_{k+1} - \frac{1}{4}[(1 - \kappa)\Delta_+ + (1 + \kappa)\Delta_-]_{k+1},\end{aligned}\tag{4.2}$$

where

$$\begin{aligned}(\Delta_+)_k &= \mathbf{W}_{k+1} - \mathbf{W}_k \\ (\Delta_-)_k &= \mathbf{W}_k - \mathbf{W}_{k-1}.\end{aligned}\tag{4.3}$$

When $\kappa = -1$, (4.2) gives second-order fully upwind spatial differencing, while $\kappa = 1/3$ gives third-order upwind-biased differencing. Limiting of higher-order terms can be employed at this stage of the grid-aligned flux function in order to eliminate numerically-induced oscillations near regions of high gradient such as shock waves.

In the evolution stage of the flux computation, the flux at the interface is computed as a function of the left and right states obtained from (4.1) or (4.2). As discussed in the introduction, in a Godunov-type solver this stage numerically models the physical process defined by the one-dimensional Riemann problem. This process is illustrated in figure 4.1. At time zero, a membrane separating the left and right states ruptures, and a shock wave, a contact discontinuity, and an expansion fan propagate into either side, with strengths and velocities depending upon the initial conditions. The flux at the interface can be determined when these strengths and velocities are known.

The grid-aligned solver of Roe [4] is an approximate Riemann solver, in which the Euler equations are linearized about an average state and solved exactly. When used in a two-dimensional scheme the eigenvectors of the matrix in the linearized system of equations, representing acoustic, shear, and entropy waves, are assumed to propagate in a direction normal to the grid interface.

The grid-aligned flux function of Roe, representing the inviscid flux Φ (3.6) in the two-dimensional Euler equations or Navier-Stokes equations, is given below. The flux at a face is computed using any one of the following three equations (all three are equivalent):

$$\begin{aligned}
 \Phi &= \Phi_{\mathbf{L}} + \sum_{\hat{\lambda}_k < 0} \hat{\lambda}_k \hat{\Omega}_k \hat{\mathbf{R}}_k \\
 \Phi &= \Phi_{\mathbf{R}} - \sum_{\hat{\lambda}_k > 0} \hat{\lambda}_k \hat{\Omega}_k \hat{\mathbf{R}}_k \\
 \Phi &= \frac{1}{2} (\Phi_{\mathbf{L}} + \Phi_{\mathbf{R}}) - \frac{1}{2} \sum_{k=1}^4 |\hat{\lambda}_k| \hat{\Omega}_k \hat{\mathbf{R}}_k.
 \end{aligned} \tag{4.4}$$

The last equation can be interpreted as a central difference term plus a dissipation

term. The eigenvectors are given by

$$\begin{aligned}
\hat{\mathbf{R}}_1 &= [1, \hat{u} + \hat{a}\cos\theta_g, \hat{v} + \hat{a}\sin\theta_g, \hat{H} + \hat{a}\hat{q}_g]^T \\
\hat{\mathbf{R}}_2 &= [1, \hat{u} - \hat{a}\cos\theta_g, \hat{v} - \hat{a}\sin\theta_g, \hat{H} - \hat{a}\hat{q}_g]^T \\
\hat{\mathbf{R}}_3 &= [0, -\hat{a}\sin\theta_g, \hat{a}\cos\theta_g, \hat{a}\hat{r}_g]^T \\
\hat{\mathbf{R}}_4 &= [1, \hat{u}, \hat{v}, \frac{1}{2}(\hat{u}^2 + \hat{v}^2)]^T
\end{aligned} \tag{4.5}$$

for the equations written in conserved-variable form. These eigenvectors correspond to the eigenvectors \mathbf{P}_k given by (2.42) for the equations written in primitive-variable form, and represent, respectively, +acoustic, -acoustic, shear, and entropy waves. The k th wave of this system has a strength $\hat{\Omega}_k$, evaluated as the k th component of the vector $\hat{\Omega}$:

$$\hat{\Omega} = \begin{bmatrix} \frac{1}{2\hat{q}^2} (\Delta p + \hat{\rho}\hat{a}\Delta q_g) \\ \frac{1}{2\hat{a}^2} (\Delta p - \hat{\rho}\hat{a}\Delta q_g) \\ \frac{1}{\hat{a}} \hat{\rho} \Delta r_g \\ \frac{1}{\hat{a}^2} (\hat{a}^2 \Delta \rho - \Delta p) \end{bmatrix}, \tag{4.6}$$

where $\Delta(\cdot) = (\cdot)_R - (\cdot)_L$ and

$$\begin{aligned}
q_g &= u\cos\theta_g + v\sin\theta_g \\
r_g &= -u\sin\theta_g + v\cos\theta_g.
\end{aligned} \tag{4.7}$$

The wavespeeds are

$$\begin{aligned}
\hat{\lambda}_1 &= \hat{q}_g + \hat{a} \\
\hat{\lambda}_2 &= \hat{q}_g - \hat{a} \\
\hat{\lambda}_3 &= \hat{q}_g \\
\hat{\lambda}_4 &= \hat{q}_g.
\end{aligned} \tag{4.8}$$

The Roe-averaged values (denoted by hats) are defined as

$$\begin{aligned}
\hat{\rho} &= \sqrt{\rho_L \rho_R} \\
\hat{u} &= u_L w + u_R (1 - w) \\
\hat{v} &= v_L w + v_R (1 - w) \\
\hat{H} &= H_L w + H_R (1 - w) \\
\hat{a} &= \sqrt{(\gamma - 1) \left[\hat{H} - \frac{1}{2} (\hat{u}^2 + \hat{v}^2) \right]},
\end{aligned} \tag{4.9}$$

where $w = \sqrt{\rho_L}/(\sqrt{\rho_L} + \sqrt{\rho_R})$. The values \hat{q}_g and \hat{r}_g in (4.5) and (4.8) are given by (4.7) with Roe-averaged values \hat{u} and \hat{v} replacing u and v .

The wavestrengths $\hat{\Omega}_k$ given in (4.6) result from satisfying the equation

$$\Delta \mathbf{U} = \mathbf{U}_R - \mathbf{U}_L = \sum_{k=1}^4 \hat{\Omega}_k \hat{\mathbf{R}}_k. \quad (4.10)$$

In other words, the sum of the eigenvectors times their corresponding strengths describes the difference in states across an interface. A geometric interpretation of this will be given below. Since the $\hat{\mathbf{R}}_k$ are eigenvectors of the matrix $\partial \hat{\Phi} / \partial \mathbf{U}$, the additional equality

$$\Delta \hat{\Phi} = \hat{\Phi}_R - \hat{\Phi}_L = \sum_{k=1}^4 \hat{\lambda}_k \hat{\Omega}_k \hat{\mathbf{R}}_k \quad (4.11)$$

is also satisfied. It can be seen from (4.4) that if all of the wavespeeds are positive in the grid-normal direction, the flux computed at the interface will be the flux from the left, $\hat{\Phi}_L$. Conversely, if all the wavespeeds are negative, the flux will be computed as $\hat{\Phi}_R$. In both cases this amounts to the upwind choice for $\hat{\Phi}$.

The grid-aligned model can be interpreted in a geometric sense by looking at the effects of the acoustic and shear waves in $(\Delta u, \Delta v, \Delta p)$ -space. (The entropy wave only causes a change in the density, so it is not representable in this space.) Grid-aligned acoustic waves cause a change in velocity in the grid-normal direction, along with a proportional change in the pressure and density according to the relations:

$$\begin{aligned} \text{+acoustic : } & \frac{\delta p}{\rho a^2} = \frac{\delta u}{a \cos \theta_g} = \frac{\delta v}{a \sin \theta_g} = \frac{\delta \rho}{\rho} \\ \text{-acoustic : } & \frac{\delta p}{\rho a^2} = -\frac{\delta u}{a \cos \theta_g} = -\frac{\delta v}{a \sin \theta_g} = \frac{\delta \rho}{\rho}. \end{aligned} \quad (4.12)$$

These expressions can be derived easily from the acoustic wave eigenvectors \mathbf{P}_1 and \mathbf{P}_2 in (2.42) with θ taken as θ_g . Figure 4.2(a) depicts the assumed propagation direction of the + and - acoustic waves at an arbitrary grid interface, the normal

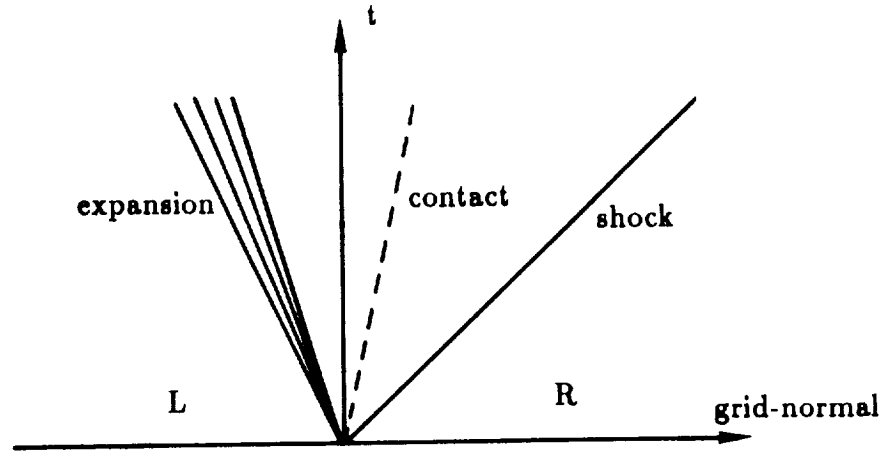
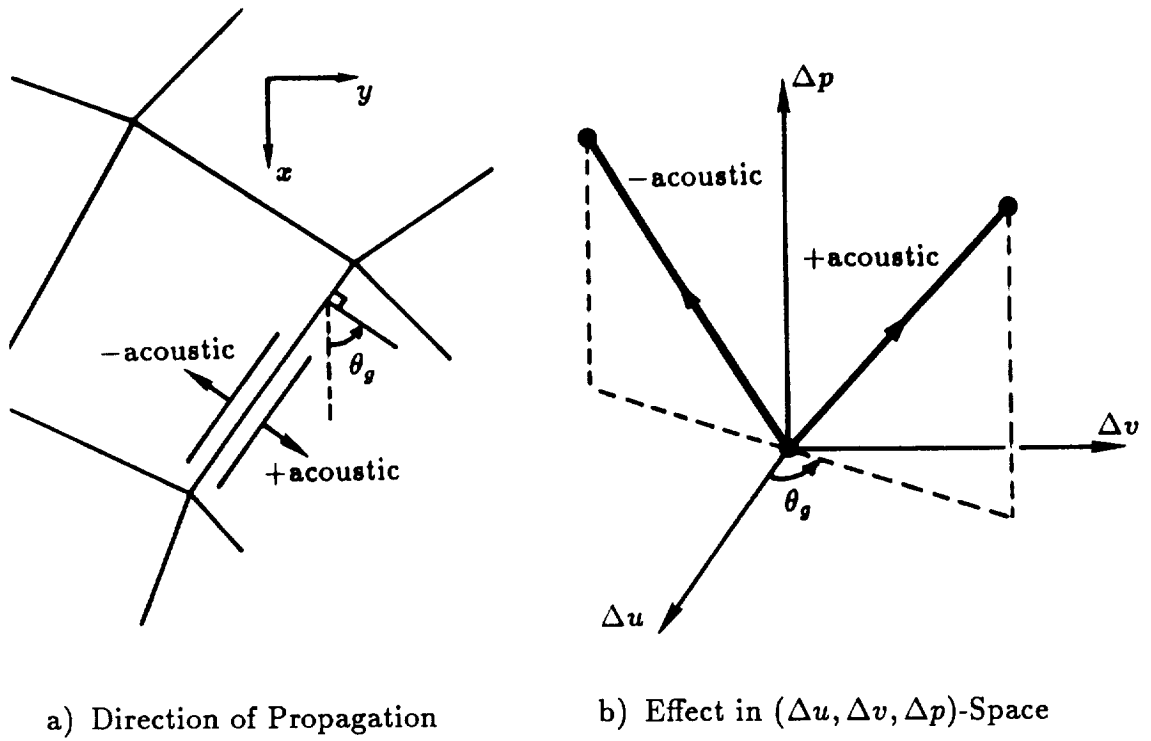


Figure 4.1: The Riemann Problem



a) Direction of Propagation

b) Effect in $(\Delta u, \Delta v, \Delta p)$ -Space

Figure 4.2: Grid-Aligned Acoustic Waves

of which makes an angle θ_g with the x -axis, while figure 4.2(b) shows the effect of each of the waves in $(\Delta u, \Delta v, \Delta p)$ -space. The change in density $\Delta\rho$ is not pictured. In this second figure, the state at a given point in space changes by an amount $(\Delta u, \Delta v, \Delta p)$ as drawn by the heavy solid lines when a + or - acoustic wave passes. The length of the lines in state space are representative of the strengths of the waves.

The shear wave also propagates in the grid-normal direction, as shown in figure 4.3(a). However, shear waves cause a change in velocity *normal* to the direction in which they propagate, with no change in the pressure or density; this is dictated by the relation:

$$\text{shear : } -\frac{\delta u}{a \sin \theta_g} = \frac{\delta v}{a \cos \theta_g}; \quad (4.13)$$

This expression can be derived from \mathbf{P}_3 in (2.42). Hence the velocity change across a shear wave is in the direction shown in figure 4.3(b) in $(\Delta u, \Delta v, \Delta p)$ -space, where again the length of the line in this space is proportional to the strength of the wave.

Given a left state L and a right state R at an interface, the grid-aligned flux function of Roe interprets the difference with a combination of +acoustic, -acoustic, shear, and entropy waves such that (4.10) is satisfied. An example is drawn in figure 4.4. L, the representation of the state to the left of the cell face, is placed at the origin, and the right state R is located at $(\Delta u, \Delta v, \Delta p)$, as determined by the differences between L and R. All waves propagate in the θ_g -direction, represented by the vertical plane in the figure. The effects of the two acoustic waves and the shear wave are shown in the figure as heavy solid lines (the entropy wave is not represented). The acoustic waves cause a change in velocity in the θ_g -direction along with proportional changes in pressure, while the shear wave causes a change in velocity normal to θ_g . Since this is a linearized model,

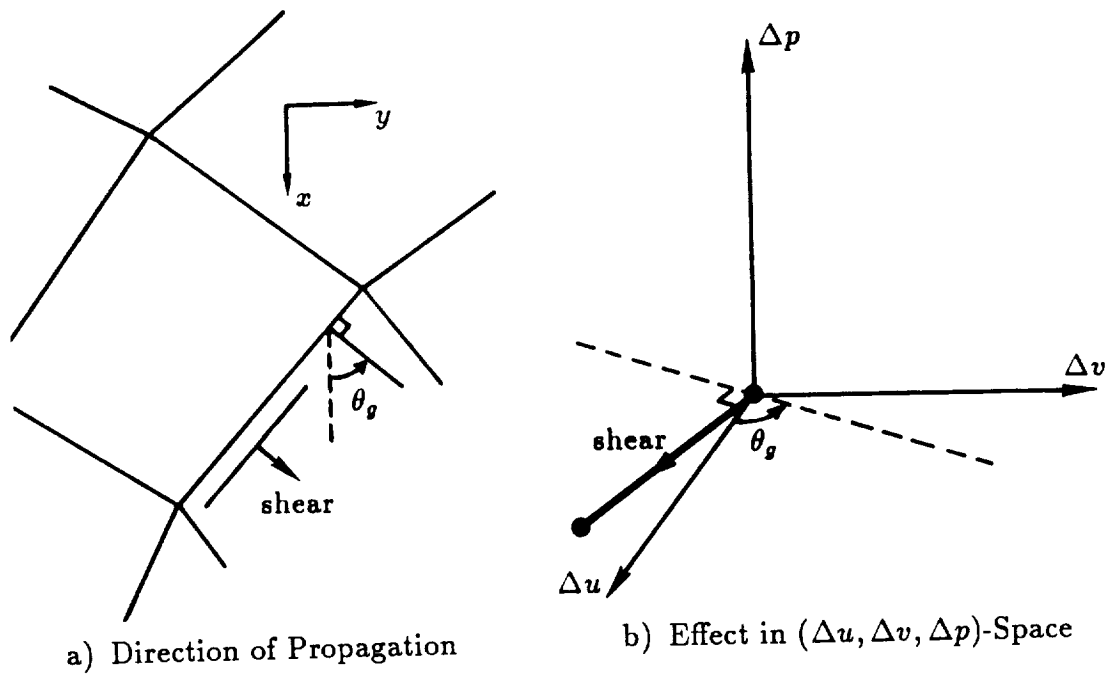


Figure 4.3: Grid-Aligned Shear Wave

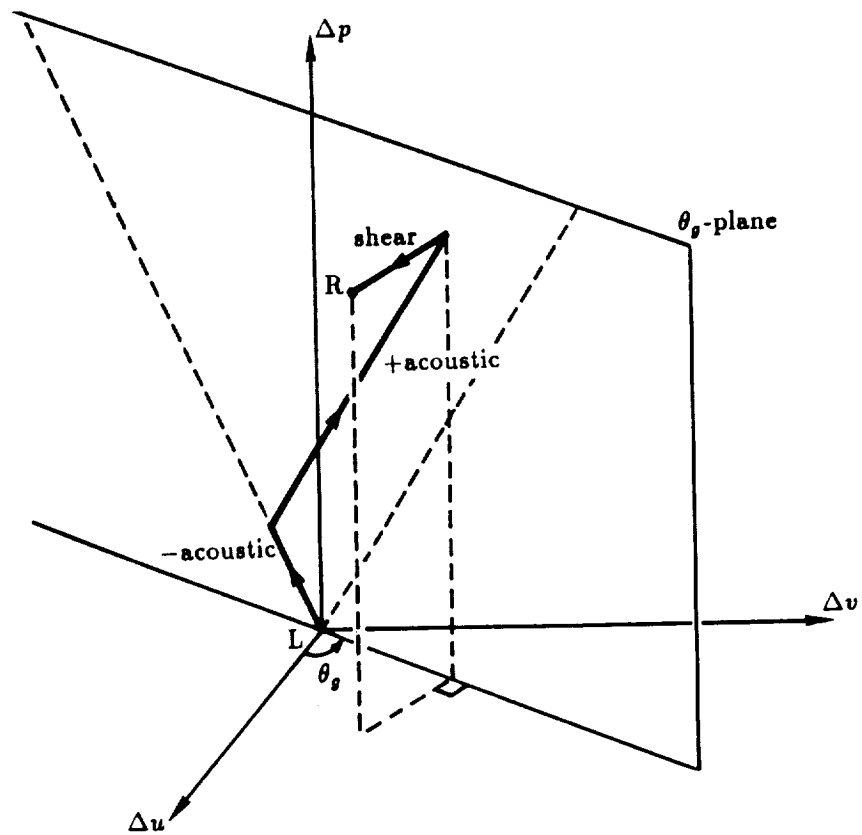
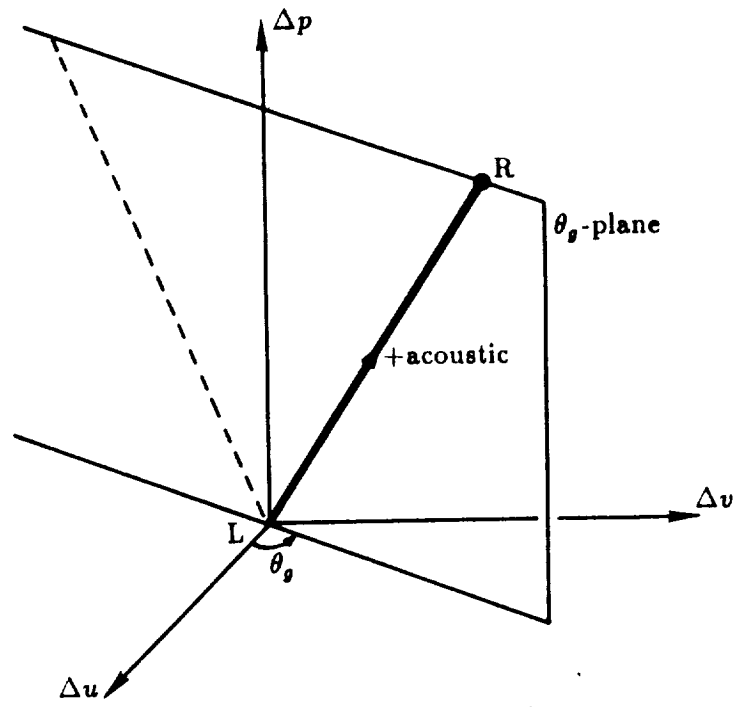


Figure 4.4: Grid-Aligned Wave Decomposition

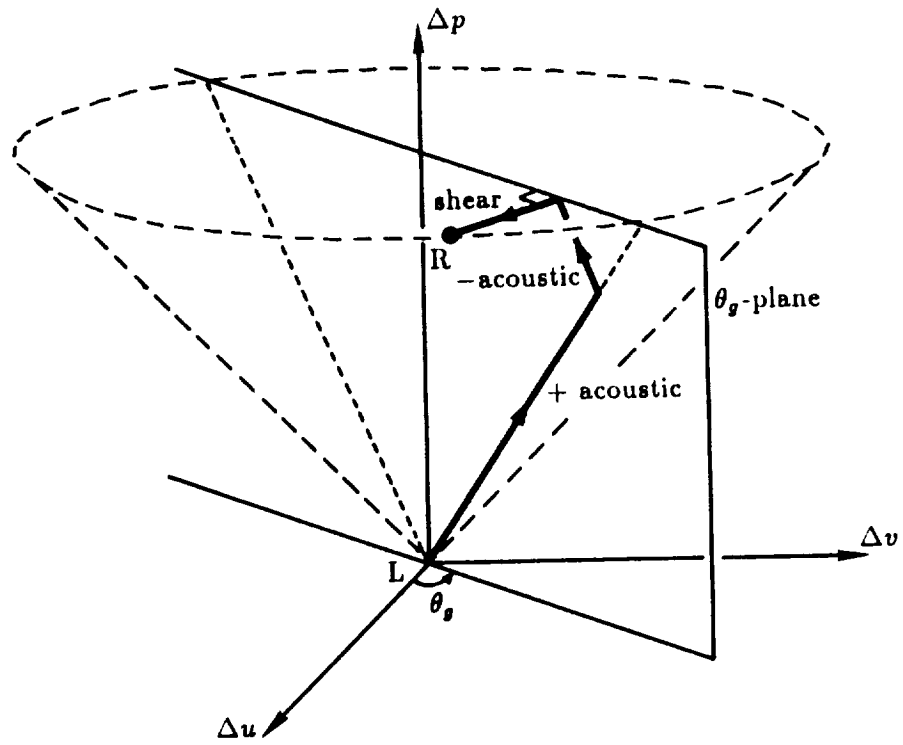
the order in which the waves are taken is immaterial, and there is no difference between shock-type and expansion-type acoustic waves.

A steady shock wave that is aligned with a mesh interface is interpreted correctly by this model, as depicted in figure 4.5(a): the difference between the states L and R is described essentially by a single acoustic wave. However, the grid-aligned method smears a shock wave that lies oblique to the mesh. The difference in states in this case cannot be described by a single acoustic wave since the velocity-difference vector $\vec{V}_R - \vec{V}_L$ is *not* in the θ_g -direction. Hence the model must introduce both a shear wave as well as an acoustic wave of the opposite family to account for the discrepancy in $\Delta\vec{V}$. These extra waves, depicted in figure 4.5(b), add dissipation which smears the numerical solution. The cone delineated by the dashed lines in figure 4.5(b) is defined by the effects of all acoustic waves of a given strength and arbitrary orientation, with one endstate at L. It is referred to in Chapter 5 as the “acoustic cone.”

The grid-aligned flux function can also misinterpret a pure shear wave that lies oblique to a grid face. This situation is illustrated in figures 4.6(a) and (b). In figure 4.6(a) left and right states are indicated on a $(\Delta u, \Delta v, \Delta p)$ -diagram. There is no pressure difference between L and R, and the velocity-difference vector $\vec{V}_R - \vec{V}_L$ is at some angle other than 90° to the θ_g -direction (it would be normal to the θ_g -direction for the case of a shear wave aligned with the grid face, and the wave model would interpret the difference with a single shear wave of the type shown in figure 4.3(b)). The grid-aligned scheme now includes two acoustic waves in its interpretation of the difference in states. These waves add dissipation which smears the numerical solution. Additionally, if the wavespeeds associated with each of these acoustic waves are of opposite sign, then the scheme computes a flux at the interface with a pressure that is different from the correct pressure by an amount Δp , as shown in figure 4.6(b). In this figure, a time history of the



a) Aligned With Grid



b) Oblique to Grid

Figure 4.5: Grid-Aligned Wave Model Interpretation of a Single Shock Wave

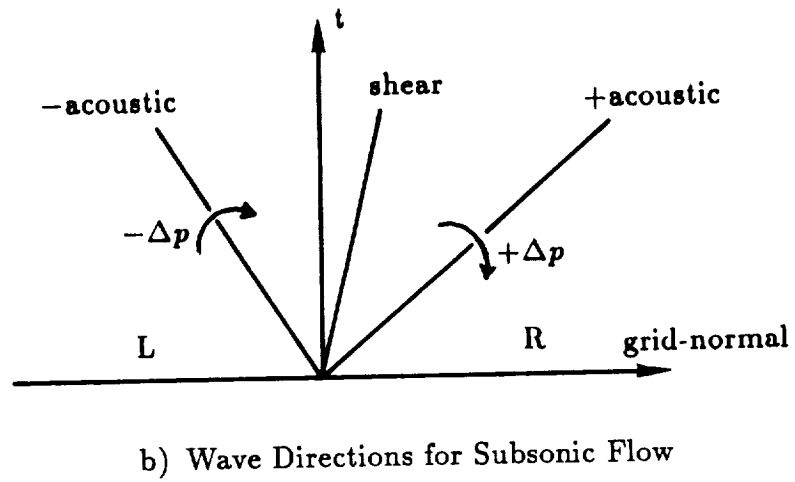
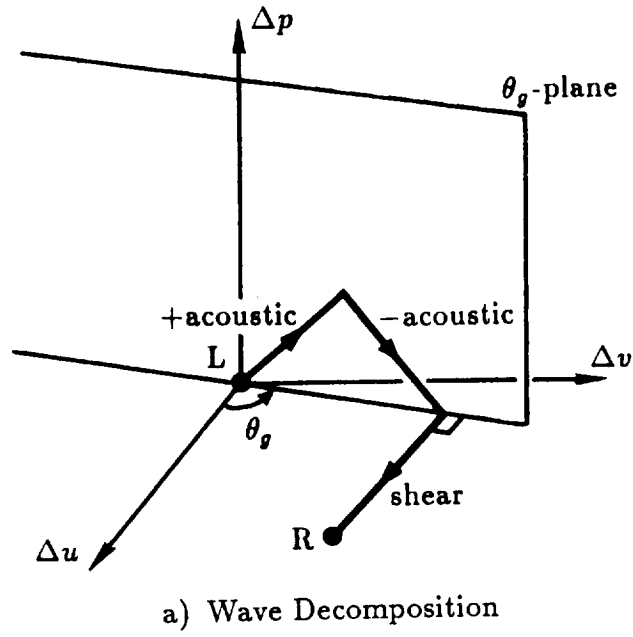


Figure 4.6: Grid-Aligned Wave Model Interpretation of an Oblique Shear Wave

wave locations is drawn in relation to the grid-normal direction. The flux at the interface is computed as either the left flux plus the change across left-running waves or, equivalently, the right flux minus the change across the right-running waves. In either case it can be seen that the incorrect pressure is given at the interface.

CHAPTER 5

GRID-INDEPENDENT FLUX FUNCTION

The motivation behind the development of the present grid-independent approximate Riemann solver is the desire to be able to recognize and appropriately model both shock and shear waves regardless of their orientation with respect to the grid. The method for accomplishing this goal is described in this chapter.

The *projection* stage of the flux computation is identical to that of the grid-aligned method described in Chapter 4. In other words, primitive variables are interpolated along grid lines using either (4.1) or (4.2). This stage is different from that of many of the grid-independent methods under development by other researchers, which assign values to faces via interpolation in some grid-independent direction. However, since this latter type of interpolation can be very complicated and costly, it was decided early in the development of the current scheme only to use grid-aligned interpolation.

It is then the job of the flux function to make use of this information in an intelligent fashion during the *evolution* stage of the flux computation. This is accomplished in the following way:

- (1) A primary direction of wave propagation is chosen that is more representative of the physics of the local flowfield than the direction defined by the grid.

- (2) The difference in L and R states is represented with a combination of

acoustic, shear, and entropy waves.

(3) A flux is formed in the grid-normal direction from the information propagating in the physically-relevant grid-independent direction.

The next three sections of this chapter will describe in detail the methods chosen to satisfy each of these three aspects.

5.1 Wave Propagation Direction

The primary wave propagation direction used at each interface is the velocity-difference direction

$$\theta_d = \tan^{-1} \left(\frac{\Delta v}{\Delta u} \right), \quad (5.1)$$

defined from $-\frac{\pi}{2}$ to $\frac{\pi}{2}$. This represents the angle that the velocity-difference vector, $\Delta \vec{V}$, makes with the x -axis, as shown in figure 5.1 for two arbitrary states \vec{V}_L and \vec{V}_R . The θ_d -direction is chosen because in this frame the velocity components \bar{v}_L and \bar{v}_R normal to θ_d are equal, as depicted in figure 5.2. Therefore the differences between the two states can be interpreted either as a compression normal to θ_d or a shear aligned with θ_d . In figure 5.3(a), the former interpretation is illustrated. The velocity components tangential to the shock are equal (only the normal component is affected by the shock). Also, the shock wave could be propagating with some velocity \bar{u}_S in the θ_d -direction. The value of \bar{u}_S is zero for a steady shock wave. A shear-wave interpretation of the difference in velocities is illustrated in figure 5.3(b). Here, the shear wave propagates with velocity $\bar{v}_L = \bar{v}_R$ in the $(\theta_d + \frac{\pi}{2})$ -direction. This propagation velocity is zero for a steady shear wave.

Other choices for the dominant wave-propagation direction, as used by other researchers (*e.g.* [24]) for grid-independent models include the pressure-gradient direction and the flow direction. The first of these is not used in the present

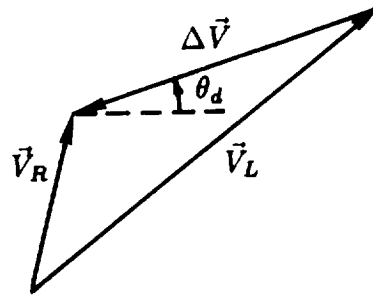


Figure 5.1: Velocity-Difference Vector

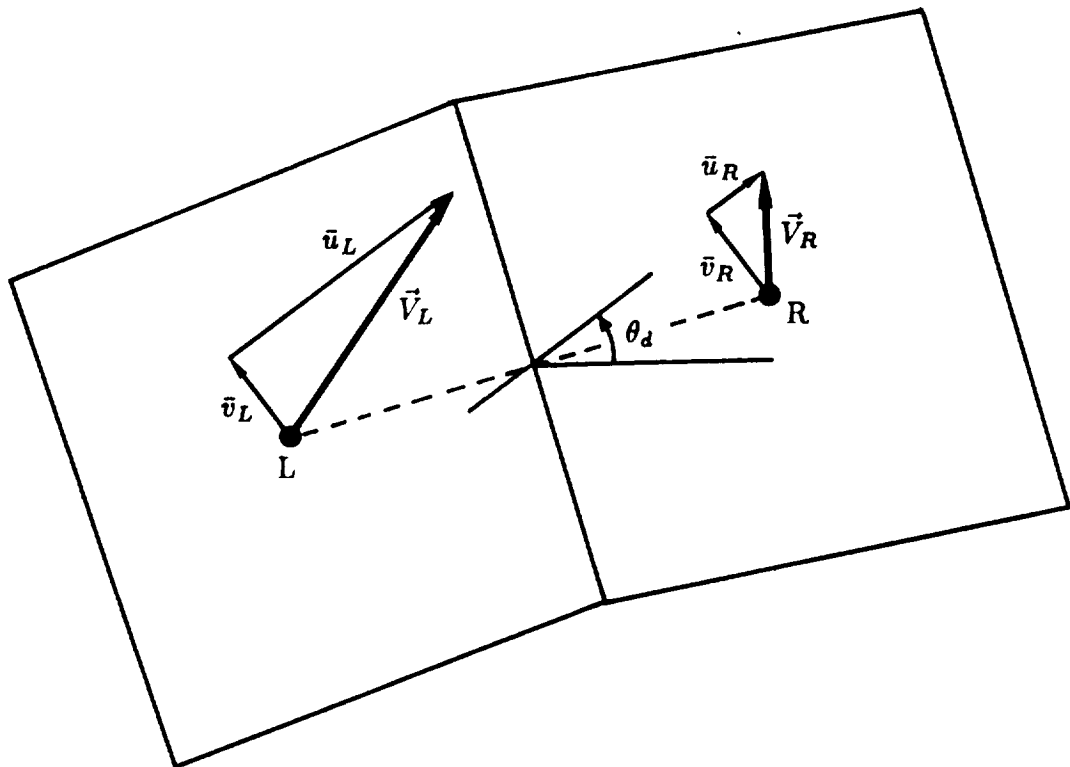


Figure 5.2: Components of \vec{V}_L and \vec{V}_R in the θ_d -Frame

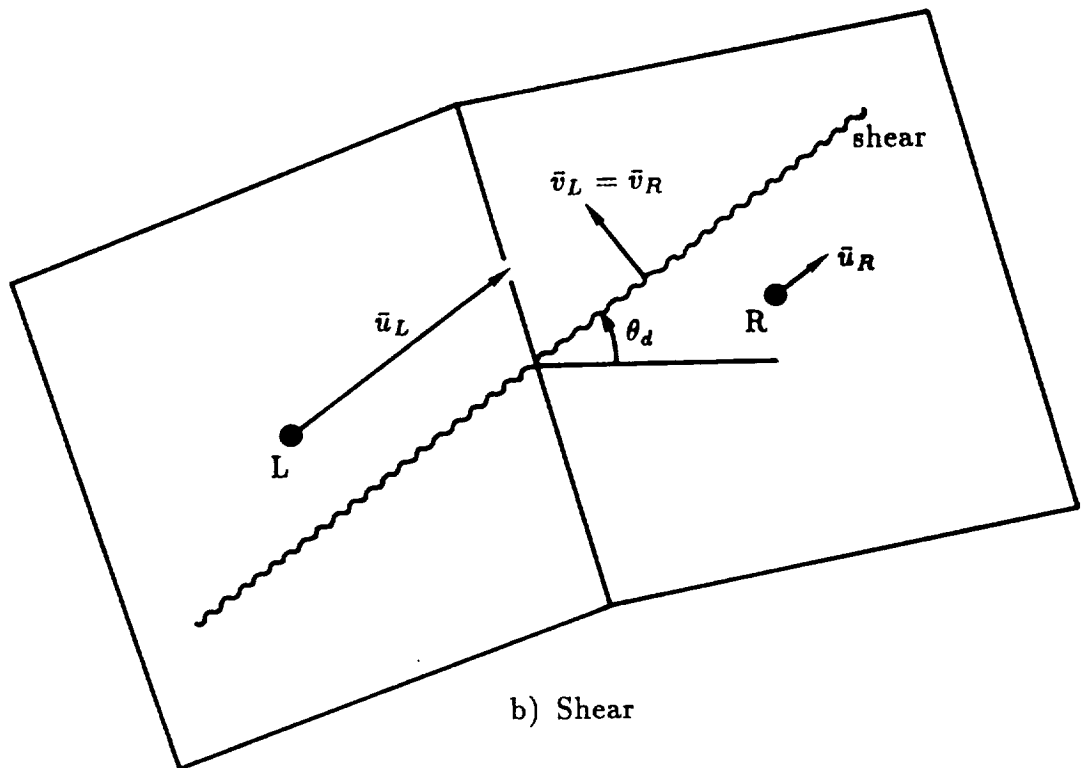
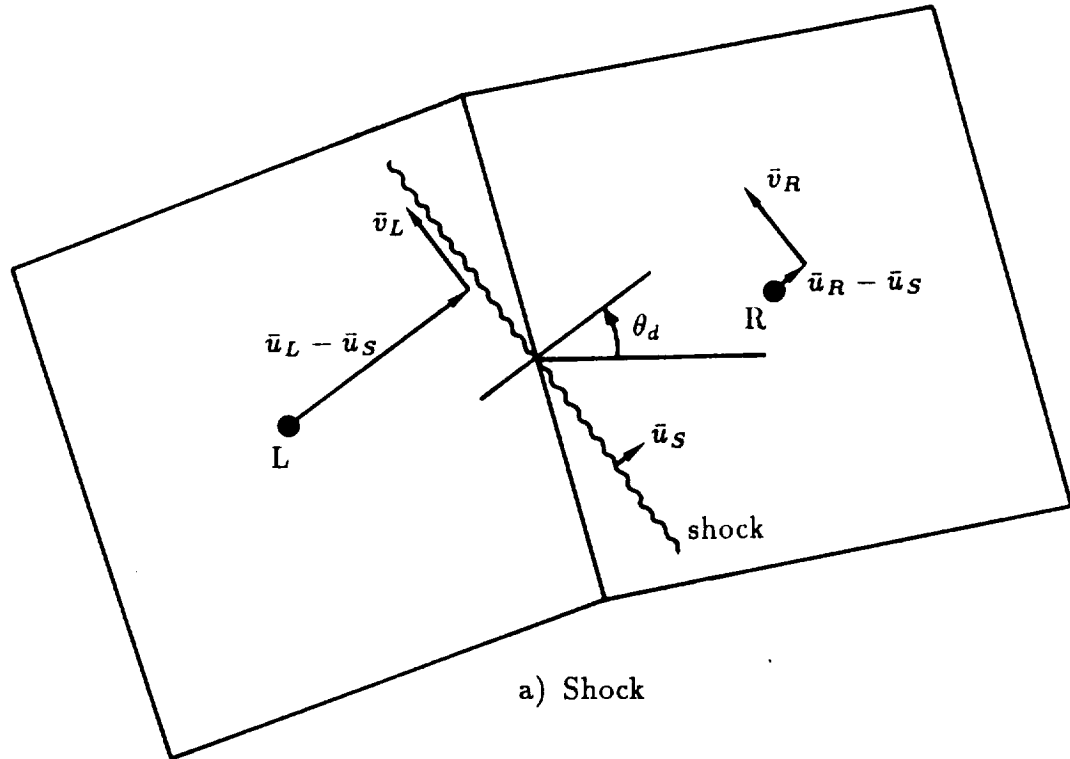


Figure 5.3: Interpretations of Velocity Difference

investigation because its calculation requires data from surrounding cell centers, and not just the left and right states interpolated along grid lines. The flow direction is not used because it is not normal to a shock that lies oblique to the flow. Hence the resolution is not as crisp as with the use of the velocity-difference direction.

5.2 Wave Decomposition

Since there are two interpretations (figures 5.3(a) and (b)) of a velocity difference in terms of a dominant wave, it is necessary that the method be able to model both types of waves as well as have some way of determining which is a better description of the true situation. The present method models both types by describing the difference in states by a combination of two acoustic waves and an entropy wave propagating in the θ_d -direction, and an additional shear wave propagating in the $(\theta_d + \frac{\pi}{2})$ -direction. This shear wave causes a change in velocity *parallel* to θ_d with no change in pressure, thus allowing for sharp capturing of oblique shear waves of the type depicted in figure 5.3(b). The propagation and effect of this $(\theta_d + \frac{\pi}{2})$ shear wave is shown in figures 5.4(a) and (b). The propagation and effect of the $+$ and $-\theta_d$ acoustic waves is shown in figures 5.5(a) and (b) for comparison.

The representation in primitive-variable form of the $(\theta_d + \frac{\pi}{2})$ shear wave is \mathbf{P}_3 in (2.42) with $\theta = \theta_d + \frac{\pi}{2}$:

$$\mathbf{P}_{(\theta_d + \pi/2)_{shear}} = \begin{bmatrix} 0 \\ -\frac{a}{\rho} \sin(\theta_d + \frac{\pi}{2}) \\ \frac{a}{\rho} \cos(\theta_d + \frac{\pi}{2}) \\ 0 \end{bmatrix} = \begin{bmatrix} 0 \\ -\frac{a}{\rho} \cos\theta_d \\ -\frac{a}{\rho} \sin\theta_d \\ 0 \end{bmatrix}. \quad (5.2)$$

The two acoustic waves and the entropy wave are represented by \mathbf{P}_1 , \mathbf{P}_2 , and \mathbf{P}_4 in (2.42), with $\theta = \theta_d$.

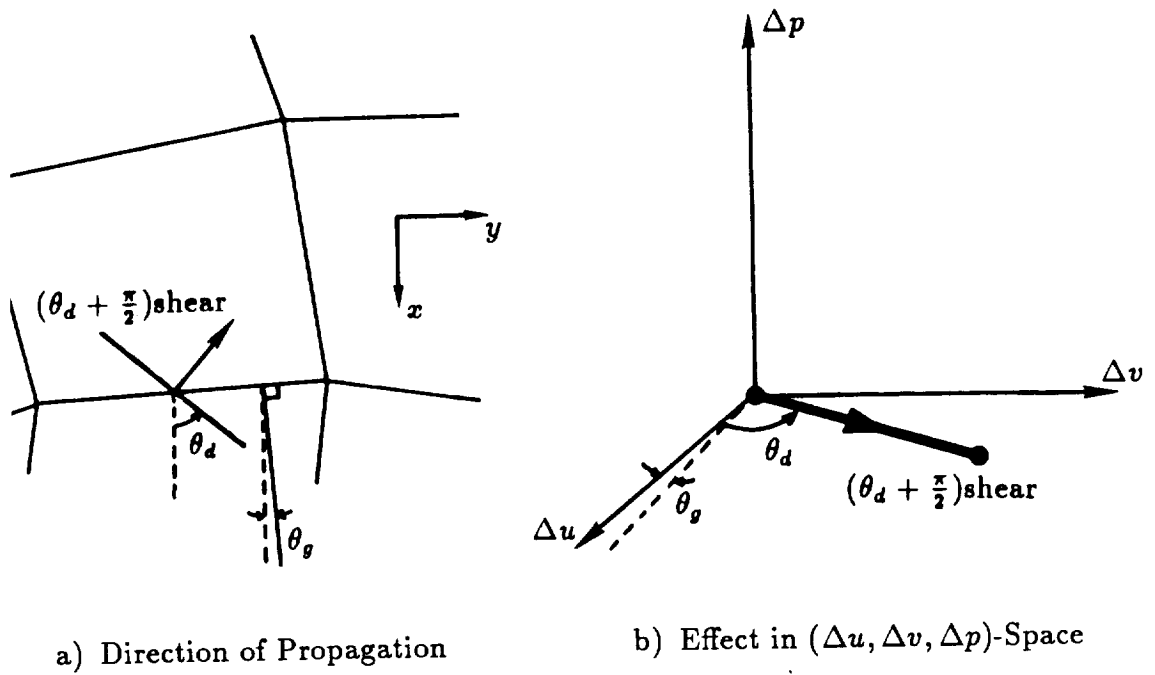


Figure 5.4: $(\theta_d + \frac{\pi}{2})$ Shear Wave

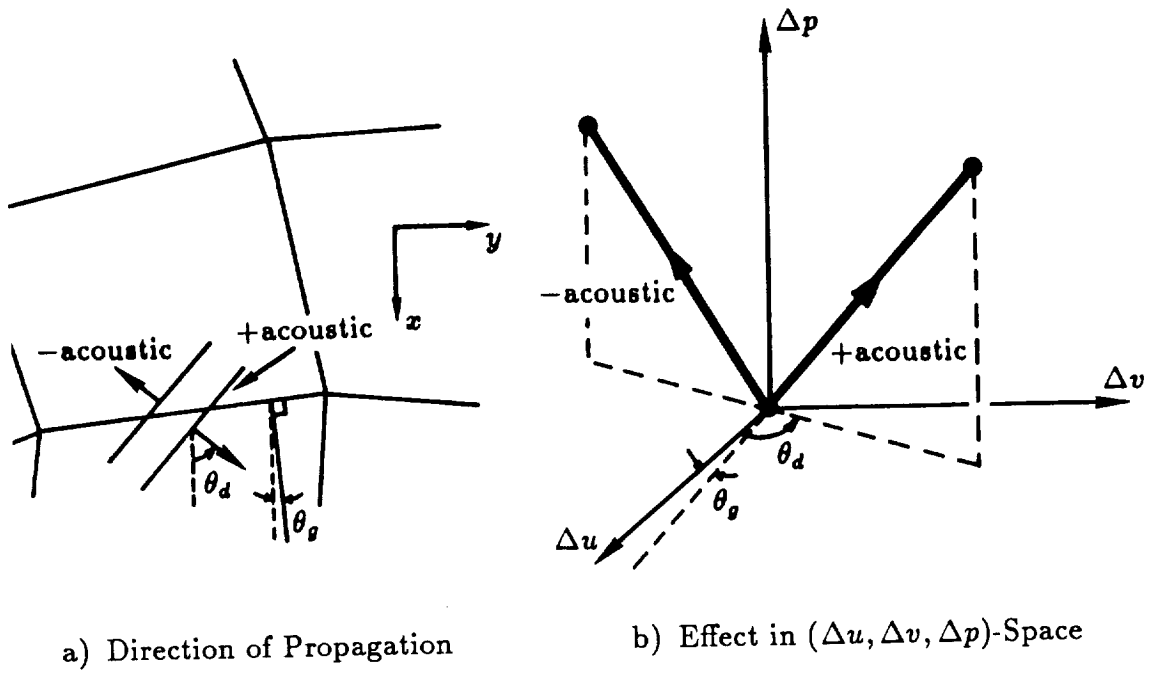


Figure 5.5: $\pm\theta_d$ Acoustic Waves

The strengths of the four waves must satisfy

$$\Delta \mathbf{W} = \sum_{k=1}^4 \hat{\Omega}_k \hat{\mathbf{P}}_k, \quad (5.3)$$

or, equivalently,

$$\Delta \mathbf{U} = \sum_{k=1}^4 \hat{\Omega}_k \hat{\mathbf{R}}_k, \quad (5.4)$$

where the $\hat{\mathbf{R}}_k$ represent the waves for the conserved-variable form of the equations:

$$\begin{aligned} \hat{\mathbf{R}}_1 &= [1, \hat{u} + \hat{a} \cos \theta_d, \hat{v} + \hat{a} \sin \theta_d, \hat{H} + \hat{a} \hat{q}_d]^T \\ \hat{\mathbf{R}}_2 &= [1, \hat{u} - \hat{a} \cos \theta_d, \hat{v} - \hat{a} \sin \theta_d, \hat{H} - \hat{a} \hat{q}_d]^T \\ \hat{\mathbf{R}}_3 &= [0, -\hat{a} \cos \theta_d, -\hat{a} \sin \theta_d, -\hat{a} \hat{q}_d]^T \\ \hat{\mathbf{R}}_4 &= [1, \hat{u}, \hat{v}, \frac{1}{2}(\hat{u}^2 + \hat{v}^2)]^T. \end{aligned} \quad (5.5)$$

The hatted variables are still Roe-averaged variables defined by (4.9), and $\hat{q}_d = \hat{u} \cos \theta_d + \hat{v} \sin \theta_d$. Unlike in the grid-aligned method described in Chapter 4, there is not a unique combination of these four waves that satisfies (5.4). Although the entropy wave always has a strength of

$$\hat{\Omega}_4 = \frac{1}{\hat{a}^2} (\hat{a}^2 \Delta \rho - \Delta p), \quad (5.6)$$

(the same as $\hat{\Omega}_4$ in (4.6) for the grid-aligned model), there is some freedom in picking the strengths of the other three waves. This reflects, as mentioned earlier, that there are two types of dominant waves, represented by figures 5.3(a) and 5.3(b), that could describe the difference in states. The model must choose which type is more likely to be representative of the true situation, and allow that type of wave to dominate in the numerical representation.

Two methods that allow the model to choose the “correct” wave type are described here. Both are a function of the pressure difference across the interface: if a large pressure difference exists, it is more likely that an acoustic wave is

primarily responsible for the difference in states. Similarly, a small difference in pressure indicates that a shear wave more likely is the primary wave.

The first method is termed the minimum-pathlength model, and is implemented by choosing the combination of waves such that the pathlength in $(\Delta u, \Delta v, \Delta p)$ -space is minimized. This minimum-pathlength model is accomplished by using either two acoustic waves and an entropy wave or one acoustic, a $(\theta_d + \frac{\pi}{2})$ shear, and an entropy wave. (Recall that the entropy wave is not representable in $(\Delta u, \Delta v, \Delta p)$ -space.) The choice depends on the location in phase space of the right state R relative to the cone defined by all acoustic waves emanating from L. By definition, R lies in the θ_d -plane. If R resides inside the “acoustic cone,” as is the case with R_1 in figure 5.6, then two acoustic waves describe the shortest path. If R resides outside the cone, as represented by R_2 in the figure, then one acoustic and a $(\theta_d + \frac{\pi}{2})$ shear wave describe the shortest path. The mathematical conditions for R inside or outside the acoustic cone are:

$$\text{Inside : } (\Delta p)^2 \geq [\hat{\rho} \hat{a} (\Delta u \cos \theta_d + \Delta v \sin \theta_d)]^2 \quad (5.7)$$

$$\text{Outside : } (\Delta p)^2 < [\hat{\rho} \hat{a} (\Delta u \cos \theta_d + \Delta v \sin \theta_d)]^2. \quad (5.8)$$

The minimum-pathlength model always uses three waves out of a choice of four possible wave types to describe the difference in states.

A second strategy is to choose the strengths of the acoustic and shear waves such that the path is in some sense *closest* to the straight line connecting L and R in phase space. More specifically, the area between the waves (taken in a certain order) and the direct path L–R is minimized. This minimum-area model is due to Parpia [27]. A geometric representation is given in figure 5.7, where again the entropy wave, although present, is not pictured. If R lies inside the acoustic cone, like R_1 in the figure, then the path that minimizes the area (shaded region) is accomplished by two acoustic waves. If R lies outside the cone, as represented by

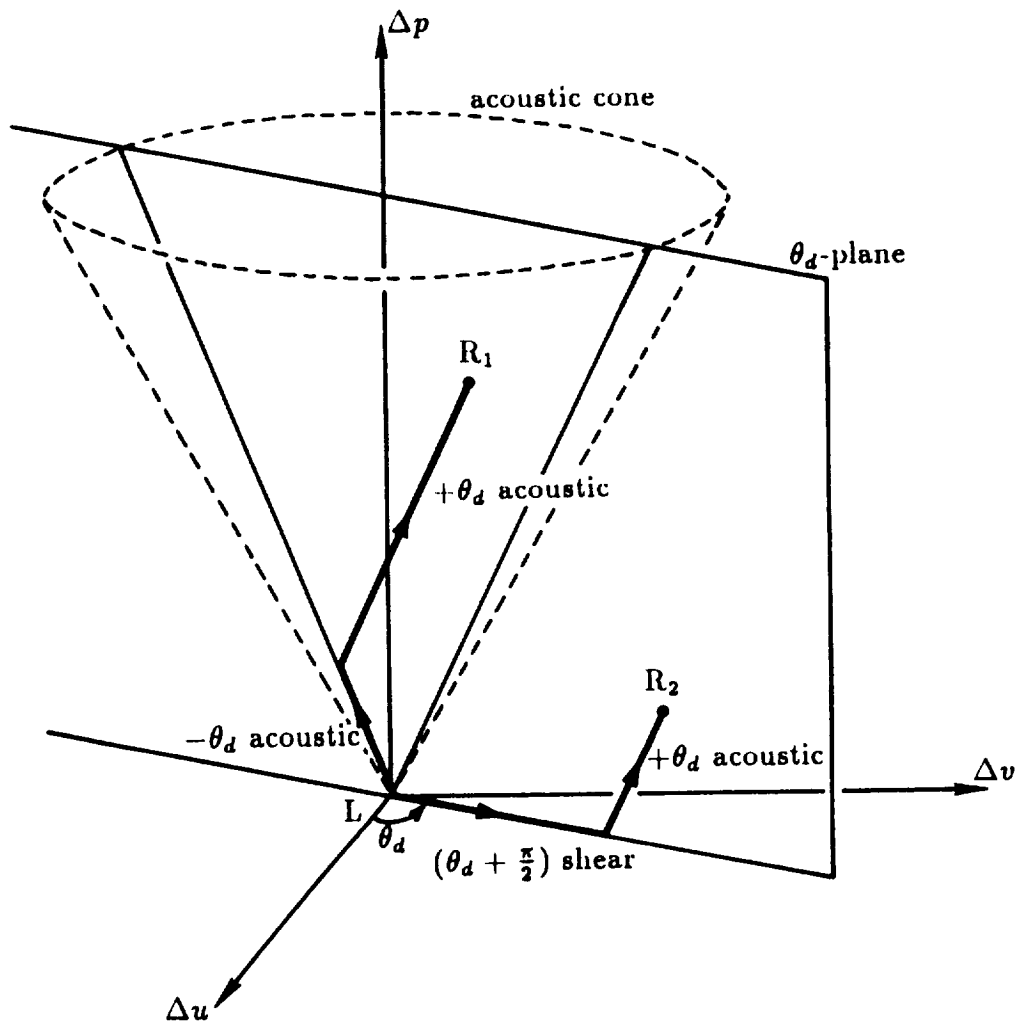


Figure 5.6: Minimum-Pathlength Model Wave Decomposition (Entropy Wave Not Pictured)

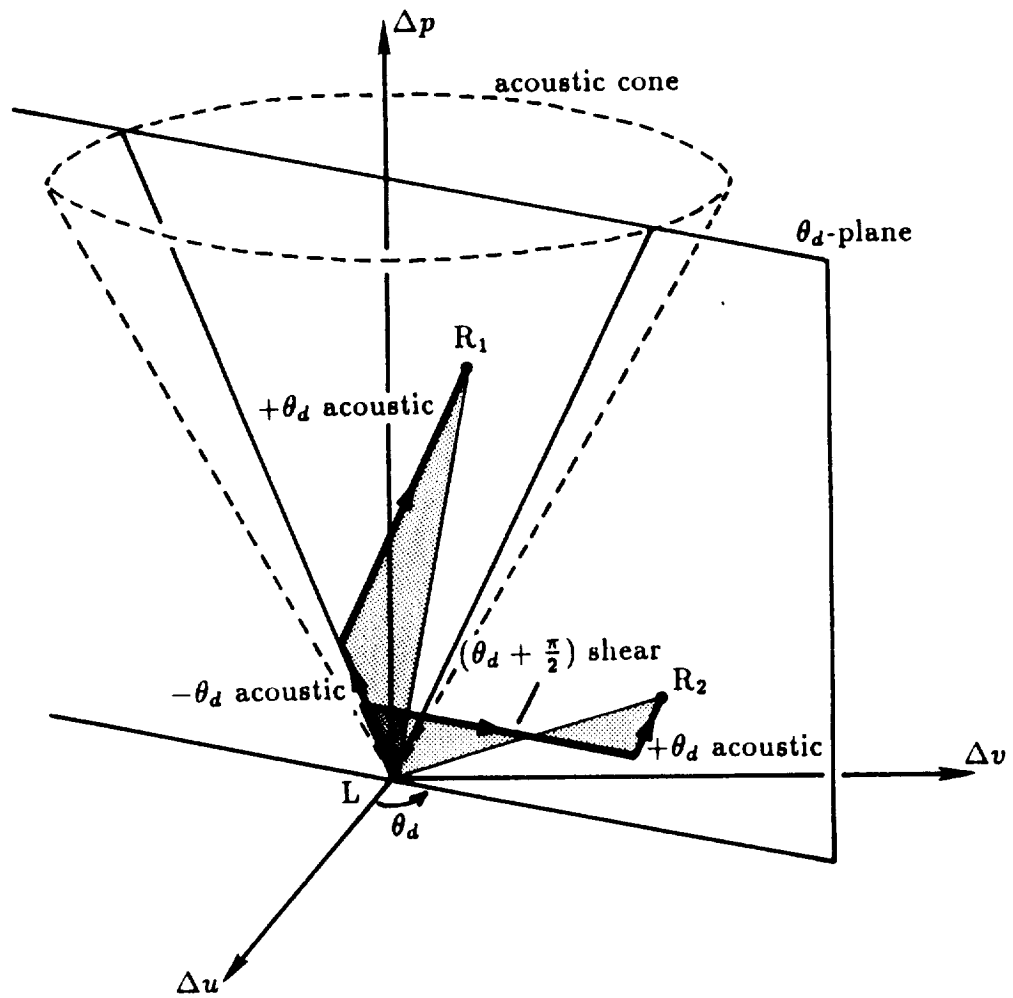


Figure 5.7: Minimum-Area Model Wave Decomposition (Entropy Wave Not Pictured)

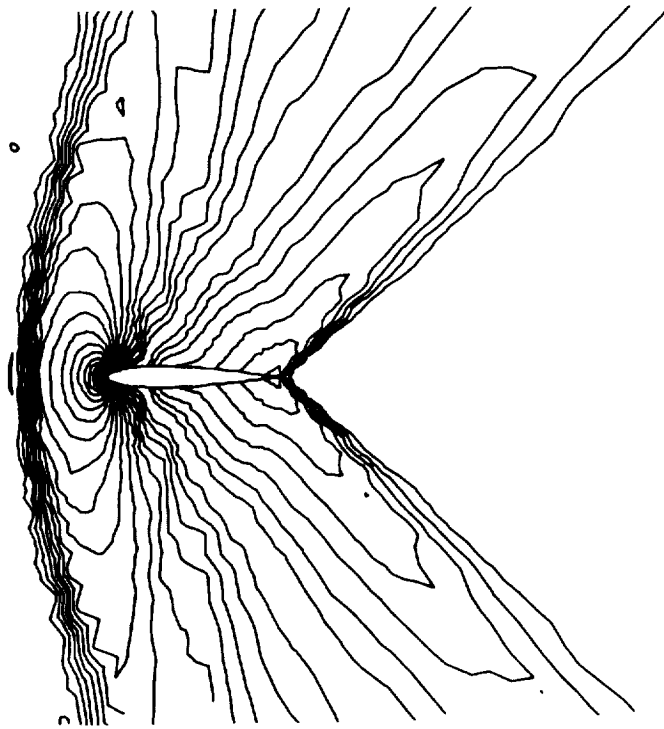
R_2 , then some combination of two acoustic waves and a $(\theta_d + \frac{\pi}{2})$ shear wave gives the minimum area. The exact expression will be given in the next section and is derived in Appendix A. The minimum-area model uses either three or four waves to describe the difference in states at each interface.

Numerical experiments show that both these models can produce nonlinear feedback that results in oscillatory flowfields. Small changes in the computed values of θ_d feed back into the solution, producing further changes in θ_d . An example of this is given in figures 5.8(a) and (b). This is an Euler computation of supersonic flow over an airfoil, to be discussed in greater detail in Chapter 8. Figure 5.8(a) shows pressure contours over the airfoil using the grid-independent model 500 iterations after a restart from a converged solution with the grid-aligned scheme. Velocity vectors showing the θ_d -directions on the ξ -faces for the last iteration are given in figure 5.8(b). These directions are very oscillatory, causing the unrealistic behavior seen in the first figure. In spite of the wild oscillations in the flowfield, this solution converges.

An easy way to inhibit this feedback is to freeze the computed values of θ_d at each face at some point in the computation, calling these θ'_d . The four wave vectors in (5.5) remain the same, only with θ'_d replacing θ_d . Since the state R does not necessarily lie in the θ'_d -plane, at least one additional wave is needed to describe the differences between the left and right states at each face. A shear wave propagating in the θ'_d -direction produces a change in velocity *normal* to θ'_d , and can therefore be used as the additional wave. It is represented by

$$\hat{\mathbf{R}}_5 = [0, -\hat{a}\sin\theta'_d, \hat{a}\cos\theta'_d, \hat{a}(-\hat{u}\sin\theta'_d + \hat{v}\cos\theta'_d)]^T. \quad (5.9)$$

A sketch of this wave is included along with the other four waves using the minimum-area model in a $(\Delta u, \Delta v, \Delta p)$ -space diagram in figure 5.9. When the projection of the right state onto the θ'_d -plane lies within the acoustic cone, then



a) Pressure Contours

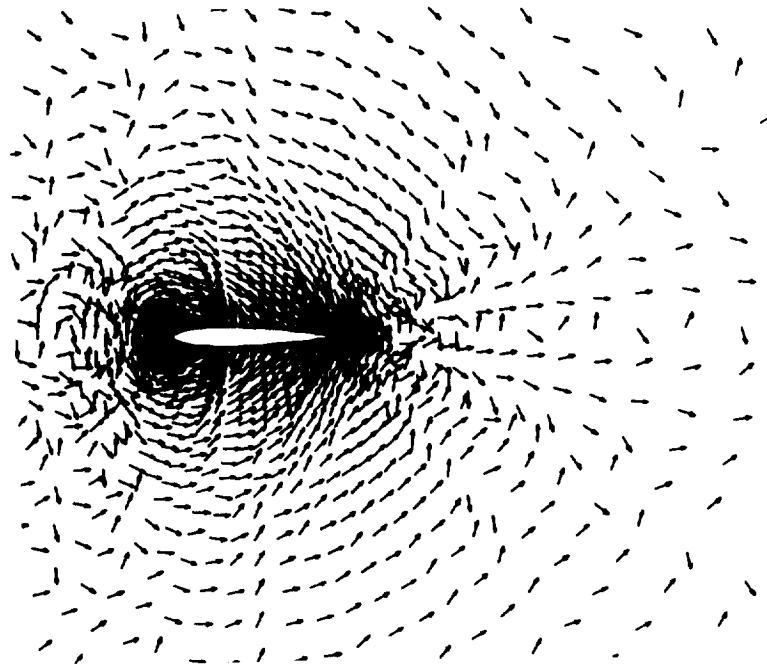
b) θ_d -Directions

Figure 5.8: Inviscid Computation of Supersonic Flow Over an Airfoil With θ_d Computed Each Iteration

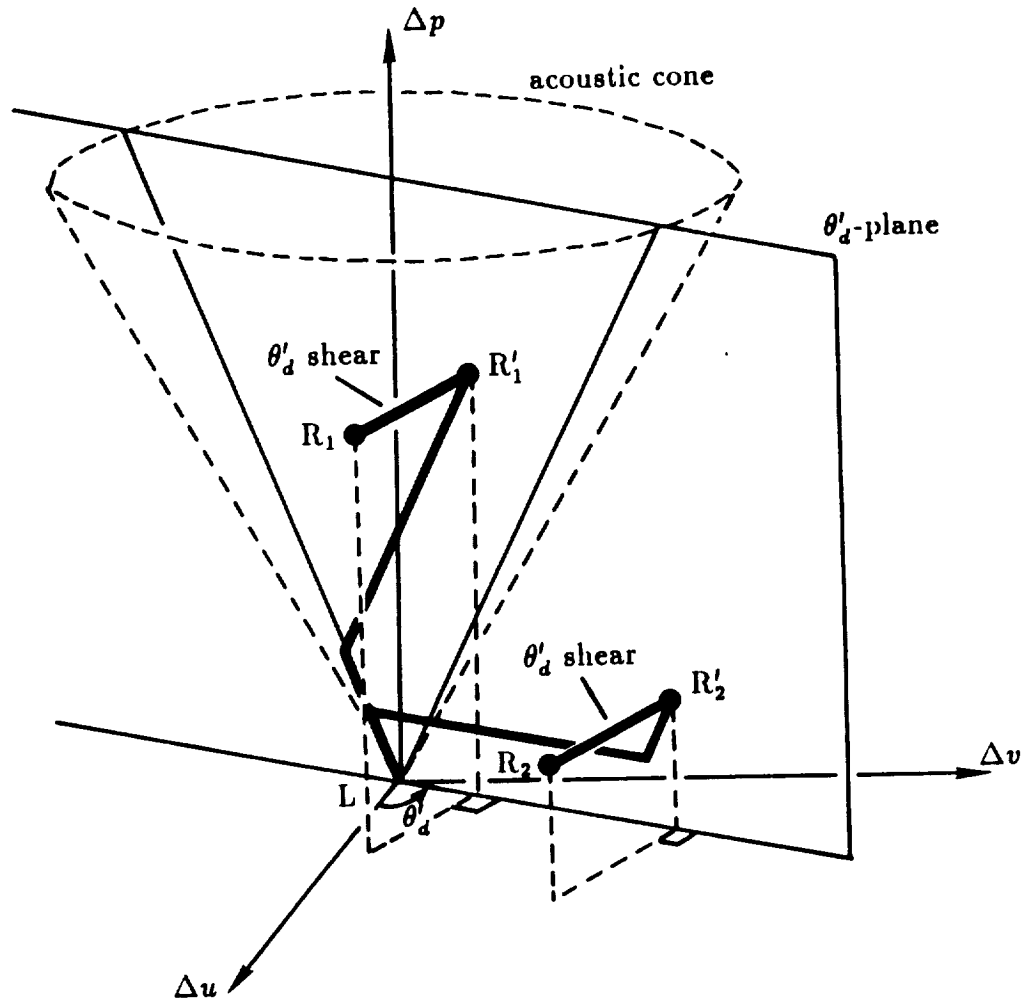
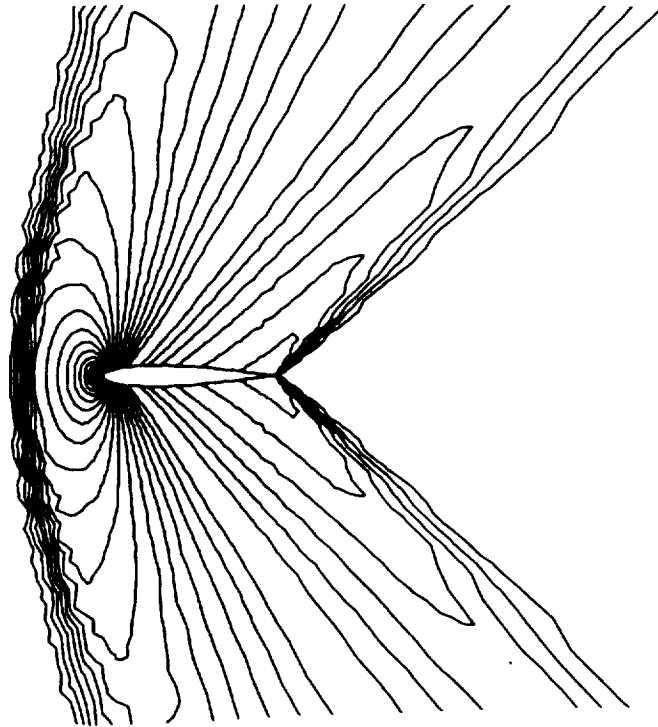


Figure 5.9: 5-Wave Model Wave Decomposition (Entropy Wave Not Pictured)



a) Pressure Contours

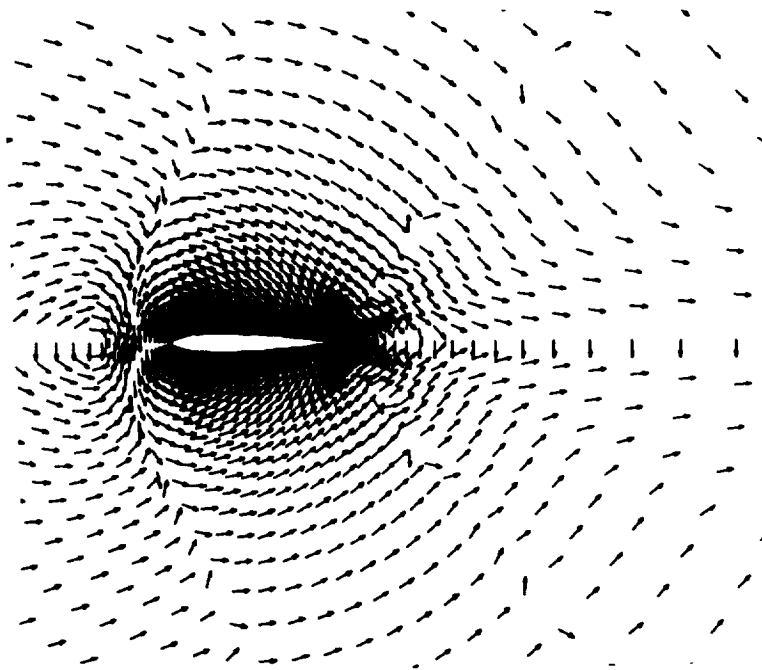
b) θ'_d -Directions

Figure 5.10: Inviscid Computation of Supersonic Flow Over an Airfoil With θ'_d Frozen

the waves are chosen as shown in the figure for right state R_1 with projection onto the θ'_d -plane R'_1 . The second case, for which the projection of the right state lies outside the acoustic cone, is shown for right state R_2 with projection onto the θ'_d -plane R'_2 ; the wave decomposition in the θ'_d -plane follows the minimum-area rule.

The same airfoil computation is shown in figures 5.10(a) and (b), where the θ_d angles are now computed during the first iteration of restart from a converged grid-aligned solution, then frozen for the remainder of the computation. Results are now relatively free from oscillations.

It should be noted at this point that a first-order interpolation procedure is used to obtain the left and right velocity values employed in equation (5.1) for θ_d even when the overall computation is second-order accurate. This is done since first-order interpolation yields smoother variations in θ_d throughout the computational domain, giving generally better solution quality. As a consequence, in a second-order computation the left and right states L and R obtained via second-order interpolation do not necessarily lie in the θ_d -plane, and the fifth shear wave \hat{R}_5 described here is necessary even when the wave propagation directions are not frozen.

5.3 Flux Formulation

5.3.1 Standard Formula

The combination of the four waves from (5.5) (with θ_d taken as θ'_d) plus the θ'_d shear wave (5.9) results in a 5-wave model, which generates a family of flux formulas with a free parameter β . This family includes both the minimum-

pathlength and minimum-area models discussed above. The flux per unit face-length normal to each grid face is calculated using

$$\Phi = \frac{1}{2} (\Phi_L + \Phi_R) - \frac{1}{2} \sum_{k=1}^5 |\hat{\lambda}_k| \hat{\Omega}_k \hat{\mathbf{R}}_k, \quad (5.10)$$

where the five waves are given by

$$\begin{aligned} \hat{\mathbf{R}}_1 &= [1, \hat{u} + \hat{a} \cos \theta'_d, \hat{v} + \hat{a} \sin \theta'_d, \hat{H} + \hat{a} \hat{q}'_d]^T \\ \hat{\mathbf{R}}_2 &= [1, \hat{u} - \hat{a} \cos \theta'_d, \hat{v} - \hat{a} \sin \theta'_d, \hat{H} - \hat{a} \hat{q}'_d]^T \\ \hat{\mathbf{R}}_3 &= [0, -\hat{a} \cos \theta'_d, -\hat{a} \sin \theta'_d, -\hat{a} \hat{q}'_d]^T \\ \hat{\mathbf{R}}_4 &= [1, \hat{u}, \hat{v}, \frac{1}{2}(\hat{u}^2 + \hat{v}^2)]^T \\ \hat{\mathbf{R}}_5 &= [0, -\hat{a} \sin \theta'_d, \hat{a} \cos \theta'_d, \hat{a} \hat{r}'_d]^T. \end{aligned} \quad (5.11)$$

These represent, respectively: $+\theta'_d$ acoustic, $-\theta'_d$ acoustic, $(\theta'_d + \frac{\pi}{2})$ shear, θ'_d entropy, and θ'_d shear waves. Also,

$$\begin{aligned} \hat{q}'_d &= \hat{u} \cos \theta'_d + \hat{v} \sin \theta'_d \\ \hat{r}'_d &= -\hat{u} \sin \theta'_d + \hat{v} \cos \theta'_d. \end{aligned} \quad (5.12)$$

The wavenumbers are defined as

$$\hat{\Omega} = \begin{bmatrix} \frac{\Delta p}{2\hat{a}^2} + \beta \frac{\hat{p}}{2\hat{a}} (\Delta u \cos \theta'_d + \Delta v \sin \theta'_d) \\ \frac{\Delta p}{2\hat{a}^2} - \beta \frac{\hat{p}}{2\hat{a}} (\Delta u \cos \theta'_d + \Delta v \sin \theta'_d) \\ (\beta - 1) \frac{\hat{p}}{\hat{a}} (\Delta u \cos \theta'_d + \Delta v \sin \theta'_d) \\ \frac{1}{\hat{a}^2} (\hat{a}^2 \Delta \rho - \Delta p) \\ \frac{\hat{p}}{\hat{a}} (-\Delta u \sin \theta'_d + \Delta v \cos \theta'_d) \end{bmatrix}. \quad (5.13)$$

The minimum-pathlength model is obtained when β is taken as

$$\beta = \min \left[\left| \frac{\Delta p / (\hat{p} \hat{a})}{\Delta u \cos \theta'_d + \Delta v \sin \theta'_d} \right|, 1 \right]. \quad (5.14)$$

In this case, the 5-wave model uses only four waves at a time since either the $(\theta'_d + \frac{\pi}{2})$ shear wavenumber or one of the acoustic wavenumbers is identically zero. The minimum-area model results when

$$\beta = \min \left[\left\{ \frac{\Delta p / (\hat{p} \hat{a})}{\Delta u \cos \theta'_d + \Delta v \sin \theta'_d} \right\}^2, 1 \right], \quad (5.15)$$

and the 5-wave model uses all five waves when R lies outside the acoustic cone, and four waves when R lies inside the acoustic cone (the $(\theta'_d + \frac{\pi}{2})$ shear strength is zero). These two expressions are derived in Appendix A. In practice, a small number $\epsilon (= 1 \times 10^{-5})$ is added to the denominators in (5.14) and (5.15) to avoid division by zero in regions of null gradient. Also, β is generally limited to be no less than 0.05, and is frozen along with θ'_d as an aid to convergence.

Numerical experiments indicate that both the minimum-pathlength and the minimum-area models give very similar results, although the minimum-area model tends to be slightly more dissipative for a wider range of test cases. Hence, it exhibits less oscillatory behavior and usually converges slightly faster. The minimum-area model is used for all the computations in Chapters 8 and 10.

The wavespeed associated with each of the waves in (5.11) is the component of the average flowspeed in the direction of wave propagation, plus or minus the average speed of sound for the acoustic waves. Since the flux (5.10) is in the grid-normal direction, however, it is necessary to take the components of these wavespeeds in the θ_g -direction. They are:

$$\begin{aligned}
 \hat{\lambda}_1 &= (\hat{q}'_d + \hat{a})\cos(\theta'_d - \theta_g) \\
 \hat{\lambda}_2 &= (\hat{q}'_d - \hat{a})\cos(\theta'_d - \theta_g) \\
 \hat{\lambda}_3 &= \hat{r}'_d\{-\sin(\theta'_d - \theta_g)\} \\
 \hat{\lambda}_4 &= \hat{q}'_d\cos(\theta'_d - \theta_g) \\
 \hat{\lambda}_5 &= \hat{q}'_d\cos(\theta'_d - \theta_g).
 \end{aligned} \tag{5.16}$$

Notice that this 5-wave model reduces to the grid-aligned approximate Riemann solver when $\theta'_d = \theta_g$ and $\beta = 1$ (*i.e.* the $(\theta'_d + \frac{\pi}{2})$ shear-strength vanishes).

5.3.2 Rotated Riemann Solver

Since the 5-wave model's wave vectors $\hat{\mathbf{R}}_k = \hat{\mathbf{R}}_k(\theta'_d)$ are *not* the eigenvectors of the matrix $\partial\hat{\Phi}/\partial\mathbf{U}$ unless $\theta'_d = \theta_g$ and $\beta = 1$, it is generally not possible to satisfy equation (4.11), *i.e.*,

$$\Delta\Phi = \Phi_{\mathbf{R}} - \Phi_{\mathbf{L}} \neq \sum_{k=1}^5 \hat{\lambda}_k \hat{\Omega}_k \hat{\mathbf{R}}_k. \quad (5.17)$$

Some question naturally arises, then, as to the appropriateness of equation (5.10) for determining the flux. A general form for the flux function is

$$\Phi = \delta \left[\Phi_{\mathbf{L}} + \sum_{\hat{\lambda}_k < 0} \hat{\lambda}_k \hat{\Omega}_k \hat{\mathbf{R}}_k \right] + (1 - \delta) \left[\Phi_{\mathbf{R}} - \sum_{\hat{\lambda}_k > 0} \hat{\lambda}_k \hat{\Omega}_k \hat{\mathbf{R}}_k \right], \quad (5.18)$$

with $(0 \leq \delta \leq 1)$. This expression reduces to formula (5.10) for $\delta = 0.5$, but gives different results for Φ using different δ since the expressions in brackets are not equal in value. This is in contrast to the grid-aligned wave model described in Chapter 4, for which (5.18) would give identical Φ for all δ , as a result of the validity of equation (4.11).

For example, if all $\hat{\lambda}$'s at a particular grid face are positive and $\delta = 1$, the flux formula yields $\Phi_{\mathbf{L}}$, the flux of the state on the "left" of the face. In the grid-aligned method this would be the correct answer. If the waves are traveling obliquely to the grid direction, however, this is not the answer produced by the standard formula (5.10). It may be argued that equation (5.10) is the correct formula because of its symmetry – it favors neither input state since it corresponds with $\delta = 0.5$ in (5.18) – but this is not always entirely clear. Hence it is difficult to say what value of δ , if any, is appropriate in (5.18) for the grid-independent model.

In order to gain further insight, it is instructive to look at a slightly different formulation of the model. In this method, as before, the first step is to determine

θ_d via equation (5.1), and the second step is to use the five waves (5.11) to describe the difference in states. The third step, the determination of the flux normal to the cell face, is performed in a different manner, however. The strengths and orientations of the five waves are used to define *four new states*, as shown in figure 5.11, which lie to the left and right of the face in the θ'_d and $(\theta'_d + \frac{\pi}{2})$ -directions. Two Roe-type approximate Riemann solvers are then used, one in each direction (θ'_d and $\theta'_d + \frac{\pi}{2}$), and the resulting fluxes are combined to give a flux on the grid face via:

$$\Phi = \Phi_{\theta'_d} \cos(\theta'_d - \theta_g) - \Phi_{\theta'_d + \pi/2} \sin(\theta'_d - \theta_g) \quad (5.19)$$

This method is hereinafter referred to as the state-determined model.

The state-determined model is similar to that of Levy [24] and Dadone and Grossman [26]. However, they use information from the surrounding flowfield to obtain the four states; the present method uses only the left and right states L and R, and applies the information in the acoustic, shear, and entropy waves to determine local gradients.

The four states \mathbf{U}_L' , \mathbf{U}_R' , \mathbf{U}_L'' , and \mathbf{U}_R'' of figure 5.11 are determined as follows. First, assume that $\cos(\theta - \theta_g) > 0$ and $\sin(\theta - \theta_g) > 0$. Results are similar for other cases. Second, assume for simplicity that θ_d is *not* frozen, *i.e.* $\theta'_d = \theta_d$, and that the difference in states is described by the minimum-pathlength model. Although the left and right states are interpolated to be at the same location on either side of a cell face, an arbitrary finite distance is assumed to separate them as shown in the figure. The states \mathbf{U}_L' and \mathbf{U}_R' are found on the wave fronts through L and R of the θ_d waves, while \mathbf{U}_L'' and \mathbf{U}_R'' lie on the fronts through L and R of the $(\theta_d + \frac{\pi}{2})$ wave. These fronts form a rectangle; the states are assumed to be in the midpoints of the rectangle's sides. Furthermore, the waves that describe the difference in states are assumed to bridge this difference in a

linear fashion. Thus, the θ_d waves have half of their full effect on \mathbf{U}_L'' and \mathbf{U}_R'' , and the $(\theta_d + \frac{\pi}{2})$ wave has half of its effect on \mathbf{U}_L' and \mathbf{U}_R' .

If equation (5.7) is true, then the difference in states is described by two acoustic waves and an entropy wave, all acting in the θ_d -direction. Hence $\mathbf{U}_L' = \mathbf{U}_L$, $\mathbf{U}_R' = \mathbf{U}_R$, and

$$\mathbf{U}_L'' = \mathbf{U}_R'' = \mathbf{U}_L + \frac{1}{2} \sum_{k=1,2,4} \hat{\Omega}_k \hat{\mathbf{R}}_k. \quad (5.20)$$

Alternatively, if equation (5.8) is true, then one acoustic and an entropy wave in the θ_d -direction and a shear wave in the $(\theta_d + \frac{\pi}{2})$ -direction are used. In this case, the formulas are:

$$\mathbf{U}_L' = \mathbf{U}_L + \frac{1}{2} \hat{\Omega}_3 \hat{\mathbf{R}}_3 \quad (5.21)$$

$$\mathbf{U}_R' = \mathbf{U}_L + \hat{\Omega}_{1 \text{ or } 2} \hat{\mathbf{R}}_{1 \text{ or } 2} + \hat{\Omega}_4 \hat{\mathbf{R}}_4 + \frac{1}{2} \hat{\Omega}_3 \hat{\mathbf{R}}_3 \quad (5.22)$$

$$\mathbf{U}_L'' = \mathbf{U}_L + \frac{1}{2} \left(\hat{\Omega}_{1 \text{ or } 2} \hat{\mathbf{R}}_{1 \text{ or } 2} + \hat{\Omega}_4 \hat{\mathbf{R}}_4 \right) + \hat{\Omega}_3 \hat{\mathbf{R}}_3 \quad (5.23)$$

$$\mathbf{U}_R'' = \mathbf{U}_L + \frac{1}{2} \left(\hat{\Omega}_{1 \text{ or } 2} \hat{\mathbf{R}}_{1 \text{ or } 2} + \hat{\Omega}_4 \hat{\mathbf{R}}_4 \right). \quad (5.24)$$

The subscripts (1 or 2) indicate that the acoustic wave $\hat{\mathbf{R}}_1$ or $\hat{\mathbf{R}}_2$ is used, depending upon which minimizes the pathlength in $(\Delta u, \Delta v, \Delta p)$ -space. Roe-averaged values are determined once at each face from states L and R, then used in each of the Riemann-solvers.

The state-determined model is naturally fairly expensive, requiring about six times as much CPU time as the grid-aligned method to compute the fluxes at the faces. It can be shown that the flux based on this state-determined model is *not* the same as the flux (5.18), regardless of the value of δ . However, it has been determined numerically that the difference between the two methods is always a minimum in the mass flux when $\delta = 0.5$. Also, if the jump between the left and right states is relatively small, then the difference between the two methods in the

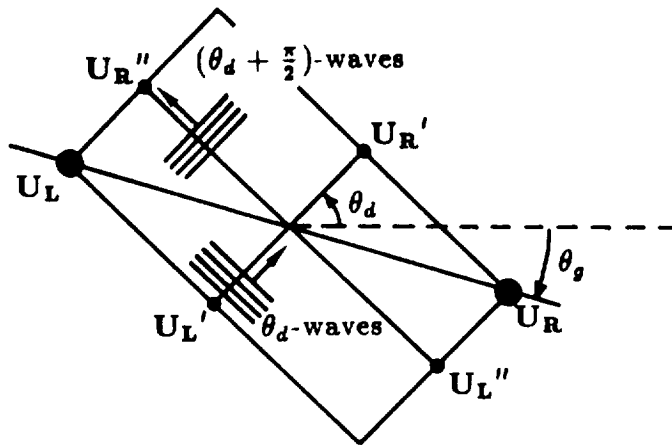
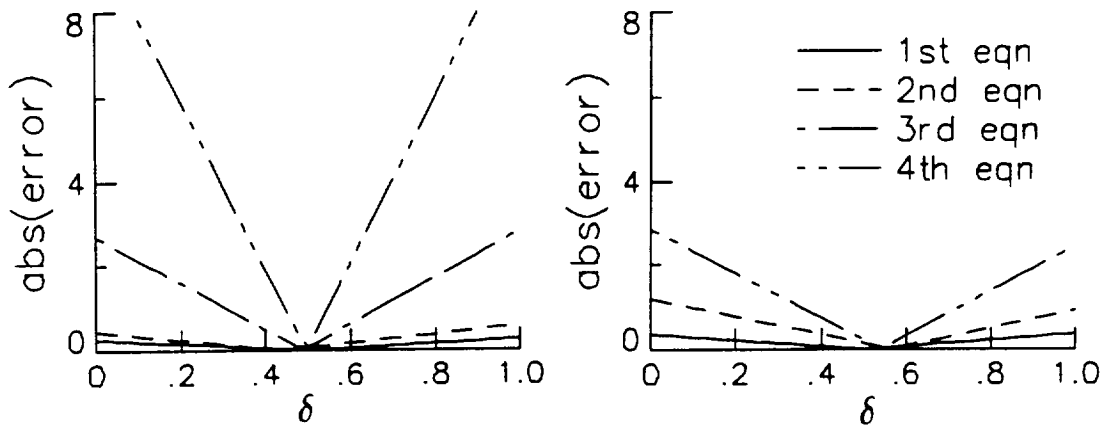


Figure 5.11: Graphical Representation of State-Determined Model



a) Pressure-Dominated Difference

b) Velocity-Dominated Difference

Figure 5.12: Typical Plots of Difference Between Standard Flux Formula and State-Determined Model

other three equations is also usually a minimum near $\delta = 0.5$. For example, figure 5.12(a) shows the absolute value of the difference between the fluxes determined by the two methods as a function of δ , where the left-state primitive variables (ρ, u, v, p) are $(1, 2, 3, 4)$, and the right-state variables are $(2, 3, 4, 10)$. θ_g is taken as 0° . These particular states have a relatively large pressure difference, so two acoustics and an entropy wave are used to describe the difference in states. A second example is given for left and right states of $(1, 1, 1, 1)$ and $(1, 2, 1, 1)$ with θ_g taken as 45° in figure 5.12(b). In this case, the difference in states is only in the velocity, and one acoustic, one shear, and one entropy wave are used to model the difference.

Hence, equation (5.18) with $\delta = 0.5$ is, in a sense, “best” for this particular form of the flux function in that it generally yields a flux very close to that given by the state-determined model. In fact, in practice the flowfields produced by the two methods are often virtually identical. Results in the remainder of the paper are therefore obtained solely with the standard formula for the 5-wave model (5.10) (which is the same as (5.18) with $\delta = 0.5$), since its expense is significantly lower than that of the state-determined model.

5.4 Recovering the Grid-Aligned Scheme

One unresolved issue facing the 5-wave model is the fact that the model does *not* reduce to the standard grid-aligned model when $\theta'_d = \theta_g$ if $\beta \neq 1$. In other words, if the $(\theta'_d + \frac{\pi}{2})$ shear wave has any strength other than zero, the standard grid-aligned flux is not obtained when the waves are assumed to travel in the grid-normal direction. Intuitively, it seems that this flux *should* be obtained. For example, if all wave speeds are positive and act in the θ_g -direction, then it seems

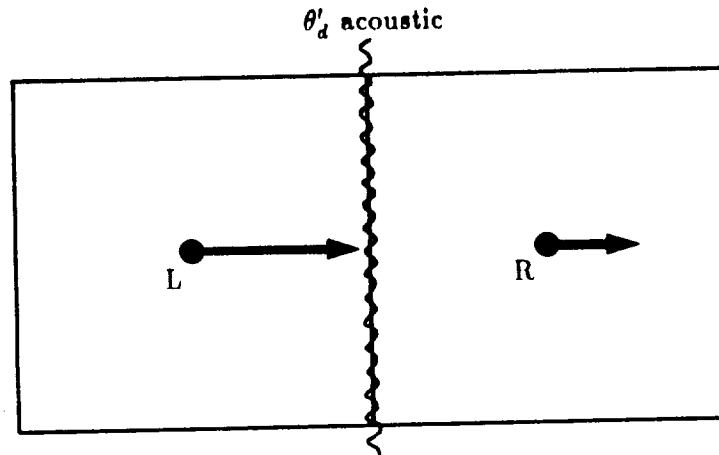
desirable that the grid-aligned upwind flux $\Phi_{\mathbf{L}}$ should be computed as the flux at the interface. But unless $\beta = 1$ (along with $\theta'_d = \theta_g$), the inequality in (5.17) holds and the flux function (5.10) does not yield $\Phi_{\mathbf{L}}$ as a result.

Also, it is difficult to imagine a steady-state circumstance when $\theta'_d = \theta_g$ and a $(\theta'_d + \frac{\pi}{2})$ shear wave exists between the states. As an example, two pictures are drawn in figure 5.13 of neighboring cells with a velocity-difference direction that coincides with the grid-normal direction. In figure 5.13(a) a relatively large pressure difference exists between the states, and a θ'_d acoustic wave is presumed by the model to describe the difference. In figure 5.13(b), no pressure difference exists, and the model describes the difference with a $(\theta'_d + \frac{\pi}{2})$ shear wave. However, this shear wave is aligned such that it passes exactly through each cell center. Even if these are assumed to lie infinitely close to either side of the wave, this is an unlikely situation. This interpretation also is obviously inconsistent with the notion that the data in each cell represent cell *averages*, for with this shear-wave orientation the averages in the left and right cell should be identical.

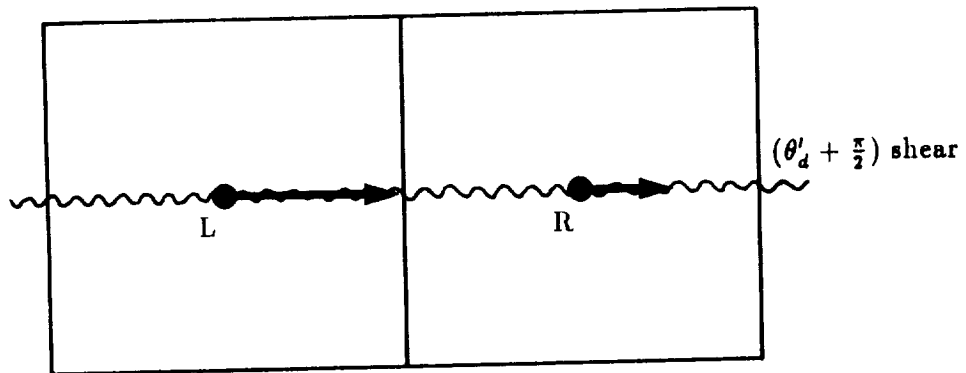
Unfortunately, it is not clear how to recover the grid-aligned method automatically when $\theta'_d = \theta_g$, while still retaining the capability of resolving oblique shear waves. Two different methods which have been attempted to resolve this issue are described in this section. The first method involves making β a function of the difference $\theta'_d - \theta_g$. When $\theta'_d = \theta_g$, the grid-aligned scheme must be recovered, so β must be made equal to 1.0. This can be enforced by choosing a new β^* as

$$\beta^* = \beta + \frac{1}{2}(1 - \beta) \{ \cos [2(\theta'_d - \theta_g)] + 1 \}, \quad (5.25)$$

where β is computed using (5.14) or (5.15). The resulting β^* , used in place of β in (5.13), varies smoothly between β and 1.0, depending on the difference between θ'_d and θ_g .



a) Relatively Large Pressure Difference



b) No Pressure Difference

Figure 5.13: Example of 5-Wave Model Interpretation of Difference in States When $\theta'_d = \theta_g$

There are two significant problems with this method. First of all, resolution of pure oblique shear waves is reduced since β^* is near zero only within a narrow range of angles ($\theta'_d - \theta_g$). Hence most pure shear waves are now interpreted using some acoustic waves as well, resulting in added dissipation and smearing of the numerical solution. The second problem arises in certain circumstances, and most notably in the case of the computation of flow over an airfoil. Around the airfoil's leading edge the grid-normal angles of a structured-grid vary rapidly through about 180° . Since the θ'_d -directions do not vary as much (see figure 5.10(b)), the β^* values resulting from (5.25) generally vary rapidly between β and 1.0. This oscillatory behavior of β^* can cause unrealistic results with "kinks" and/or oscillations in contours of flowfield variables near the leading edge.

Example solutions using β and β^* are given in figures 5.14(a) and (b). Shown are pressure contours resulting from an Euler computation over a NACA 0012 airfoil at $M = 0.3$, $\alpha = 1^\circ$, on a 65×25 C-mesh. Figure 5.14(a) shows contours using β (without equation (5.25)). Results are fairly smooth, except for irregularities due to grid coarseness. Results using β^* , shown in figure 5.14(b), shows *two* regions of local maximum pressure at the nose and large "kinks" in the contours in front of the nose. One effect of this irregular behavior is the nonconvergence of lift to the correct value as the grid is refined.

Several variations in equation (5.25) have also been attempted, including the use of functions which very rapidly transition from $\beta^* = 1$ to $\beta^* = \beta$ near $|\theta'_d - \theta_g| = 0$ and $\pm\pi$, and remain flat at β over much of the $\theta'_d - \theta_g$ range. This allows for sharper resolution of most oblique shear waves, but the second problem relating to airfoil flow remains.

The second attempted method for recovering the grid-aligned scheme when $\theta'_d = \theta_g$ involves replacing the $(\theta'_d + \frac{\pi}{2})$ shear wave with $+\theta''_d$ acoustic, $-\theta''_d$ acoustic, and θ''_d shear waves. The θ''_d angle is a function of θ'_d and θ_g : it is set equal to

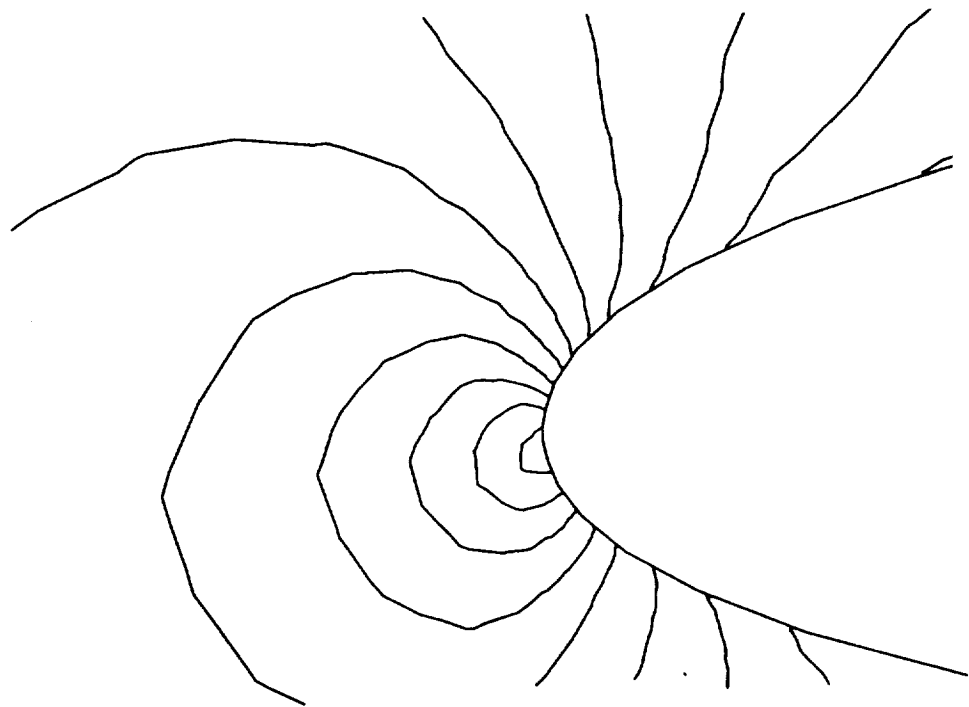
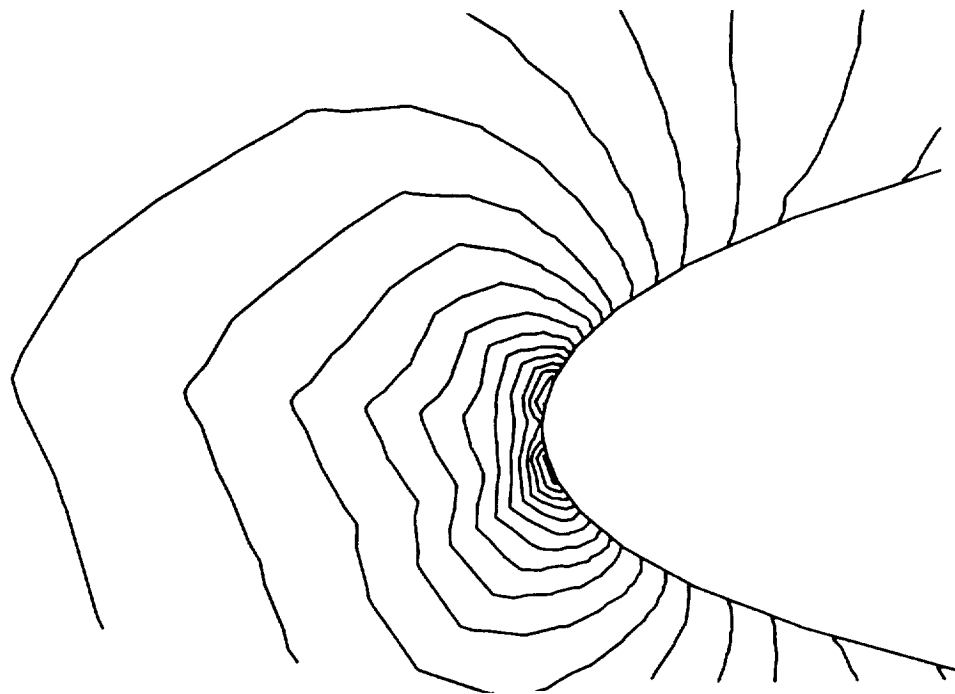
a) Using β b) Using β^*

Figure 5.14: Pressure Contours Near Leading Edge of NACA 0012 Airfoil, $M = 0.3$, $\alpha = 1^\circ$, 5-Wave Model

θ'_d when $\theta'_d = \theta_g$, and is smoothly transitioned to $\theta''_d = \theta'_d + \frac{\pi}{2}$ otherwise. Hence, when $\theta'_d = \theta_g$ the grid-aligned scheme is recovered, and when $\theta''_d = \theta'_d + \frac{\pi}{2}$ the 5-wave model is recovered. One way to accomplish the transition is to use the relation

$$\theta''_d = \theta'_d + \min\left(2|\theta'_d - \theta_g|, \frac{\pi}{2}\right). \quad (5.26)$$

The strengths of the three new waves which replace the $(\theta'_d + \frac{\pi}{2})$ shear wave are

$$\begin{aligned} \hat{\Omega}_{+\theta''_d \text{ac}} &= \frac{1-\beta}{2} \frac{\hat{\rho}}{\hat{a}} (\Delta u \cos \theta'_d + \Delta v \sin \theta'_d) (\cos \theta'_d \cos \theta''_d + \sin \theta'_d \sin \theta''_d) \\ \hat{\Omega}_{-\theta''_d \text{ac}} &= -\hat{\Omega}_{+\theta''_d \text{ac}} \\ \hat{\Omega}_{\theta''_d \text{shear}} &= (\beta-1) \frac{\hat{\rho}}{\hat{a}} (\Delta u \cos \theta'_d + \Delta v \sin \theta'_d) (\cos \theta'_d \sin \theta''_d - \sin \theta'_d \cos \theta''_d), \end{aligned} \quad (5.27)$$

The corresponding components of the wavespeeds in the grid-normal direction are

$$\begin{aligned} \lambda_{+\theta''_d \text{ac}} &= (\hat{u} \cos \theta''_d + \hat{v} \sin \theta''_d + \hat{a}) \cos(\theta''_d - \theta_g) \\ \lambda_{-\theta''_d \text{ac}} &= (\hat{u} \cos \theta''_d + \hat{v} \sin \theta''_d - \hat{a}) \cos(\theta''_d - \theta_g) \\ \lambda_{\theta''_d \text{shear}} &= (\hat{u} \cos \theta''_d + \hat{v} \sin \theta''_d) \cos(\theta''_d - \theta_g). \end{aligned} \quad (5.28)$$

Aside from the obvious drawback that this model requires a total of seven waves rather than five, it also (just as the method based on β^*) gives very unrealistic results near the leading edge of airfoils. By far the best solutions in general are still obtained using the original 5-wave model, in spite of the fact that it does not recover the grid-aligned method.

CHAPTER 6

STABILITY ANALYSIS

The stability analyses of both explicit and implicit time-marching schemes with the 5-wave model for the Euler equations are discussed in this chapter. Because of the complexity of the Navier-Stokes equations, it is much more difficult to obtain expressions for its stability. However, it has been found empirically that the stability condition for the Navier-Stokes equations for flows with relatively high cell Reynolds numbers is usually only slightly more restrictive than the CFL condition for the Euler equations [28].

6.1 Explicit Time-Marching

Writing the equations in the finite-volume form (3.5) with viscous terms ignored, the stability analysis requires the eigenvalues of the Fourier transform of the right-hand side of

$$\begin{aligned} \Delta t \frac{\partial \mathbf{U}}{\partial t} &= -\frac{\Delta t}{A} \sum_{\ell=1}^4 \Phi_{\ell} \Delta s_{\ell} \\ &= J \Delta t \mathbf{S}_i. \end{aligned} \quad (6.1)$$

The right-hand side can be expanded using the i and j indices corresponding to the ξ and η directions of a structured grid:

$$\Delta t \frac{\partial \mathbf{U}}{\partial t} = -\frac{\Delta t}{A} \left((\Phi \Delta s)_{i+\frac{1}{2},j} - (\Phi \Delta s)_{i-\frac{1}{2},j} + (\Phi \Delta s)_{i,j+\frac{1}{2}} - (\Phi \Delta s)_{i,j-\frac{1}{2}} \right). \quad (6.2)$$

The normal flux Φ per unit face-length at each of the faces is obtained with the flux function described in Chapter 5:

$$\begin{aligned}\Phi_{k+\frac{1}{2}} &= \frac{1}{2} \left\{ (\Phi_{\mathbf{L}})_{k+\frac{1}{2}} + (\Phi_{\mathbf{R}})_{k+\frac{1}{2}} \right\} - \frac{1}{2} \left\{ \sum_{m=1}^5 |\hat{\lambda}_m| \hat{\Omega}_m \hat{\mathbf{R}}_m \right\}_{k+\frac{1}{2}} \\ &= \frac{1}{2} \left\{ (\Phi_{\mathbf{L}})_{k+\frac{1}{2}} + (\Phi_{\mathbf{R}})_{k+\frac{1}{2}} \right\} - \frac{1}{2} |\hat{\mathbf{D}}|_{k+\frac{1}{2}} \left\{ (\mathbf{U}_{\mathbf{R}})_{k+\frac{1}{2}} - (\mathbf{U}_{\mathbf{L}})_{k+\frac{1}{2}} \right\},\end{aligned}\quad (6.3)$$

where k represents the index i or j . The following operator symbols are introduced:

$$\begin{aligned}\Delta_{k+\frac{1}{2}}(\cdot) &\equiv (\cdot)_{k+1} - (\cdot)_k \\ \overline{\delta}_k(\cdot) &\equiv (\cdot)_{k+1} - (\cdot)_{k-1}.\end{aligned}\quad (6.4)$$

When equation (6.3) is inserted into (6.2) at the four faces, terms such as $\Delta_{k+1/2}\Phi$ and $\overline{\delta}_k\Phi$ can arise (depending on the spatial order of accuracy). These terms are linearized using

$$\begin{aligned}\Delta_{k+\frac{1}{2}}\Phi &= \left(\frac{\partial \hat{\Phi}}{\partial \mathbf{U}} \right) \Delta_{k+\frac{1}{2}}\mathbf{U} \\ \overline{\delta}_k\Phi &= \left(\frac{\partial \hat{\Phi}}{\partial \mathbf{U}} \right) \overline{\delta}_k\mathbf{U},\end{aligned}\quad (6.5)$$

and all $\partial \hat{\Phi} / \partial \mathbf{U}$ and $|\hat{\mathbf{D}}|$ terms are also linearized about the cell center using Roe-averaged values (e.g. $|\hat{\mathbf{D}}|_{k+1/2} = |\hat{\mathbf{D}}|_{k-1/2} \equiv |\hat{\mathbf{D}}|$). It is further assumed that all cells are square with face length Δs . Linearized, equation (6.2) becomes

$$\Delta t \frac{\partial \mathbf{U}}{\partial t} = -\mathbf{L}\mathbf{U}, \quad (6.6)$$

where, for first-order spatial differencing

$$\begin{aligned}\mathbf{L} &= \frac{\Delta t}{\Delta s} \left\{ \frac{1}{2} \left(\frac{\partial \hat{\Phi}}{\partial \mathbf{U}}(\theta_g^{(i)}) \right) \overline{\delta}_i \right. \\ &\quad - \frac{1}{2} |\hat{\mathbf{D}}(\theta_g^{(i)})| (\Delta_{i+\frac{1}{2}} - \Delta_{i-\frac{1}{2}}) \\ &\quad + \frac{1}{2} \left(\frac{\partial \hat{\Phi}}{\partial \mathbf{U}}(\theta_g^{(j)}) \right) \overline{\delta}_j \\ &\quad \left. - \frac{1}{2} |\hat{\mathbf{D}}(\theta_g^{(j)})| (\Delta_{j+\frac{1}{2}} - \Delta_{j-\frac{1}{2}}) \right\}.\end{aligned}\quad (6.7)$$

For second-order fully one-sided spatial differencing:

$$\begin{aligned}
\mathbf{L} = \frac{\Delta t}{\Delta s} & \left\{ \frac{1}{2} \left(\frac{\partial \hat{\Phi}}{\partial \mathbf{U}}(\theta_g^{(i)}) \right) \left(-\frac{1}{2} \Delta_{i+\frac{3}{2}} + \frac{3}{2} \delta_i - \frac{1}{2} \Delta_{i-\frac{3}{2}} \right) \right. \\
& - \frac{1}{2} |\hat{\mathbf{D}}(\theta_g^{(i)})| \left(-\frac{1}{2} \Delta_{i+\frac{3}{2}} + \frac{3}{2} \Delta_{i+\frac{1}{2}} - \frac{3}{2} \Delta_{i-\frac{1}{2}} + \frac{1}{2} \Delta_{i-\frac{3}{2}} \right) \\
& + \frac{1}{2} \left(\frac{\partial \hat{\Phi}}{\partial \mathbf{U}}(\theta_g^{(j)}) \right) \left(-\frac{1}{2} \Delta_{j+\frac{3}{2}} + \frac{3}{2} \delta_j - \frac{1}{2} \Delta_{j-\frac{3}{2}} \right) \\
& \left. - \frac{1}{2} |\hat{\mathbf{D}}(\theta_g^{(j)})| \left(-\frac{1}{2} \Delta_{j+\frac{3}{2}} + \frac{3}{2} \Delta_{j+\frac{1}{2}} - \frac{3}{2} \Delta_{j-\frac{1}{2}} + \frac{1}{2} \Delta_{j-\frac{3}{2}} \right) \right\}. \tag{6.8}
\end{aligned}$$

The $\theta_g^{(i)}$ and $\theta_g^{(j)}$ are the directions normal to the grid faces in the i and j directions, respectively. In the present analysis, $\theta_g^{(i)}$ is prescribed, and $\theta_g^{(j)}$ is taken as $\theta_g^{(i)} + \pi/2$.

For completeness, the matrix $\partial \hat{\Phi} / \partial \mathbf{U}$ is given here: $\partial \hat{\Phi} / \partial \mathbf{U} =$

$$\begin{bmatrix} 0 & (c_x)_g & (c_y)_g & 0 \\ (c_x)_g \phi - \hat{u} \hat{q}_g & (c_x)_g (2-\gamma) \hat{u} + \hat{q}_g & (c_y)_g \hat{u} - (c_x)_g (\gamma-1) \hat{v} & (c_x)_g (\gamma-1) \\ (c_y)_g \phi - \hat{v} \hat{q}_g & (c_x)_g \hat{v} - (c_y)_g (\gamma-1) \hat{u} & (c_y)_g (2-\gamma) \hat{v} + \hat{q}_g & (c_y)_g (\gamma-1) \\ (2\phi - \gamma \hat{E}) \hat{q}_g & \hat{C}_{42} & \hat{C}_{43} & \gamma \hat{q}_g \end{bmatrix}, \tag{6.9}$$

where $\hat{C}_{42} \equiv (c_x)_g (\gamma \hat{E} - \phi) - (\gamma-1) \hat{u} \hat{q}_g$ and $\hat{C}_{43} \equiv (c_y)_g (\gamma \hat{E} - \phi) - (\gamma-1) \hat{v} \hat{q}_g$. Also,

$$\phi \equiv \frac{\gamma-1}{2} (\hat{u}^2 + \hat{v}^2) \tag{6.10}$$

$$\hat{q}_g \equiv (c_x)_g \hat{u} + (c_y)_g \hat{v}.$$

The terms $(c_x)_g$ and $(c_y)_g$ represent the components of the grid-face unit normal in the x and y coordinate directions, respectively. In other words, $(c_x)_g = \cos \theta_g$ and $(c_y)_g = \sin \theta_g$.

$|\hat{\mathbf{D}}|$ is the matrix that satisfies

$$|\hat{\mathbf{D}}| \Delta \mathbf{U} = \sum_k |\hat{\lambda}_k| \hat{\Omega}_k \hat{\mathbf{R}}_k, \tag{6.11}$$

where the summation is over all the waves. For the 5-wave model, the elements

of $|\hat{\mathbf{D}}|$ are given by:

$$\begin{aligned}
|\hat{\mathbf{D}}|_{j1} &= |\hat{\lambda}_4| (\hat{\mathbf{R}}_4)_j + \phi \xi_1 - \xi_2 \hat{u} - \xi_3 \hat{v} \\
|\hat{\mathbf{D}}|_{j2} &= -(\gamma - 1) \hat{u} \xi_1 + \xi_2 \\
|\hat{\mathbf{D}}|_{j3} &= -(\gamma - 1) \hat{v} \xi_1 + \xi_3 \\
|\hat{\mathbf{D}}|_{j4} &= (\gamma - 1) \xi_1,
\end{aligned} \tag{6.12}$$

where

$$\begin{aligned}
\xi_1 &= \frac{1}{2\hat{a}^2} \left\{ |\hat{\lambda}_1| (\hat{\mathbf{R}}_1)_j + |\hat{\lambda}_2| (\hat{\mathbf{R}}_2)_j - 2 |\hat{\lambda}_4| (\hat{\mathbf{R}}_4)_j \right\} \\
\xi_2 &= \frac{\beta}{2\hat{a}} \cos\theta'_d \left\{ |\hat{\lambda}_1| (\hat{\mathbf{R}}_1)_j - |\hat{\lambda}_2| (\hat{\mathbf{R}}_2)_j \right\} + \frac{\beta - 1}{\hat{a}} \cos\theta'_d |\hat{\lambda}_3| (\hat{\mathbf{R}}_3)_j \\
&\quad - \frac{1}{\hat{a}} \sin\theta'_d |\hat{\lambda}_5| (\hat{\mathbf{R}}_5)_j \\
\xi_3 &= \frac{\beta}{2\hat{a}} \sin\theta'_d \left\{ |\hat{\lambda}_1| (\hat{\mathbf{R}}_1)_j - |\hat{\lambda}_2| (\hat{\mathbf{R}}_2)_j \right\} + \frac{\beta - 1}{\hat{a}} \sin\theta'_d |\hat{\lambda}_3| (\hat{\mathbf{R}}_3)_j \\
&\quad + \frac{1}{\hat{a}} \cos\theta'_d |\hat{\lambda}_5| (\hat{\mathbf{R}}_5)_j
\end{aligned} \tag{6.13}$$

and $(\hat{\mathbf{R}}_i)_j$ represents the j th element of the vector $\hat{\mathbf{R}}_i$, as defined in (5.11). The $\hat{\lambda}$'s are defined in (5.16). It should be noted that for the grid-aligned model described in Chapter 4, the $|\hat{\mathbf{D}}|$ matrix which satisfies (6.11) can be written as

$$|\hat{\mathbf{D}}|_{(grid-aligned)} = \left| \frac{\partial \hat{\Phi}}{\partial \mathbf{U}} \right| = \hat{\mathbf{R}} |\hat{\Lambda}| \hat{\mathbf{R}}^{-1}, \tag{6.14}$$

whereas this is not true for the 5-wave model, since its $\hat{\mathbf{R}}_k$ are *not* the eigenvectors of the $\partial \hat{\Phi} / \partial \mathbf{U}$ matrix.

In order to obtain the Fourier transform of the right-hand side of (6.6), the Fourier symbols for the difference operators are inserted into the equation. These symbols are:

$$\begin{aligned}
\mathfrak{F}(\Delta_{k+\frac{3}{2}}) &= e^{i2\zeta^{(k)}} - e^{i\zeta^{(k)}} \\
\mathfrak{F}(\Delta_{k+\frac{1}{2}}) &= e^{i\zeta^{(k)}} - 1 \\
\mathfrak{F}(\Delta_{k-\frac{1}{2},j}) &= 1 - e^{-i\zeta^{(k)}} \\
\mathfrak{F}(\Delta_{k-\frac{3}{2}}) &= e^{-i\zeta^{(k)}} - e^{-i2\zeta^{(k)}} \\
\mathfrak{F}(\overline{\delta}_k) &= e^{i\zeta^{(k)}} - e^{-i\zeta^{(k)}},
\end{aligned} \tag{6.15}$$

where k represents the index i or j , and $\zeta^{(i)}$ and $\zeta^{(j)}$ are the wavelengths of the perturbations in the i and j directions, respectively. For first-order spatial differencing (\mathbf{L} defined by (6.7)), the Fourier transform of the right-hand side of (6.6) is:

$$\begin{aligned} \mathfrak{S}(-\mathbf{L}) = & -\frac{\nu}{\{\omega(\theta_g^{(i)}) + \omega(\theta_g^{(j)})\}} \left[\left| \hat{\mathbf{D}}(\theta_g^{(i)}) \right| (1 - \cos\zeta^{(i)}) + \right. \\ & i \left(\frac{\partial \hat{\Phi}}{\partial \mathbf{U}}(\theta_g^{(i)}) \right) \sin\zeta^{(i)} + \left| \hat{\mathbf{D}}(\theta_g^{(j)}) \right| (1 - \cos\zeta^{(j)}) + \\ & \left. i \left(\frac{\partial \hat{\Phi}}{\partial \mathbf{U}}(\theta_g^{(j)}) \right) \sin\zeta^{(j)} \right], \end{aligned} \quad (6.16)$$

where the variable ν is the CFL number, defined as

$$\nu = \left\{ \omega(\theta_g^{(i)}) + \omega(\theta_g^{(j)}) \right\} \frac{\Delta t}{\Delta s}, \quad (6.17)$$

for square cells with face length Δs . Here, $\omega(\theta_g^{(i)})$ and $\omega(\theta_g^{(j)})$ are the maximum wave speeds $|\hat{q}| + \hat{a}$ in each of the grid directions. $\mathfrak{S}(-\mathbf{L})$ is a complex-valued 4×4 matrix.

For stability, the locus of the eigenvalues of the Fourier transform, often called the ‘‘Fourier footprint,’’ must lie inside the stability boundary of the time-marching scheme. In general, the Fourier footprint of the 5-wave model is a function of ν , the Mach number $M = \sqrt{u^2 + v^2}/a$, the flow angle $\alpha = \tan^{-1}(v/u)$, β , θ'_d , and $\theta_g^{(i)}$, as well as the perturbation wavelengths $\zeta^{(i)}$ and $\zeta^{(j)}$. Since the Fourier footprint is a function of so many variables, it is difficult to perform a thorough numerical analysis. However, an extensive number of variations in the independent variables have been tested. In each case $\zeta^{(i)}$ and $\zeta^{(j)}$ are both cycled through 17 values from $-\pi$ to π inclusive, and four eigenvalues are obtained at each of the 289 conditions. Based on the results obtained the following trends are noted:

- (1) The relative magnitudes of the eigenvalues are strongly dependent on the Mach number. In general, increasing M increases the magnitudes, but at larger and larger M an asymptotic limit is reached.

(2) Many of the modes of the Fourier footprint can have eigenvalues that lie on the imaginary axis. In particular, this occurs when α and θ'_d differ by 90° .

From this analysis, it is clear that the explicit forward-Euler time stepping scheme would be unstable for many of the modes, since the stability boundary for forward-Euler is a unit circle centered at $(-1, 0)$ and does not include any part of the imaginary axis except the origin. However, 2-stage or higher schemes can be designed that satisfy this requirement. For example, the 4-stage scheme

$$\begin{aligned}
 \mathbf{U}^{(1)} &= \mathbf{U}^{(n)} + \eta J \Delta t \mathbf{S}_i^{(n)} \\
 \mathbf{U}^{(2)} &= \mathbf{U}^{(n)} + \frac{1}{3} J \Delta t \mathbf{S}_i^{(1)} \\
 \mathbf{U}^{(3)} &= \mathbf{U}^{(n)} + \frac{1}{2} J \Delta t \mathbf{S}_i^{(2)} \\
 \mathbf{U}^{(n+1)} &= \mathbf{U}^{(n)} + J \Delta t \mathbf{S}_i^{(3)}
 \end{aligned} \tag{6.18}$$

has a stability region including a finite part of the imaginary axis whenever $\eta < 0.6756$. Its amplification factor is given by $P(z) = 1 + z + \frac{1}{2}z^2 + \frac{1}{6}z^3 + \frac{1}{6}\eta z^4$. The stability boundary is defined by $|P(z)| = 1$.

An attempt was made to devise a “worst case” Fourier footprint for this scheme by choosing independent variables that yield the largest eigenvalue extent in the *Real-Imaginary* plane. Of all the combinations of variables tested, the one that gave the largest footprint was: $M = 100$, $\alpha = 90^\circ$, $\beta = 0$, $\theta_g^{(i)} = 0^\circ$, and $\theta'_d = 22.5^\circ$. Given this footprint, an η of about 0.15 is “optimum” for the 4-stage scheme in the sense that it allows for the largest ν for stability. A plot of the Fourier footprint at its maximum $\nu = 1.75$, along with the corresponding time stepping stability boundary using $\eta = 0.15$ is shown in figure 6.1. This exercise was also performed for 2, 3, and 5-stage schemes. Although not shown, for these cases the maximum CFL numbers for stability turn out to be $\nu = 0.7$, 1.2, and 1.9, respectively. Hence increasing the number of stages yields increasing benefit in stability, but the difference in maximum allowable CFL number between 4 and

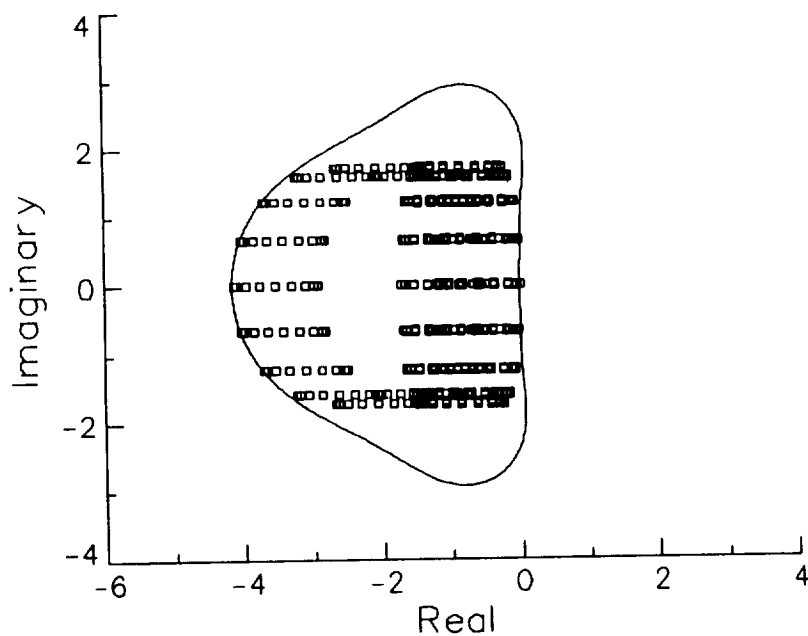


Figure 6.1: Stability Boundary of 4-Stage Time-Marching Scheme, and "Worst-Case" Fourier Footprint of First-Order Spatial-Differencing Scheme for $\nu = 1.75$

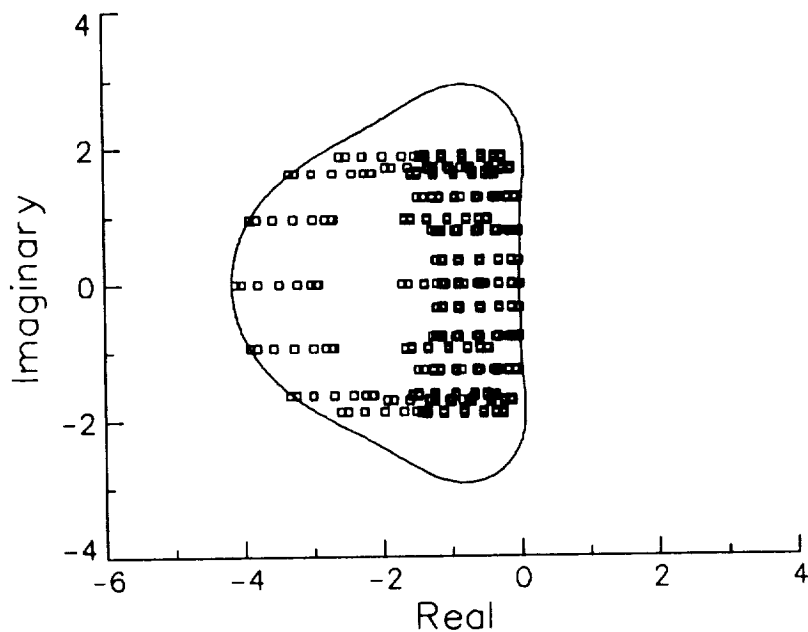


Figure 6.2: Stability Boundary of 4-Stage Time-Marching Scheme, and "Worst-Case" Fourier Footprint of Second-Order Spatial-Differencing Scheme for $\nu = 0.87$

5 stages is small relative to the extra work involved in computing the extra stage. Therefore, in the present paper the 4-stage scheme is used for all explicit Euler computations. Note that since the Fourier footprint is highly dependent on Mach number, the maximum allowable ν is actually higher than 1.75 for M lower than 100. For example, at $M = 3$ the maximum CFL number is about 2.2, while at $M = 1$ it is about 2.5, according to this linearized stability analysis.

For second-order spatial differencing (\mathbf{L} defined by (6.8)), the Fourier transform of the right-hand side of (6.6) is:

$$\begin{aligned} \mathfrak{S}(-\mathbf{L}) = & -\frac{\nu}{\{\omega(\theta_g^{(i)}) + \omega(\theta_g^{(j)})\}} \left[\left| \hat{\mathbf{D}}(\theta_g^{(i)}) \right| \left(-2\cos\zeta^{(i)} + \frac{1}{2}\cos 2\zeta^{(i)} + \frac{3}{2} \right) + \right. \\ & i \left(\frac{\partial \hat{\Phi}}{\partial \mathbf{U}}(\theta_g^{(i)}) \right) \left(2\sin\zeta^{(i)} - \frac{1}{2}\sin 2\zeta^{(i)} \right) + \left| \hat{\mathbf{D}}(\theta_g^{(j)}) \right| \left(-2\cos\zeta^{(j)} + \right. \\ & \left. \left. \frac{1}{2}\cos 2\zeta^{(j)} + \frac{3}{2} \right) + i \left(\frac{\partial \hat{\Phi}}{\partial \mathbf{U}}(\theta_g^{(j)}) \right) \left(2\sin\zeta^{(j)} - \frac{1}{2}\sin 2\zeta^{(j)} \right) \right]. \end{aligned} \quad (6.19)$$

A “worst-case” Fourier footprint is again accomplished using the same variables as for first order, only this time the maximum ν turns out to be 0.87 for the 4-stage scheme with $\eta = 0.15$. A plot of the Fourier footprint along with the stability boundary is given in figure 6.2. Again, at lower M the maximum CFL number is less restrictive. For $M = 3$ the maximum ν is about 1.3, while at $M = 1$ it is about 1.5.

6.2 Implicit Time-Marching

Ignoring the viscous terms, the implicit factored equation (3.15) can be written as

$$\begin{aligned} \left[\mathbf{I} + J\Delta t\delta_\xi \left(\frac{\partial \mathbf{F}^*}{\partial \mathbf{U}} \right) \right] \left[\mathbf{I} + J\Delta t\delta_\eta \left(\frac{\partial \mathbf{G}^*}{\partial \mathbf{U}} \right) \right] \Delta_t \mathbf{U}^{(n)} \\ = -J\Delta t(\delta_\xi \mathbf{F}^* + \delta_\eta \mathbf{G}^*). \end{aligned} \quad (6.20)$$

Recall that the left-hand side Jacobian derivatives are written with first-order accuracy, resulting in block tridiagonals for each coordinate-direction sweep. Splitting the Jacobian derivatives into + and - parts and expanding the right-hand side, (6.20) becomes

$$\begin{aligned} & [\mathbf{I} + J\Delta t(\delta_i^- \mathbf{A}_i^+ + \delta_i^+ \mathbf{A}_i^-)] [\mathbf{I} + J\Delta t(\delta_j^- \mathbf{B}_j^+ + \delta_j^+ \mathbf{B}_j^-)] \Delta_t \mathbf{U}^{(n)} \\ & = -J\Delta t(\mathbf{F}_{i+\frac{1}{2},j}^* - \mathbf{F}_{i-\frac{1}{2},j}^* + \mathbf{G}_{i,j+\frac{1}{2}}^* - \mathbf{G}_{i,j-\frac{1}{2}}^*), \end{aligned} \quad (6.21)$$

where the first-order operators are defined as: $\delta_k^+(\cdot) \equiv (\cdot)_{k+1} - (\cdot)_k$ and $\delta_k^-(\cdot) \equiv (\cdot)_k - (\cdot)_{k-1}$, and k represents the index i or j . Approximate inviscid Jacobians are currently employed on the left-hand side for \mathbf{A}_i^\pm and \mathbf{B}_i^\pm , as defined in (3.20) and (3.22).

The right-hand side of (6.21) is identical to the right-hand side of the explicit form (6.2), since $\Phi\Delta s$ on ξ -faces equals \mathbf{F}^* , $\Phi\Delta s$ on η -faces equals \mathbf{G}^* , and $J = 1/A$. Hence, after linearizing the right-hand side as described in the last section, (6.21) can be written:

$$\mathbf{M}\Delta_t \mathbf{U}^{(n)} = -\mathbf{L}\mathbf{U}, \quad (6.22)$$

where \mathbf{L} is given by (6.7) or (6.8) and

$$\mathbf{M} = [\mathbf{I} + J\Delta t(\delta_i^- \mathbf{A}_i^+ + \delta_i^+ \mathbf{A}_i^-)] [\mathbf{I} + J\Delta t(\delta_j^- \mathbf{B}_j^+ + \delta_j^+ \mathbf{B}_j^-)]. \quad (6.23)$$

The Fourier symbols for the first-order difference operators in (6.23) are

$$\begin{aligned} \mathfrak{F}(\delta_k^+) &= e^{i\zeta^{(k)}} - 1 \\ \mathfrak{F}(\delta_k^-) &= 1 - e^{-i\zeta^{(k)}}. \end{aligned} \quad (6.24)$$

Linearizing the \mathbf{A}_i and \mathbf{B}_i terms on the left-hand side of (6.22) about the cell center using Roe-averaged values, then taking the Fourier transform of the whole equation, the following expression for the amplification matrix \mathbf{g} results:

$$\{\mathfrak{F}(\mathbf{M})\}(\mathbf{g} - \mathbf{I}) = \mathfrak{F}(-\mathbf{L}), \quad (6.25)$$

where $\mathfrak{S}(-\mathbf{L})$ is given by (6.16) for first-order right-hand side spatial accuracy or (6.19) for second-order, and $\mathfrak{S}(\mathbf{M})$ is the Fourier transform of \mathbf{M} , given by

$$\mathfrak{S}(\mathbf{M}) = \left\{ \mathbf{I} + \frac{\nu}{\{\omega(\theta_g^{(i)}) + \omega(\theta_g^{(j)})\}} \left[\left| \frac{\partial \hat{\Phi}}{\partial \mathbf{U}}(\theta_g^{(i)}) \right| (1 - \cos \zeta^{(i)}) + i \left(\frac{\partial \hat{\Phi}}{\partial \mathbf{U}}(\theta_g^{(i)}) \right) \sin \zeta^{(i)} \right] \right\} * \left\{ \mathbf{I} + \frac{\nu}{\{\omega(\theta_g^{(i)}) + \omega(\theta_g^{(j)})\}} \left[\left| \frac{\partial \hat{\Phi}}{\partial \mathbf{U}}(\theta_g^{(j)}) \right| (1 - \cos \zeta^{(j)}) + i \left(\frac{\partial \hat{\Phi}}{\partial \mathbf{U}}(\theta_g^{(j)}) \right) \sin \zeta^{(j)} \right] \right\}. \quad (6.26)$$

Equation (6.25) can be rearranged to give the generalized eigenvalue problem:

$$[\mathfrak{S}(\mathbf{M}) + \mathfrak{S}(-\mathbf{L})] \vec{x} = g [\mathfrak{S}(\mathbf{M})] \vec{x}, \quad (6.27)$$

where g is any of the complex eigenvalues, and $[\mathfrak{S}(\mathbf{M}) + \mathfrak{S}(-\mathbf{L})]$ and $[\mathfrak{S}(\mathbf{M})]$ are complex 4×4 matrices.

The stability characteristics of the implicit equation are determined by cycling through 17 of each of the frequencies $\zeta^{(i)}$ and $\zeta^{(j)}$ from 0 to 2π inclusive. (The combinations when both $\zeta^{(i)}$ and $\zeta^{(j)}$ equal either 0 or 2π are excluded since they yield eigenvalues of 1.0 automatically for a consistent scheme.) The generalized eigenvalue problem is solved using a subroutine from the International Mathematics and Statistics Library (IMSL). The maximum eigenvalue, the average eigenvalue, and the smoothing factor are determined as a function of the CFL number ν . The maximum eigenvalue serves as an indication of stability: its value must remain at or below 1.0 for stability. The smoothing factor is the maximum eigenvalue when $\max(\zeta^{(i)}, \zeta^{(j)})$ lies between $\pi/2$ and $3\pi/2$. It corresponds to the damping of high frequencies, and serves as an indication of the possible effectiveness of a multigrid method if it was applied to the scheme. The average eigenvalue simply gives a measure of the mean of all the eigenvalues over the whole frequency range.

Again, the stability is a function of a large number of independent variables, including the parameters ν , M , α , β , θ'_d , and θ'_g , so a thorough numerical analysis is difficult. For first-order spatial accuracy, the "worst case" parameters of all the variations tested were determined to be: $M = 100$, $\alpha = 90^\circ$, $\theta'_d = 22.5^\circ$, $\theta'_g = 0^\circ$, and $\beta = 0$ (although $\beta = 1$ gives a similar result here). As can be seen in figure 6.3 in a plot of the eigenvalue parameters as a function of CFL number, the maximum ν insuring stability is 2.5. For the different conditions of $M=100$, $\alpha = 45^\circ$, $\theta'_d = 45^\circ$, $\theta'_g = 0^\circ$, and $\beta = 0$, the scheme is stable only up to $\nu = 0.05$, the lowest limit found, as shown in figure 6.4(a). However, at these conditions the stability is a strong function of β . When $\beta = 0.05$, the maximum ν for stability increases to 2.5, as shown in figure 6.4(b). Higher β give even larger maximum allowable CFL numbers for these particular parameters. As was mentioned in Chapter 5, β is limited to be greater than 0.05 as an aid to convergence, as determined empirically for solutions using explicit time-marching. Now it is clear that this limiting is necessary from the standpoint of stability for implicit-time marching as well.

All other variations in parameters that were tested give stability limits that are either equally or less restrictive than those of figures 6.3 and 6.4. Hence, with β limited to be greater than 0.05, the CFL limit for the first-order implicit scheme is about 2.5. As was true for explicit-time marching, the stability limit derived here for $M=100$ is somewhat overrestrictive for flows at lower Mach numbers. In practice, at reasonably low Mach numbers (less than about 3 or so) the stability limit appears to be about $\nu = 4$.

When second-order spatial differencing on the right-hand side is employed, the CFL limit for stability is more restrictive. Figure 6.5 shows the stability plot for $M = 100$, $\alpha = 90^\circ$, $\theta'_d = 22.5^\circ$, $\theta'_g = 0^\circ$, and $\beta = 0$ (although $\beta = 1$ gives a similar result here). The maximum $\nu = 1.4$ for stability for this case. For the

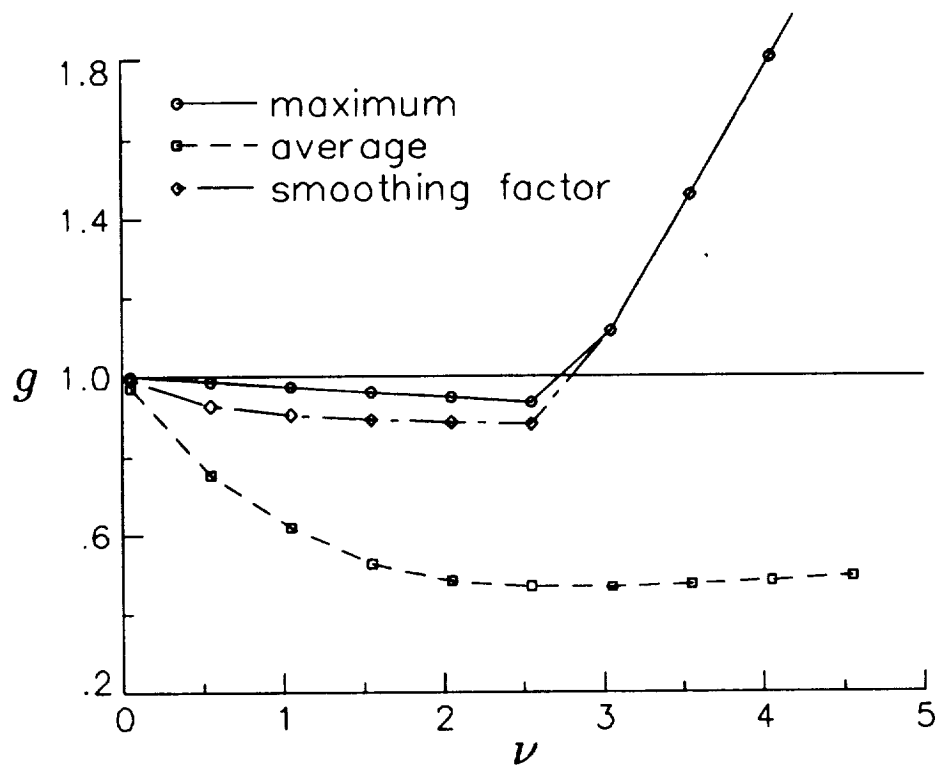


Figure 6.3: Eigenvalues as Function of CFL Number for Implicit Scheme, First-Order, $M = 100$, $\alpha = 90^\circ$, $\theta'_d = 22.5^\circ$, $\theta_g = 0^\circ$, $\beta = 0$

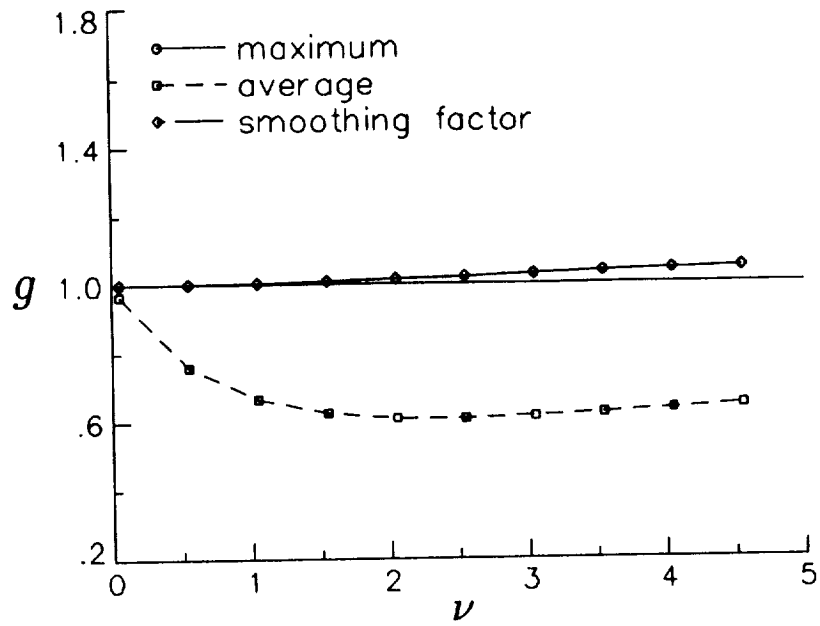
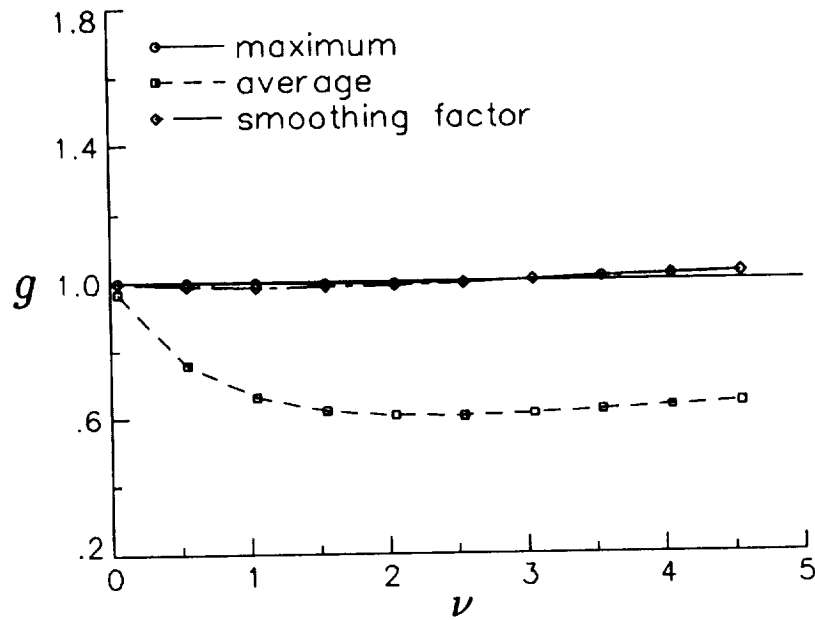
a) $\beta = 0$ b) $\beta = 0.05$

Figure 6.4: Eigenvalues as Function of CFL Number for Implicit Scheme, First-Order, $M = 100$, $\alpha = 45^\circ$, $\theta'_d = 45^\circ$, $\theta_g = 0^\circ$

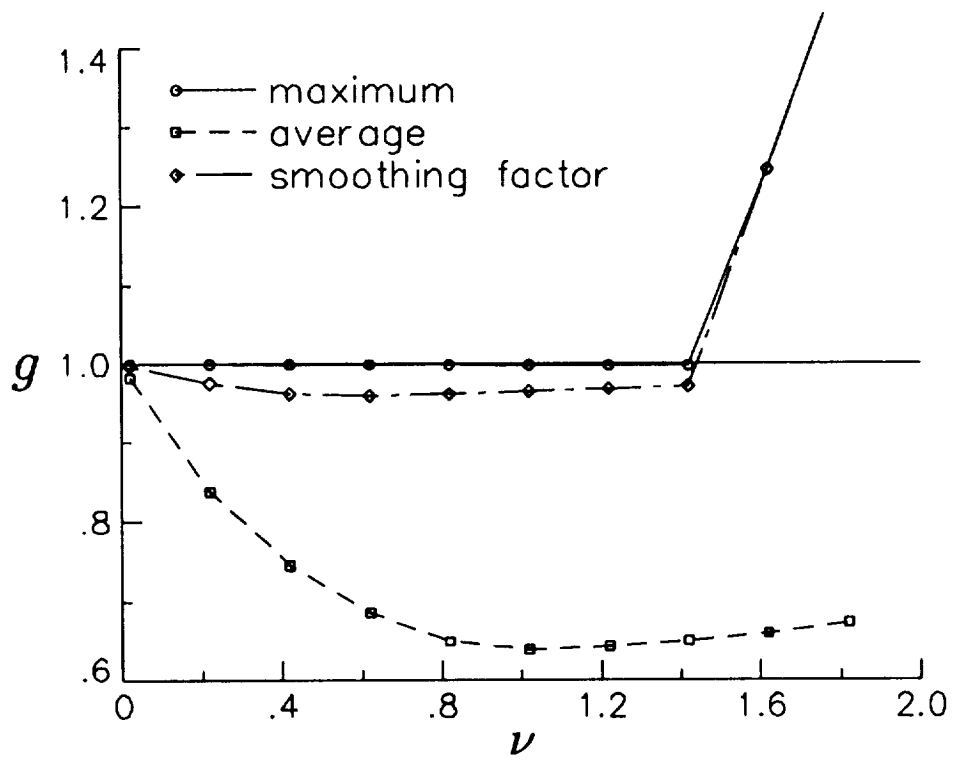


Figure 6.5: Eigenvalues as Function of CFL Number for Implicit Scheme, Second-Order, $M = 100$, $\alpha = 90^\circ$, $\theta'_d = 22.5^\circ$, $\theta_g = 0^\circ$, $\beta = 0$

conditions $M=100$, $\alpha = 45^\circ$, $\theta'_d = 45^\circ$, $\theta_g = 0^\circ$, and $\beta = 0$, the scheme is stable only up to the lowest limit of $\nu = 0.01$, as shown in figure 6.6(a). When β is limited to be greater than 0.05, then the stability limit for this case increases to about 0.3, as shown in figure 6.6(b). Hence, since other combinations of variables tested give similar or better stability limits, the maximum ν for stability for the second-order implicit scheme is about 0.3. Again, at lower Mach numbers this stability restriction can be relaxed somewhat. In practice, at Mach numbers less than about 3 the stability limit is about $\nu = 2$.

Naturally the question arises as to whether some left-hand side approximate Jacobians other than (3.20) and (3.22) can be devised to give better stability properties for the implicitly-advanced 5-wave model. It turns out that if the approximate Jacobians are taken as:

$$\begin{aligned} (\mathbf{A}_i)^+ &= \frac{1}{2} \left\{ \left(\frac{\partial \mathbf{F}^*}{\partial \mathbf{U}} \right)_i + |\hat{\mathbf{D}}(\theta_g^{(i)})|_{i+\frac{1}{2}} \right\} \\ (\mathbf{A}_i)^- &= \frac{1}{2} \left\{ \left(\frac{\partial \mathbf{F}^*}{\partial \mathbf{U}} \right)_{i+1} - |\hat{\mathbf{D}}(\theta_g^{(i)})|_{i+\frac{1}{2}} \right\} \end{aligned} \quad (6.28)$$

$$\begin{aligned} (\mathbf{B}_i)^+ &= \frac{1}{2} \left\{ \left(\frac{\partial \mathbf{G}^*}{\partial \mathbf{U}} \right)_j + |\hat{\mathbf{D}}(\theta_g^{(j)})|_{j+\frac{1}{2}} \right\} \\ (\mathbf{B}_i)^- &= \frac{1}{2} \left\{ \left(\frac{\partial \mathbf{G}^*}{\partial \mathbf{U}} \right)_{j+1} - |\hat{\mathbf{D}}(\theta_g^{(j)})|_{j+\frac{1}{2}} \right\}, \end{aligned} \quad (6.29)$$

where $|\hat{\mathbf{D}}|$ is defined in (6.11), then the Fourier transform of the linearized left-hand side operator is given by

$$\begin{aligned} \mathfrak{S}(\mathbf{M}) = & \left\{ \mathbf{I} + \frac{\nu}{\{\omega(\theta_g^{(i)}) + \omega(\theta_g^{(j)})\}} \left[|\hat{\mathbf{D}}(\theta_g^{(i)})|(1 - \cos\zeta^{(i)}) + \right. \right. \\ & \left. \left. i \left(\frac{\partial \hat{\Phi}}{\partial \mathbf{U}}(\theta_g^{(i)}) \right) \sin\zeta^{(i)} \right] \right\} * \left\{ \mathbf{I} + \frac{\nu}{\{\omega(\theta_g^{(i)}) + \omega(\theta_g^{(j)})\}} \left[|\hat{\mathbf{D}}(\theta_g^{(j)})|(1 - \right. \right. \\ & \left. \left. \cos\zeta^{(j)}) + i \left(\frac{\partial \hat{\Phi}}{\partial \mathbf{U}}(\theta_g^{(j)}) \right) \sin\zeta^{(j)} \right] \right\}. \end{aligned} \quad (6.30)$$

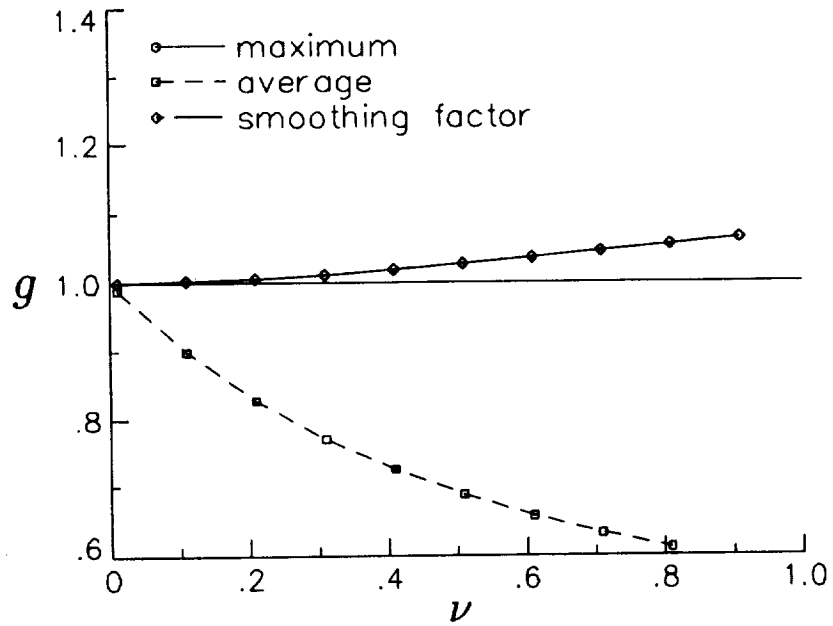
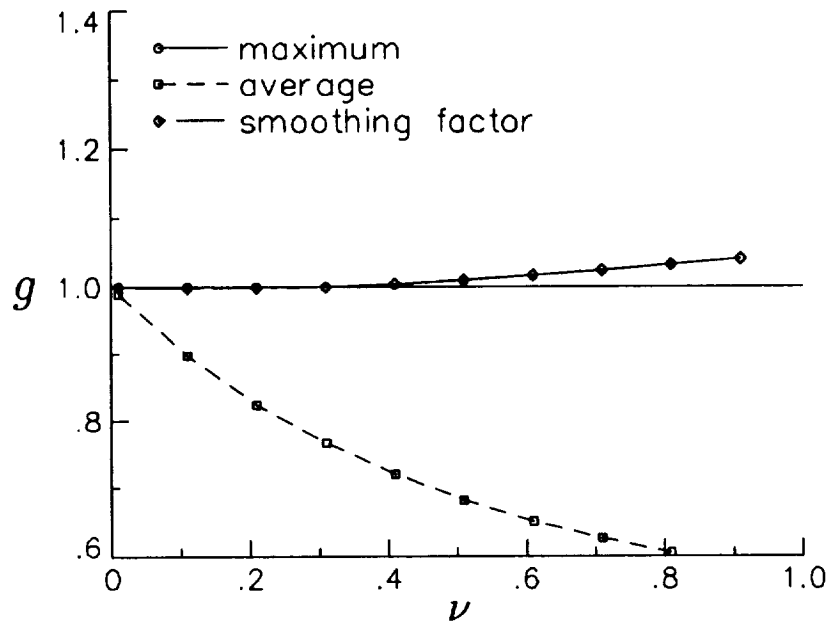
a) $\beta = 0$ b) $\beta = 0.05$

Figure 6.6: Eigenvalues as Function of CFL Number for Implicit Scheme, Second-Order, $M = 100$, $\alpha = 45^\circ$, $\theta'_d = 45^\circ$, $\theta_g = 0^\circ$

Numerical analysis of the resulting generalized eigenvalue problem shows this method to be unconditionally stable for first-order spatially accurate computations. This linearized analytical result is confirmed in practice as well. First-order results have been seen to be stable at CFL numbers as high as 1000, although the optimum ν for convergence generally occurs between about 5 and 10.

Unfortunately, use of (6.28) and (6.29) in conjunction with a second-order right-hand side for the 5-wave model proves in practice to be even *less* stable than when the grid-aligned Jacobians (3.20) and (3.22) are used. An example of a stability analysis is shown in figure 6.7 for the same conditions as figure 6.5, only now the Fourier transform of the left-hand side (6.30) is used in place of (6.26). The maximum ν for stability is only 0.6, compared with 1.4 for the grid-aligned approximate left-hand side.

In order to attempt to improve the stability properties of the 5-wave model for second-order accurate computations using the approximately-factored implicit scheme, the method is reformulated using second-order left-hand side spatial accuracy. This makes it necessary to solve a block-pentadiagonal system rather than tridiagonals during each sweep. The procedure outlined by Barth [29] is followed to determine an appropriate form for the approximate left-hand side Jacobians for second-order accuracy. The end result is given here for the i th row of the block-banded matrix for the first sweep in solving the Euler equations:

$$\left[\dots, 0, (\mathbf{N}_1)_i, (\mathbf{N}_2)_i, ((\mathbf{N}_3)_i + \mathbf{I}/(J\Delta t)), (\mathbf{N}_4)_i, (\mathbf{N}_5)_i, 0, \dots \right], \quad (6.31)$$

with

$$(\mathbf{N}_1)_i = \frac{1}{4} \left[\left(\frac{\partial \mathbf{F}^*}{\partial \mathbf{U}} \right)_{i-2} + \left| \hat{\mathbf{D}}(\theta_g^{(i)}) \right|_{i-1/2} \right] \quad (6.32)$$

$$(\mathbf{N}_2)_i = - \left[\left(\frac{\partial \mathbf{F}^*}{\partial \mathbf{U}} \right)_{i-1} + \frac{3}{4} \left| \hat{\mathbf{D}}(\theta_g^{(i)}) \right|_{i-1/2} + \frac{1}{4} \left| \hat{\mathbf{D}}(\theta_g^{(i)}) \right|_{i+1/2} \right] \quad (6.33)$$

$$(\mathbf{N}_3)_i = \frac{3}{4} \left[\left| \hat{\mathbf{D}}(\theta_g^{(i)}) \right|_{i+1/2} + \left| \hat{\mathbf{D}}(\theta_g^{(i)}) \right|_{i-1/2} \right] \quad (6.34)$$

$$(\mathbf{N}_4)_i = \left[\left(\frac{\partial \mathbf{F}^*}{\partial \mathbf{U}} \right)_{i+1} - \frac{3}{4} \left| \hat{\mathbf{D}}(\theta_g^{(i)}) \right|_{i+1/2} - \frac{1}{4} \left| \hat{\mathbf{D}}(\theta_g^{(i)}) \right|_{i-1/2} \right] \quad (6.35)$$

$$(\mathbf{N}_5)_i = -\frac{1}{4} \left[\left(\frac{\partial \mathbf{F}^*}{\partial \mathbf{U}} \right)_{i+2} - \left| \hat{\mathbf{D}}(\theta_g^{(i)}) \right|_{i+1/2} \right]. \quad (6.36)$$

A similar form results for the second sweep. A stability analysis is carried out using

$$\mathbf{M} = [\mathbf{I} + J\Delta t(\partial_i^- \mathbf{A}_i^+ + \partial_i^+ \mathbf{A}_i^-)] [\mathbf{I} + J\Delta t(\partial_j^- \mathbf{B}_j^+ + \partial_j^+ \mathbf{B}_j^-)]. \quad (6.37)$$

The ∂_k^\pm are defined to be the following second-order difference operators:

$$\begin{aligned} \partial_k^+(\cdot) &= -\frac{3}{2}(\cdot)_k + 2(\cdot)_{k+1} - \frac{1}{2}(\cdot)_{k+2} \\ \partial_k^-(\cdot) &= \frac{3}{2}(\cdot)_k - 2(\cdot)_{k-1} + \frac{1}{2}(\cdot)_{k-2}, \end{aligned} \quad (6.38)$$

where k represents the index i or j . The Fourier symbols of these operators are:

$$\begin{aligned} \mathfrak{S}(\partial_k^+) &= -\frac{3}{2} + 2e^{i\zeta^{(k)}} - \frac{1}{2}e^{i2\zeta^{(k)}} \\ \mathfrak{S}(\partial_k^-) &= \frac{3}{2} - 2e^{-i\zeta^{(k)}} + \frac{1}{2}e^{-i2\zeta^{(k)}}. \end{aligned} \quad (6.39)$$

The Fourier transform of \mathbf{M} , with terms linearized about the cell-center using Roe-averaged values, becomes:

$$\begin{aligned} \mathfrak{S}(\mathbf{M}) &= \left\{ \mathbf{I} + \frac{\nu}{\{\omega(\theta_g^{(i)}) + \omega(\theta_g^{(j)})\}} \left[\left| \hat{\mathbf{D}}(\theta_g^{(i)}) \right| \left(-2\cos\zeta^{(i)} + \frac{1}{2}\cos 2\zeta^{(i)} + \right. \right. \right. \\ &\quad \left. \left. \frac{3}{2} \right) + i \left(\frac{\partial \hat{\Phi}}{\partial \mathbf{U}}(\theta_g^{(i)}) \right) \left(2\sin\zeta^{(i)} - \frac{1}{2}\sin 2\zeta^{(i)} \right) \right] \right\} * \left\{ \mathbf{I} + \right. \\ &\quad \left. \frac{\nu}{\{\omega(\theta_g^{(i)}) + \omega(\theta_g^{(j)})\}} \left[\left| \hat{\mathbf{D}}(\theta_g^{(j)}) \right| \left(-2\cos\zeta^{(j)} + \frac{1}{2}\cos 2\zeta^{(j)} + \frac{3}{2} \right) + \right. \right. \\ &\quad \left. \left. i \left(\frac{\partial \hat{\Phi}}{\partial \mathbf{U}}(\theta_g^{(j)}) \right) \left(2\sin\zeta^{(j)} - \frac{1}{2}\sin 2\zeta^{(j)} \right) \right] \right\}. \end{aligned} \quad (6.40)$$

This linearized analysis shows the block pentadiagonal approximate-factorization method to be unconditionally stable in conjunction with a second-order spatially accurate right-hand side. In practice, however, the method is found to be stable

only up to CFL numbers of about 100 or so. This disagreement between theory and practice arises as a result of the highly nonlinear nature of the 5-wave model. The stability analysis is only a linearized approximation. Although the practical maximum allowable CFL number of 100 represents a dramatic improvement over the value of 2 that results when the grid-aligned left-hand side is employed, the optimum *rate* of convergence for steady-state calculations is still obtained for relatively low CFL numbers between about $\nu = 2$ and $\nu = 6$.

Example convergence plots are shown in figure 6.8 for second-order spatially accurate computations of an inviscid shock reflection off a flat plate ($M_\infty = 2.9$) using the 5-wave model. When the grid-independent approximate Jacobians (pentadiagonal LHS) are employed, CFL numbers up to about 100 can be used, but the optimum rate of convergence is obtained at a CFL number of $\nu = 3$ for this case. Results with $\nu = 2$ are also shown for direct comparison with the result using the grid-aligned left-hand side Jacobians (tridiagonal LHS). Due to the inconsistency inherent in the use of grid-aligned left-hand side linearizations with the grid-independent right-hand side, the rate of convergence of the latter method tapers off as the solution approaches steady-state. However, both methods reduce the L_2 -norm of the residual to 10^{-8} in about the same number of iterations.

In summary, the stability properties of the 5-wave model, advanced implicitly in time using an approximate-factorization algorithm, can be improved dramatically through the proper choice of approximate Jacobians. However, for simplicity and consistency all implicit computations in the present study employ the grid-aligned approximate Jacobians described in Chapter 3. Although the corresponding maximum CFL numbers are more restrictive, they are usually high enough for most problems to allow for an acceptable rate of convergence. On the other hand, if the 5-wave model was to be used for higher Mach number flows where the stability restrictions using the grid-aligned left-hand side are more severe, or in

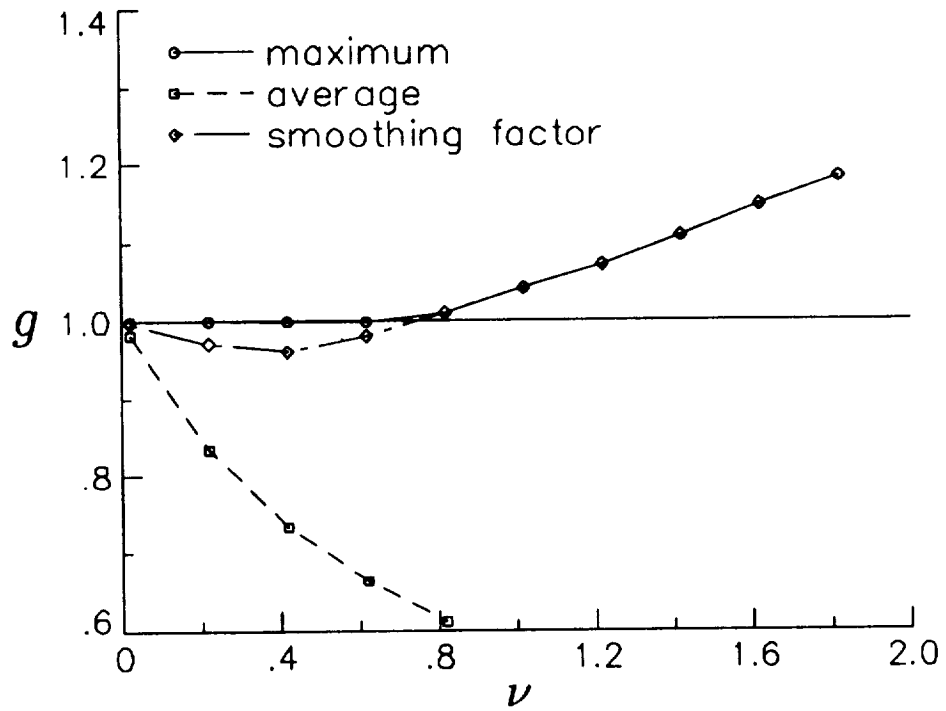


Figure 6.7: Same as Figure 6.5, Except Approximate Jacobians (6.28) and (6.29) Used on Left-Hand Side

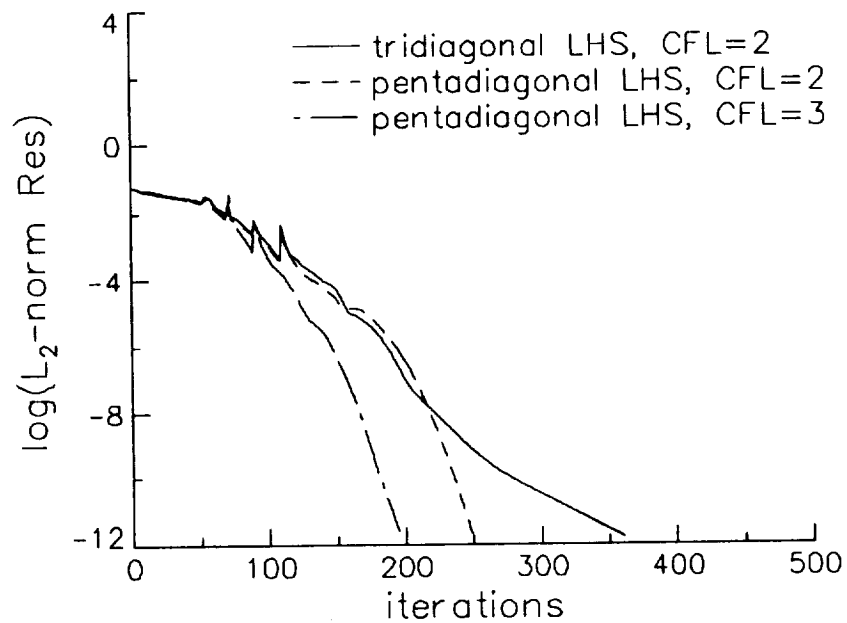


Figure 6.8: Convergence Histories for Implicit A-F Scheme Applied to Second-Order Accurate Euler Computation Using 5-Wave Model

time-accurate computations where each mesh cell is advanced at a constant time step, it would probably be necessary to employ the grid-independent left-hand side terms in order to be able to advance the implicit solution at a reasonable rate. For second-order computations, this would entail the use of a block pentadiagonal solver.

CHAPTER 7

MONOTONICITY ANALYSIS

The method for analyzing the monotonicity of the two-dimensional Euler equations is derived from considerations of the scalar convection equation $u_t + au_x = 0$. The results of the Euler equations analysis are considered to be valid for the Navier-Stokes equations as well, since the viscous terms add dissipation which tends to mitigate numerical oscillations that may occur near regions of strongly varying gradients.

7.1 Scalar Wave Equation

The one-dimensional scalar convection equation is written in finite-volume form, with forward-Euler time stepping (i is a given cell bordered by $(i - 1)$ to the left and $(i + 1)$ to the right):

$$u_i^{(n+1)} = u_i^{(n)} - \frac{\Delta t}{\Delta x} (f_{i+\frac{1}{2}} - f_{i-\frac{1}{2}}). \quad (7.1)$$

Here $f_{i+1/2}$ and $f_{i-1/2}$ are the fluxes on the $(i + 1/2)$ and $(i - 1/2)$ cell faces, respectively, and Δx is the distance between the gridpoints. Consider now a computational stencil in which $u_i^{(n+1)}$ only depends on $u_i^{(n)}$, $u_{i+1}^{(n)}$, and $u_{i-1}^{(n)}$. Godunov [3] showed that one way to insure that spurious oscillations do not develop is to require that variations in u in each cell in the computational stencil causes a variation *in the same direction* in cell i . In other words, if u_{i-1} increases, then u_i

should also increase, or at worst remain unchanged. A similar requirement holds for changes in the $(i + 1)$ st cell. These requirements can be written

$$\frac{\partial u_i^{(n+1)}}{\partial u_{i+1}^{(n)}} \geq 0 \quad \text{and} \quad \frac{\partial u_i^{(n+1)}}{\partial u_{i-1}^{(n)}} \geq 0 \quad (7.2)$$

or, since $f_{i+1/2}$ is identical to $f(u_{i+1}, u_i)$ and $f_{i-1/2}$ is identical to $f(u_i, u_{i-1})$,

$$\frac{\partial f_{i+\frac{1}{2}}}{\partial u_{i+1}} \leq 0 \quad \text{and} \quad \frac{\partial f_{i-\frac{1}{2}}}{\partial u_{i-1}} \geq 0. \quad (7.3)$$

A third restriction is $\partial u_i^{(n+1)} / \partial u_i^{(n)} \geq 0$, but this merely limits the time step.

As an example of the usefulness of this analysis, consider first-order upwind differencing, which is already known to be monotone:

$$\begin{aligned} f_{i+\frac{1}{2}} &= \frac{1}{2}a(u_{i+1} + u_i) - \frac{1}{2}|a|(u_{i+1} - u_i) \\ f_{i-\frac{1}{2}} &= \frac{1}{2}a(u_i + u_{i-1}) - \frac{1}{2}|a|(u_i - u_{i-1}). \end{aligned} \quad (7.4)$$

Here, $\partial f_{i+1/2} / \partial u_{i+1} = \frac{1}{2}(a - |a|)$, which is non-positive, and $\partial f_{i-1/2} / \partial u_{i-1} = \frac{1}{2}(a + |a|)$, which is non-negative. Hence first-order upwind differencing satisfies (7.3), as expected. A counter-example is central-differencing, which is already known *not* to be monotone:

$$\begin{aligned} f_{i+\frac{1}{2}} &= \frac{1}{2}a(u_{i+1} + u_i) \\ f_{i-\frac{1}{2}} &= \frac{1}{2}a(u_i + u_{i-1}). \end{aligned} \quad (7.5)$$

Here, it is seen that (7.3) can never be satisfied except for the degenerate case of $a = 0$, since both $\partial f_{i+1/2} / \partial u_{i+1}$ and $\partial f_{i-1/2} / \partial u_{i-1} = \frac{1}{2}a$.

7.2 Euler Equations

The ideas from the last section extend in a straightforward manner to the one-dimensional Euler equations. These can be diagonalized yielding three non-linearly coupled convection equations, each which describes the convection of a

“characteristic variable.” Satisfying requirement (7.2) for each of these variables then implies monotonicity for the numerical scheme.

Extension of this analysis technique for use with the two-dimensional Euler equations is not as simple because the equations are not diagonalizable in general, as discussed in Chapter 2. However, the influence of variations in the conserved variables can be decoupled locally, as described below. First, the two-dimensional Euler equations are written in finite-volume form with forward-Euler time stepping, and it is assumed for simplicity that the mesh is made up of square cells with face length Δs :

$$\mathbf{U}_{i,j}^{(n+1)} = \mathbf{U}_{i,j}^{(n)} - \frac{\Delta t}{\Delta s} \left(\Phi_{i+\frac{1}{2},j} - \Phi_{i-\frac{1}{2},j} + \Phi_{i,j+\frac{1}{2}} - \Phi_{i,j-\frac{1}{2}} \right), \quad (7.6)$$

\mathbf{U} are the conserved variables and Φ are the fluxes per unit face-length on the cell faces, given by (5.10). It is assumed that the computational stencil is made up of only (i, j) , $(i + 1, j)$, $(i - 1, j)$, $(i, j + 1)$, and $(i, j - 1)$, so that in one time step $\mathbf{U}_{i,j}$ is only a function of its initial value and the values in the four immediate neighboring cells. Thus this analysis only applies to a spatially first-order accurate scheme.

Now, instead of one equation, there are four coupled equations, and the quantity $\partial \mathbf{U}_{i,j}^{(n+1)} / \partial \mathbf{U}_{i+1,j}^{(n)}$, for example, is not a single variable but a 4×4 matrix. The matrices $\partial \mathbf{U}_{i,j}^{(n+1)} / \partial \mathbf{U}_k^{(n)}$, where $k = (i + 1, j)$, $(i - 1, j)$, $(i, j + 1)$, $(i, j - 1)$, are termed the “influence matrices.” The four eigenvalues of each influence matrix represent the change of certain characteristic variables at (i, j) caused by the change in those same four variables in the corresponding neighboring cell. Since the equations describe the convection of these characteristic variables, non-negativity of the eigenvalues of each influence matrix implies monotonicity for the corresponding set of characteristic variables. Note, however, that the characteristic variables associated with the cells $(i \pm 1, j)$ are not the same as those for cells

$(i, j \pm 1)$, except for the entropy; therefore it is not clear what the combined effect of these monotonicity properties is. Nonetheless, this approach is utilized to help define a limiting procedure for reducing oscillations in two-dimensional solutions.

The conditions equivalent to (7.2) for the two-dimensional Euler equations are

$$\text{e.v.} \left(\frac{\partial \mathbf{U}_{i,j}^{(n+1)}}{\partial \mathbf{U}_k^{(n)}} \right) \geq 0 \quad k = (i+1, j), (i-1, j), (i, j+1), (i, j-1) \quad (7.7)$$

or, equivalently,

$$\begin{aligned} \text{e.v.} \left(\frac{\partial \Phi_{i+\frac{1}{2},j}}{\partial \mathbf{U}_{i+1,j}} \right) &\leq 0 & \text{e.v.} \left(\frac{\partial \Phi_{i,j+\frac{1}{2}}}{\partial \mathbf{U}_{i,j+1}} \right) &\leq 0 \\ \text{e.v.} \left(\frac{\partial \Phi_{i-\frac{1}{2},j}}{\partial \mathbf{U}_{i-1,j}} \right) &\geq 0 & \text{e.v.} \left(\frac{\partial \Phi_{i,j-\frac{1}{2}}}{\partial \mathbf{U}_{i,j-1}} \right) &\geq 0, \end{aligned} \quad (7.8)$$

where $\text{e.v.}(\cdot)$ represents "the eigenvalues of (\cdot) ". If the grid-normal angle θ_g is varied over the full range of possible angles, then satisfying all four inequalities in (7.8) is redundant. Satisfying the two inequalities on opposing faces (say the $(i+1/2, j)$ face and the $(i-1/2, j)$ face) is then sufficient to insure this monotonicity property.

In order to proceed with the monotonicity analysis for the 5-wave grid-independent model, (5.10) is written in slightly different form:

$$\begin{aligned} \Phi_{i+\frac{1}{2},j} = \frac{1}{2}(\Phi_{i+1,j} + \Phi_{i,j}) - \frac{1}{2} \{ [\hat{\mathbf{R}}^*] | [\hat{\mathbf{\Lambda}}^*] \cos(\theta'_d - \theta_g) | \hat{\mathbf{\Omega}}^* + \\ [\hat{\mathbf{R}}^{**}] | [\hat{\mathbf{\Lambda}}^{**}] (-\sin(\theta'_d - \theta_g)) | \hat{\mathbf{\Omega}}^{**} \}. \end{aligned} \quad (7.9)$$

$[\hat{\mathbf{R}}^*]$ is the matrix of wave vectors acting in the θ'_d -direction ($\hat{\mathbf{R}}_{1,2,4,5}$ in (5.11)). $[\hat{\mathbf{R}}^{**}]$ is the corresponding matrix of wave vectors acting in the $(\theta'_d + \frac{\pi}{2})$ -direction (only the shear vector, $\hat{\mathbf{R}}_3$ in (5.11), is used in the 5-wave model). Then $[\hat{\mathbf{\Lambda}}^*] = \text{diag}(\hat{q}'_d + \hat{a}, \hat{q}'_d - \hat{a}, \hat{q}'_d, \hat{q}'_d)$ and $[\hat{\mathbf{\Lambda}}^{**}] = \text{diag}(\hat{r}'_d + \hat{a}, \hat{r}'_d - \hat{a}, \hat{r}'_d, \hat{r}'_d)$ are the corresponding wavestrengths in those same directions. The wavestrengths are

$$\hat{\mathbf{\Omega}}^* = \begin{bmatrix} \frac{\Delta p}{2\hat{a}^2} + \beta \frac{\hat{p}}{2\hat{a}} (\Delta u \cos \theta'_d + \Delta v \sin \theta'_d) \\ \frac{\Delta p}{2\hat{a}^2} - \beta \frac{\hat{p}}{2\hat{a}} (\Delta u \cos \theta'_d + \Delta v \sin \theta'_d) \\ \frac{1}{\hat{a}^2} (\hat{a}^2 \Delta \rho - \Delta p) \\ \frac{\hat{p}}{\hat{a}} (-\Delta u \sin \theta'_d + \Delta v \cos \theta'_d) \end{bmatrix} \quad (7.10)$$

$$\hat{\Omega}^{**} = \begin{bmatrix} 0 \\ 0 \\ 0 \\ (\beta - 1) \frac{\hat{p}}{\hat{a}} (\Delta u \cos \theta'_d + \Delta v \sin \theta'_d) \end{bmatrix}. \quad (7.11)$$

The present study concentrates on the variations in $\hat{\Omega}^*$ and $\hat{\Omega}^{**}$. It is assumed that the wave vectors, wavespeeds, and θ'_d are constant, and all variables are taken as the Roe-averaged values. In addition, β , although a function of Δu , Δv , and Δp , is considered constant in order to simplify the final expressions. With these assumptions, this becomes a linearized analysis and one can obtain

$$\frac{\partial \Phi_{i+\frac{1}{2},j}}{\partial \mathbf{U}_{i+1,j}} = \frac{1}{2} \frac{\partial \hat{\Phi}}{\partial \mathbf{U}}(\theta_g) - \frac{1}{2} \left\{ [\hat{\mathbf{R}}^*][\hat{\Lambda}^*] \cos(\theta'_d - \theta_g) \left| \frac{\partial \hat{\Omega}^*}{\partial \mathbf{U}_R} + [\hat{\mathbf{R}}^{**}][\hat{\Lambda}^{**}] (-\sin(\theta'_d - \theta_g)) \left| \frac{\partial \hat{\Omega}^{**}}{\partial \mathbf{U}_R} \right. \right\}. \quad (7.12)$$

In a similar fashion, for the $(i - 1/2)$ face

$$\frac{\partial \Phi_{i-\frac{1}{2},j}}{\partial \mathbf{U}_{i-1,j}} = \frac{1}{2} \frac{\partial \hat{\Phi}}{\partial \mathbf{U}}(\theta_g) - \frac{1}{2} \left\{ [\hat{\mathbf{R}}^*][\hat{\Lambda}^*] \cos(\theta'_d - \theta_g) \left| \frac{\partial \hat{\Omega}^*}{\partial \mathbf{U}_L} + [\hat{\mathbf{R}}^{**}][\hat{\Lambda}^{**}] (-\sin(\theta'_d - \theta_g)) \left| \frac{\partial \hat{\Omega}^{**}}{\partial \mathbf{U}_L} \right. \right\}. \quad (7.13)$$

The monotonicity constraints are

$$\begin{aligned} \text{e.v.} \left(\frac{\partial \Phi_{i+\frac{1}{2}}}{\partial \mathbf{U}_{i+1}} \right) &\leq 0 \\ \text{e.v.} \left(\frac{\partial \Phi_{i-\frac{1}{2}}}{\partial \mathbf{U}_{i-1}} \right) &\geq 0. \end{aligned} \quad (7.14)$$

The derivative matrices for the 5-wave model can be found as $\partial \hat{\Omega}^* / \partial \mathbf{U}_R =$

$$\begin{bmatrix} \frac{\gamma-1}{4\hat{a}^2}(\hat{u}^2 + \hat{v}^2) - \frac{\beta \hat{q}'_d}{2\hat{a}} & -\frac{(\gamma-1)\hat{u}}{2\hat{a}^2} + \frac{\beta \cos \theta'_d}{2\hat{a}} & -\frac{(\gamma-1)\hat{v}}{2\hat{a}^2} + \frac{\beta \sin \theta'_d}{2\hat{a}} & \frac{\gamma-1}{2\hat{a}^2} \\ \frac{\gamma-1}{4\hat{a}^2}(\hat{u}^2 + \hat{v}^2) + \frac{\beta \hat{q}'_d}{2\hat{a}} & -\frac{(\gamma-1)\hat{u}}{2\hat{a}^2} - \frac{\beta \cos \theta'_d}{2\hat{a}} & -\frac{(\gamma-1)\hat{v}}{2\hat{a}^2} - \frac{\beta \sin \theta'_d}{2\hat{a}} & \frac{\gamma-1}{2\hat{a}^2} \\ 1 - \frac{(\gamma-1)(\hat{u}^2 + \hat{v}^2)}{2\hat{a}^2} & \frac{(\gamma-1)\hat{u}}{\hat{a}^2} & \frac{(\gamma-1)\hat{v}}{\hat{a}^2} & -\frac{(\gamma-1)}{\hat{a}^2} \\ -\frac{\hat{r}'_d}{\hat{a}} & -\frac{\sin \theta'_d}{\hat{a}} & \frac{\cos \theta'_d}{\hat{a}} & 0 \end{bmatrix}, \quad (7.15)$$

$$\frac{\partial \hat{\Omega}^{**}}{\partial \mathbf{U}_R} = \begin{bmatrix} 0 & 0 & 0 & 0 \\ 0 & 0 & 0 & 0 \\ 0 & 0 & 0 & 0 \\ -\frac{(\beta-1)\hat{q}'_d}{\hat{a}} & \frac{(\beta-1)\cos \theta'_d}{\hat{a}} & \frac{(\beta-1)\sin \theta'_d}{\hat{a}} & 0 \end{bmatrix}, \quad (7.16)$$

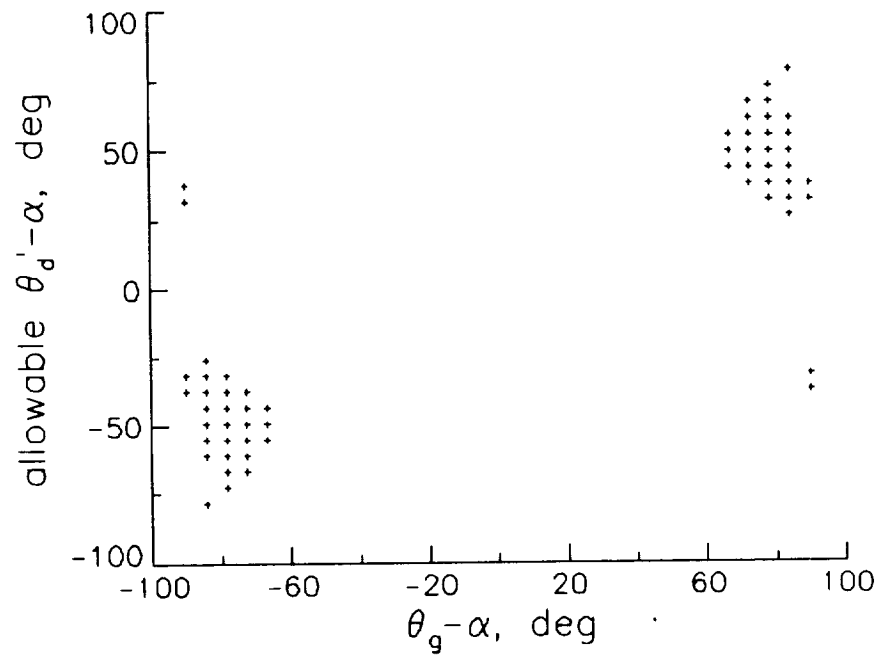
and $(\partial\hat{\Omega}^*/\partial\mathbf{U}_L) = -(\partial\hat{\Omega}^*/\partial\mathbf{U}_R)$, and $(\partial\hat{\Omega}^{**}/\partial\mathbf{U}_L) = -(\partial\hat{\Omega}^{**}/\partial\mathbf{U}_R)$.

The monotonicity analysis is carried out numerically. The Mach number M , flow angle α , and β are chosen, then θ_g and θ'_d are each varied independently between -90° and 90° with incremental changes of $\pi/32$. Eigenvalues are computed for each condition. They are usually real numbers, but can also be complex conjugates; in such cases only the real parts are considered. If they meet the criteria of equation (7.14), then monotonicity is preserved at that condition. It turns out that plotting $(\theta'_d - \alpha)$ vs. $(\theta_g - \alpha)$ removes the dependence on α (in other words, plots are the same regardless of the value of α).

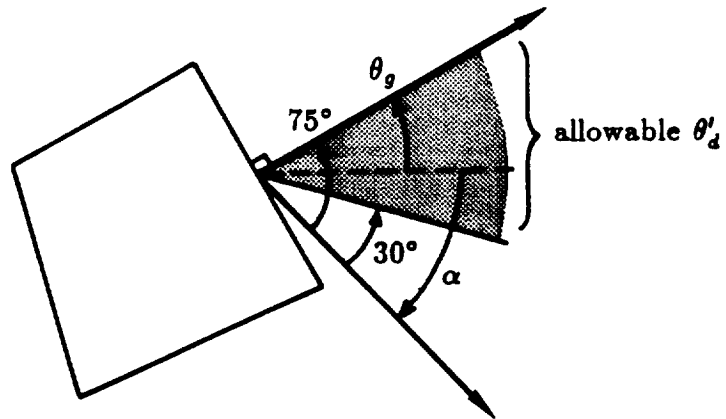
A sample plot is shown in figure 7.1(a). The conditions are $M=3$, $\beta=0.95$. There are two very small regions where monotonicity is preserved. (Note that some points may be missing from these monotonicity plots wherever the eigenvalue solver does not converge within a specified number of iterations. However, we are more interested in general regions than in specific points.) As a specific example, from the figure it is seen that the scheme is monotone for approximately $30^\circ < \theta'_d - \alpha < 75^\circ$ when $\theta_g - \alpha = 75^\circ$. These example allowable conditions are sketched in figure 7.1(b).

It is also evident from figure 7.1(a) that if $(\theta_g - \alpha)$ lies between roughly -60° and 60° , then *no* θ'_d chosen will insure monotonicity. Other β 's less than 1.0 produce similar plots. Only when $\beta = 1.0$ is there always *some* θ'_d that will yield a monotone scheme, as shown in figures 7.2(a) through (c). Here, the diagonal where $\theta'_d = \theta_g$ corresponds to the grid-aligned scheme. The effect of Mach number is also shown in the figures. At low Mach numbers, only the grid-aligned method is monotone (*i.e.* θ'_d must = θ_g and β must = 1.0), while at higher supersonic Mach numbers the monotone region is extended slightly from the $M=3$ case.

It is clear from this analysis that the restrictions on allowable θ'_d for a mono-



a) Monotonicity Regions



b) Approximate Allowable θ'_d When $\theta_g - \alpha = 75^\circ$

Figure 7.1: Monotonicity for $M = 3, \beta = 0.95$

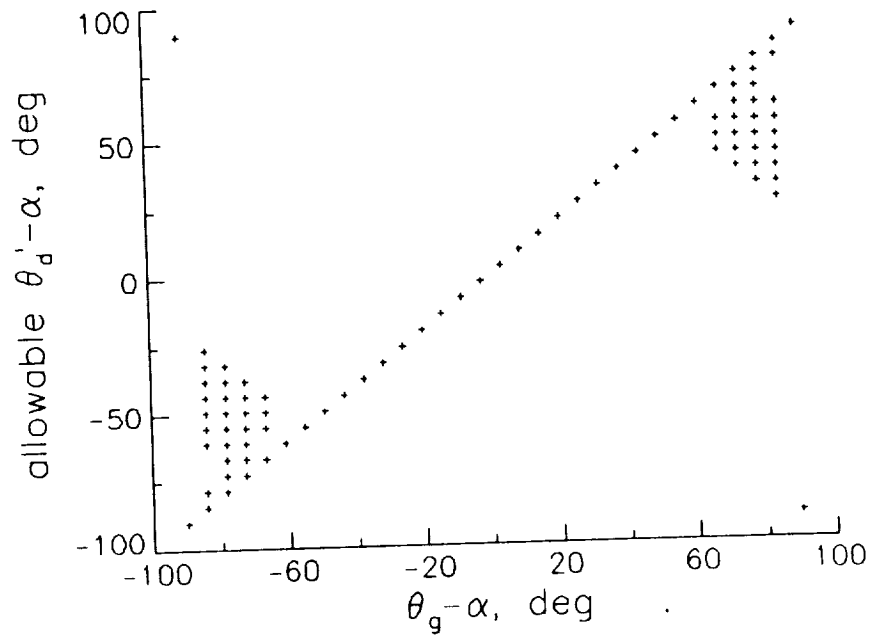
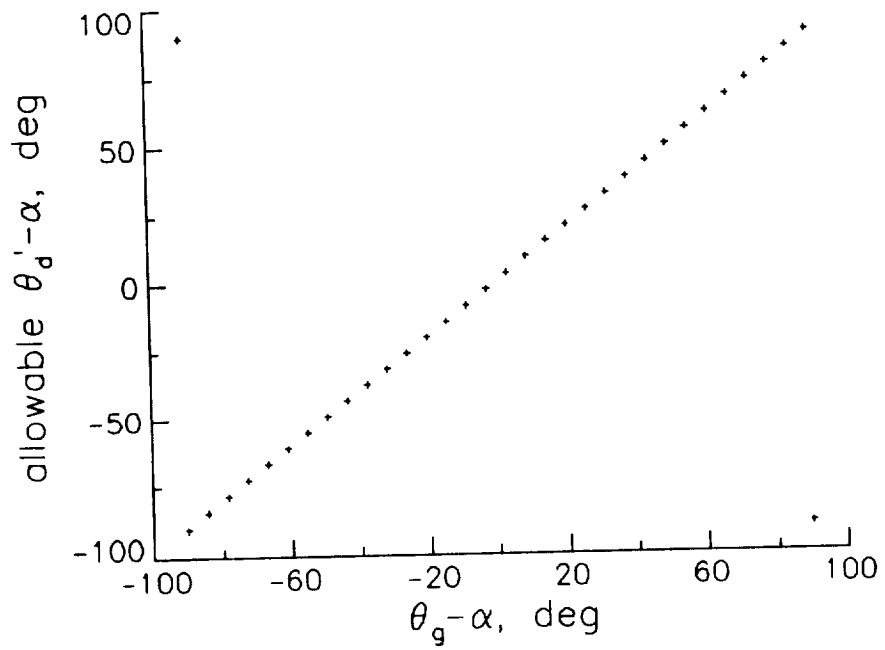
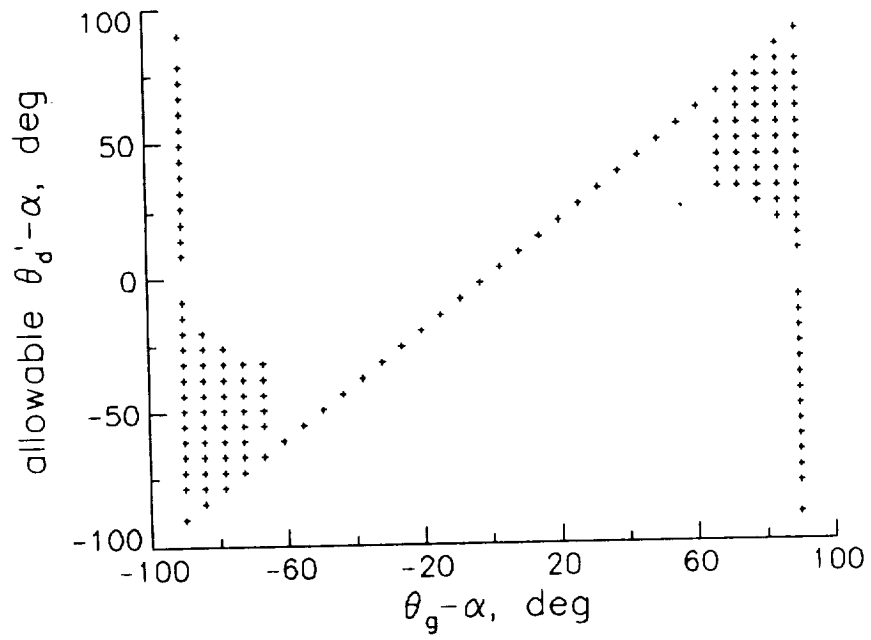
a) $M = 3, \beta = 1$ b) $M = 0.3, \beta = 1$

Figure 7.2: Monotonicity Regions



c) $M = 10, \beta = 1$

Figure 7.2: Concluded

tone scheme given by this analysis are quite severe, if not impossible to meet. Fortunately, in practice it appears that the restrictions on θ'_d can be relaxed somewhat while still maintaining reasonably non-oscillatory solutions near discontinuities for a wide variety of flows.

Through an extensive amount of numerical experimentation with actual solutions to the Euler equations, the following observations have been made regarding reducing the oscillatory behavior of the grid-independent model to an “acceptable” level:

(1) When $M > 1$, best results are obtained when θ'_d is limited to lie between $\alpha + K * \text{sign}(\theta_g - \alpha)$ and θ_g . K is a small number for lower Mach numbers and is larger for higher Mach numbers.

(2) When $M \ll 1$, θ'_d does not need to be restricted, except in a very small region (see (3) below). Between $M = 0$ and $M = 1$, the allowable region is transitioned smoothly between the subsonic and supersonic cases.

(3) In the boundary layer region of Navier-Stokes solutions, odd-even point decoupling can occur when θ'_d is taken as $(\theta_g \pm \frac{\pi}{2})$, and $\alpha \approx \theta'_d$. This condition occurs on grid interfaces in the boundary layer that are aligned with the flow direction, and is due to the fact that all components of the θ'_d -wavespeeds in the grid direction equal zero, and the $(\theta'_d + \frac{\pi}{2})$ shear wave has an extremely small wavespeed. Hence the dissipation is very small, and the result is essentially central-differencing in that direction. By limiting the angle θ'_d to lie outside of a small region near $(\theta'_d - \alpha) = 0$ at $(\theta_g - \alpha) = \pm 90^\circ$, this decoupling can be alleviated. Numerical examples of viscous flows both with and without θ'_d -limiting will be given in Chapter 8.

An attempt has been made to parameterize the “monotonicity regions” in accordance with the three observations made above. The empirically-generated

θ'_d -limited regions for four different Mach numbers are shown in figures 7.3(a) through (d). It should be stressed that the determination of these regions is based only loosely on theory and primarily on numerical experimentation. The following empirical scheme has been found to give good results for a wide variety of problems. It is by no means deemed to be the best scheme for improving the monotonicity properties of the 5-wave model. First, some variables are defined:

$$y_1 \equiv \frac{(\theta_g - \alpha) + \pi/2}{1 - \min(M, 1)^4 + 0.01} \quad (7.17)$$

$$y_2 \equiv \frac{(\theta_g - \alpha) - \pi/2}{1 - \min(M, 1)^4 + 0.01} \quad (7.18)$$

$$y_3 \equiv -\frac{\pi}{8} \left\{ \tanh\left(\frac{M-20}{12}\right) + 1 \right\} \quad (7.19)$$

$$y_4 \equiv \frac{\pi}{8} \left\{ \tanh\left(\frac{M-20}{12}\right) + 1 \right\}. \quad (7.20)$$

$$y_5 \equiv (\theta_g - \alpha) + \frac{\pi}{2} - \frac{\pi}{2} \min(M, 1)^4 \quad (7.21)$$

$$y_6 \equiv (\theta_g - \alpha) - \frac{\pi}{2} + \frac{\pi}{2} \min(M, 1)^4 \quad (7.22)$$

$$y_7 \equiv +\sqrt{\max\left[\left(\frac{\pi}{9}\right)^2 - \left\{(\theta_g - \alpha) + \frac{\pi}{2}\right\}^2, 0\right]} \quad (7.23)$$

$$y_8 \equiv -y_7 \quad (7.24)$$

$$y_9 \equiv +\sqrt{\max\left[\left(\frac{\pi}{9}\right)^2 - \left\{(\theta_g - \alpha) - \frac{\pi}{2}\right\}^2, 0\right]} \quad (7.25)$$

$$y_{10} \equiv -y_9 \quad (7.26)$$

$$y_{11} \equiv \min(y_6, \max(y_4, y_9)) \quad (7.27)$$

$$y_{12} \equiv \max(y_5, \min(y_3, y_8)). \quad (7.28)$$

The allowable regions are then taken as:

$$(\theta'_d - \alpha) > \max(y_1, y_7)$$

$$(\theta'_d - \alpha) < \min(y_2, y_{10}) \quad (7.29)$$

$$y_{11} < (\theta'_d - \alpha) < y_{12}.$$

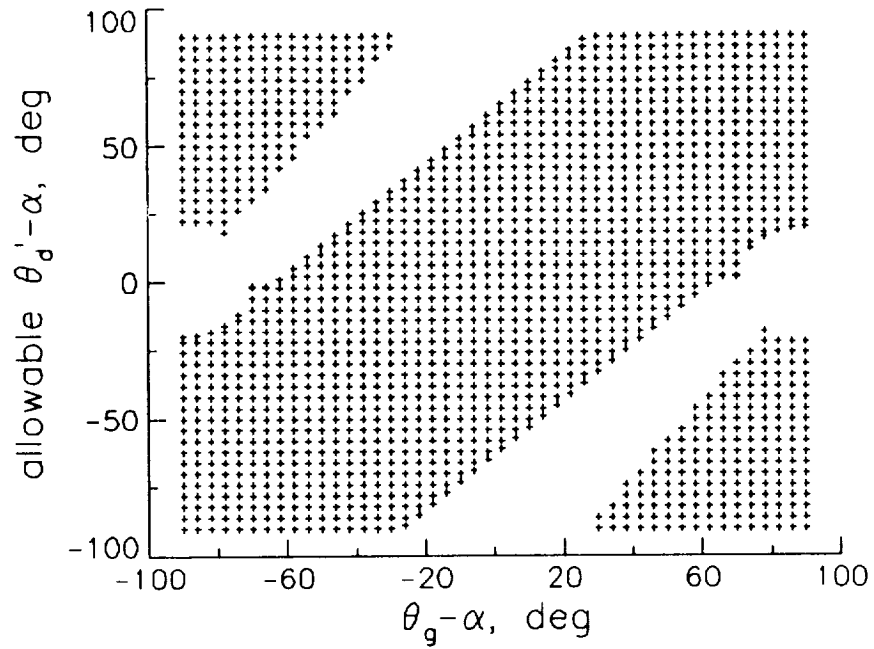
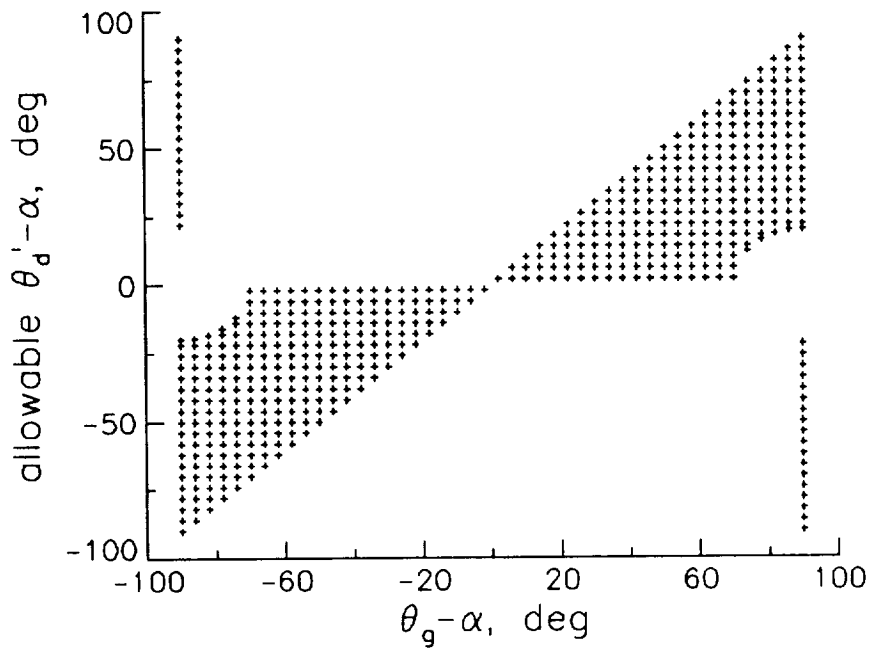
a) $M = 0.3$ b) $M = 1.2$

Figure 7.3: Empirically-Determined Monotonicity Regions

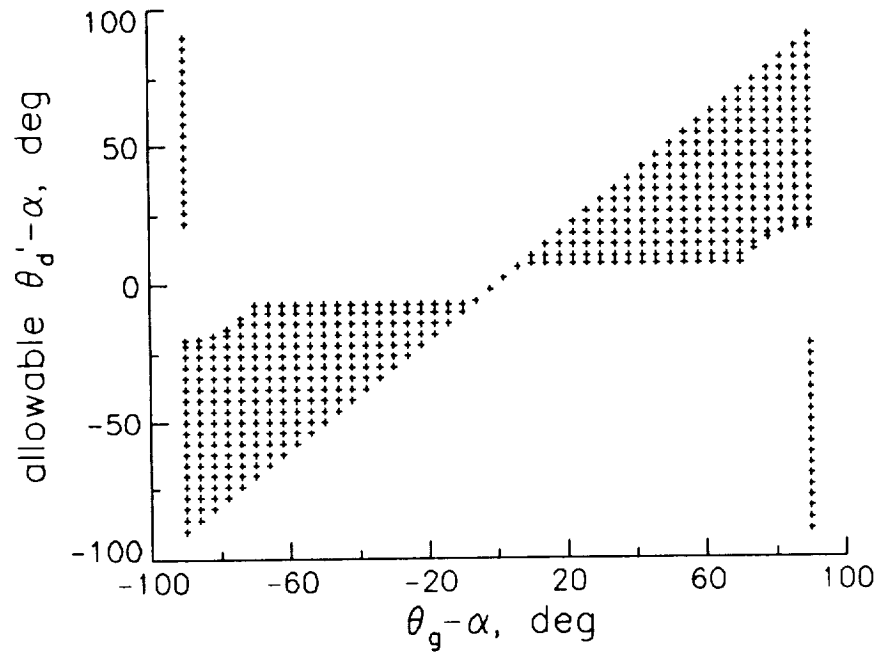
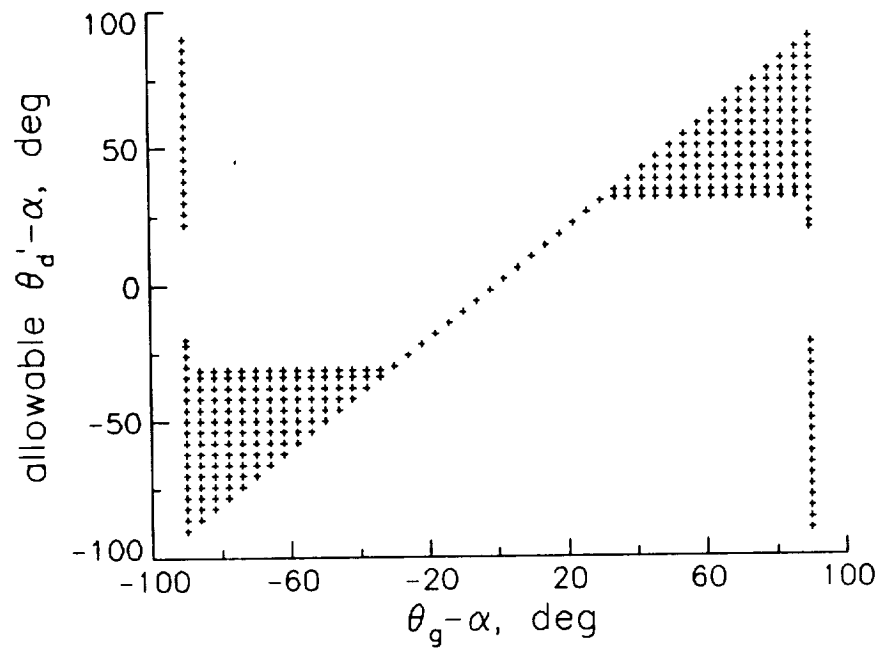
c) $M = 10$ d) $M = 25$

Figure 7.3: Concluded

If $(\theta'_d - \alpha)$ does not lie within one of the allowable regions, then it is limited to either y_{11} or y_{12} , whichever is closer.

CHAPTER 8

TWO-DIMENSIONAL RESULTS

8.1 Euler Computations

Both first-order and second-order two-dimensional Euler computations are performed for several different cases in this section. Unless otherwise noted, second-order computations do not utilize any type of limiting of higher-order terms for either the grid-aligned or grid-independent computations. This is done in order to avoid confusion with and separate the effects of the θ'_d -limiting procedure.

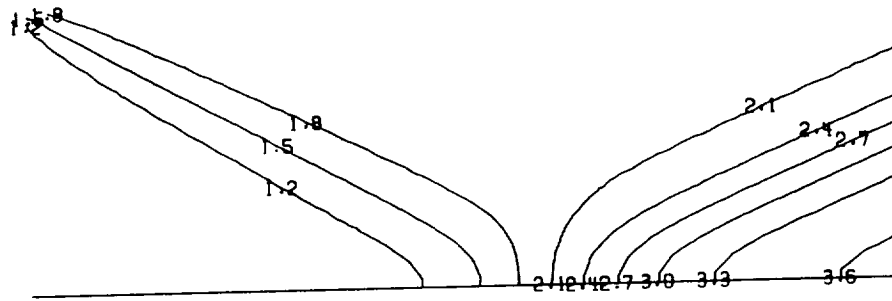
8.1.1 Shock Reflection

The $M = 2.9$ inviscid shock reflection case is computed on a Cartesian mesh 4.8 units wide by 1.6 units high. An oblique shock enters the domain from the upper left corner, reflects off the bottom wall, and exits out the right end. The flow is turned through an angle of 10° by the incident shock. The nondimensional boundary conditions (nondimensionalized by combinations of $\bar{\rho}_\infty$ and \bar{a}_∞) are: at inflow $\rho = 1$, $\rho u = 2.9$, $\rho v = 0$, and $\rho E = 5.9907$; at the top boundary $\rho = 1.6328$, $\rho u = 4.3272$, $\rho v = -0.7630$, and $\rho E = 9.5091$; at the back boundary, outflow conditions are set by second-order extrapolation from the interior; at the body along the bottom wall, simple reflection boundary conditions are used.

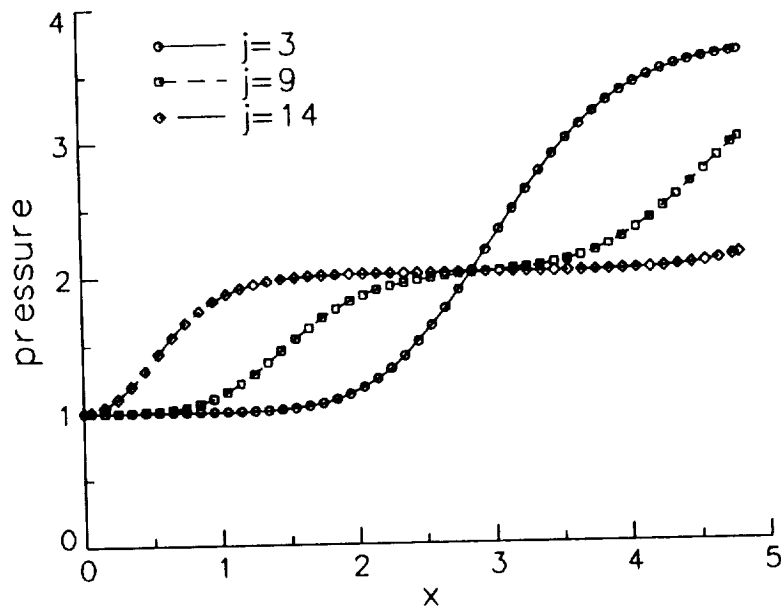
Computations are performed using explicit four-stage time-marching. They are initiated from freestream conditions and are run until the L_2 -norm of the residual of all four equations drops below 1×10^{-12} . Computations are performed on two different mesh sizes: a 49×17 mesh and a 97×33 mesh.

First-order computations using the grid-aligned solver, run at a CFL number of $\nu = 2.2$, converge in 158 iterations on the coarse mesh and 258 iterations on the fine mesh. Nondimensional pressure contours and pressure values along three $j =$ constant cuts (left to right through the mesh) are shown in figures 8.1 and 8.2. First-order results using the 5-wave model are also obtained using $\nu = 2.2$. The θ_d values are frozen using the following procedure: they are computed every iteration for the first 20 iterations, then only once every 20 iterations until the log of the L_2 -norm of the residual drops to below -3.5 . After this, the θ_d values remain frozen. The 5-wave model is run on the coarser mesh both with and without the θ'_d -limiting derived in Chapter 7. The solution converges in 245 iterations (θ'_d not limited) and 191 iterations (θ'_d -limited). On the finer mesh the solution converges in 319 iterations (θ'_d -limited). The results are given in figures 8.3 through 8.5. On both meshes, the 5-wave model gives sharper shock wave resolution than the grid-aligned scheme. The θ'_d -unlimited method produces the sharpest resolution, but at the cost of oscillatory behavior near the discontinuities. When the θ'_d -limiting procedure is employed, 5-wave model results are still significantly sharper than the grid-aligned results, and appear to be monotone as well for this problem.

The grid-aligned model on the 97×33 grid converges in about 14.1 CPU seconds on the Cray 2 computer, while the 5-wave model requires about 25.4 CPU seconds (θ'_d -limited). Thus, the 5-wave model is about 1.8 times more costly than the grid-aligned model to reach the same level of convergence for this case. Per iteration, the 5-wave model is about 1.5 times more costly. A significant percentage of this cost is associated with the limiting of the θ'_d -directions. Without

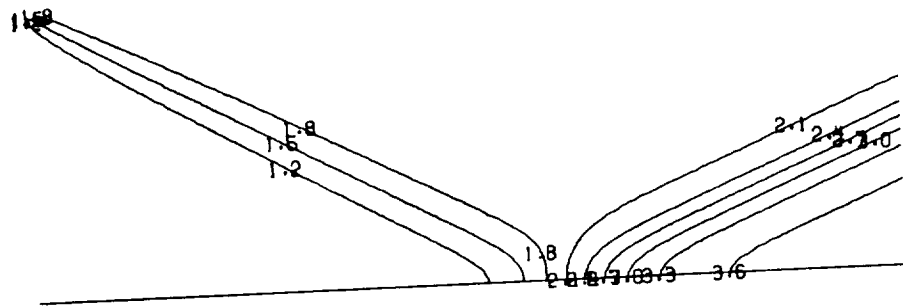


a) Pressure Contours

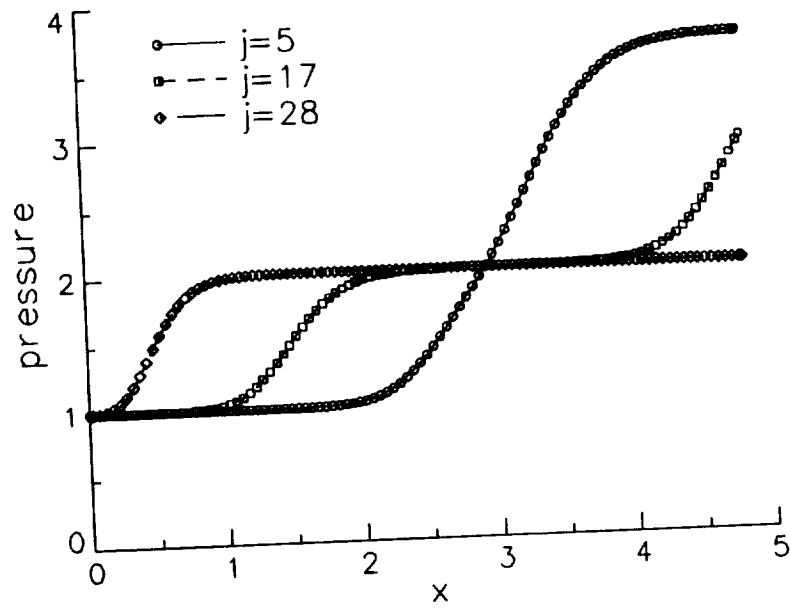


b) Pressure Along $j = \text{Constant}$ Lines

Figure 8.1: Shock Reflection, First-Order, Grid-aligned, 49×17

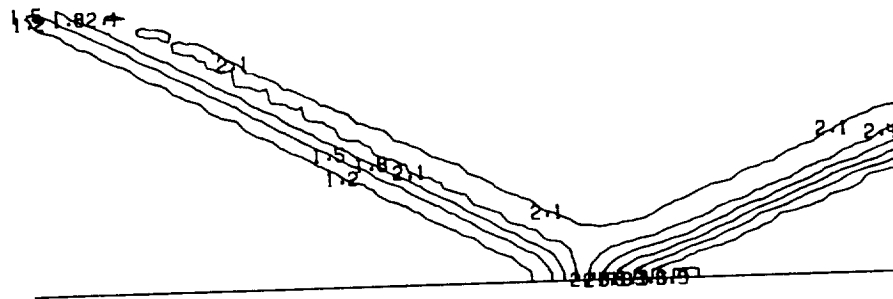


a) Pressure Contours

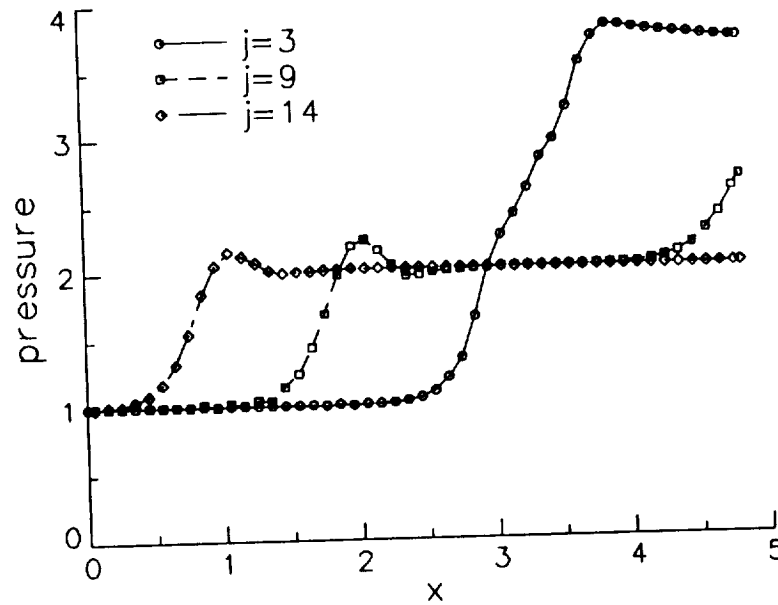


b) Pressure Along $j = \text{Constant}$ Lines

Figure 8.2: Shock Reflection, First-Order, Grid-aligned, 97×33

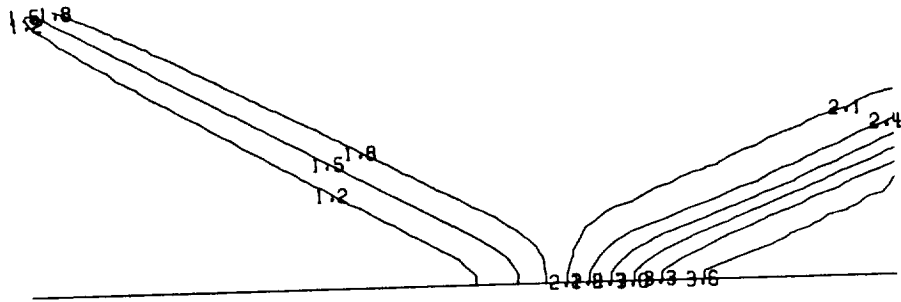


a) Pressure Contours

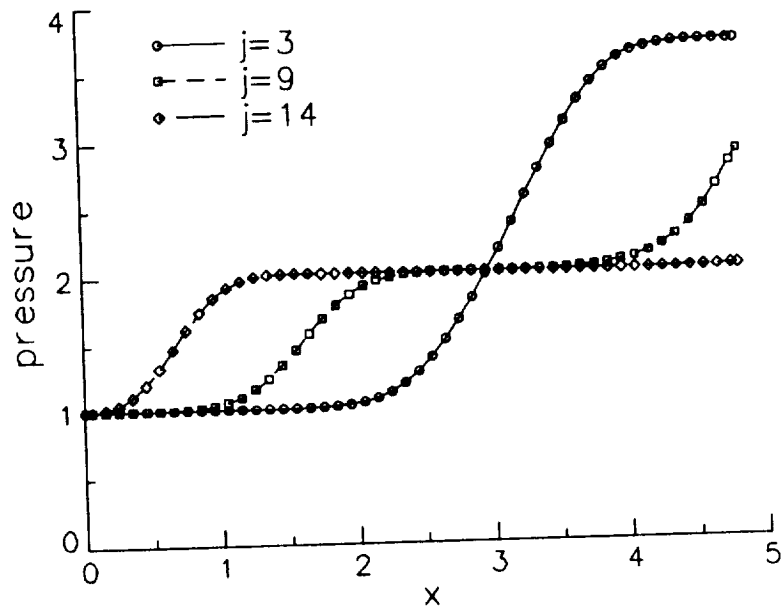


b) Pressure Along $j = \text{Constant}$ Lines

Figure 8.3: Shock Reflection, First-Order, 5-Wave (θ'_d -Unlimited), 49×17

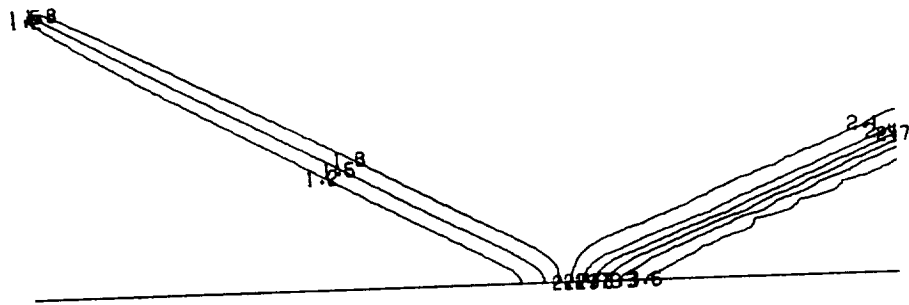


a) Pressure Contours

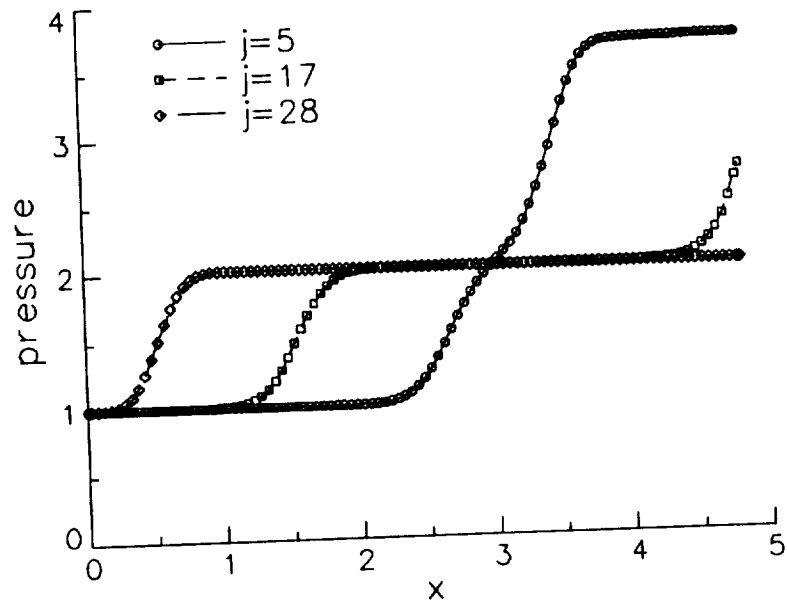


b) Pressure Along $j = \text{Constant}$ Lines

Figure 8.4: Shock Reflection, First-Order, 5-Wave (θ'_d -Limited), 49×17



a) Pressure Contours



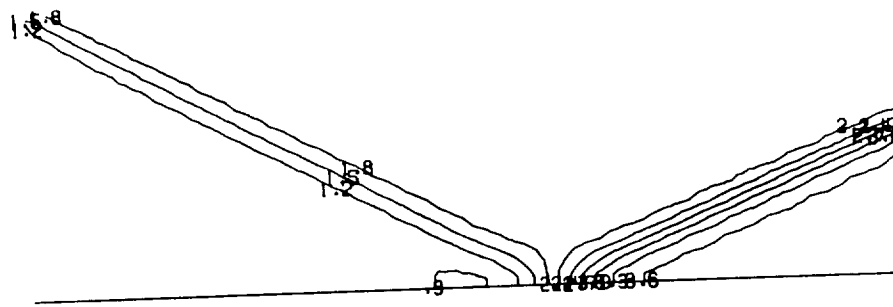
b) Pressure Along $j = \text{Constant}$ Lines

Figure 8.5: Shock Reflection, First-Order, 5-Wave (θ'_d -Limited), 97×33

θ'_d -limiting, the 5-wave model is only about 1.2 times more costly than the grid-aligned model per iteration.

Second-order results for this problem are obtained using a CFL number of $\nu = 1.1$. Grid-aligned model results are shown in figures 8.6 and 8.7 on the two grids. Since no limiting of higher-order terms is employed, there are undershoots present in the solutions forward of each shock wave. These solutions converge the L_2 -norm of the residual of all four equations to 1×10^{-12} in 249 and 423 iterations, respectively. Second-order 5-wave model results are given in figures 8.8 through 8.10. A θ'_d -unlimited solution on the 49×17 mesh (figure 8.8) shows very sharp shocks, but a large amount of oscillatory behavior is also present aft of the shocks. This solution converges in 494 iterations. When θ'_d -limiting is used, these oscillations are reduced in magnitude, while still maintaining slightly sharper shock resolution than the grid-aligned method as shown in figure 8.9. In the figure, the wiggles in the "3.6"-level contour are caused by oscillations which are still present downstream of the reflected shock. The 5-wave θ'_d -limited solution on the 97×33 grid is shown in figure 8.10. Again, results are slightly sharper than the grid-aligned method on the same grid and additional oscillations are visible downstream of the reflected shock. The θ'_d -limited solutions converge in 391 and 659 iterations, respectively, on the coarse and fine grids.

For the shock reflection problem, the 5-wave model appears to be a viable alternative to the grid-aligned model for first-order computations. When θ'_d -limiting is employed, results appear to be free from spurious oscillations, and shocks are captured with fewer interior points than the grid-aligned method. In fact, the 49×17 5-wave solution gives comparable resolution to the grid-aligned solution on a mesh with four times as many mesh cells. For second-order computations, very little advantage of the 5-wave model over the grid-aligned model is seen. Results are slightly sharper, but the extra cost for the method may outweigh its



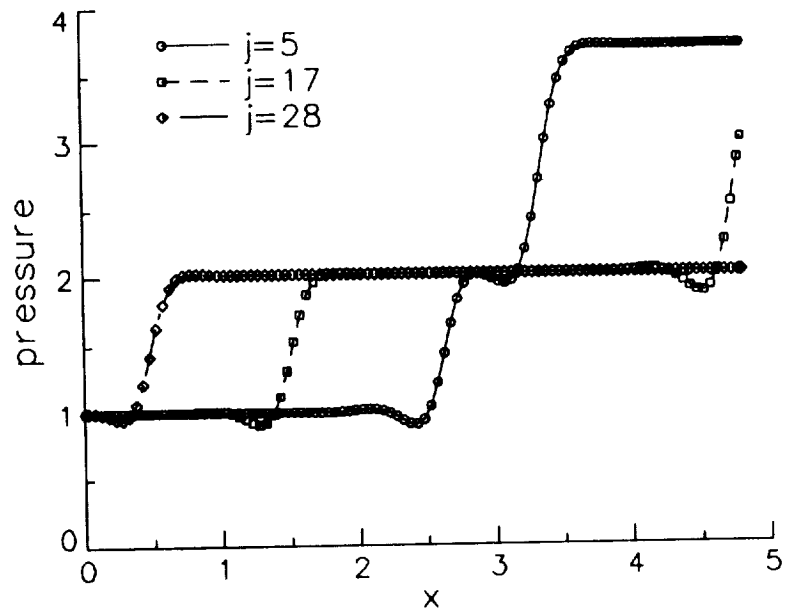
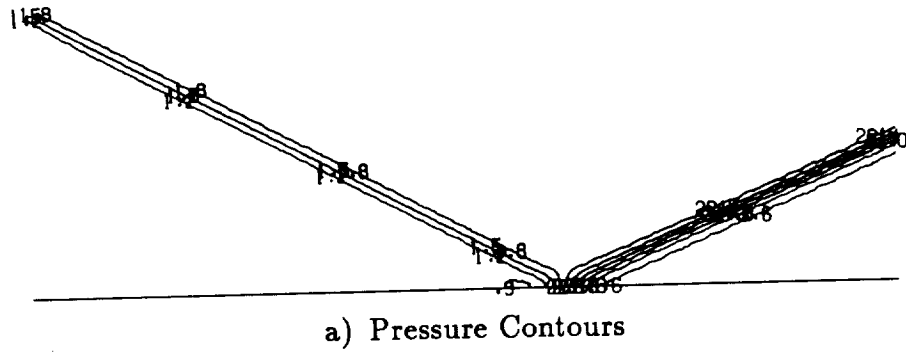
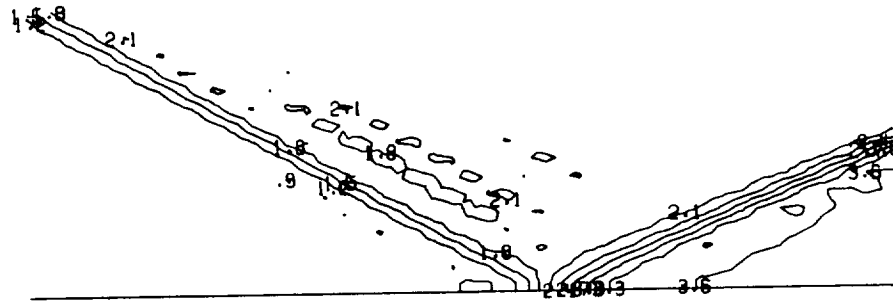


Figure 8.7: Shock Reflection, Second-Order, Grid-aligned, 97×33



a) Pressure Contours

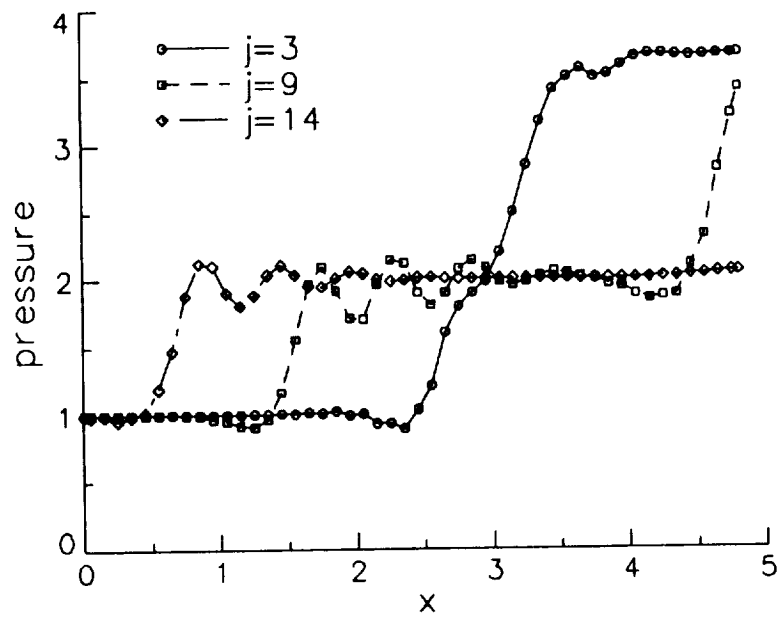
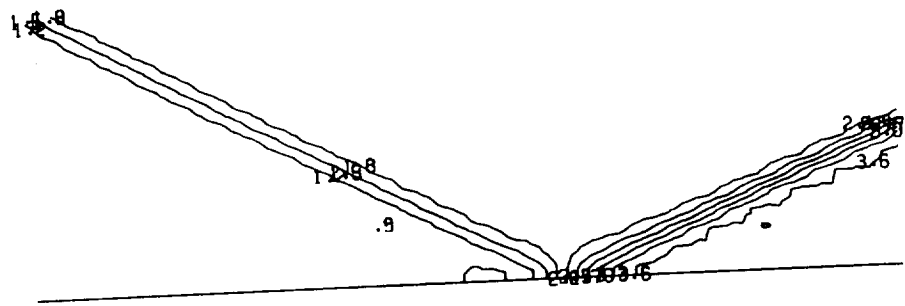
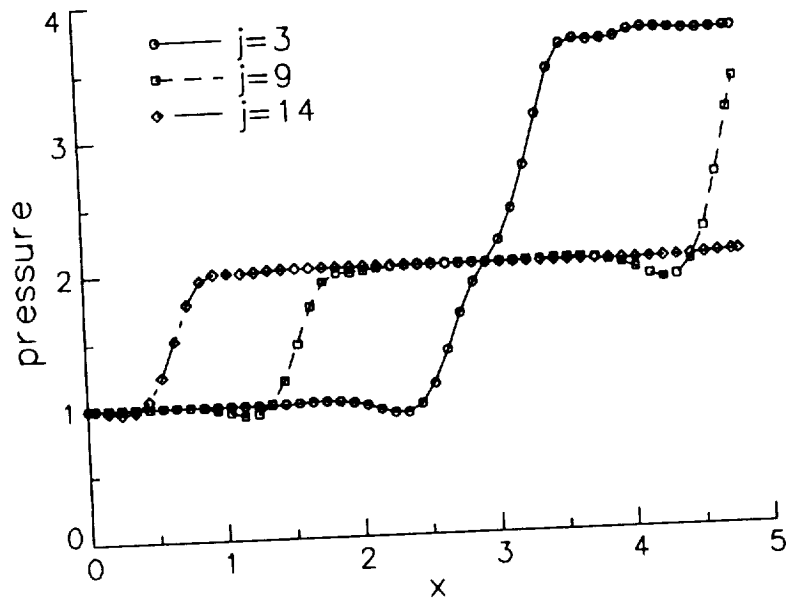
b) Pressure Along $j = \text{Constant}$ Lines

Figure 8.8: Shock Reflection, Second-Order, 5-Wave (θ'_d -Unlimited),
 49×17



a) Pressure Contours



b) Pressure Along $j = \text{Constant}$ Lines

Figure 8.9: Shock Reflection, Second-Order, 5-Wave (θ'_d -Limited),
 49×17

small advantage. Also, small oscillations still plague the solutions.

8.1.2 Ramp Flow in a Channel

Euler computations are performed for supersonic channel flow with a 15° finite-length ramp at an inflow Mach number of 2.0 on a 49×17 grid. This case was first used to test grid-independent flow solvers by Levy *et al.* [24]. The grid is 3 units long by 1 unit high. The ramp begins at $x = 0.5$ units and is 0.5 units long. At the end of the ramp, the bottom channel wall again becomes parallel to the top wall. A picture of the grid is given in figure 8.11. The boundary conditions are uniform freestream inflow at the left, second-order extrapolation at the right, and simple reflection conditions at the top and bottom walls. For this case, some extra dissipation necessary to prevent oscillations in the 5-wave model solution near the bottom wall in the region of the expansion fan was provided by using the grid-aligned scheme in combination with the simple reflection boundary conditions to obtain the flux at the lower wall.

A first-order computation using the grid-aligned method is shown in figure 8.12. As in the shock reflection case, an explicit four-stage time-marching scheme is employed using a CFL number of $\nu = 2.2$. Figure 8.12(a) shows Mach number contours, while figure 8.12(b) shows Mach number values along two $j = \text{constant}$ lines (left to right through the mesh). It can be seen that this grid-aligned first-order result smears the primary shock a good deal and barely shows evidence of the two reflected shocks. The 5-wave model with no θ'_d limiting, shown in figure 8.13, shows extremely sharp resolution of the shocks. However, significant oscillations are also present in the solution. When θ'_d -limiting is employed, the oscillations essentially disappear, but much of the resolution of the 5-wave model

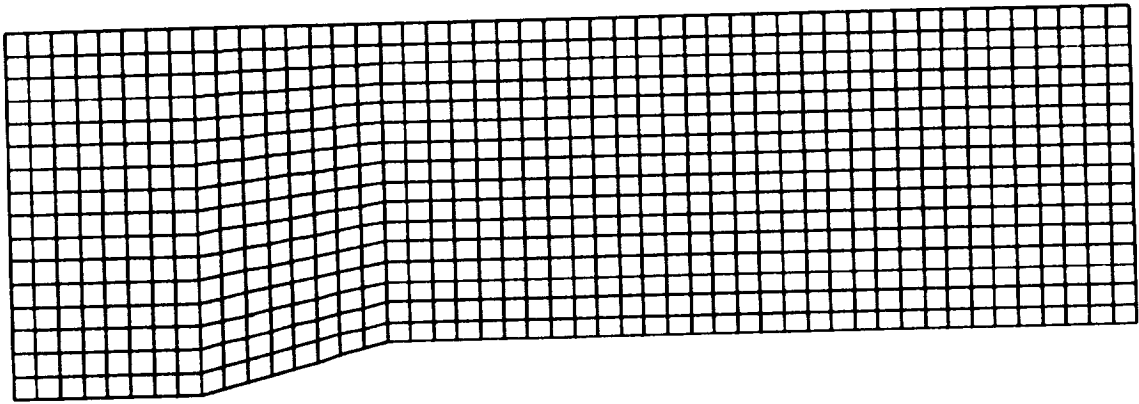
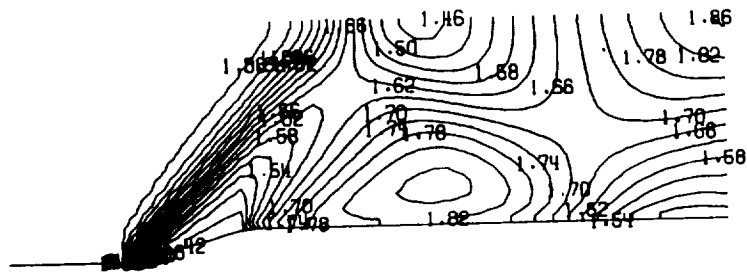
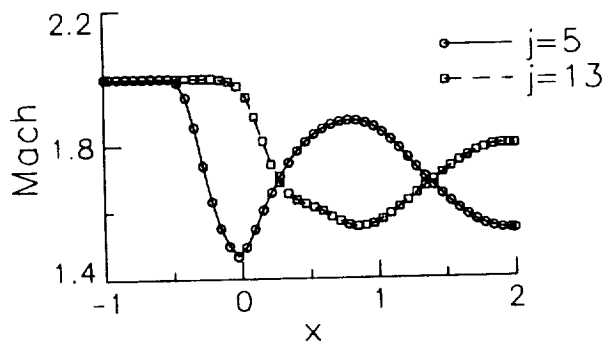


Figure 8.11: Ramp Flow 49×17 Grid



a) Mach Number Contours



b) Mach Number Along $j = \text{Constant}$ Lines

Figure 8.12: Ramp Flow, First-Order, Grid-aligned

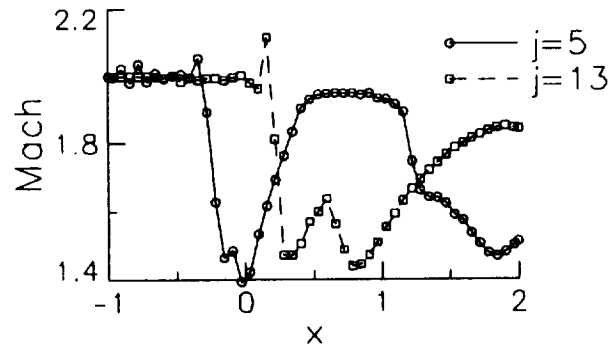
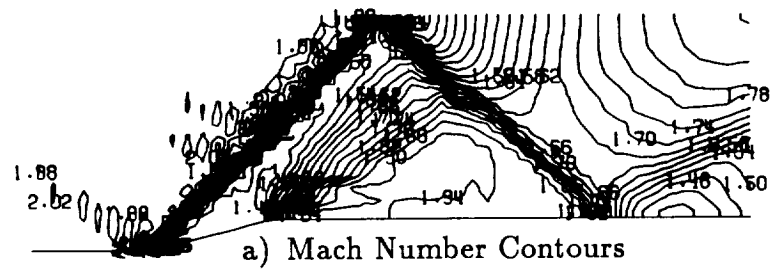


Figure 8.13: Ramp Flow, First-Order, 5-Wave (θ'_d -Unlimited)

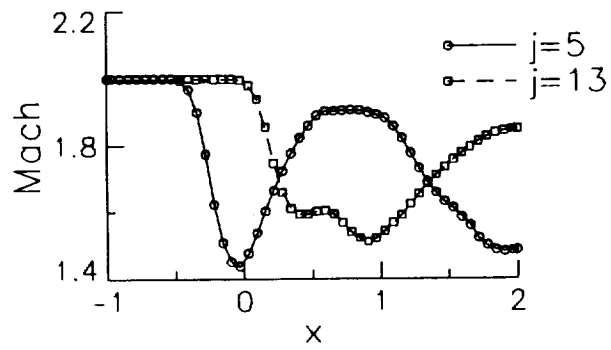
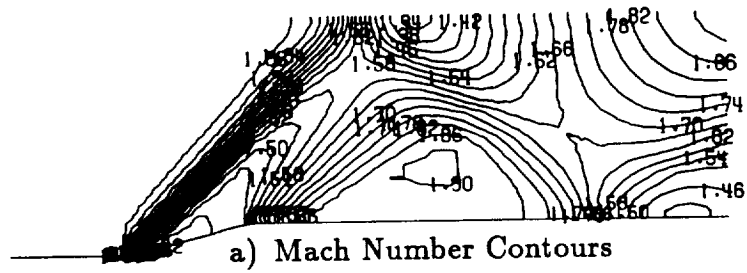


Figure 8.14: Ramp Flow, First-Order, 5-Wave (θ'_d -Limited)

is also lost. These results are shown in figure 8.14. They are still sharper than the grid-aligned results. The results from figures 8.12, 8.13 and 8.14 converge the L_2 -norm of the residual of all four equations to 1×10^{-12} in 263, 346, and 315 iterations, respectively. The 5-wave model uses the same strategy for freezing θ_d described for the shock reflection case.

Second-order solutions are obtained with $\nu = 1.1$. Results using the grid-aligned model are shown in figure 8.15, while 5-wave model results without and with θ'_d -limiting are shown in figures 8.16 and 8.17, respectively. When no θ'_d -limiting is employed, results are very sharp but oscillatory. The θ'_d -limited solution is significantly less oscillatory, and is slightly sharper than the grid-aligned solution. However, as for the second-order shock reflection case, the amount of benefit probably does not outweigh the disadvantages in this case.

8.1.3 Oblique Supersonic Shear

The oblique shear wave case is computed on a 61×21 Cartesian mesh 3 units wide by 1 unit high. Fluid enters the domain from the lower face at a 45° angle and exits out the top face. To the left of the shear wave $M = 1.812$, while to the right $M = 1.510$; there is one transition cell where $M = 1.661$. There is no pressure change through the shear. The nondimensional boundary conditions are: to the left of the shear $\rho = 1$, $\rho u = 1.282$, $\rho v = 1.282$, and $\rho E = 3.427$; to the right of the shear $\rho = 1$, $\rho u = 1.068$, $\rho v = 1.068$, and $\rho E = 2.926$; at the transition zone $\rho = 1$, $\rho u = 1.175$, $\rho v = 1.175$, and $\rho E = 3.165$; on the top and right boundaries, outflow conditions are obtained using second-order extrapolation.

The exact solution is shown in figure 8.18. Figure 8.18(a) shows Mach number contours while figure 8.18(b) shows Mach number values along three $j = \text{constant}$

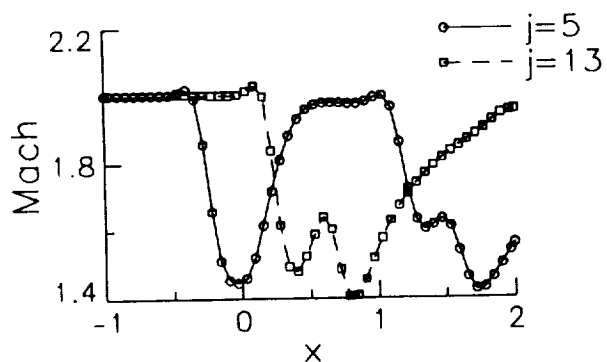
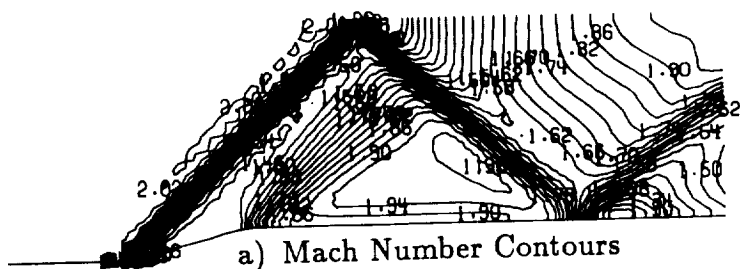


Figure 8.15: Ramp Flow, Second-Order, Grid-aligned

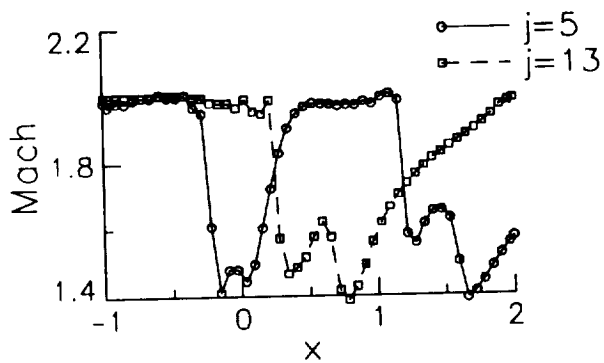
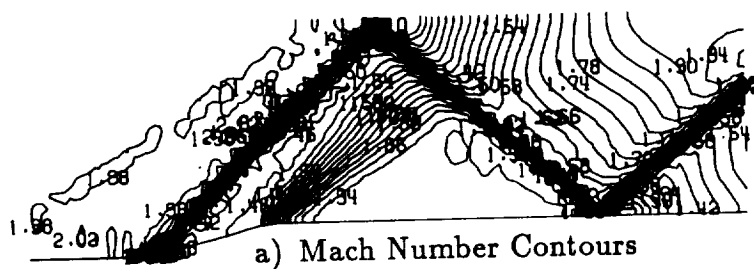


Figure 8.16: Ramp Flow, Second-Order, 5-Wave (θ'_a -Unlimited)

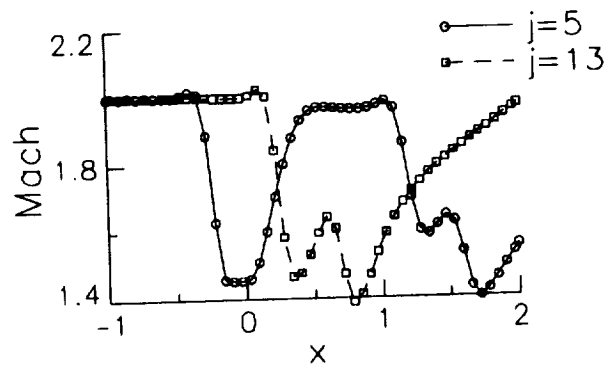
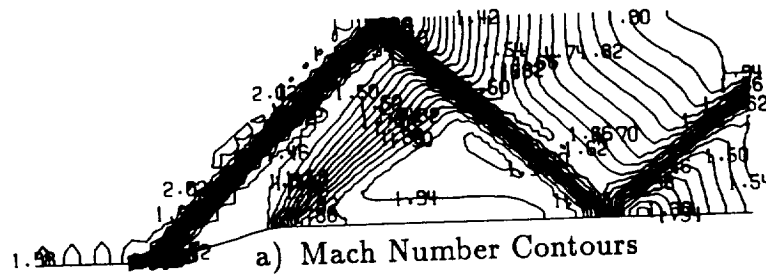


Figure 8.17: Ramp Flow, Second-Order, 5-Wave (θ'_d -Limited)

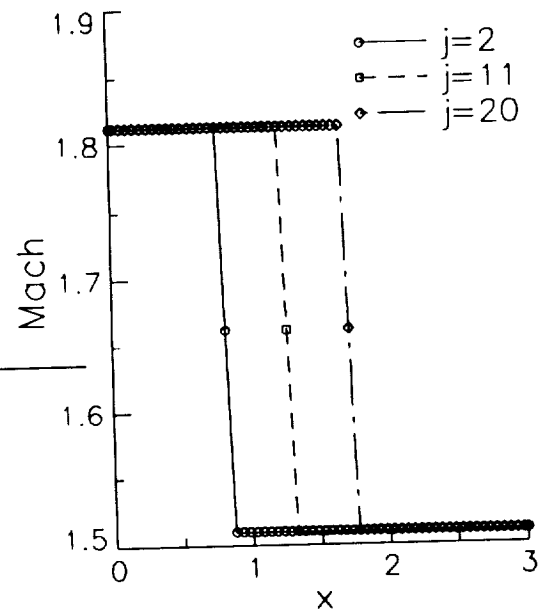
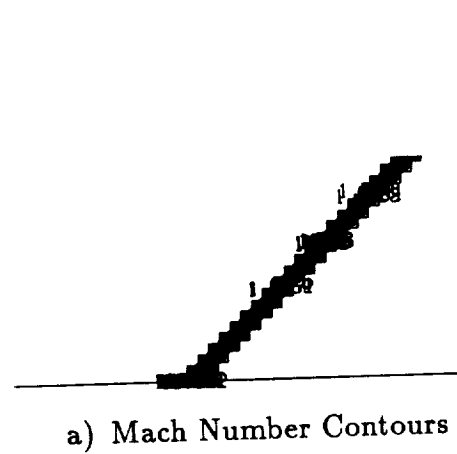


Figure 8.18: Oblique Shear, Exact Solution

lines through the mesh. All computations are performed using four-stage explicit time-marching. When initiated from the exact solution, a first-order Euler computation using the grid-aligned method smears the shear wave significantly, as shown in figure 8.19. The first-order 5-wave model, with θ'_d -limiting, converges to the results shown in figure 8.20. Results are significantly sharper, although there is still some oscillatory behavior near the discontinuity. For this particular example, the initial condition for the 5-wave model is the grid-aligned solution. The θ_d values are recomputed once every 30 iterations until the log of the L_2 -norm of the residual drops below -3.5 , after which they remain frozen. It should be noted that if β is allowed to be zero (instead of being restricted to be greater than 0.05) and the outflow boundary conditions are extrapolated from 45° upstream (instead of in a grid-aligned fashion), then the 5-wave model can maintain the exact solution in one iteration when the exact solution is the initial condition.

Second-order solutions using the grid-aligned and 5-wave models are shown in figures 8.21 and 8.22. The grid-aligned results are now fairly sharp, comparable in width to the first-order 5-wave results. The second-order 5-wave results are even sharper, however. The shear wave is now resolved with almost no spreading at all. Because this is a fairly weak shear wave case, the grid-aligned model does not yield any noteworthy pressure distortions as a result of misinterpreting the oblique shear wave. Both the grid-aligned and 5-wave models produce pressure fields in error from the exact solution by less than 0.5%. This 45° supersonic shear wave case demonstrates an advantage of the 5-wave model over the grid-aligned model. For both first and second-order computations, the model resolves the oblique shear wave with significantly fewer interior points than the grid-aligned method.

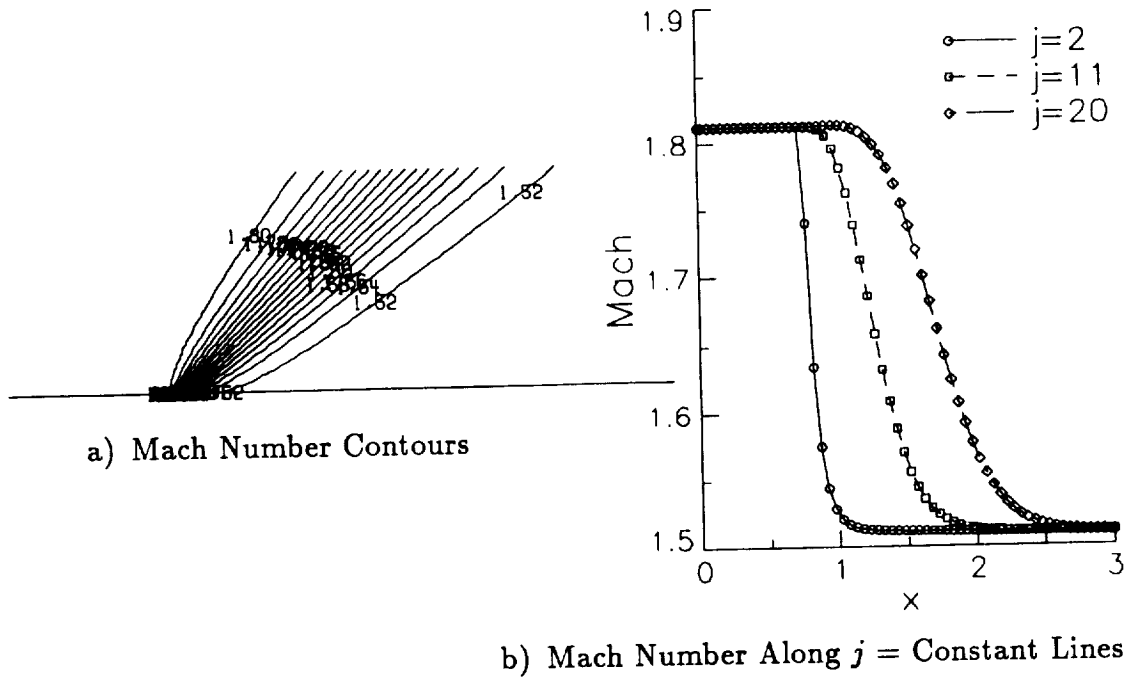


Figure 8.19: Oblique Shear, First-Order, Grid-Aligned

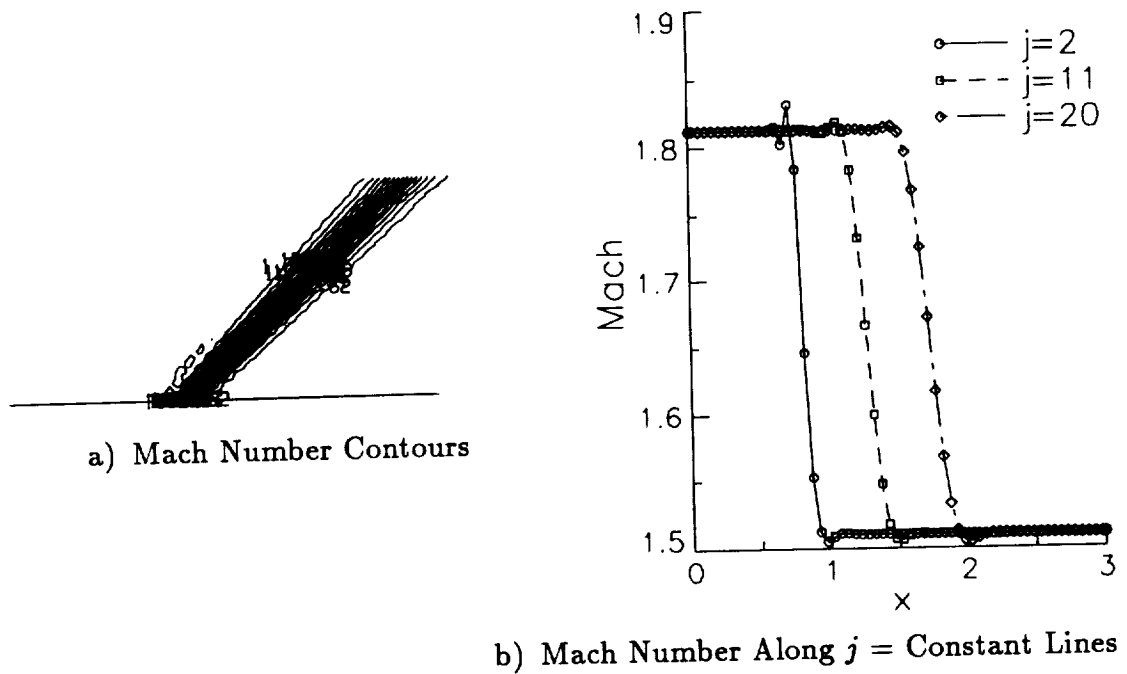


Figure 8.20: Oblique Shear, First-Order, 5-Wave

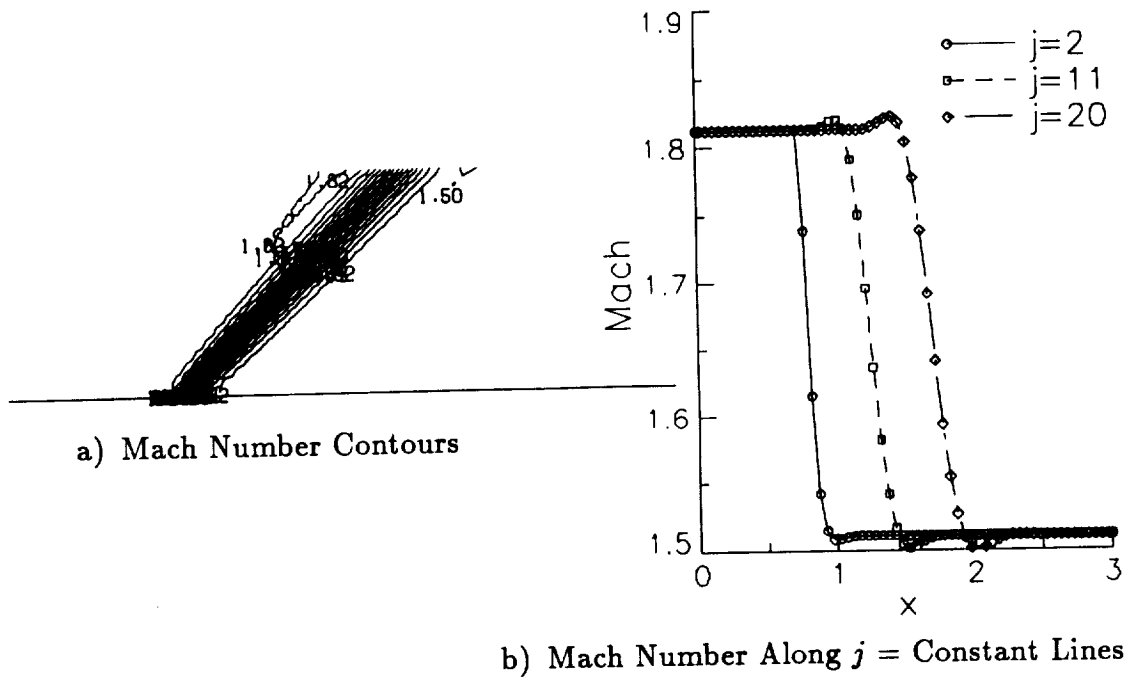


Figure 8.21: Oblique Shear, Second-Order, Grid-Aligned

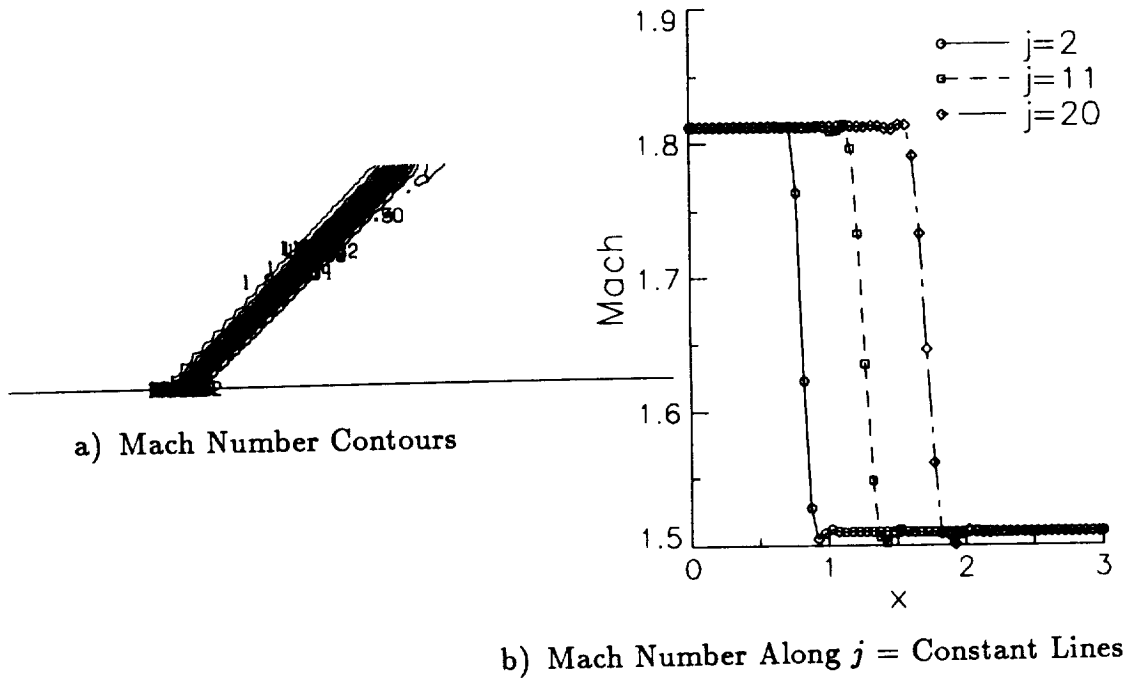


Figure 8.22: Oblique Shear, Second-Order, 5-Wave

8.1.4 Supersonic Flow Over an Airfoil

Euler computations are performed for the NACA 0012 airfoil at $M = 1.2$, $\alpha = 0^\circ$ on several different grids. The finest is a 257×73 O-mesh with an outer boundary extent of 20 chords and an average minimum spacing at the body of 0.0031 chords. It is shown in figure 8.23. Two coarser meshes, a 129×37 and a 65×19 , result from removing every other point from the next finest mesh. The inflow/outflow boundary conditions in the farfield for supersonic flow are simply freestream values when the grid boundary cell is an inflow boundary (*i.e.* the outward-pointing grid-face normal points into the freestream direction), and are extrapolated from the interior using second-order interpolation when it is an outflow boundary. The boundary conditions at the body are simple reflection conditions, and periodic boundary conditions are enforced where the grid meets itself behind the airfoil.

These airfoil results, as well as all results to follow in the remainder of the paper, are computed using the implicit approximate-factorization time-stepping procedure. The CFL numbers at which the solutions are advanced are taken in accordance with the analysis performed in Chapter 6. Results are not converged to machine zero in general; sufficient convergence is assumed when the L_2 -norm of the residual drops by at least 4 orders of magnitude and/or the lift and drag values settle down and do not vary significantly with further iterations.

At the conditions enumerated above, the NACA 0012 airfoil has a flowfield with a curved bow shock located in front of the airfoil and oblique shocks emanating from the trailing edge. Figures 8.24 through 8.26 show results for the first-order accurate grid-aligned model on the three successively finer grids. Shown are nondimensional pressure contours, plotted in increments of 0.05 (the freestream

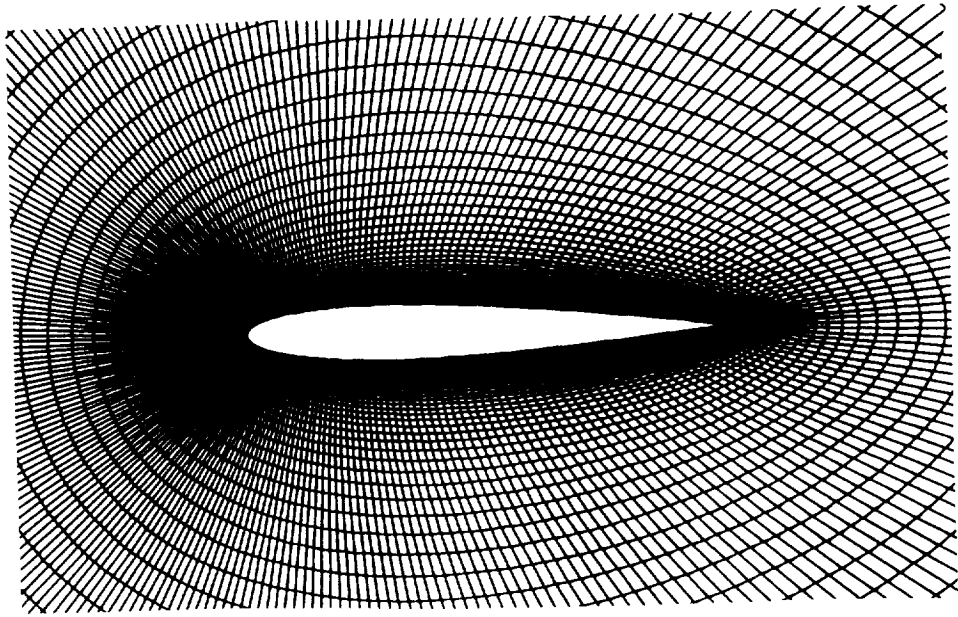
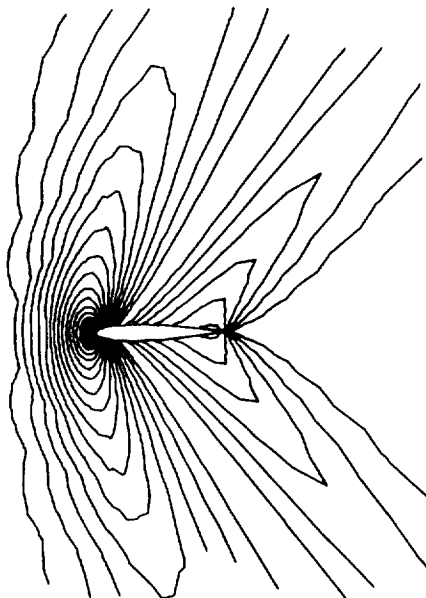
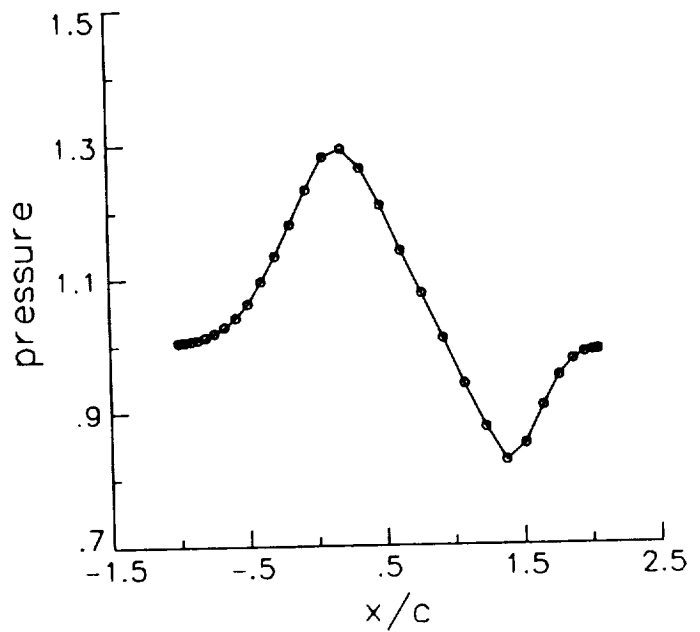


Figure 8.23: NACA 0012 257 \times 73 O-Grid

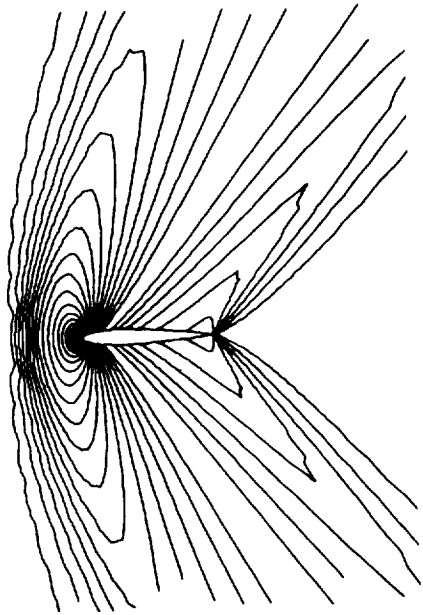


a) Pressure Contours

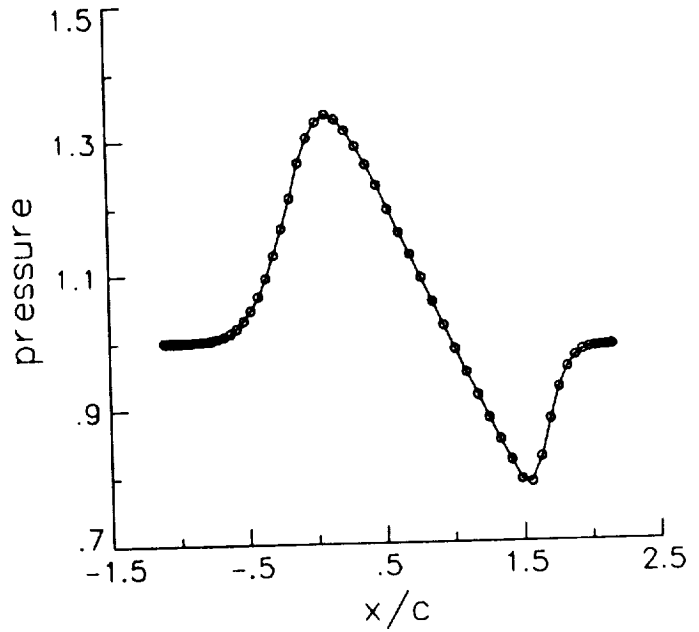


b) Pressure Along $j = \text{Constant}$ Line

Figure 8.24: Supersonic Airfoil-Flow, First-Order, Grid-Aligned, 65 \times 19

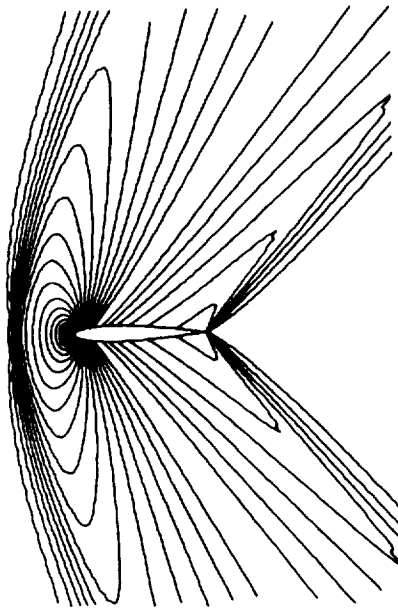


a) Pressure Contours

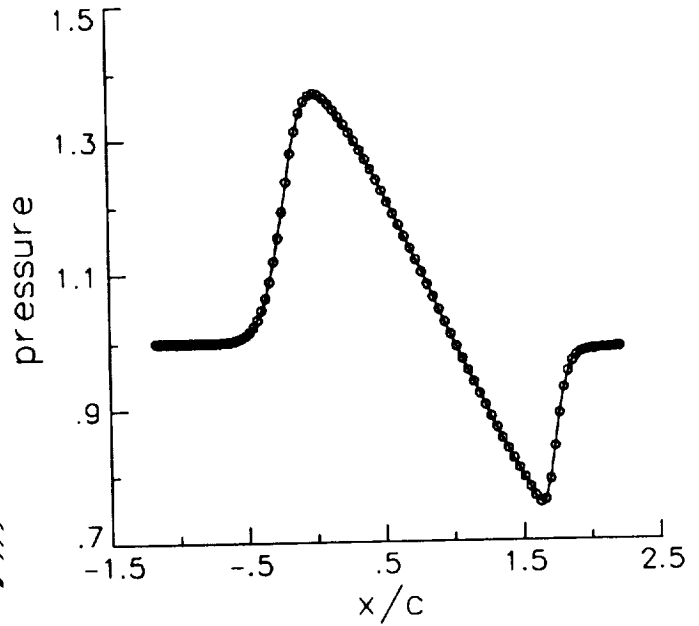


b) Pressure Along $j = \text{Constant}$ Line

Figure 8.25: Supersonic Airfoil-Flow, First-Order, Grid-Aligned, 129×37



a) Pressure Contours



b) Pressure Along $j = \text{Constant}$ Line

Figure 8.26: Supersonic Airfoil-Flow, First-Order, Grid-Aligned, 257×73

value of 1.0 is not plotted), as well as pressure along a $j = \text{constant}$ grid line over the upper half of the airfoil. The $j = \text{constant}$ grid line is taken at $j = 11$, $j = 21$, and $j = 41$ for the three grids. Its location is shown in figure 8.27. The two finer meshes produce reasonable-looking results, although the shock waves are very smeared. The coarsest mesh (65×19) produces very poor results, but this grid is so coarse that a good solution would not be expected in any case. First-order 5-wave model results (with θ'_d -limiting) are computed by restarting the corresponding grid-aligned solution with θ_d frozen. Results are shown in figures 8.28 through 8.30. The shock waves are captured much more sharply by this method, although there are still some small oscillations present near the discontinuities. The 65×19 mesh is again too coarse to produce a reasonable-looking solution.

In an effort to explore the grid-sensitivity of the grid-aligned and 5-wave models, computed drag values are plotted for each of the grids in figure 8.31. For a first-order scheme, it is expected that the results behave in a linear fashion when plotted *vs.* the inverse of the square root of the total number of gridpoints. This indeed appears to be the case for both methods (on grid sizes of 129×37 or finer). The drag coefficient is approaching about 0.0955 as the grid approaches infinite refinement. The 5-wave model produces drag values in closer agreement with this "correct" value on all three grid sizes tested. For example, on the 257×73 grid, the 5-wave model gives a drag value 2.0% in error from the extrapolated "exact" value, while the grid-aligned result is 6.5% in error.

Second-order computations using the grid-aligned model on the three grids are given in figures 8.32 through 8.34. Results now have much sharper resolution. Since no limiting of higher-order terms is performed in these computations, some undershoots and overshoots are present near the computed shock waves. Second-order 5-wave model results are given in figures 8.35 through 8.37. These results are

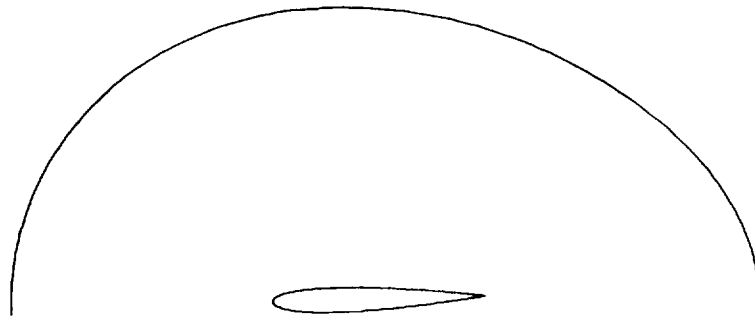
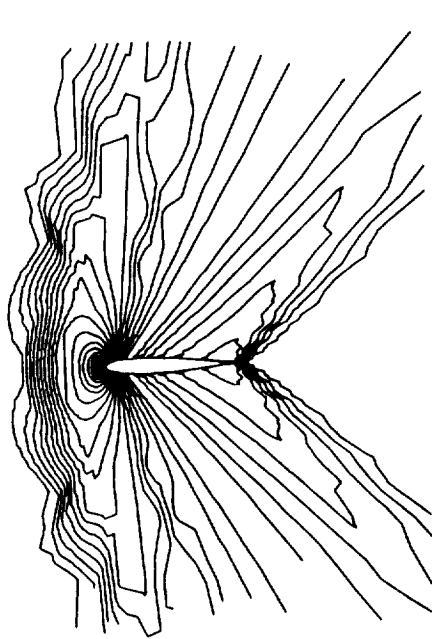
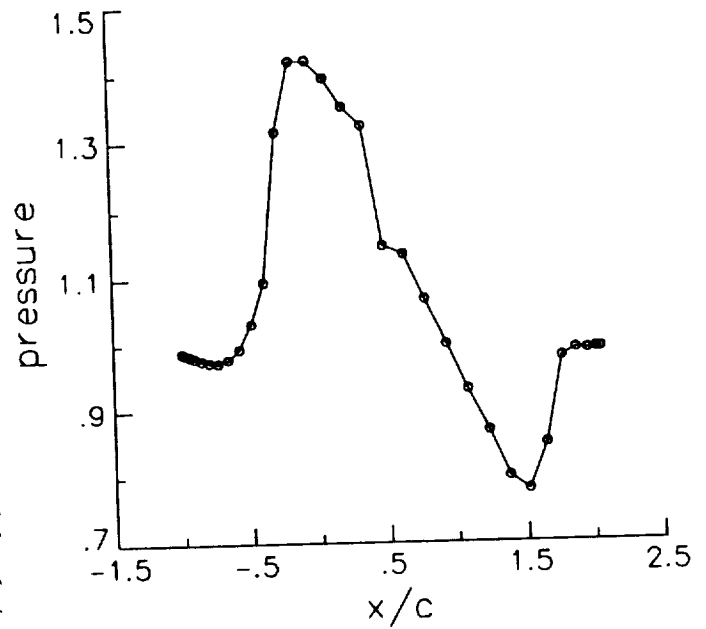


Figure 8.27: Supersonic Airfoil-Flow, Location of $j = \text{Constant}$ Line

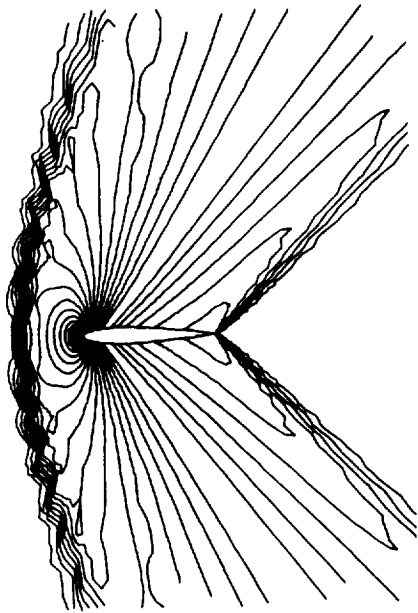


a) Pressure Contours

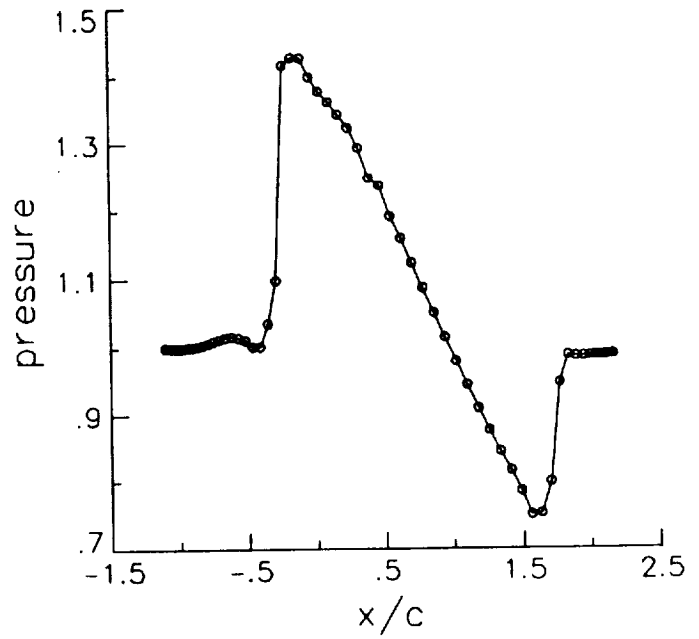
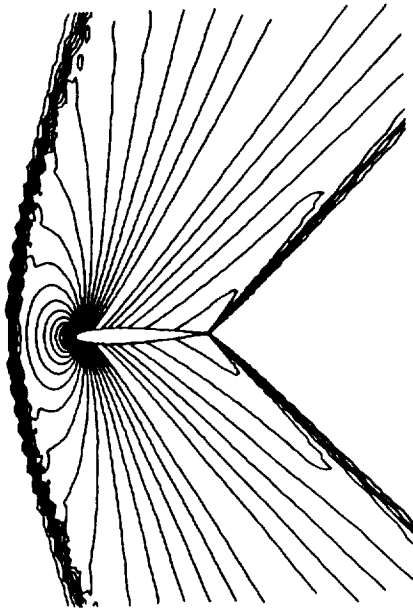


b) Pressure Along $j = \text{Constant}$ Line

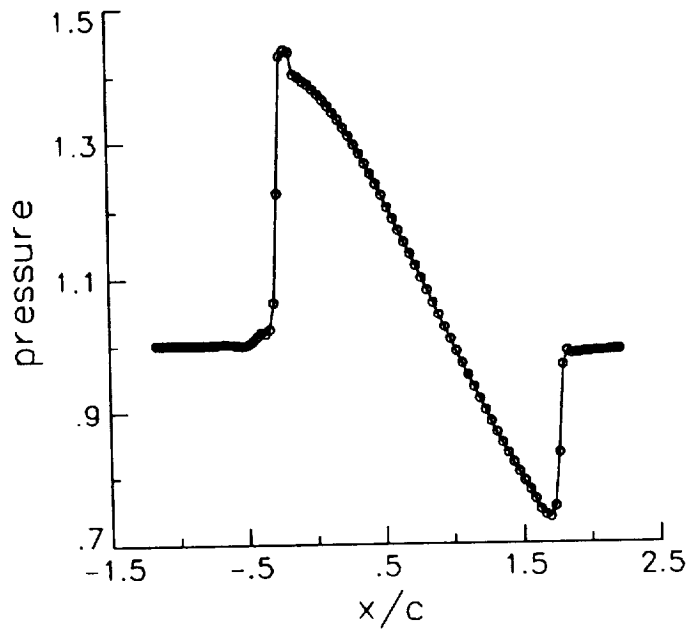
Figure 8.28: Supersonic Airfoil-Flow, First-Order, 5-Wave, 65×19



a) Pressure Contours

b) Pressure Along $j = \text{Constant}$ LineFigure 8.29: Supersonic Airfoil-Flow, First-Order, 5-Wave, 129×37 

a) Pressure Contours

b) Pressure Along $j = \text{Constant}$ LineFigure 8.30: Supersonic Airfoil-Flow, First-Order, 5-Wave, 257×73

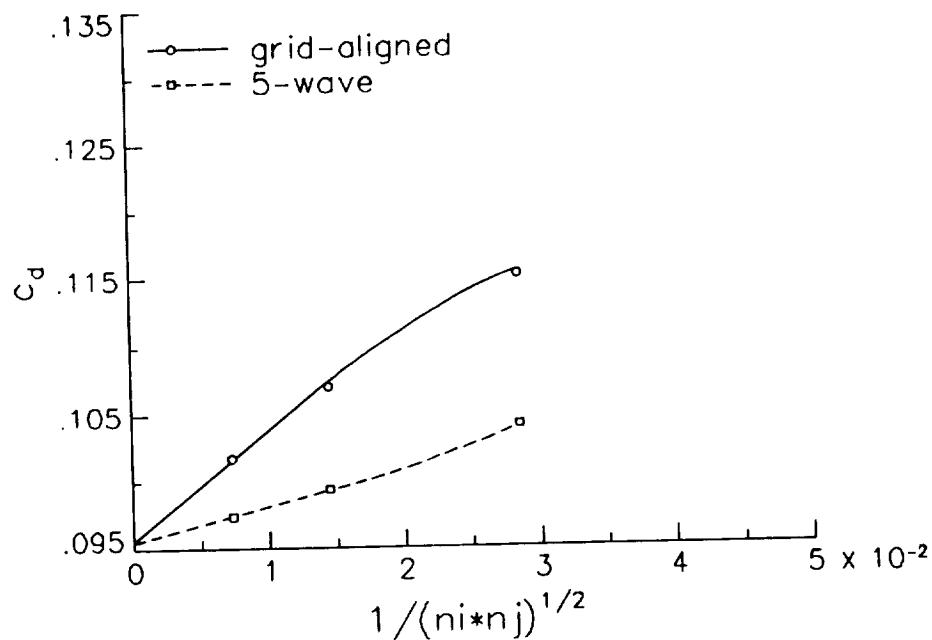


Figure 8.31: Grid-Convergence Study for Supersonic Airfoil-Flow, First-Order

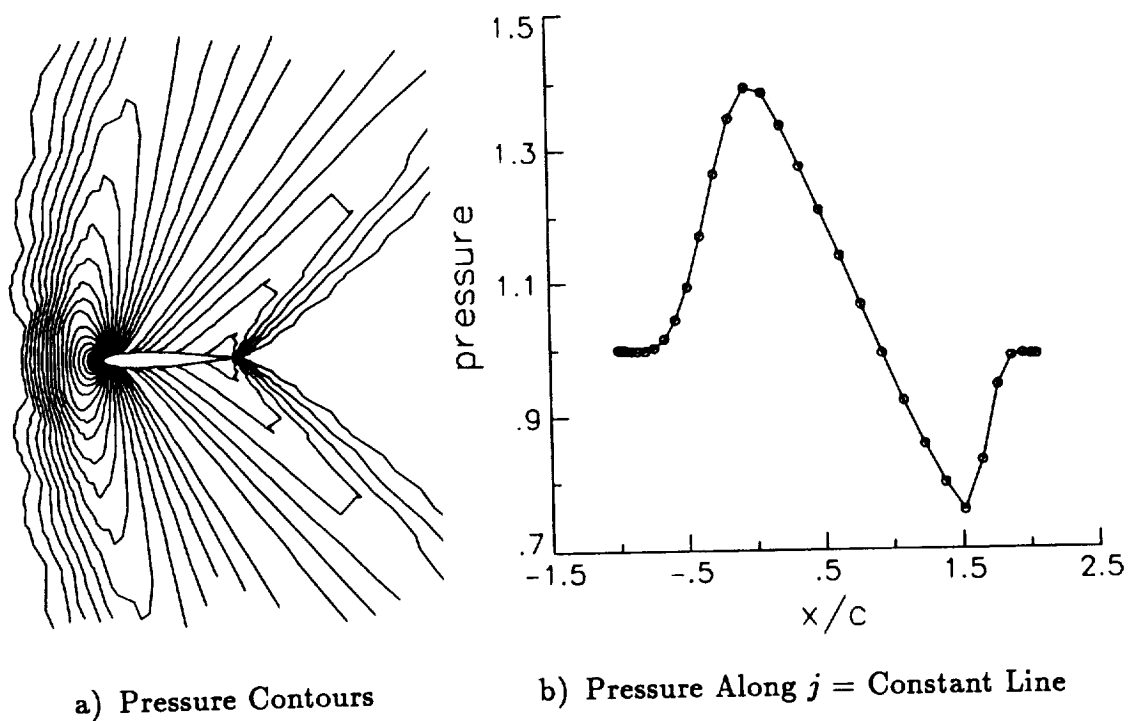
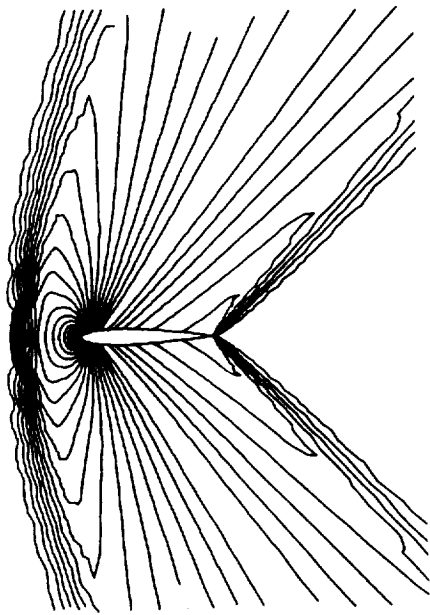
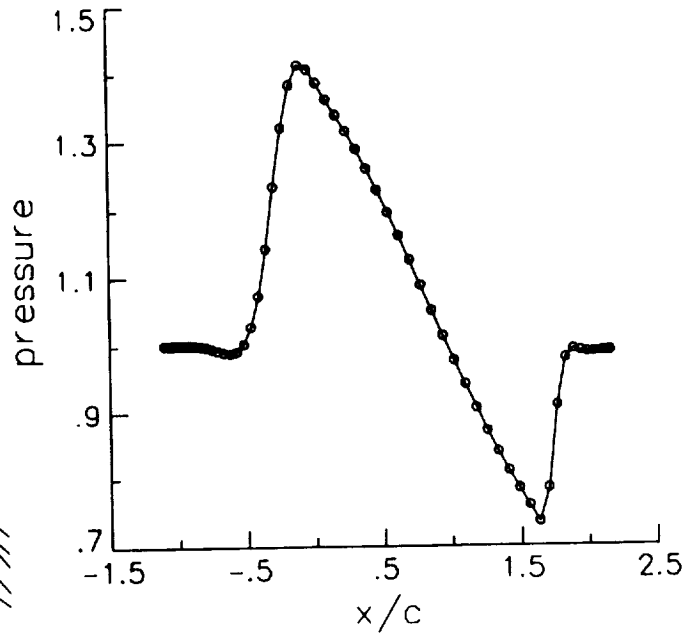


Figure 8.32: Supersonic Airfoil-Flow, Second-Order, Grid-Aligned, 65×19

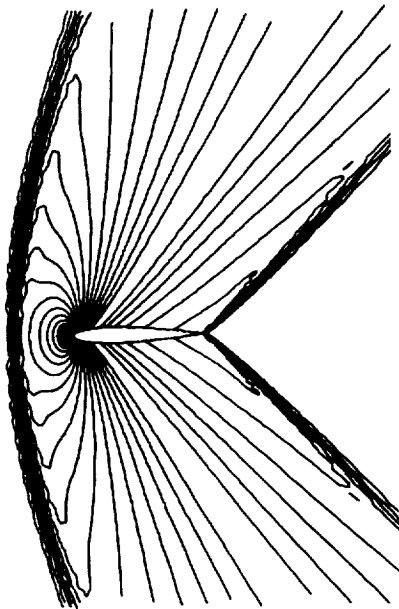


a) Pressure Contours

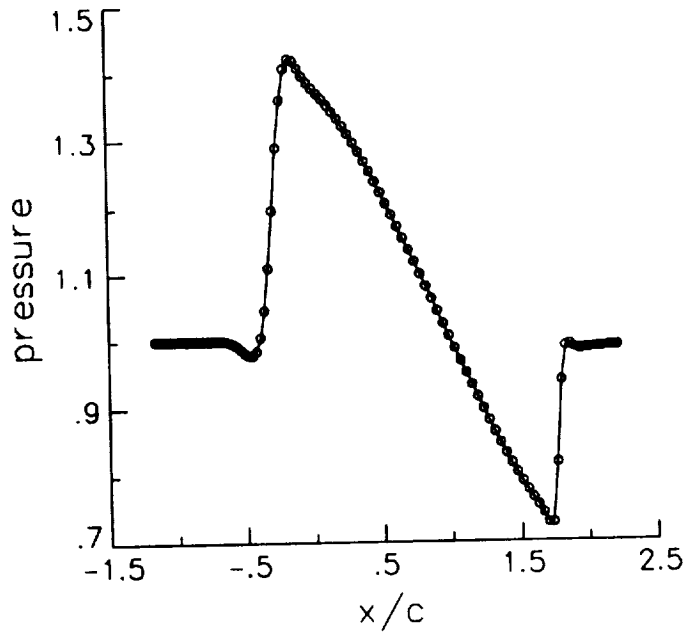


b) Pressure Along $j = \text{Constant}$ Line

Figure 8.33: Supersonic Airfoil-Flow, Second-Order, Grid-Aligned, 129 × 37

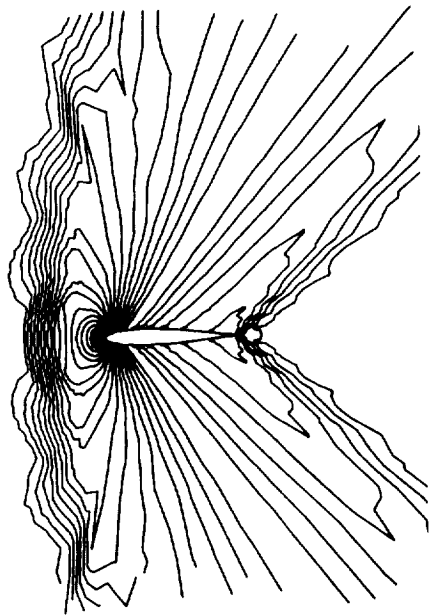


a) Pressure Contours

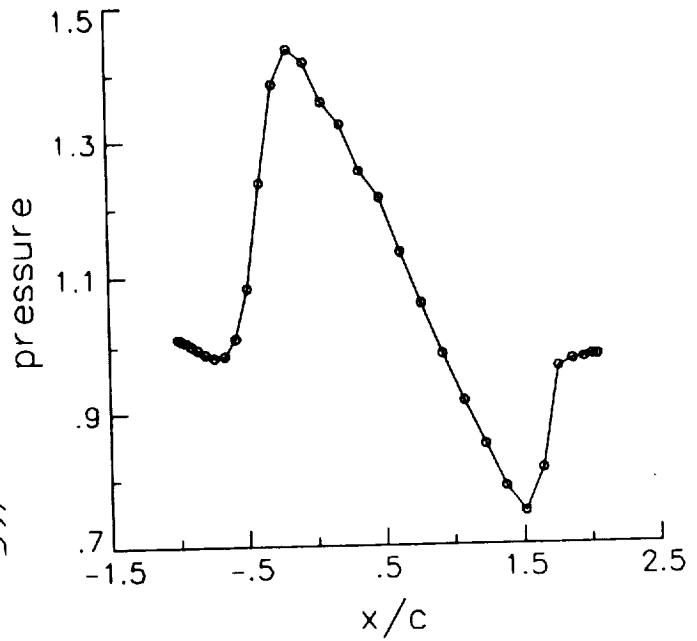


b) Pressure Along $j = \text{Constant}$ Line

Figure 8.34: Supersonic Airfoil-Flow, Second-Order, Grid-Aligned, 257 × 73

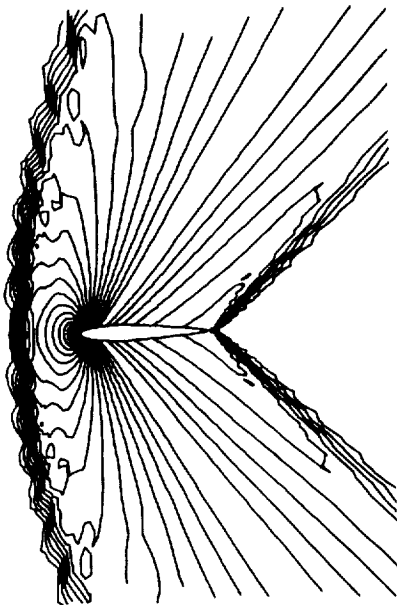


a) Pressure Contours

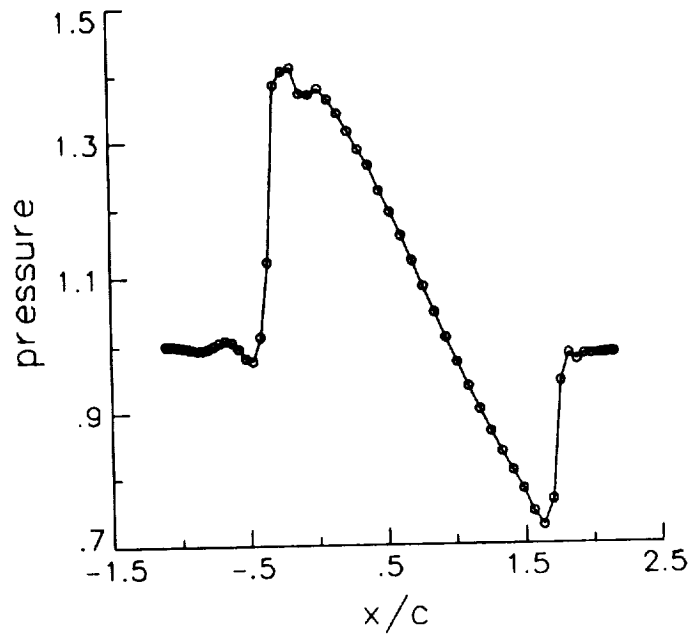


b) Pressure Along $j = \text{Constant}$ Line

Figure 8.35: Supersonic Airfoil-Flow, Second-Order, 5-Wave, 65×19



a) Pressure Contours



b) Pressure Along $j = \text{Constant}$ Line

Figure 8.36: Supersonic Airfoil-Flow, Second-Order, 5-Wave, 129×37

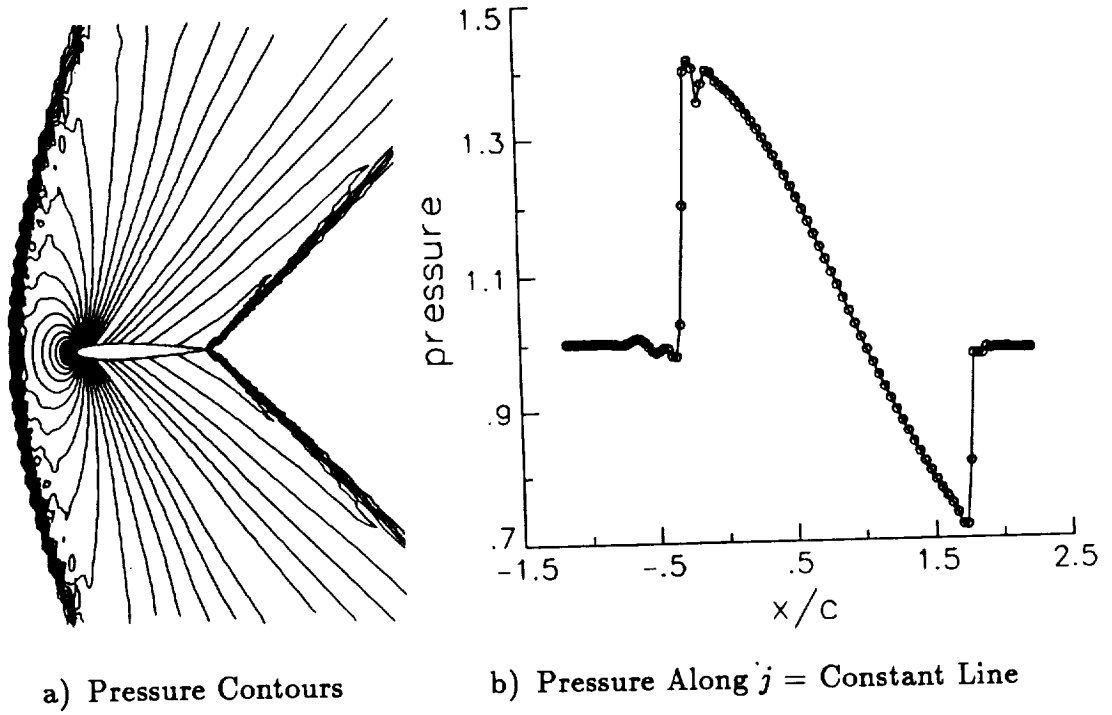


Figure 8.37: Supersonic Airfoil-Flow, Second-Order, 5-Wave, 257×73

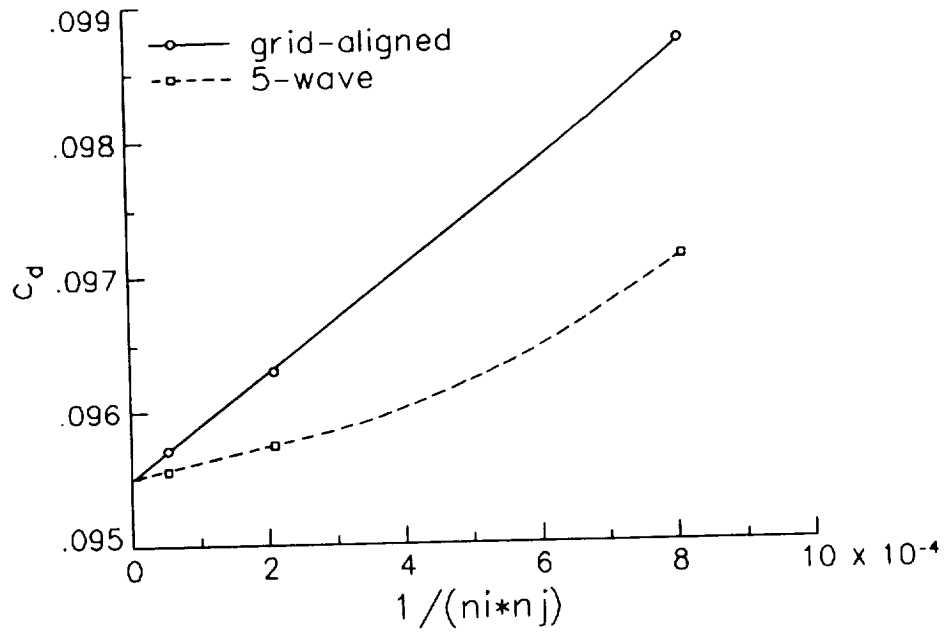


Figure 8.38: Grid-Convergence Study for Supersonic Airfoil-Flow, Second-Order

still somewhat sharper than the grid-aligned results, but there are also significant oscillations near the shocks. Computed drag coefficient values are plotted as a function of the inverse of the grid size in figure 8.38. Second-order results behave linearly when plotted this way (for a sufficiently fine mesh). The drag coefficient again extrapolates to about 0.0955 on an infinitely fine mesh for both methods. The 5-wave model gives better predictions for the drag on all three grids. On the finest, it deviates from the extrapolated value by 0.05% while the grid-aligned method deviates by 0.22%.

In summary, use of the 5-wave model for supersonic flow over an airfoil results in sharper shock resolution and better airfoil drag prediction than the grid-aligned model. The increase in shock resolution is more dramatic for first-order computational accuracy, although even second-order results show a noticeable difference. In spite of the fact that θ'_d -limiting was employed, both first and second-order 5-wave model results are somewhat oscillatory near the computed shock waves.

The effect of limiting the higher-order terms in the second-order solution using the 5-wave model is investigated at this point. A computation is performed on the finest mesh with the "min-mod" limiter employed. This limiter is described in more detail by Anderson *et al.* [30]. Results are shown in figure 8.39. The shock waves are resolved with the same number of interior points as figure 8.37, but now the amount of oscillations near the discontinuities is reduced. Hence the use of standard limiters for second-order computations seems to be viable in conjunction with the 5-wave θ'_d -limited model. While the limiter does not guarantee oscillation-free solutions for this model, it does seem to reduce the amount of oscillations present.

8.1.5 Subsonic Flow Over an Airfoil

A grid convergence study is performed using the Euler equations for subsonic flow over an airfoil in order to investigate the effect of the 5-wave model on an airfoil flowfield where no shock waves are present. The conditions are $M = 0.3$ and $\alpha = 1^\circ$, and results are computed on the same three O-meshes used in the supersonic airfoil flow study. Boundary conditions on the body are again simple reflection conditions, and periodic boundary conditions are applied where the mesh meets itself behind the airfoil. The inflow/outflow boundary conditions applied at the outer boundary for subsonic flow are obtained using characteristic theory. To summarize, the local Riemann invariants R^+ and R^- are constructed as

$$\begin{aligned} R^+ &= q_g^{(i)} + \frac{2a^{(i)}}{\gamma - 1} \\ R^- &= q_g^{(o)} - \frac{2a^{(o)}}{\gamma - 1}, \end{aligned} \quad (8.1)$$

where q_g indicates the velocity normal to the outer grid boundary face and the superscripts “(i)” and “(o)” indicate that conditions are taken from inside and outside (= freestream) the grid boundary, respectively. The normal velocity and speed of sound at the face are then taken as

$$\begin{aligned} (q_g)_f &= \frac{1}{2}(R^+ + R^-) \\ a_f &= \frac{\gamma - 1}{4}(R^+ - R^-). \end{aligned} \quad (8.2)$$

If $(q_g)_f \geq 0$, the entropy s_f and the tangential velocity $(r_g)_f$ are extrapolated from inside the grid boundary. Otherwise, they are taken as the freestream values. The density boundary condition is then obtained using

$$\rho_f = \left(\frac{a_f^2}{s_f} \right)^{1/\gamma}. \quad (8.3)$$

The u and v velocity components are constructed from $(q_g)_f$ and $(r_g)_f$, and the energy is calculated using the equation of state.

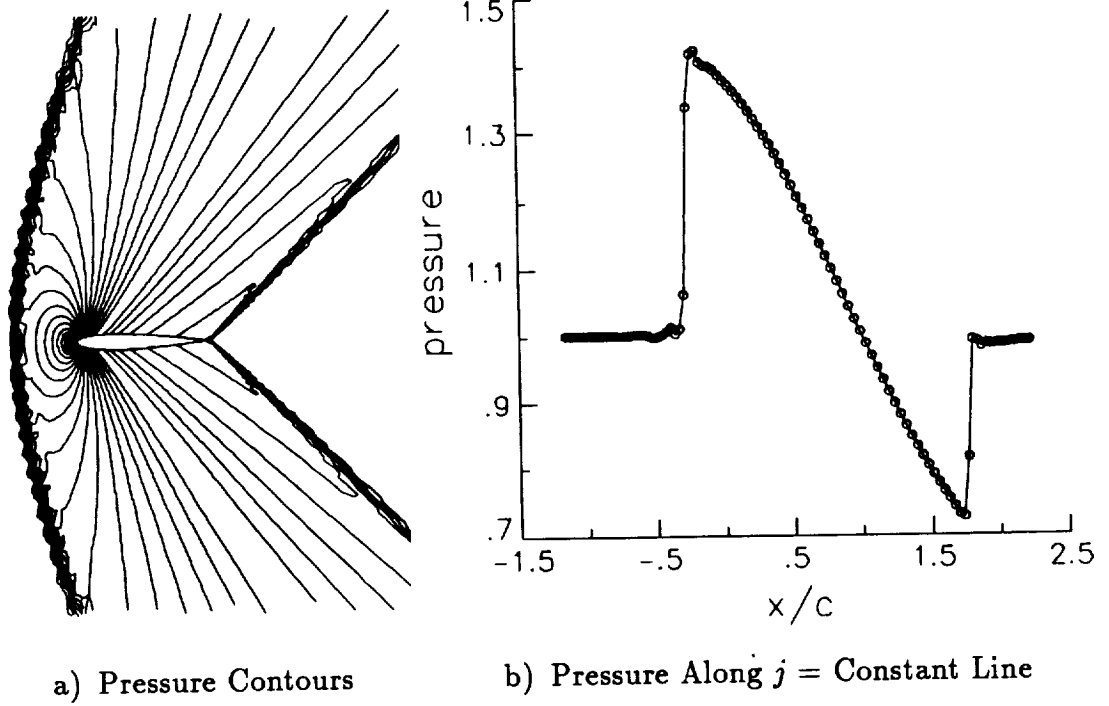


Figure 8.39: Supersonic Airfoil-Flow, Second-Order, 5-Wave, 257×73 , Min-Mod Limiter Employed

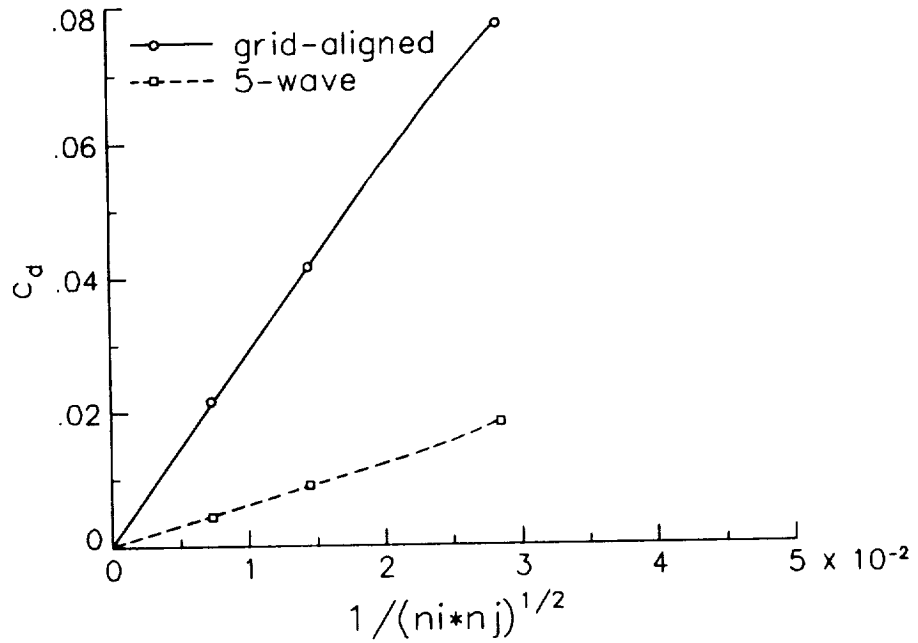


Figure 8.40: Grid-Convergence Study for Subsonic Airfoil-Flow, First-Order

Figure 8.40 is a plot of computed drag coefficient *vs.* the inverse of the square root of the grid density for the grid-aligned scheme and the 5-wave model on the three grids using first-order spatial discretization. The “exact” Euler solution should give zero drag. The 5-wave model, restarted from the grid-aligned solution with θ_d frozen, gives a far better prediction of the drag than the grid-aligned scheme for all three grids. Entropy contours (where entropy is defined as $p/(\rho^\gamma) - 1$) for both methods are given in figures 8.41 and 8.42. Contour values plotted are in increments of 0.001 for both figures. These figures indicate significantly lower entropy production over the airfoil surface using the 5-wave model. The maximum entropy values for the grid-aligned model are 0.0303, 0.0251, and 0.0183 for the coarsest through finest meshes, respectively. For the 5-wave model the maximum values are only 0.0052, 0.0028, and 0.0018.

It is believed that the difference in entropy levels is due to the different ways that the two models interpret the flow near the stagnation point of the airfoil. Near the stagnation point, the flow undergoes very rapid turning with relatively small changes in pressure. The grid-aligned model interprets this turning to be in part due to the action of + and - acoustic waves with nearly offsetting Δp 's. Because the local flow is subsonic, the wavespeeds associated with each of these acoustic waves are of opposite sign, so the flux computed at interfaces near the leading edge is assigned a pressure which is too high or low by an amount Δp . This results in increased entropy generation. In contrast, the 5-wave model interprets the rapid turning near the stagnation point to be due primarily to the action of a $(\theta'_d + \frac{\pi}{2})$ shear wave, which has no associated pressure jump across it. Numerical entropy generation is lower as a consequence.

Total pressure loss values ($= (p_{t\infty} - p_t)/p_{t\infty}$) along the upper surface of the airfoil are plotted for the grid-aligned and the 5-wave models in figures 8.43(a) and (b). The total pressure loss approaches zero for both models as the grid is

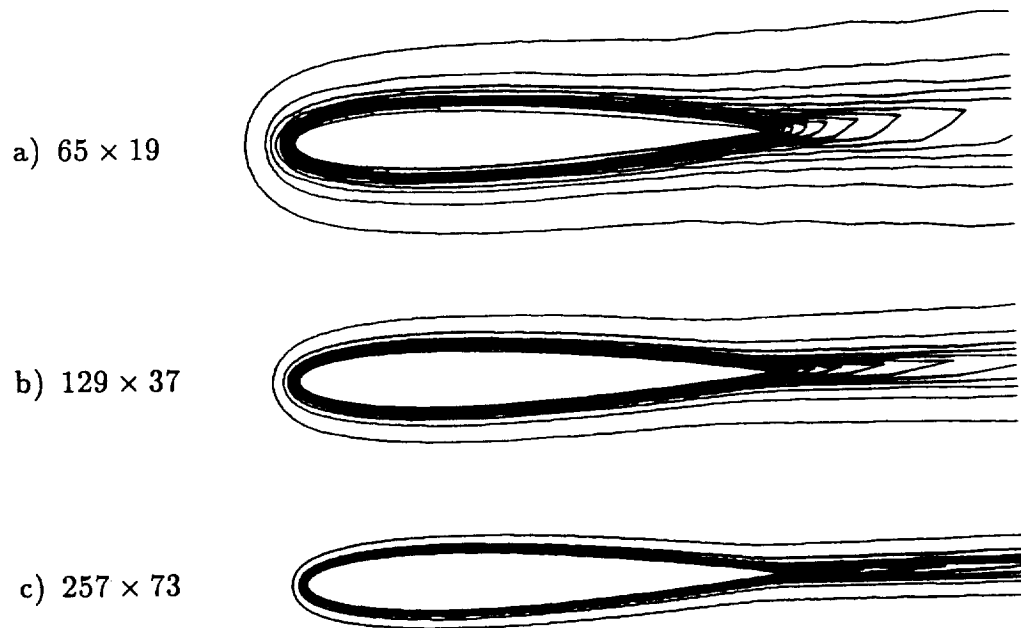


Figure 8.41: Subsonic Airfoil-Flow, Entropy Contours, First-Order, Grid-Aligned

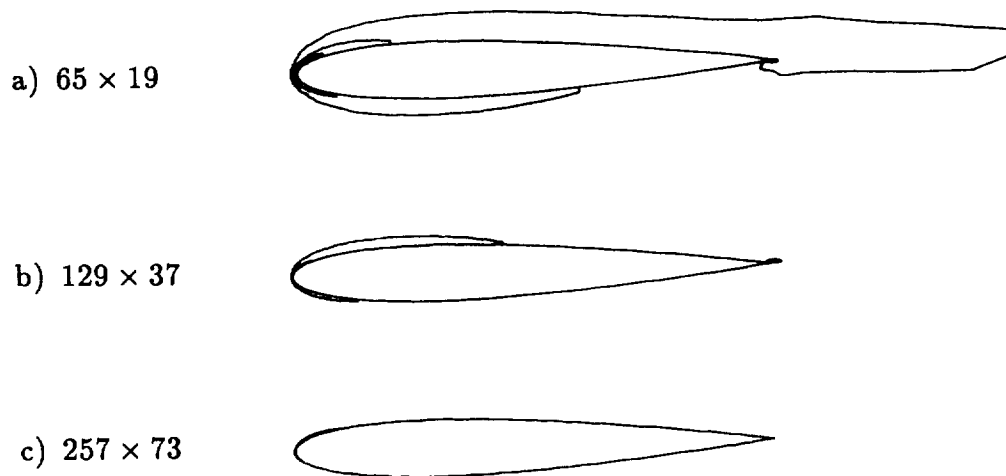
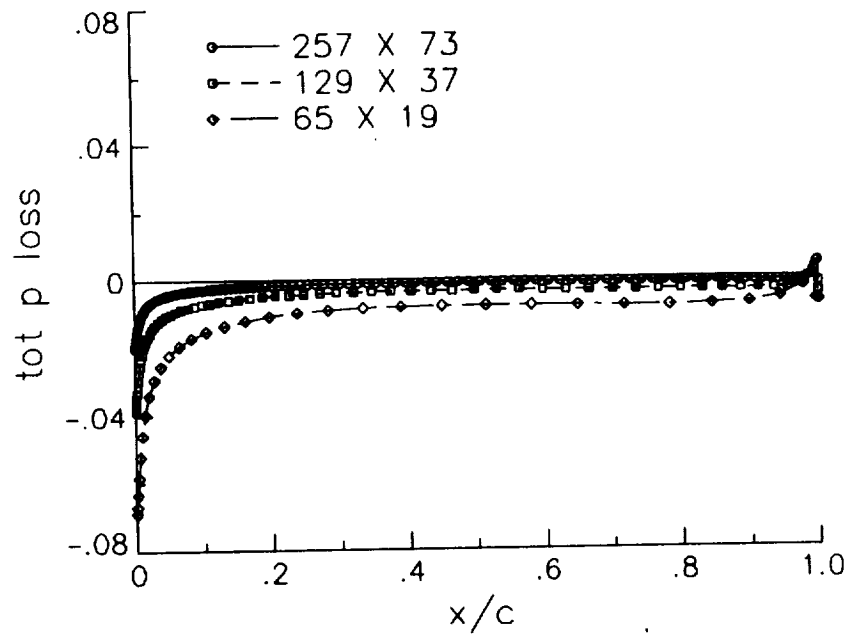
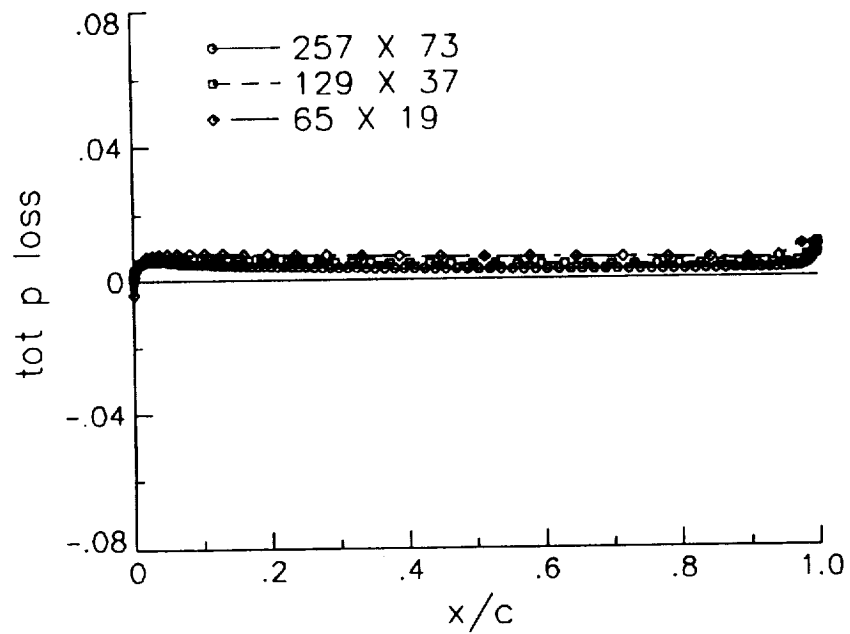


Figure 8.42: Subsonic Airfoil-Flow, Entropy Contours, First-Order, 5-Wave



a) Grid-Aligned



b) 5-Wave

Figure 8.43: Subsonic Airfoil-Flow, Upper Surface Total Pressure Loss, First-Order

refined, as expected. Near the leading edge the grid-aligned model shows much higher magnitudes than the 5-wave model, reflecting the higher entropy generated there. Over the majority of the surface of the airfoil on the finest mesh, however, the grid-aligned model shows lower total pressure loss values. It appears that these are approaching zero at a faster rate than those from the 5-wave model as the grid is refined. The reason for this is unknown.

Drag coefficient values from the grid-sensitivity study for second-order accurate computations are plotted in figure 8.44. Again, the 5-wave model gives lower values than the grid-aligned model, but in this case the difference is not so dramatic as for first-order. This is reflected in the entropy contours as well, shown in figure 8.45 for grid-aligned and 8.46 for the 5-wave model. (Contour values plotted are in increments of 5×10^{-5} for both figures.) The 5-wave model appears to have only slightly lower entropy values overall. The maximum values for the grid-aligned method are 0.0018, 0.0011, and 0.0006 on the coarsest to finest grids, respectively, while the maximum values for the 5-wave model are 0.0015, 0.0009, and 0.0007. Total pressure loss values on the airfoil upper surface are plotted in figures 8.47(a) and (b). In general, results are similar for the two methods. The 5-wave model gives somewhat higher values just aft of the leading edge than the grid-aligned model on all three grids, but values near the trailing edge are lower. For completeness, the pressure contours resulting from the second-order fine mesh 5-wave model solution are shown in figure 8.48. Pressure levels in increments of 0.005 are plotted. The grid-aligned result on the finest mesh is identical to this figure, so it is not shown.

In summary, first-order computations using the 5-wave model give lower numerical entropy generation in a subsonic Euler computation over an airfoil. As a result, the drag prediction is nearer to the correct result of zero. Second-order computations using the 5-wave model still give better drag prediction than the

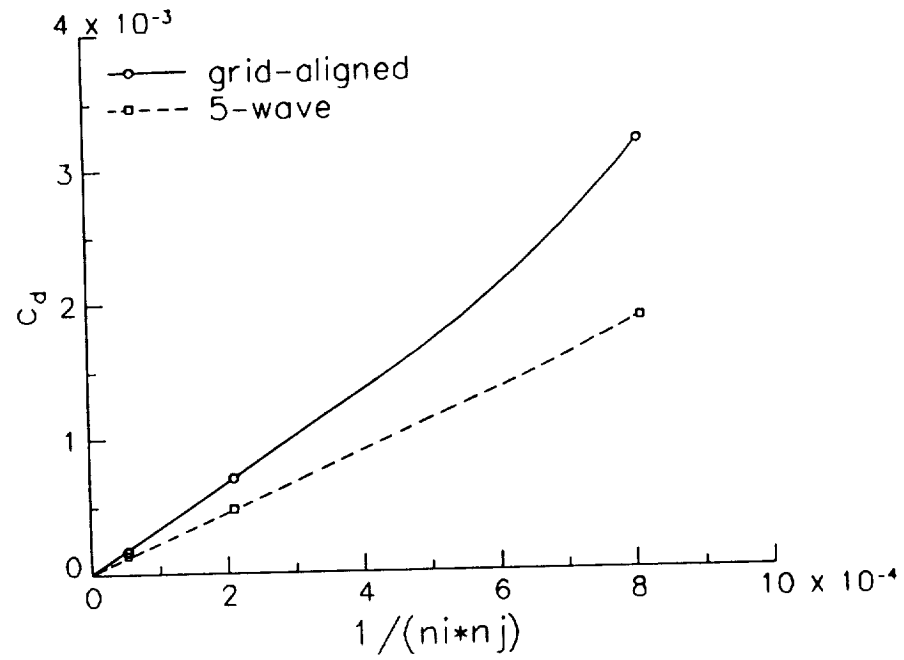


Figure 8.44: Grid-Convergence Study for Subsonic Airfoil-Flow, Second-Order

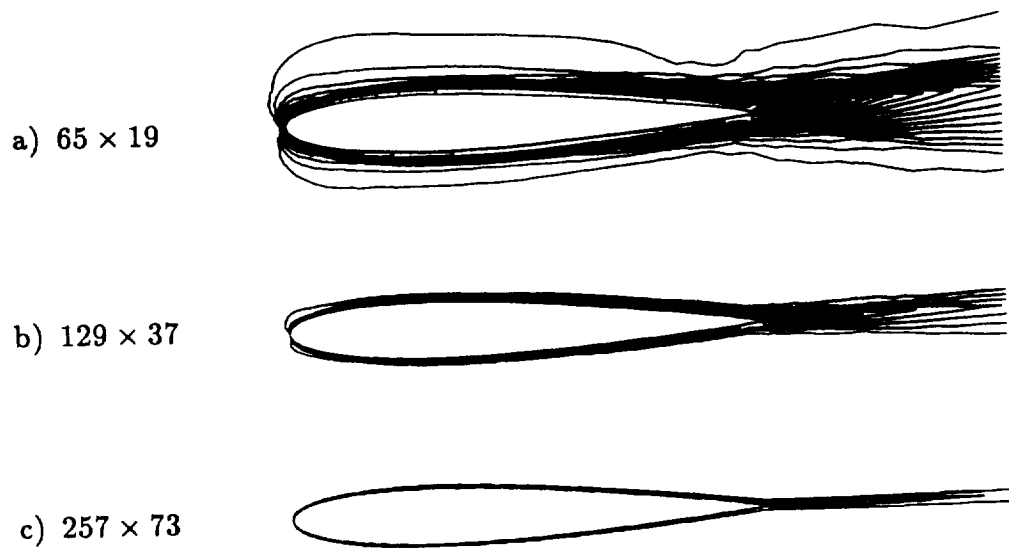


Figure 8.45: Subsonic Airfoil-Flow, Entropy Contours, Second-Order, Grid-Aligned

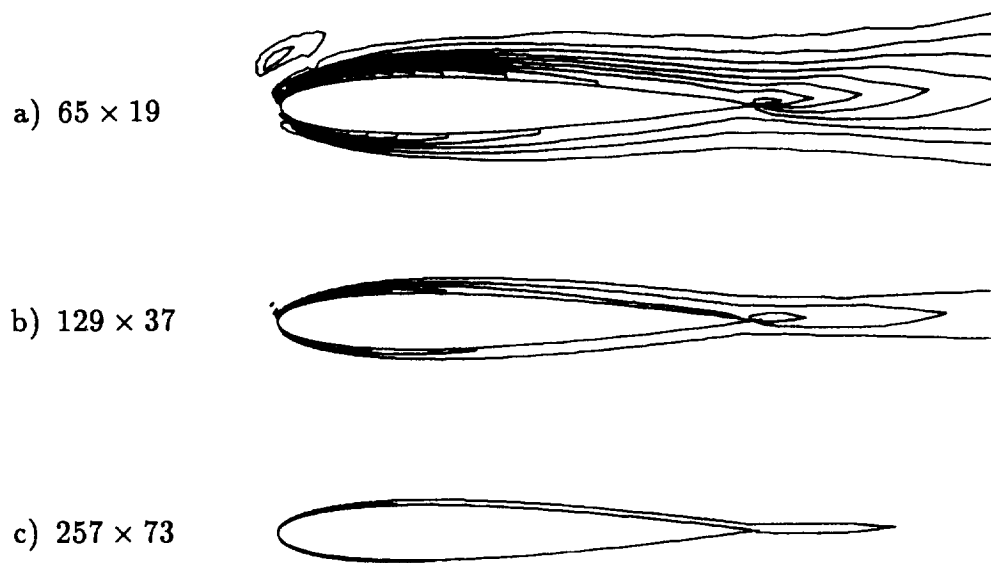
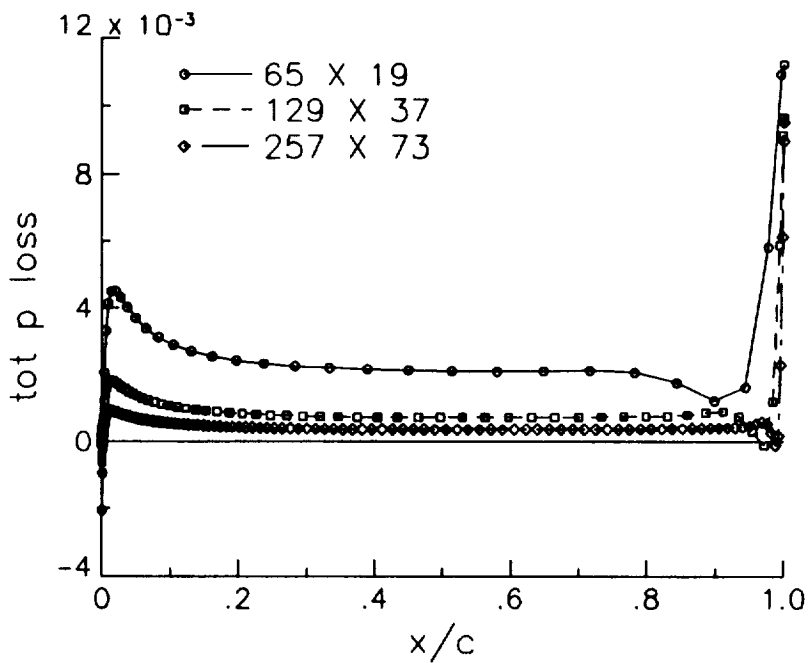
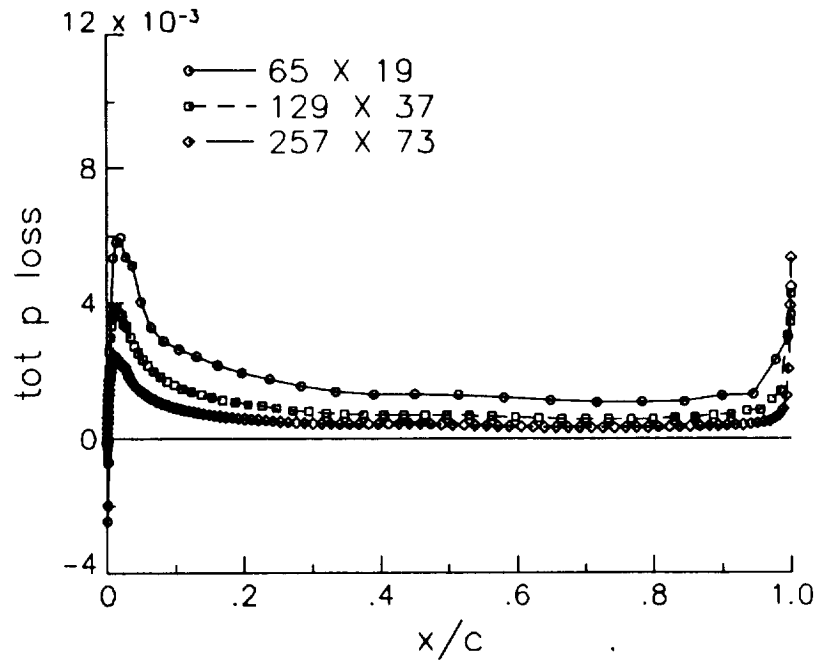


Figure 8.46: Subsonic Airfoil-Flow, Entropy Contours, Second-Order, 5-Wave



a) Grid-Aligned

Figure 8.47: Subsonic Airfoil-Flow, Upper Surface Total Pressure Loss, Second-Order



b) 5-Wave

Figure 8.47: Concluded

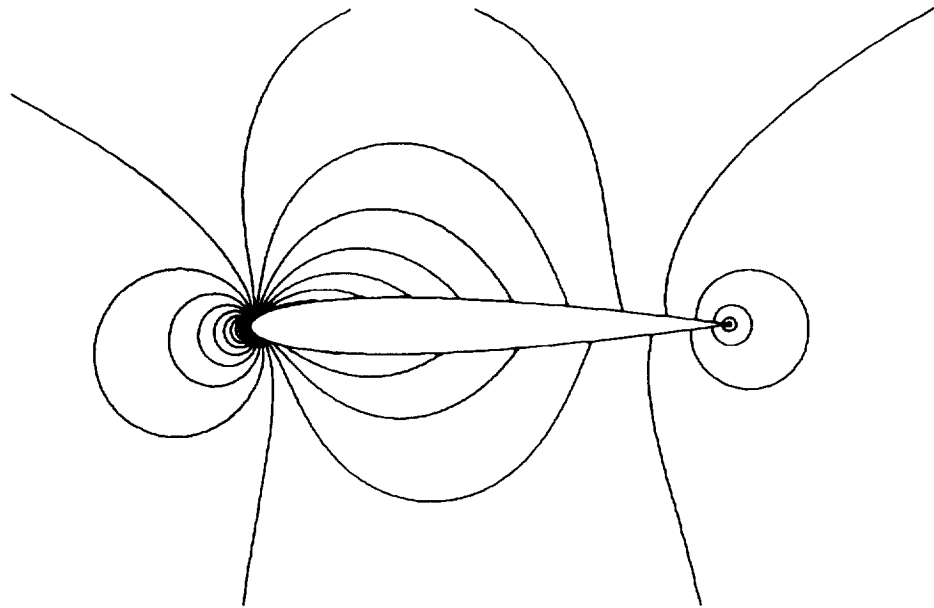


Figure 8.48: Subsonic Airfoil-Flow, Pressure Contours, Second-Order, 257 x 73

grid-aligned method, but the difference is not as great as for first-order. Entropy levels are similar for the two methods. Hence there does not appear to be a significant advantage to using the 5-wave model over the grid-aligned method for second-order computations of subsonic airfoil flows such as this.

8.2 Navier-Stokes Computations

Only second-order spatial accuracy is used for all Navier-Stokes computations. No limiting of higher-order terms is employed. All solutions are advanced in time using the implicit approximately-factored algorithm, and convergence is assumed to be reached when the L_2 -norm of the residual drops by at least 4 orders of magnitude and/or the lift and drag values settle down and do not vary significantly with further iterations.

8.2.1 Shock/Boundary-Layer Interaction

A shock/boundary-layer interaction is computed over a flat plate in a domain that is 1.84 units wide by approximately 1.29 units high. The plate is assumed to start 0.24 units from the left. The finest grid employed is a 93×141 with minimum spacing at the wall of 9×10^{-5} units. It is shown in figure 8.49. Coarser meshes of 47×71 and 24×36 are obtained by removing every other point from the next finest mesh.

The inflow Mach number is 2.0, and the Reynolds number per unit length is 296,000. Laminar flow is assumed. A shock wave enters from the left of the domain at a height of 0.7930 units. It has an angle such that it impinges on the plate 1.0 unit from the leading edge. The flow is turned through an angle of 3.1° . The

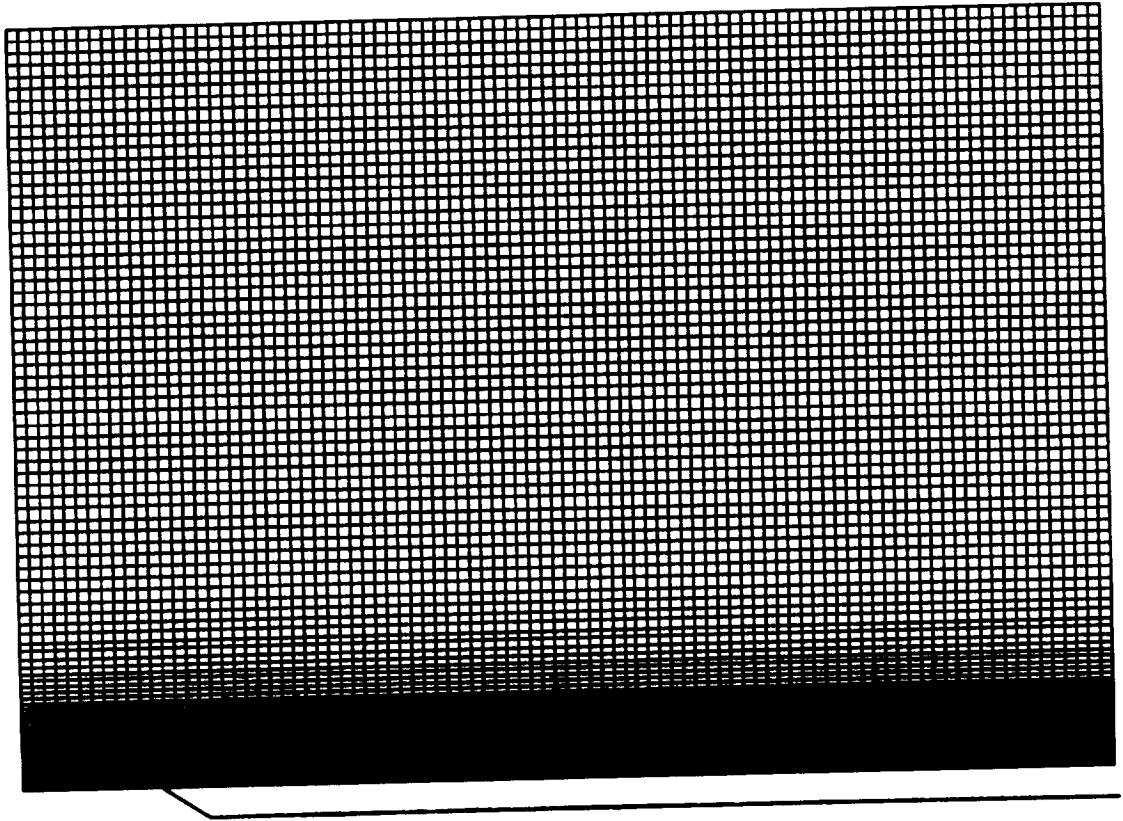


Figure 8.49: Shock/Boundary-Layer Interaction 93×141 Grid

boundary conditions at inflow (below the shock) are: $\rho = 1$, $\rho u = 2$, $\rho v = 0$, $\rho E = 3.78571$. Above the shock and along the top wall: $\rho = 1.13038$, $\rho u = 2.18509$, $\rho v = -0.11834$, $\rho E = 4.23855$. At the right wall all variables are extrapolated from the interior using second-order interpolation. Along the bottom wall in front of the plate symmetry conditions are applied, and on the plate itself no slip, zero pressure gradient, and adiabatic wall boundary conditions are assumed. For this problem, the thin-layer Navier-Stokes equations are employed: it is assumed that viscous terms arising from derivatives in the streamwise direction are negligible in comparison to the viscous terms arising from derivatives normal to the wall.

Pressure contours for the grid-aligned model on the three grids are shown in figure 8.50, while 5-wave model results are shown in figure 8.51. (The 5-wave model results are obtained by restarting the grid-aligned solutions with θ_d frozen.) Values in the figures are plotted from 0.84 to 1.44 in steps of 0.03. Results are very similar for both methods, with the exception that the 5-wave model gives slightly sharper shock resolution. Also, some oscillatory behavior is evident near the plate leading edge as well as at the shock inflow location for the 5-wave model. Skin friction plots over the plate surface are given in figure 8.52 for the two methods. In figure 8.52(a) it is seen that the grid-aligned method gives reasonable levels on all three grids, with the greatest discrepancies between the solutions occurring in the separated region and near reattachment. The 5-wave model, on the other hand, gives very high skin friction levels on the coarsest mesh (as shown in figure 8.52(b)), indicating that the velocity profiles are predicted to be too full. This can be seen in the computed velocity profiles at two locations on the plate in figure 8.53, in comparison with grid-aligned results on the same grid. On the two finer grids, the 5-wave model gives consistent skin friction results in good agreement with the grid-aligned model.

It is not known why the 5-wave model predicts fuller profiles on the coarsest

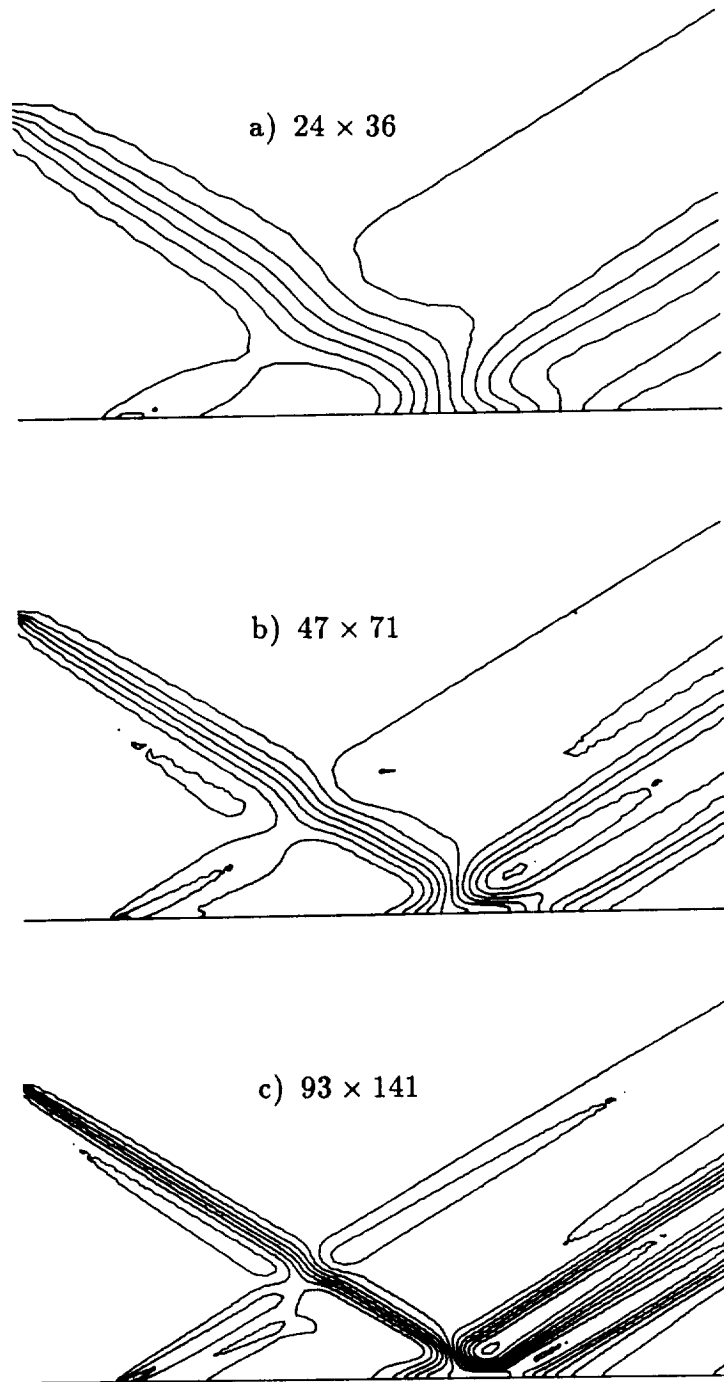


Figure 8.50: Shock/Boundary-Layer Interaction, Pressure Contours, Grid-Aligned

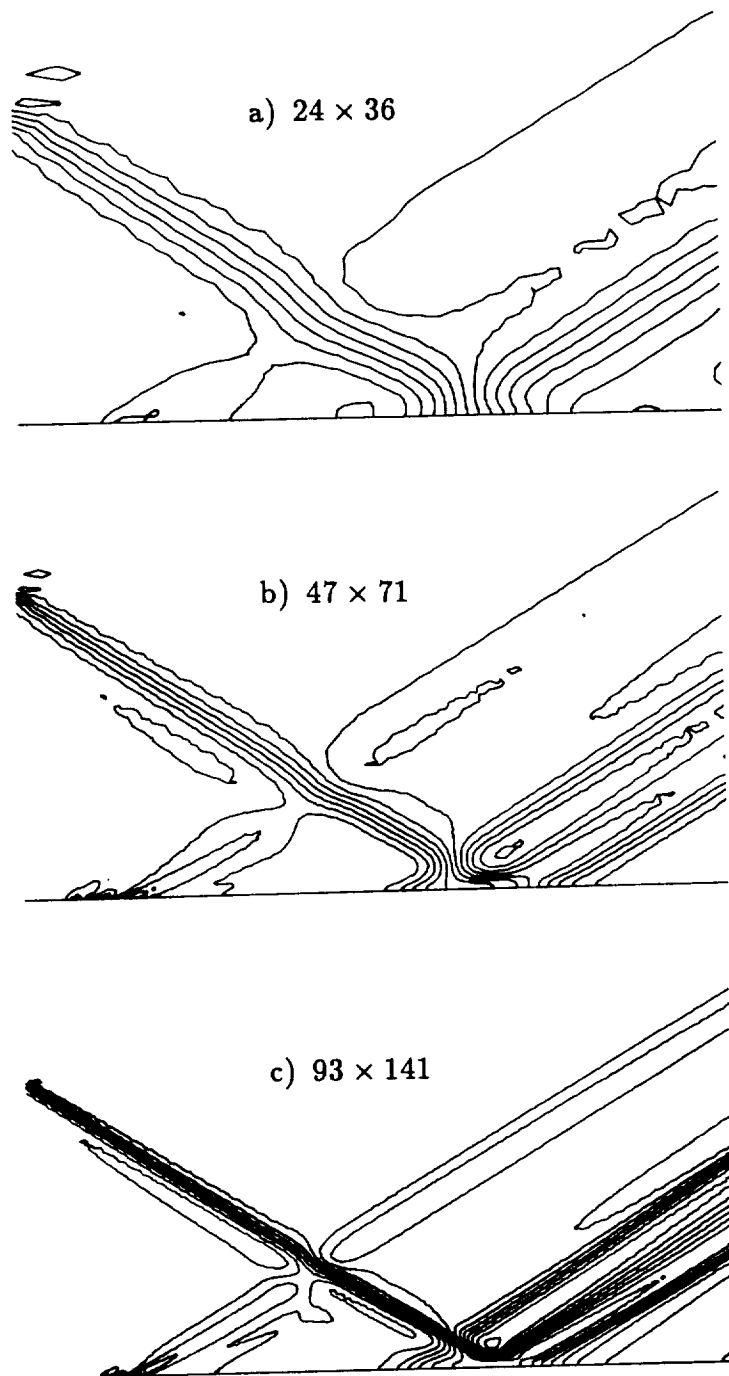
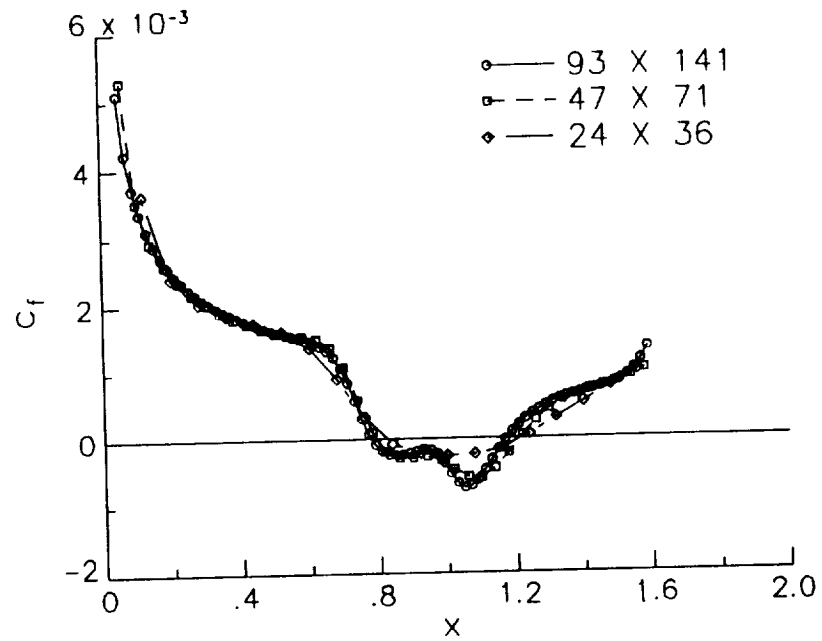
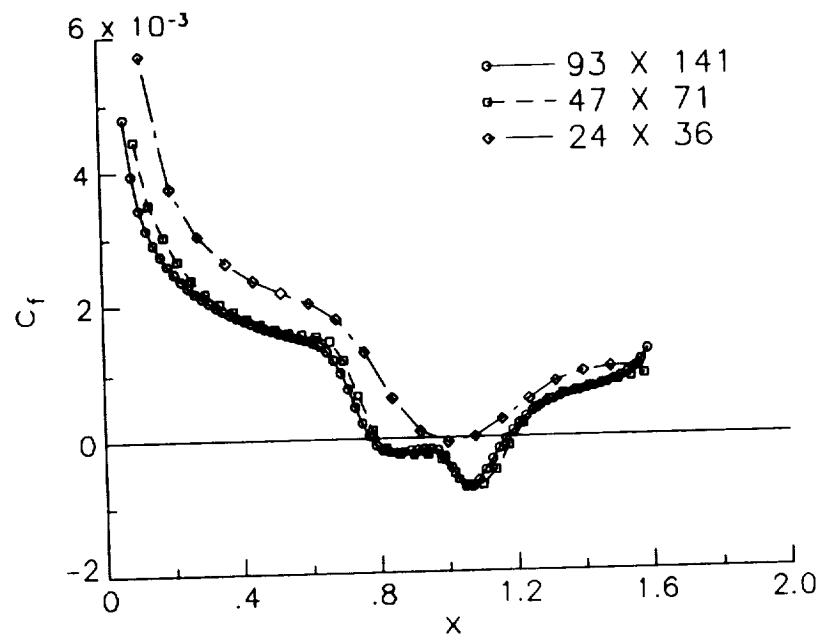


Figure 8.51: Shock/Boundary-Layer Interaction, Pressure Contours, 5-Wave



a) Grid-Aligned



b) 5-Wave

Figure 8.52: Shock/Boundary-Layer Interaction, Skin Friction

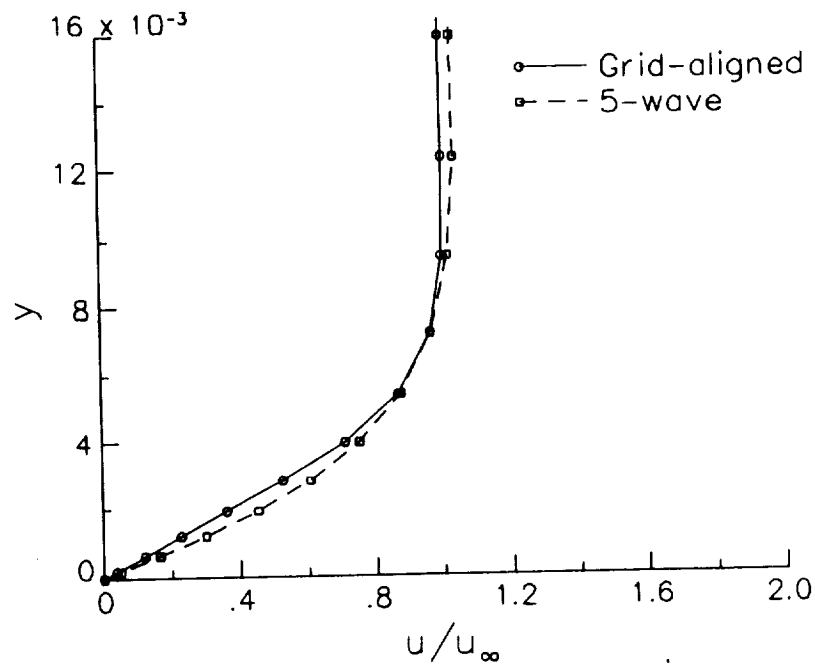
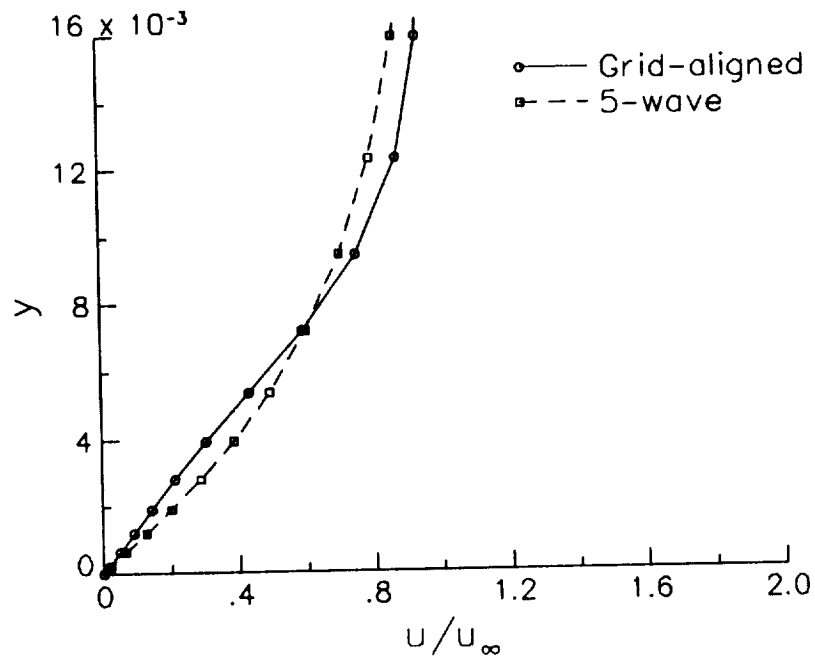
a) $x = 0.4$ b) $x = 1.5$

Figure 8.53: Shock/Boundary-Layer Interaction, Boundary-Layer Profiles, 24×36

mesh for this case. Aside from this discrepancy, the model behaves much as expected, considering the results from the earlier Euler shock reflection case. For this second-order computation, the shock structure is captured slightly better than when the grid-aligned scheme is used, but some oscillations also appear in the flowfield. The very small increase in shock resolution does not seem to be worth the added expense and increased oscillatory behavior of the 5-wave model.

8.2.2 Subsonic Separated Flow Over an Airfoil

A specific case where an advantage of the 5-wave model over the grid-aligned model is fully realized in a second-order computation is for viscous separated flow over a NACA 0012 airfoil at $M = 0.5$, $\alpha = 3^\circ$, and $Re = 5000$. Full Navier-Stokes computations are performed on a series of C-meshes. The finest, a 257×97 grid with outer boundary extent of 14 chords and average minimum spacing on the body of 2×10^{-4} chords, is shown in figure 8.54. There are 176 cell faces on the airfoil. Coarser meshes are obtained by removing every other gridpoint from the next finest mesh. Subsonic inflow/outflow boundary conditions are applied on the outer boundary, and no slip, zero pressure gradient, and adiabatic wall conditions are used at the body. Continuation conditions are applied on the wake cut.

This test case was first discussed by Venkatakrishnan [31]. He found that on even reasonably fine meshes, the grid-aligned upwind scheme does a poor job for this case since there is a detached shear layer emanating from about mid-chord on the airfoil upper surface which is not oriented with the grid. The shear is misinterpreted by the grid-aligned model as a combination of shear and compression/expansion, with the end result of a distortion in the computed pressure. Grid-aligned results on the three grids showing this pressure distortion are shown

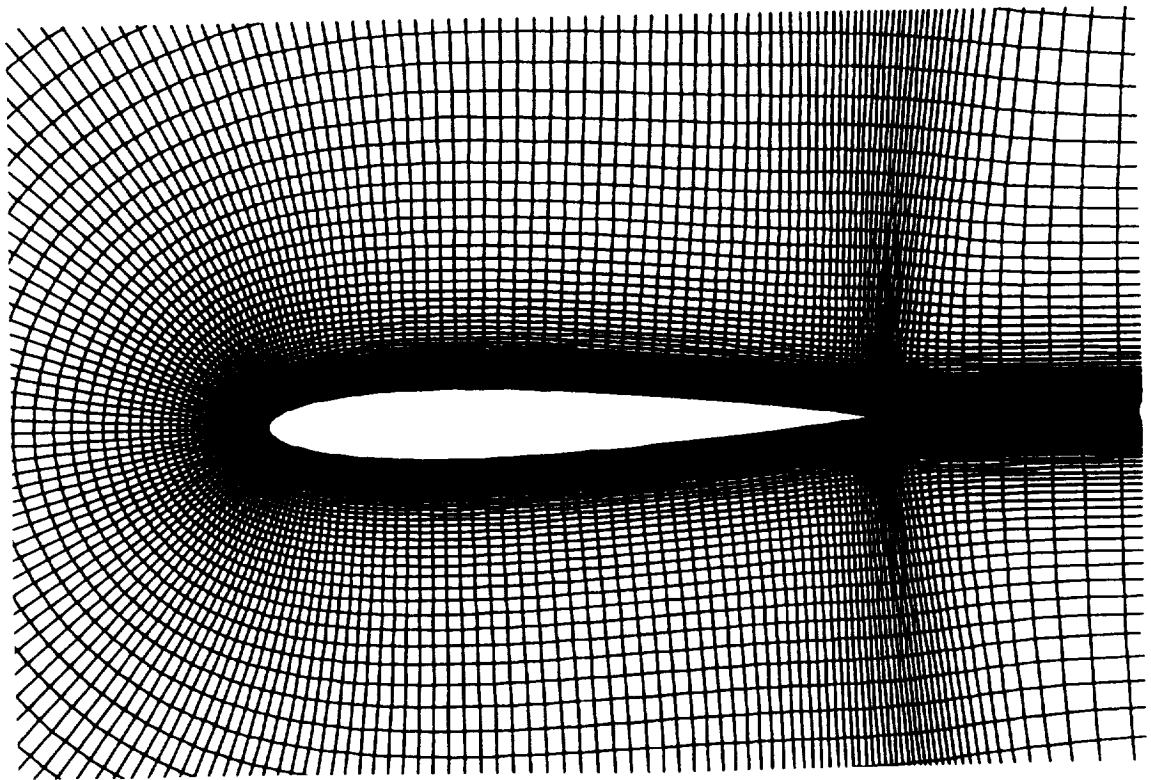


Figure 8.54: NACA 0012 257 × 97 C-Grid

in figure 8.55. Pressure contours are plotted in increments of 0.005. As the grid is refined the distortion diminishes in extent, but does not go away on these grids.

The 5-wave model is run by restarting the grid-aligned solutions with θ_d frozen. Results are plotted in figure 8.56. On all three grids, the pressure distortion is essentially eliminated. Lift coefficient values, plotted as a function of the inverse of the number of gridpoints in figure 8.57, show that both models are approaching the same value of $c_l \approx 0.055$ as the mesh is refined. In spite of the fact that the 5-wave model does a good job of reducing the pressure distortion on all three meshes, the lift is seriously overpredicted (by about 120%) on the coarsest one. This can be seen in a plot of surface pressure coefficient on the 65×25 grid, given in figure 8.58. The surface pressure values given by the 5-wave model are significantly lower than the grid-aligned values over the upper surface, as well as slightly higher over the lower surface. On the other grids the two models are in closer agreement, although the grid-aligned model is always closer to the "correct" extrapolated lift coefficient. Drag coefficient values are plotted in figure 8.59. Figure 8.59(a) shows the total drag coefficient, while figure 8.59(b) breaks the drag coefficient into its friction drag and pressure drag components. Both models do reasonable jobs of predicting the drag on the two finest meshes.

In summary, the 5-wave model can essentially eliminate pressure distortions which arise in a separated viscous flow computation due to misinterpretation of oblique shear waves by the grid-aligned scheme. However, the surface pressure levels (and hence the lift coefficient) predicted by the 5-wave model are more sensitive to grid density than those predicted by the grid-aligned model, so a fairly fine mesh is required for a reasonable level of accuracy in this regard. Since the grid-aligned method shows pressure distortions on even the 257×97 grid, the 5-wave model appears to be worth the additional effort in this case.

All results obtained for the Navier-Stokes cases to this point using the 5-wave

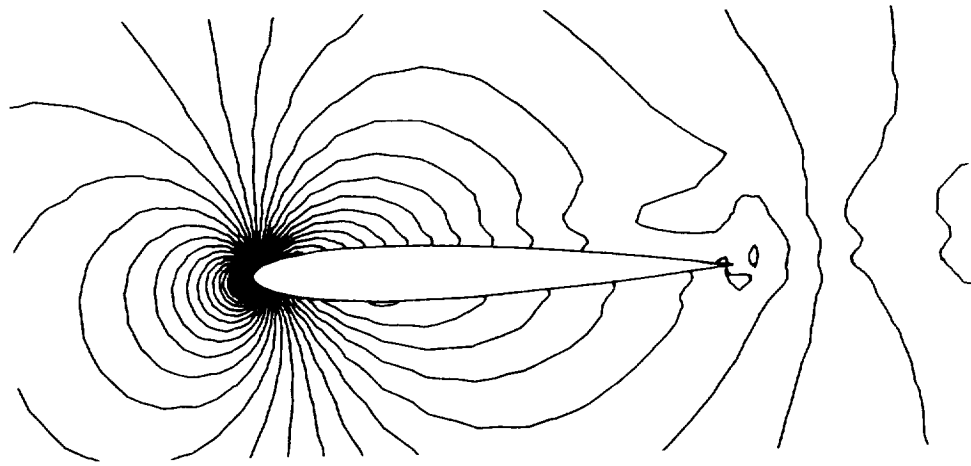
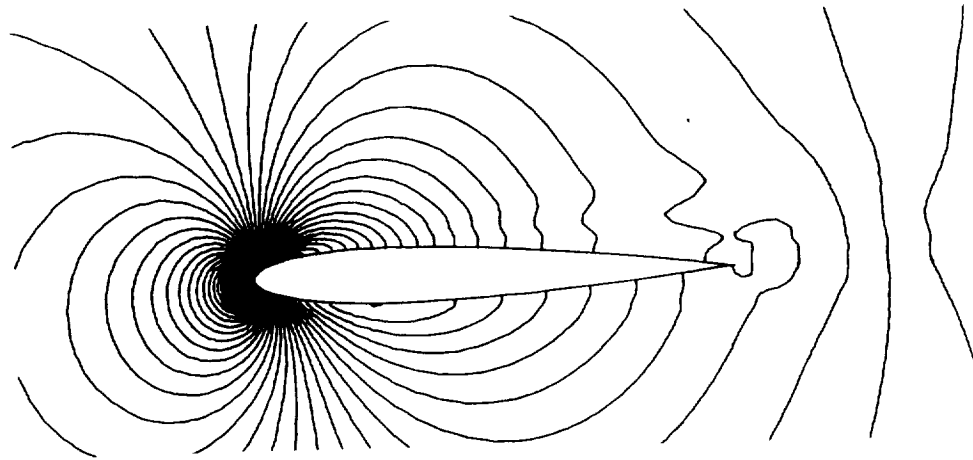
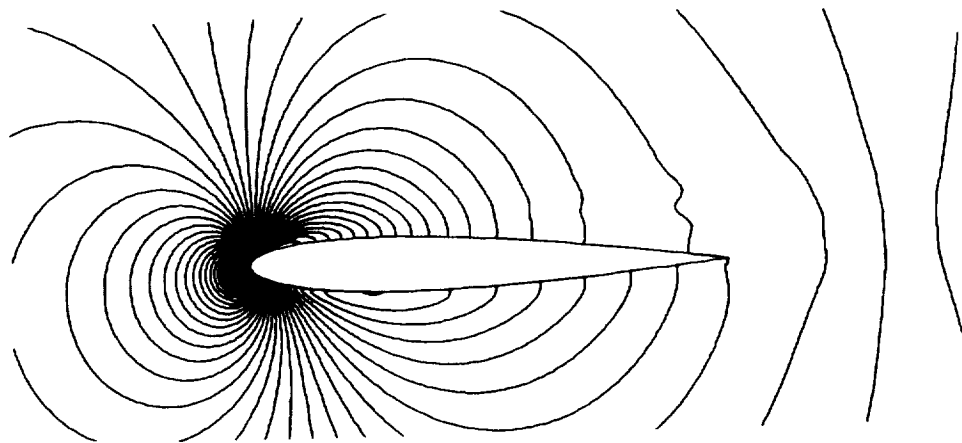
a) 65×25 b) 129×49 c) 257×97

Figure 8.55: Viscous Airfoil-Flow, Pressure Contours, Grid-Aligned

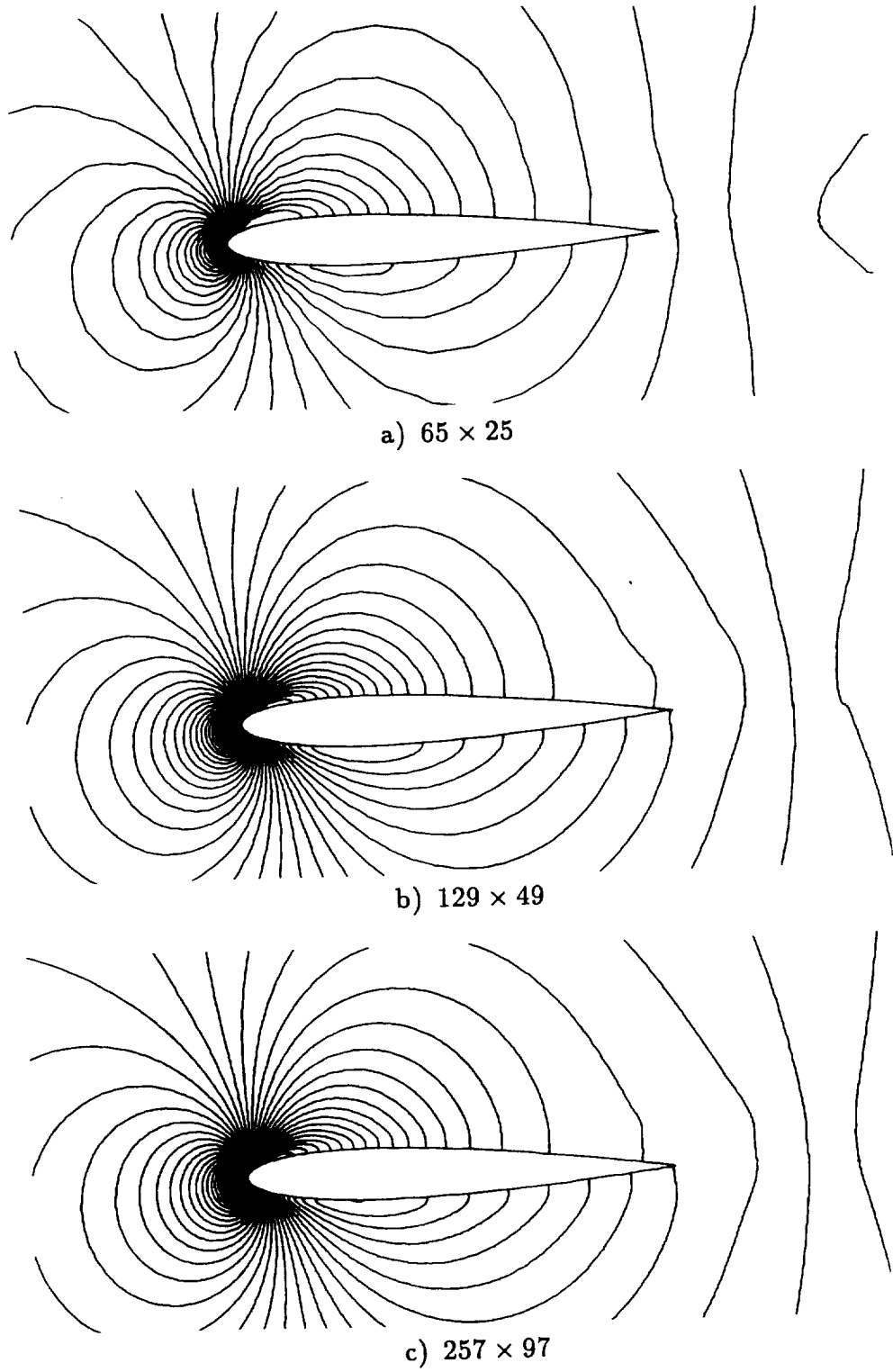


Figure 8.56: Viscous Airfoil-Flow, Pressure Contours, 5-Wave

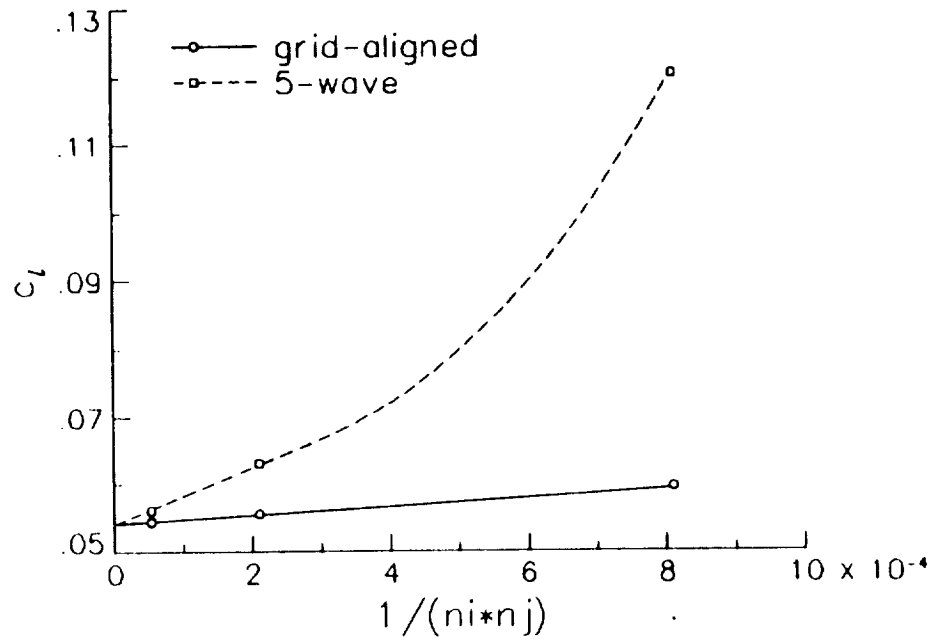


Figure 8.57: Lift-Coefficient Grid-Convergence Study for Viscous Airfoil-Flow

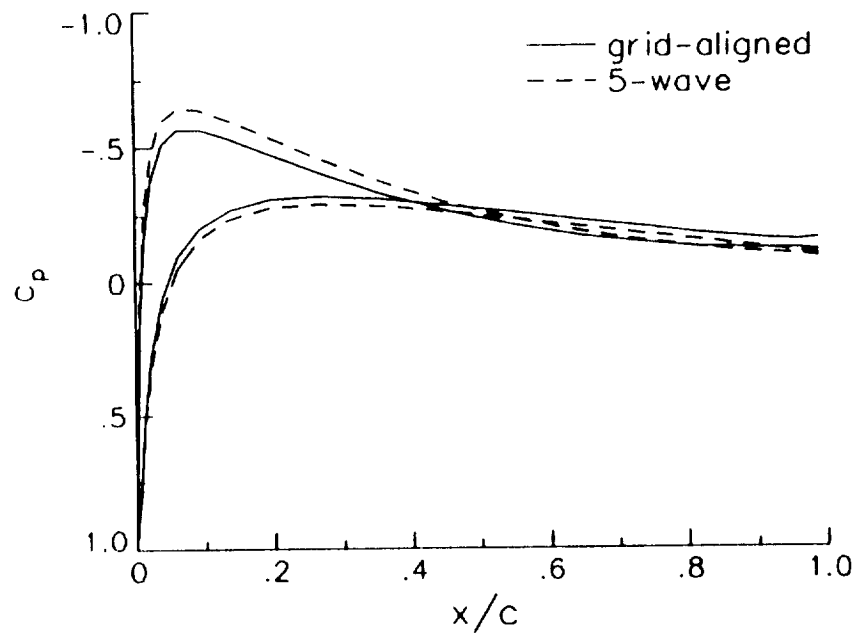
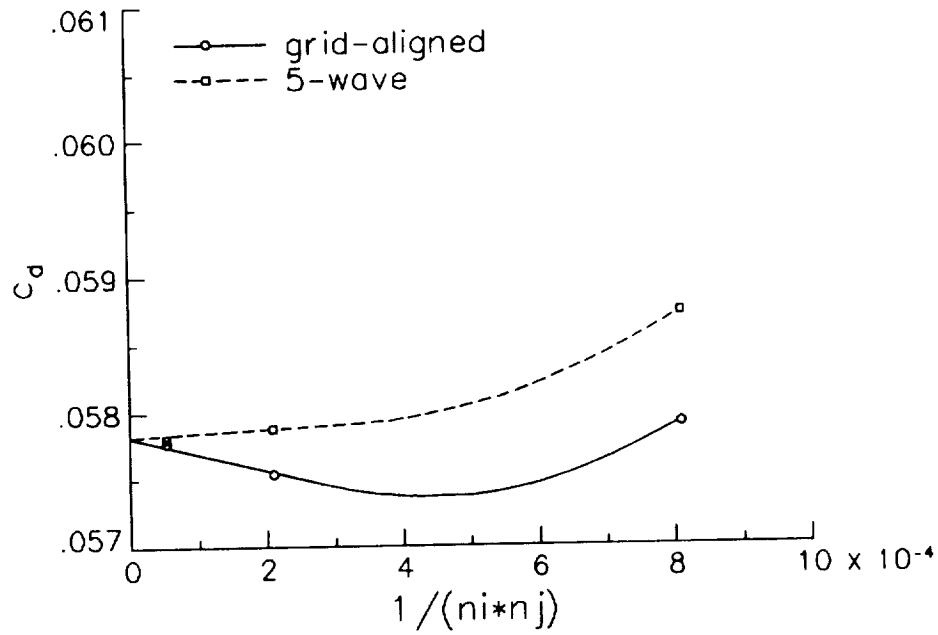
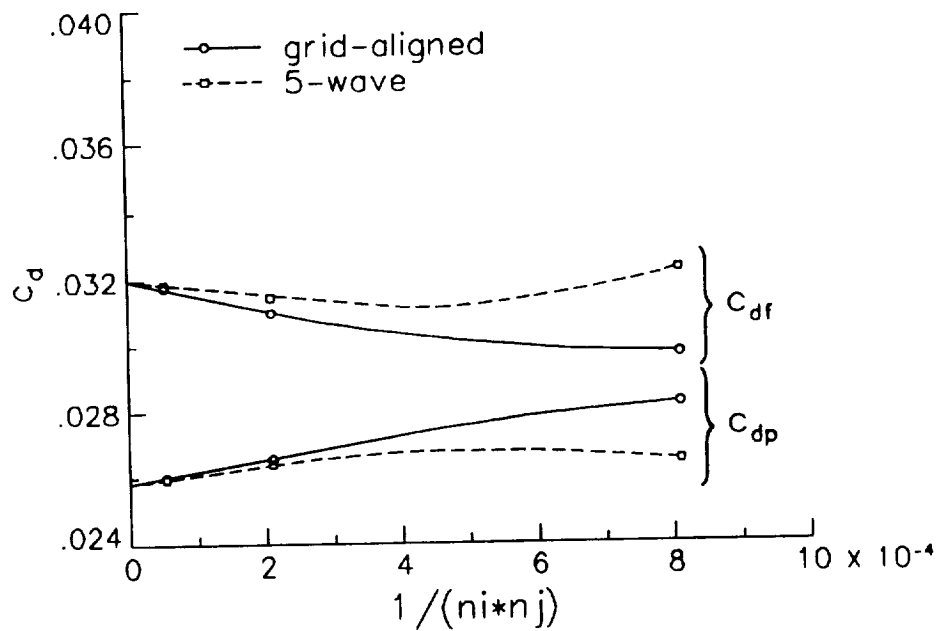


Figure 8.58: Viscous Airfoil-Flow, Surface Pressure Coefficients, 65×25



a) Total Drag Coefficient



b) Friction and Pressure Drag Coefficients

Figure 8.59: Drag-Coefficient Grid-Convergence Study for Viscous Airfoil-Flow

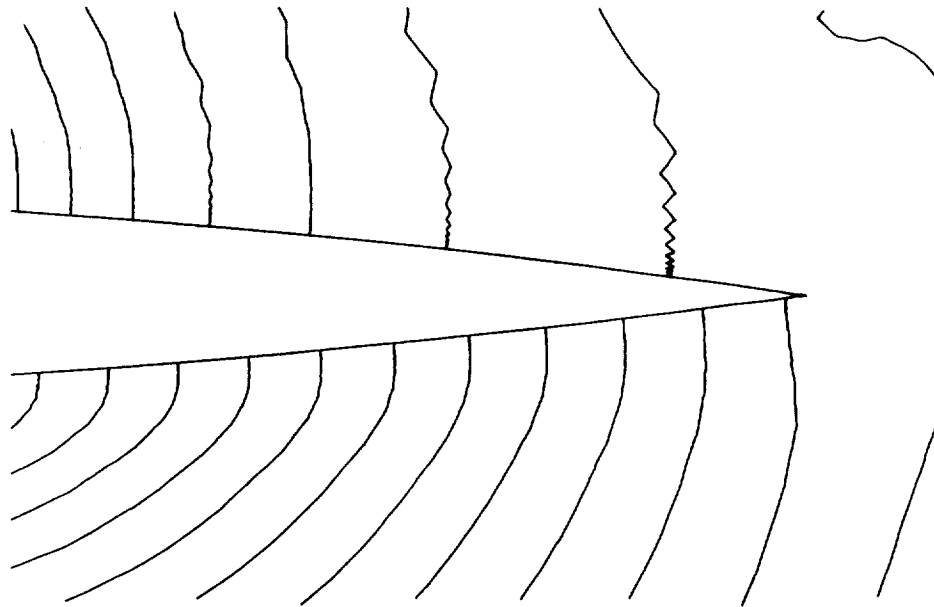


Figure 8.60: Viscous Airfoil-Flow, Pressure Contours, 5-Wave (θ'_d -Unlimited), 129×49

model have employed θ'_d -limiting. When θ'_d -limiting is *not* employed, the odd-even point decoupling mentioned in Chapter 7 can occur in the boundary layer. An example is shown in figure 8.60. Pressure contours over the rear half of the airfoil are shown for computations on a 129×49 grid. Several of the contours show the oscillatory behavior.

CHAPTER 9

EXTENSION TO THREE DIMENSIONS

9.1 Governing Equations

The nondimensional Navier-Stokes equations in curvilinear coordinates and conservation form can be written in three dimensions as:

$$\frac{\partial \mathbf{U}^*}{\partial t} + \frac{\partial \mathbf{F}^*}{\partial \xi} + \frac{\partial \mathbf{G}^*}{\partial \eta} + \frac{\partial \mathbf{H}^*}{\partial \zeta} = \frac{\partial \mathbf{F}_v^*}{\partial \xi} + \frac{\partial \mathbf{G}_v^*}{\partial \eta} + \frac{\partial \mathbf{H}_v^*}{\partial \zeta}, \quad (9.1)$$

where

$$\mathbf{U}^* = \frac{1}{J} \begin{bmatrix} \rho \\ \rho u \\ \rho v \\ \rho w \\ \rho E \end{bmatrix} \quad (9.2)$$

$$\mathbf{F}^* = \frac{1}{J} \begin{bmatrix} \rho u^* \\ \rho u^* u + \xi_x p \\ \rho u^* v + \xi_y p \\ \rho u^* w + \xi_z p \\ \rho u^* H \end{bmatrix} \quad (9.3)$$

$$\mathbf{G}^* = \frac{1}{J} \begin{bmatrix} \rho v^* \\ \rho v^* u + \eta_x p \\ \rho v^* v + \eta_y p \\ \rho v^* w + \eta_z p \\ \rho v^* H \end{bmatrix} \quad (9.4)$$

$$\mathbf{H}^* = \frac{1}{J} \begin{bmatrix} \rho w^* \\ \rho w^* u + \zeta_x p \\ \rho w^* v + \zeta_y p \\ \rho w^* w + \zeta_z p \\ \rho w^* H \end{bmatrix} \quad (9.5)$$

$$\mathbf{F}_v^* = \frac{1}{J} \begin{bmatrix} 0 \\ \xi_x \tau_{11} + \xi_y \tau_{12} + \xi_z \tau_{13} \\ \xi_x \tau_{21} + \xi_y \tau_{22} + \xi_z \tau_{23} \\ \xi_x \tau_{31} + \xi_y \tau_{32} + \xi_z \tau_{33} \\ \xi_x (V_j \tau_{1j} - \dot{Q}_1) + \xi_y (V_j \tau_{2j} - \dot{Q}_2) + \xi_z (V_j \tau_{3j} - \dot{Q}_3) \end{bmatrix} \quad (9.6)$$

$$\mathbf{G}_v^* = \frac{1}{J} \begin{bmatrix} 0 \\ \eta_x \tau_{11} + \eta_y \tau_{12} + \eta_z \tau_{13} \\ \eta_x \tau_{21} + \eta_y \tau_{22} + \eta_z \tau_{23} \\ \eta_x \tau_{31} + \eta_y \tau_{32} + \eta_z \tau_{33} \\ \eta_x (V_j \tau_{1j} - \dot{Q}_1) + \eta_y (V_j \tau_{2j} - \dot{Q}_2) + \eta_z (V_j \tau_{3j} - \dot{Q}_3) \end{bmatrix} \quad (9.7)$$

$$\mathbf{H}_v^* = \frac{1}{J} \begin{bmatrix} 0 \\ \zeta_x \tau_{11} + \zeta_y \tau_{12} + \zeta_z \tau_{13} \\ \zeta_x \tau_{21} + \zeta_y \tau_{22} + \zeta_z \tau_{23} \\ \zeta_x \tau_{31} + \zeta_y \tau_{32} + \zeta_z \tau_{33} \\ \zeta_x (V_j \tau_{1j} - \dot{Q}_1) + \zeta_y (V_j \tau_{2j} - \dot{Q}_2) + \zeta_z (V_j \tau_{3j} - \dot{Q}_3) \end{bmatrix} \quad (9.8)$$

$$\begin{aligned} u^* &= \xi_x u + \xi_y v + \xi_z w \\ v^* &= \eta_x u + \eta_y v + \eta_z w \\ w^* &= \zeta_x u + \zeta_y v + \zeta_z w. \end{aligned} \quad (9.9)$$

All variables are nondimensional as defined in Chapter 2. The terms u^* , v^* , and w^* are the contravariant velocity components, and V_1 , V_2 , and V_3 represent u , v , and w , respectively. τ_{ij} and \dot{Q}_i are given by (2.14) and (2.15), but now

$$\begin{aligned} \frac{\partial}{\partial X_1} &= \xi_x \frac{\partial}{\partial \xi} + \eta_x \frac{\partial}{\partial \eta} + \zeta_x \frac{\partial}{\partial \zeta} \\ \frac{\partial}{\partial X_2} &= \xi_y \frac{\partial}{\partial \xi} + \eta_y \frac{\partial}{\partial \eta} + \zeta_y \frac{\partial}{\partial \zeta} \\ \frac{\partial}{\partial X_3} &= \xi_z \frac{\partial}{\partial \xi} + \eta_z \frac{\partial}{\partial \eta} + \zeta_z \frac{\partial}{\partial \zeta}. \end{aligned} \quad (9.10)$$

The ideal gas equation of state is given by

$$p = (\gamma - 1)\rho \left(E - \frac{u^2 + v^2 + w^2}{2} \right). \quad (9.11)$$

Also, Stokes' hypothesis, $\lambda + (2/3)\mu = 0$, and Sutherland's law (2.34) are assumed to apply, and γ is taken as 1.4 and Pr is taken as 0.72.

In three dimensions, the inverse of the metric Jacobian J is given by:

$$J^{-1} = x_\xi(y_\eta z_\zeta - y_\zeta z_\eta) - y_\xi(x_\eta z_\zeta - x_\zeta z_\eta) + z_\xi(x_\eta y_\zeta - x_\zeta y_\eta), \quad (9.12)$$

and the metrics of the transformation are

$$\begin{aligned} \xi_x &= J(y_\eta z_\zeta - y_\zeta z_\eta) & \xi_y &= J(z_\eta x_\zeta - z_\zeta x_\eta) & \xi_z &= J(x_\eta y_\zeta - x_\zeta y_\eta) \\ \eta_x &= J(y_\zeta z_\xi - y_\xi z_\zeta) & \eta_y &= J(z_\zeta x_\xi - z_\xi x_\zeta) & \eta_z &= J(x_\zeta y_\xi - x_\xi y_\zeta) \\ \zeta_x &= J(y_\xi z_\eta - y_\eta z_\xi) & \zeta_y &= J(z_\xi x_\eta - z_\eta x_\xi) & \zeta_z &= J(x_\xi y_\eta - x_\eta y_\xi). \end{aligned} \quad (9.13)$$

The Euler equations are the same as the Navier-Stokes equations (9.1), except that the viscous terms \mathbf{F}_v^* , \mathbf{G}_v^* , and \mathbf{H}_v^* are taken as zero.

9.2 Spatial and Temporal Discretization

Since only Euler computations are performed in three dimensions in this study, the discretizations described here will not include viscous terms. The basic scheme employed is CFL3D [32]. It is an implicit finite-volume method, in which the left-hand side is approximately factored and $\Delta_t \mathbf{U}^{(n)}$ is solved for in three sweeps through the mesh:

$$\begin{aligned} \left[\frac{\mathbf{I}}{J\Delta t} + \delta_\xi \frac{\partial \mathbf{F}^*}{\partial \mathbf{U}} \right] \Delta_t \mathbf{U}' &= \mathbf{T} \\ \left[\frac{\mathbf{I}}{J\Delta t} + \delta_\eta \frac{\partial \mathbf{G}^*}{\partial \mathbf{U}} \right] \Delta_t \mathbf{U}'' &= \frac{\mathbf{I}}{J\Delta t} \Delta_t \mathbf{U}' \\ \left[\frac{\mathbf{I}}{J\Delta t} + \delta_\zeta \frac{\partial \mathbf{H}^*}{\partial \mathbf{U}} \right] \Delta_t \mathbf{U}^{(n)} &= \frac{\mathbf{I}}{J\Delta t} \Delta_t \mathbf{U}'', \end{aligned} \quad (9.14)$$

where the terms $\Delta_t \mathbf{U}'$ and $\Delta_t \mathbf{U}''$ are intermediate results. The conserved variables are updated at the cell centers using

$$\mathbf{U}^{(n+1)} = \mathbf{U}^{(n)} + \Delta_t \mathbf{U}^{(n)}. \quad (9.15)$$

The right-hand side \mathbf{T} in (9.14) is defined by

$$\mathbf{T} \equiv - \left(\delta_{\xi} \mathbf{F}^* + \delta_{\eta} \mathbf{G}^* + \delta_{\zeta} \mathbf{H}^* \right), \quad (9.16)$$

and

$$\begin{aligned} \delta_{\xi} \mathbf{F}^* &= \mathbf{F}^*_{i+\frac{1}{2},j,k} - \mathbf{F}^*_{i-\frac{1}{2},j,k} \\ \delta_{\eta} \mathbf{G}^* &= \mathbf{G}^*_{i,j+\frac{1}{2},k} - \mathbf{G}^*_{i,j-\frac{1}{2},k} \\ \delta_{\zeta} \mathbf{H}^* &= \mathbf{H}^*_{i,j,k+\frac{1}{2}} - \mathbf{H}^*_{i,j,k-\frac{1}{2}}. \end{aligned} \quad (9.17)$$

The right-hand side terms in (9.17) are the fluxes at the six faces of a computational cell, evaluated through the use of a flux function, as described in sections 9.3 and 9.4. The right-hand side \mathbf{T} can also be written in the form

$$\mathbf{T} \equiv - \sum_{\ell=1}^6 \Phi_{\ell} \Delta A_{\ell}, \quad (9.18)$$

where the summation is over the six faces of the computational cell, ΔA_{ℓ} is the area of cell face ℓ , and Φ is the normal flux per unit face-area, given by:

$$\Phi = \begin{bmatrix} \rho q_g \\ \rho q_g u + p(c_x)_g \\ \rho q_g v + p(c_y)_g \\ \rho q_g w + p(c_z)_g \\ \rho q_g H \end{bmatrix}. \quad (9.19)$$

The variables c_x , c_y , and c_z represent the components of the unit-normal direction vector \vec{n} in the x , y , and z directions, respectively. They are written in spherical coordinates as:

$$\begin{aligned} c_x &\equiv \cos\theta \cos\psi \\ c_y &\equiv \sin\theta \cos\psi \\ c_z &\equiv \sin\psi. \end{aligned} \quad (9.20)$$

The subscript g is used to indicate the grid-face normal angle. For example, $(c_x)_g = \cos\theta_g \cos\psi_g$. The angles θ_g , ψ_g and the grid-face normal direction vector \vec{n}_g are pictured in figure 9.1. The variable q_g is the outward velocity normal to the cell face, given by

$$q_g = u(c_x)_g + v(c_y)_g + w(c_z)_g. \quad (9.21)$$

The implicit spatial derivatives of the convective and pressure terms are spatially first-order accurate, resulting in block-tridiagonal inversions for each sweep. Approximate left-hand side Jacobians of the form given in Chapter 3 are employed regardless of whether the grid-aligned or the grid-independent model is employed on the right-hand side.

9.3 Grid-Aligned Flux Function

The normal flux per unit face-area in three dimensions can be computed using the grid-aligned flux function:

$$\Phi = \frac{1}{2}(\Phi_L + \Phi_R) - \frac{1}{2} \sum_{k=1}^4 |\hat{\lambda}_k| \hat{\Omega}_k \hat{\mathbf{R}}_k, \quad (9.22)$$

where the waves are represented by the vectors

$$\hat{\mathbf{R}}_1 = \begin{bmatrix} 1 \\ \hat{u} + \hat{a}(c_x)_g \\ \hat{v} + \hat{a}(c_y)_g \\ \hat{w} + \hat{a}(c_z)_g \\ \hat{H} + \hat{a}\hat{q}_g \end{bmatrix} \quad (9.23)$$

$$\hat{\mathbf{R}}_2 = \begin{bmatrix} 1 \\ \hat{u} - \hat{a}(c_x)_g \\ \hat{v} - \hat{a}(c_y)_g \\ \hat{w} - \hat{a}(c_z)_g \\ \hat{H} - \hat{a}\hat{q}_g \end{bmatrix} \quad (9.24)$$

$$\hat{\mathbf{R}}_3 = \begin{bmatrix} 0 \\ -\hat{a}(\Delta r_1)_g \\ -\hat{a}(\Delta r_2)_g \\ -\hat{a}(\Delta r_3)_g \\ -\hat{a}\{\hat{u}(\Delta r_1)_g + \hat{v}(\Delta r_2)_g + \hat{w}(\Delta r_3)_g\} \end{bmatrix} \quad (9.25)$$

$$\hat{\mathbf{R}}_4 = \begin{bmatrix} 1 \\ \hat{u} \\ \hat{v} \\ \hat{w} \\ \frac{1}{2}(\hat{u}^2 + \hat{v}^2 + \hat{w}^2) \end{bmatrix}. \quad (9.26)$$

The terms Δr_1 , Δr_2 , and Δr_3 are given by

$$\begin{aligned}\Delta r_1 &\equiv ((c_x)^2 - 1)\Delta u + (c_x)(c_y)\Delta v + (c_x)(c_z)\Delta w \\ \Delta r_2 &\equiv (c_y)(c_x)\Delta u + ((c_y)^2 - 1)\Delta v + (c_y)(c_z)\Delta w \\ \Delta r_3 &\equiv (c_z)(c_x)\Delta u + (c_z)(c_y)\Delta v + ((c_z)^2 - 1)\Delta w\end{aligned}\tag{9.27}$$

and the subscript g indicates that the components $((c_x)_g, (c_y)_g, (c_z)_g)$ of the grid-normal direction \vec{n}_g are used. The Roe-averaged outward velocity normal to the cell face is

$$\hat{q}_g \equiv \hat{u}(c_x)_g + \hat{v}(c_y)_g + \hat{w}(c_z)_g.\tag{9.28}$$

The vectors (9.23) through (9.26) represent, respectively, + acoustic, - acoustic, shear, and entropy waves. $\hat{\mathbf{R}}_1$, $\hat{\mathbf{R}}_2$, and $\hat{\mathbf{R}}_4$ are eigenvectors of the linearized three-dimensional Euler equations, while $\hat{\mathbf{R}}_3$ is a linear combination of the remaining *two* eigenvectors, which, along with $\hat{\mathbf{R}}_1$, $\hat{\mathbf{R}}_2$, and $\hat{\mathbf{R}}_4$, span the eigenspace of this system. The expression for the combined shear wave $\hat{\mathbf{R}}_3$ is derived in Appendix B, and a geometric interpretation of its effects in state space is given below.

The vector of wavestrengths is given by:

$$\hat{\mathbf{\Omega}} = \begin{bmatrix} \frac{1}{2\hat{q}^2} (\Delta p + \hat{\rho}\hat{a}\Delta q_g) \\ \frac{1}{2\hat{a}^2} (\Delta p - \hat{\rho}\hat{a}\Delta q_g) \\ \frac{\hat{\rho}}{\hat{a}} \\ \frac{1}{\hat{a}^2} (\hat{a}^2\Delta\rho - \Delta p) \end{bmatrix},\tag{9.29}$$

where

$$\Delta q_g \equiv \Delta u(c_x)_g + \Delta v(c_y)_g + \Delta w(c_z)_g.\tag{9.30}$$

The wavespeeds are all in the \vec{n}_g -direction and are given by:

$$\begin{aligned}\hat{\lambda}_1 &= \hat{q}_g + \hat{a} \\ \hat{\lambda}_2 &= \hat{q}_g - \hat{a} \\ \hat{\lambda}_3 &= \hat{q}_g \\ \hat{\lambda}_4 &= \hat{q}_g.\end{aligned}\tag{9.31}$$

The Roe-averaged (hatted) values are still defined by (4.9).

In three dimensions, the $(\Delta u, \Delta v, \Delta p)$ -space interpretation of the wave decomposition is not as helpful as it was in two dimensions, since the jump Δw is now important. Instead, when describing the action of the three-dimensional waves, the Δp -“direction” is ignored, and jumps are plotted in $(\Delta u, \Delta v, \Delta w)$ -space. Hence the change in pressure caused by an acoustic wave cannot be represented.

Figure 9.2(a) shows the change in velocity associated with a $+\vec{n}_g$ acoustic wave, while figure 9.2(b) shows the change for a $-\vec{n}_g$ acoustic wave. Each of these waves also causes a positive change in pressure and a change in density, which are not pictured. Similar to the two-dimensional case, the entropy wave causes only a change in density (with no change in velocity or pressure), so it is not representable at all in $(\Delta u, \Delta v, \Delta w)$ -space. Finally, there are two independent eigenvectors, as discussed in Appendix B, which represent shear in the plane perpendicular to the \vec{n}_g -direction. Any two eigenvectors in this plane are independent provided that the directions of the corresponding velocity jumps are perpendicular. An example of two such waves is given in figure 9.3. These waves propagate in the \vec{n}_g -direction, which is normal to the change in velocity across both of the waves.

The two shear waves can be replaced by the single shear wave (9.25) with strength $\hat{\rho}/\hat{a}$. Its net result is the sum of the velocity changes across the other two. This single shear is, in effect, the wave that causes a change in states from R to R', where R' is the point in $(\Delta u, \Delta v, \Delta w)$ -space on the line from L with direction \vec{n}_g where the perpendicular line from R intersects. This is illustrated in figure 9.4, along with hypothetical + and - acoustic waves.

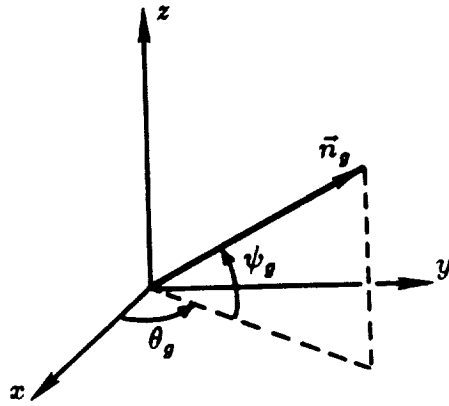
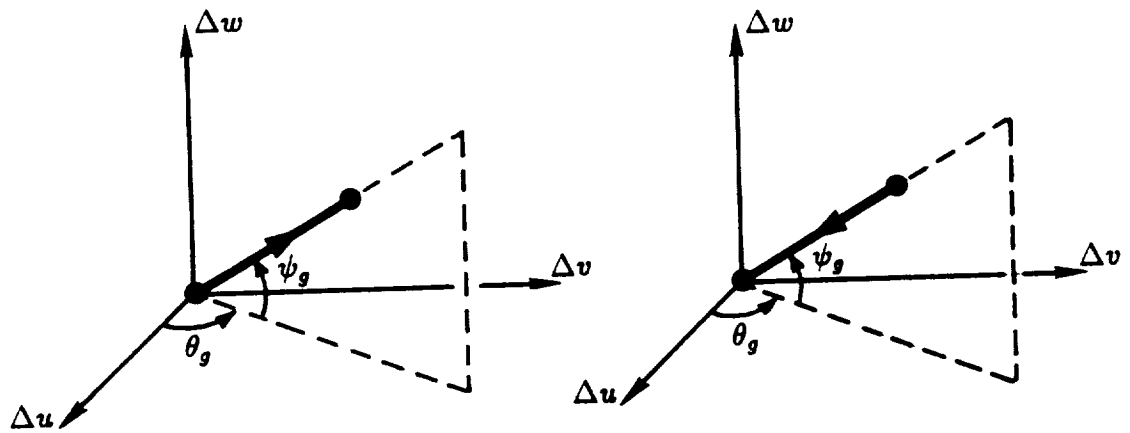


Figure 9.1: Grid Face Normal Angles



a) + Acoustic

b) - Acoustic

Figure 9.2: Effect of Acoustic Waves

9.4 Grid-Independent Flux Function

The dominant direction of wave propagation for the grid-independent wave model is again assumed to be the velocity-difference direction. For three-dimensional flow, this direction is given by \vec{n}_d , defined by the angles (θ_d, ψ_d) , which are obtained using:

$$\begin{aligned}\theta_d &= \tan^{-1}\left(\frac{\Delta v}{\Delta u}\right) \\ \psi_d &= \tan^{-1}\left(\frac{\Delta w * \text{sign}(\Delta u)}{\sqrt{\Delta u^2 + \Delta v^2}}\right).\end{aligned}\tag{9.32}$$

The angles are each defined from $-\frac{\pi}{2}$ to $\frac{\pi}{2}$.

As in the two-dimensional grid-independent model, the wave types and strengths for the three-dimensional model describe the difference between the left and right states. The wave-propagation direction can be frozen as \vec{n}'_d (defined by the angles (θ'_d, ψ'_d)), resulting in the requirement of a shear wave of type similar to the shear wave used in the grid-aligned model. The end result is, again, a 5-wave model, which is computed using:

$$\Phi = \frac{1}{2}(\Phi_L + \Phi_R) - \frac{1}{2} \sum_{k=1}^5 |\hat{\lambda}_k| \hat{\Omega}_k \hat{\mathbf{R}}_k.\tag{9.33}$$

The $\hat{\mathbf{R}}_k$ are given by

$$\hat{\mathbf{R}}_1 = \begin{bmatrix} 1 \\ \hat{u} + \hat{a}(c_x)'_d \\ \hat{v} + \hat{a}(c_y)'_d \\ \hat{w} + \hat{a}(c_z)'_d \\ \hat{H} + \hat{a}\hat{q}'_d \end{bmatrix}\tag{9.34}$$

$$\hat{\mathbf{R}}_2 = \begin{bmatrix} 1 \\ \hat{u} - \hat{a}(c_x)'_d \\ \hat{v} - \hat{a}(c_y)'_d \\ \hat{w} - \hat{a}(c_z)'_d \\ \hat{H} - \hat{a}\hat{q}'_d \end{bmatrix}\tag{9.35}$$

$$\hat{\mathbf{R}}_3 = \begin{bmatrix} 0 \\ -\hat{a}(c_x)'_d \\ -\hat{a}(c_y)'_d \\ -\hat{a}(c_z)'_d \\ -\hat{a}\hat{q}'_d \end{bmatrix} \quad (9.36)$$

$$\hat{\mathbf{R}}_4 = \begin{bmatrix} 1 \\ \hat{u} \\ \hat{v} \\ \hat{w} \\ \frac{1}{2}(\hat{u}^2 + \hat{v}^2 + \hat{w}^2) \end{bmatrix} \quad (9.37)$$

$$\hat{\mathbf{R}}_5 = \begin{bmatrix} 0 \\ -\hat{a}(\Delta r_1)'_d \\ -\hat{a}(\Delta r_2)'_d \\ -\hat{a}(\Delta r_3)'_d \\ -\hat{a}\{\hat{u}(\Delta r_1)'_d + \hat{v}(\Delta r_2)'_d + \hat{w}(\Delta r_3)'_d\} \end{bmatrix} \quad (9.38)$$

where

$$\hat{q}'_d \equiv \hat{u}(c_x)'_d + \hat{v}(c_y)'_d + \hat{w}(c_z)'_d. \quad (9.39)$$

The parameters c_x , c_y , c_z , and Δr_1 , Δr_2 , Δr_3 are still defined by (9.20) and (9.27). The subscript d and the prime ($'$) indicate the frozen direction \vec{n}'_d . For example, $(c_x)'_d = \cos\theta'_d \cos\psi'_d$.

The vector of wavenumbers is given by:

$$\hat{\mathbf{\Omega}} = \begin{bmatrix} \frac{\Delta p}{2\hat{a}^2} + \frac{\beta\hat{p}}{2\hat{a}}(\Delta u(c_x)'_d + \Delta v(c_y)'_d + \Delta w(c_z)'_d) \\ \frac{\Delta p}{2\hat{a}^2} - \frac{\beta\hat{p}}{2\hat{a}}(\Delta u(c_x)'_d + \Delta v(c_y)'_d + \Delta w(c_z)'_d) \\ (\beta - 1)\frac{\hat{p}}{\hat{a}}(\Delta u(c_x)'_d + \Delta v(c_y)'_d + \Delta w(c_z)'_d) \\ \frac{1}{\hat{a}^2}(\hat{a}^2\Delta\rho - \Delta p) \\ \frac{\hat{p}}{\hat{a}} \end{bmatrix}. \quad (9.40)$$

The parameter β is similar in form to that derived in two dimensions. For the minimum-pathlength model,

$$\beta = \min \left[\left| \frac{\Delta p / (\hat{p}\hat{a})}{\Delta u(c_x)'_d + \Delta v(c_y)'_d + \Delta w(c_z)'_d} \right|, 1 \right]. \quad (9.41)$$

The minimum-area model, used for all computations in this study, results when

$$\beta = \min \left[\left\{ \frac{\Delta p / (\hat{p}\hat{a})}{\Delta u(c_x)'_d + \Delta v(c_y)'_d + \Delta w(c_z)'_d} \right\}^2, 1 \right]. \quad (9.42)$$

The parameter β is generally limited to be no less than 0.05 and is frozen along with \vec{n}'_d as an aid to convergence.

The effects of the acoustic waves $\hat{\mathbf{R}}_1$ and $\hat{\mathbf{R}}_2$ as well as the shear wave $\hat{\mathbf{R}}_3$ can be plotted in $(\Delta u, \Delta v, \Delta w)$ -space. Plots look the same as the grid-aligned wave plots (figures 9.2(a), 9.2(b), and 9.4) except that the angles are now given by θ'_d and ψ'_d . The shear wave $\hat{\mathbf{R}}_3$ is henceforward referred to as the $(\vec{n}'_d + \frac{\pi}{2})$ shear wave, in order to parallel the $(\theta'_d + \frac{\pi}{2})$ shear wave from the two-dimensional theory of Chapter 5. It causes a change of velocity in the \vec{n}'_d -direction, as pictured in figure 9.5. Therefore the direction of propagation of the wave itself must be 90° to this. Unlike the two-dimensional case, however, in three dimensions there are an infinite number of directions perpendicular to the \vec{n}'_d -direction. This is tantamount to saying that the difference in velocity between two states L and R (with no pressure difference) can be attributed to an infinite number of shear wave types, each of which travels in a different direction perpendicular to \vec{n}'_d .

An illustration of this concept is given in figures 9.6(a) through (e). For this example a first-order computation is assumed, where two neighboring cells have velocities $\vec{V}_L = (1,0,0)$, $\vec{V}_R = (1,1,0)$. Also, the \vec{n}_d -direction is assumed to be computed from these velocity values (*i.e.* they are not frozen from an earlier time step). Figure 9.6(a) shows the geometry, including the velocity-difference vector $\Delta\vec{V}$ which indicates the direction \vec{n}_d . One type of shear wave that could describe this difference in states is a "layer-type" shear, as pictured in figure 9.6(b). Across this shear plane the velocity vector both rotates and lengthens. There is no velocity component normal to the "layer-type" shear wave, so it is steady with drift velocity $\bar{u}_S = 0$.

Other interpretations of the velocity difference are shown in figures 9.6(c) through (e). In each of these, the shear wave *does* have a drift velocity \bar{u}_S . This drift velocity is always normal to the \vec{n}_d -direction. It is a maximum in figure

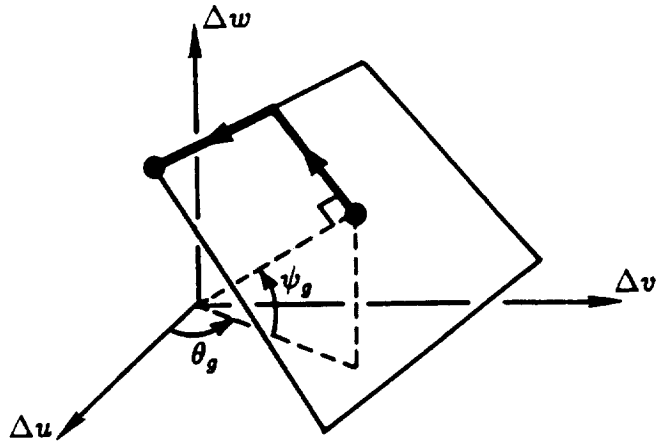


Figure 9.3: Effect of Two Perpendicular Shear Waves

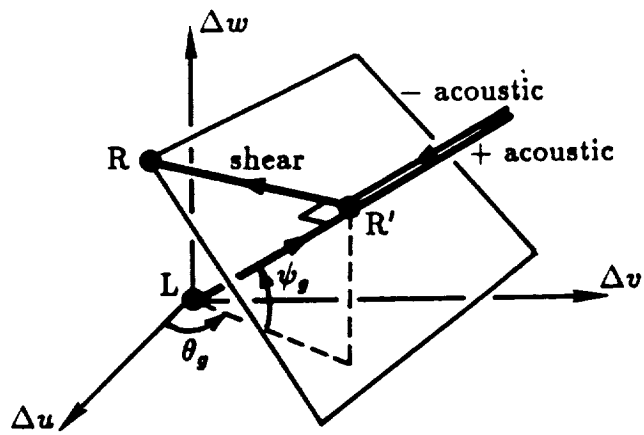


Figure 9.4: Wave Decomposition, Including Combined Shear Wave

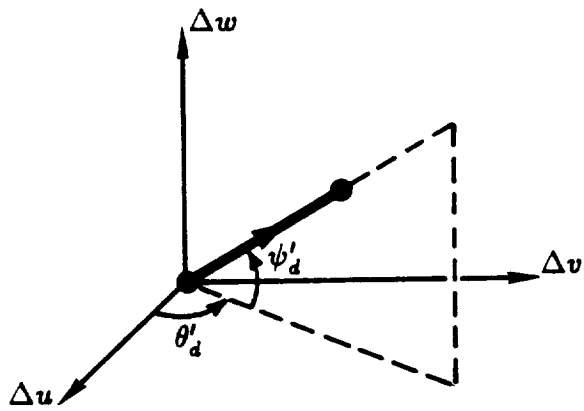
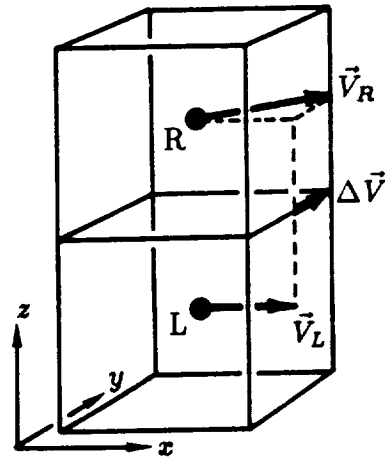
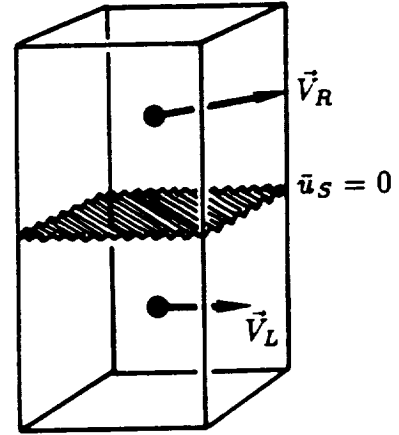


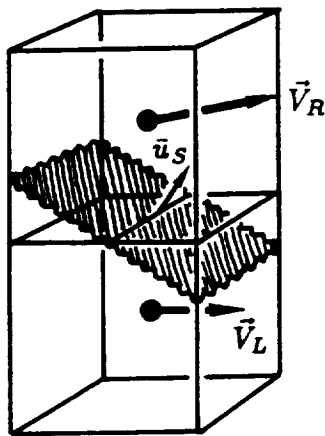
Figure 9.5: Effect of $(\vec{n}'_d + \frac{\pi}{2})$ Shear Wave



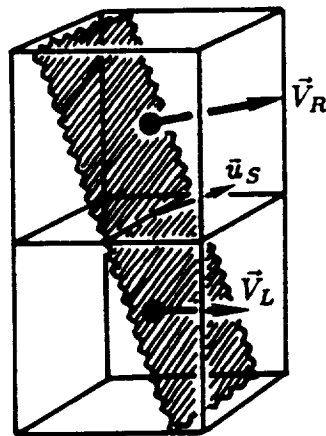
a) Geometry



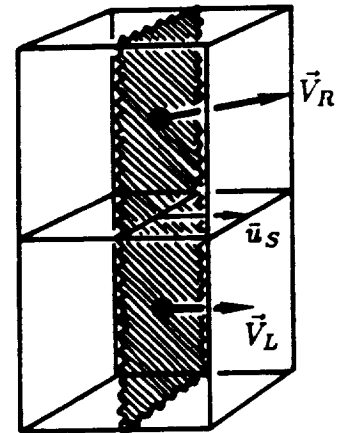
b) "Layer-Type" Shear



c) Increasing \bar{u}_s



d) Increasing \bar{u}_s



e) "2-D-Type" Shear

Figure 9.6: Illustration of Possible Shear Wave Interpretations

9.6(e), for the case of the “2-D-type” shear wave. It is termed “2-D” because the drift velocity is parallel to the plane defined by the velocity vectors \vec{V}_L and \vec{V}_R (with origins of the vectors at the same point). Across a “2-D-type” shear wave the velocity vector lengthens, but there is no rotation. It should also be noted that although the wave passes through both points L and R in figure 9.6(e), it is assumed that L lies infinitesimally to one side of the wave and R to the other.

The initial strategy used to determine the direction of propagation of the $(\vec{n}'_d + \frac{\pi}{2})$ shear wave involved the grid geometry. The distance vector \vec{D}_g , which connects the cell centers of the neighboring states L and R (see figure 9.7), would be compared to the plane defined by the velocity vectors. If \vec{D}_g was at right angles to the velocity plane, then a “layer-type” shear would be assumed. This corresponds exactly to the situation pictured in figure 9.6(b). If \vec{D}_g lay parallel to the velocity plane, then a “2-D-type” shear would be assumed. Anything else would fall somewhere between the two types of shear. An easy method of implementation would be to find the normalized projection of \vec{D}_g onto the plane which is perpendicular to the direction vector \vec{n}'_d . This direction would then be taken as the direction of shear wave propagation. The shear wave drift velocity would simply be the component of $(\hat{u}, \hat{v}, \hat{w})$ taken in this direction.

However, this strategy has two undesirable properties. First of all, it brings grid-dependency back into the solution. Second, and most importantly, it does not allow for sharp capturing of steady three-dimensional oblique shear waves through which the velocity undergoes rotation. For example, the steady-state type of shear shown in figure 9.7 is *not* interpreted by this model as pictured; instead, the difference in states is construed to be due to a different shear wave with non-zero drift velocity. This misinterpretation adds dissipation to the computed solution and smears the final steady-state result.

The best propagation direction for the $(\vec{n}'_d + \frac{\pi}{2})$ shear wave seems to be the

one that yields the lowest dissipation. This is given by the “layer-type” shear wave interpretation, which always has drift velocity $\bar{u}_S = 0$ when \vec{n}_d is computed every time step. When the direction \vec{n}_d is frozen, the drift velocity is no longer necessarily zero, but it is generally very small. The unit normal direction vector is computed as the direction perpendicular to both \vec{V}_L and \vec{V}_R using the following formulas:

$$\begin{aligned} a &= v_L w_R - w_L v_R \\ b &= w_L u_R - u_L w_R \\ c &= u_L v_R - v_L u_R \\ d &= \sqrt{a^2 + b^2 + c^2}. \end{aligned} \tag{9.43}$$

Then, if $d \neq 0$,

$$((c_x)_S, (c_y)_S, (c_z)_S) = \left(\frac{a}{d}, \frac{b}{d}, \frac{c}{d} \right). \tag{9.44}$$

If $d = 0$ the arbitrary unit-normal direction (which is perpendicular to the \vec{n}'_d -direction) is chosen:

$$((c_x)_S, (c_y)_S, (c_z)_S) = (-\cos\theta_d \sin\psi_d, -\sin\theta_d \sin\psi_d, \cos\psi_d). \tag{9.45}$$

The drift velocity of the shear is then computed as the component of $(\hat{u}, \hat{v}, \hat{w})$ in the $((c_x)_S, (c_y)_S, (c_z)_S)$ -direction:

$$\bar{u}_S = \hat{u}(c_x)_S + \hat{v}(c_y)_S + \hat{w}(c_z)_S. \tag{9.46}$$

Again, if the \vec{n}_d -direction is not frozen, then $((c_x)_S, (c_y)_S, (c_z)_S)$ is computed from the same \vec{V}_L, \vec{V}_R that formed $(\hat{u}, \hat{v}, \hat{w})$, and \bar{u}_S turns out to be identically zero. However, if the \vec{n}'_d -direction is frozen from a previous iteration, then $((c_x)_S, (c_y)_S, (c_z)_S)$ is frozen as $((c_x)'_S, (c_y)'_S, (c_z)'_S)$ and $\bar{u}'_S = \hat{u}(c_x)'_S + \hat{v}(c_y)'_S + \hat{w}(c_z)'_S$ may have a finite value.

Finally, the components of the wavespeeds of all five waves in the grid-normal

direction are written:

$$\begin{aligned}
\hat{\lambda}_1 &= (\hat{q}'_d + \hat{a}) \{ (c_x)'_d(c_x)_g + (c_y)'_d(c_y)_g + (c_z)'_d(c_z)_g \} \\
\hat{\lambda}_2 &= (\hat{q}'_d - \hat{a}) \{ (c_x)'_d(c_x)_g + (c_y)'_d(c_y)_g + (c_z)'_d(c_z)_g \} \\
\hat{\lambda}_3 &= \bar{u}'_S \{ (c_x)'_S(c_x)_g + (c_y)'_S(c_y)_g + (c_z)'_S(c_z)_g \} \\
\hat{\lambda}_4 &= \hat{q}'_d \{ (c_x)'_d(c_x)_g + (c_y)'_d(c_y)_g + (c_z)'_d(c_z)_g \} \\
\hat{\lambda}_5 &= \hat{q}'_d \{ (c_x)'_d(c_x)_g + (c_y)'_d(c_y)_g + (c_z)'_d(c_z)_g \}.
\end{aligned} \tag{9.47}$$

9.5 Stability Analysis

Following similar linearization procedures as for two dimensions, as well as making the assumption that all cells are cubes with edge length Δs , the three-dimensional Euler equations can be written as

$$\Delta t \frac{\partial \mathbf{U}}{\partial t} = -\mathbf{L}\mathbf{U}, \tag{9.48}$$

where \mathbf{L} is a matrix of difference operators. For first-order spatial differencing, the Fourier transform of the right-hand side turns out to be:

$$\begin{aligned}
\mathfrak{S}(-\mathbf{L}) &= - \frac{\nu}{\{\omega(\vec{n}_g^{(i)}) + \omega(\vec{n}_g^{(j)}) + \omega(\vec{n}_g^{(k)})\}} \left[\left| \hat{\mathbf{D}}(\vec{n}_g^{(i)}) \right| (1 - \cos\zeta^{(i)}) + \right. \\
&\quad i \left(\frac{\partial \hat{\Phi}}{\partial \mathbf{U}}(\vec{n}_g^{(i)}) \right) \sin\zeta^{(i)} + \left| \hat{\mathbf{D}}(\vec{n}_g^{(j)}) \right| (1 - \cos\zeta^{(j)}) + \\
&\quad i \left(\frac{\partial \hat{\Phi}}{\partial \mathbf{U}}(\vec{n}_g^{(j)}) \right) \sin\zeta^{(j)} + \left| \hat{\mathbf{D}}(\vec{n}_g^{(k)}) \right| (1 - \cos\zeta^{(k)}) + \\
&\quad \left. i \left(\frac{\partial \hat{\Phi}}{\partial \mathbf{U}}(\vec{n}_g^{(k)}) \right) \sin\zeta^{(k)} \right].
\end{aligned} \tag{9.49}$$

For second-order differencing it is:

$$\begin{aligned}
\Im(-\mathbf{L}) = & -\frac{\nu}{\{\omega(\vec{n}_g^{(i)}) + \omega(\vec{n}_g^{(j)}) + \omega(\vec{n}_g^{(k)})\}} \left[\left| \hat{\mathbf{D}}(\vec{n}_g^{(i)}) \right| \left(-2\cos\zeta^{(i)} + \right. \right. \\
& \left. \left. \frac{1}{2}\cos 2\zeta^{(i)} + \frac{3}{2} \right) + i \left(\frac{\partial \hat{\Phi}}{\partial \mathbf{U}}(\vec{n}_g^{(i)}) \right) \left(2\sin\zeta^{(i)} - \frac{1}{2}\sin 2\zeta^{(i)} \right) + \right. \\
& \left| \hat{\mathbf{D}}(\vec{n}_g^{(j)}) \right| \left(-2\cos\zeta^{(j)} + \frac{1}{2}\cos 2\zeta^{(j)} + \right. \\
& \left. \frac{3}{2} \right) + i \left(\frac{\partial \hat{\Phi}}{\partial \mathbf{U}}(\vec{n}_g^{(j)}) \right) \left(2\sin\zeta^{(j)} - \frac{1}{2}\sin 2\zeta^{(j)} \right) + \\
& \left| \hat{\mathbf{D}}(\vec{n}_g^{(k)}) \right| \left(-2\cos\zeta^{(k)} + \frac{1}{2}\cos 2\zeta^{(k)} + \right. \\
& \left. \left. \frac{3}{2} \right) + i \left(\frac{\partial \hat{\Phi}}{\partial \mathbf{U}}(\vec{n}_g^{(k)}) \right) \left(2\sin\zeta^{(k)} - \frac{1}{2}\sin 2\zeta^{(k)} \right) \right]. \tag{9.50}
\end{aligned}$$

The variable ν is the CFL number, defined as

$$\nu = \left\{ \omega(\vec{n}_g^{(i)}) + \omega(\vec{n}_g^{(j)}) + \omega(\vec{n}_g^{(k)}) \right\} \frac{\Delta t}{\Delta s}, \tag{9.51}$$

for cubic cells with edge length Δs . The $\vec{n}_g^{(i)}$, $\vec{n}_g^{(j)}$, and $\vec{n}_g^{(k)}$ are the direction-vectors normal to the grid faces in the i , j , and k directions, respectively. They are defined by the angles θ_g and ψ_g (see figure 9.1). In the present analysis, $\theta_g^{(i)}$ and $\psi_g^{(i)}$ are prescribed for the direction $\vec{n}_g^{(i)}$, then $\vec{n}_g^{(j)}$ is taken as $(\theta_g^{(i)}, \psi_g^{(i)} + \pi/2)$. The vector $\vec{n}_g^{(k)}$ is taken as the vector perpendicular to the other two. Also, $\omega(\vec{n}_g^{(i)})$, $\omega(\vec{n}_g^{(j)})$, and $\omega(\vec{n}_g^{(k)})$ are the maximum wave speeds $|\hat{q}| + \hat{a}$ in each of the grid directions. $\Im(-\mathbf{L})$ is a complex-valued 5×5 matrix.

The three-dimensional flux Jacobian matrix is given by $\partial \hat{\Phi} / \partial \mathbf{U} =$

$$\begin{bmatrix}
0 & (c_x)_g & (c_y)_g & (c_z)_g & 0 \\
(c_x)_g \phi - \hat{u} \hat{q}_g & (c_x)_g b \hat{u} + \hat{q}_g & (c_y)_g \hat{u} - (c_x)_g f \hat{v} & (c_z)_g \hat{u} - (c_x)_g f \hat{w} & (c_x)_g f \\
(c_y)_g \phi - \hat{v} \hat{q}_g & (c_x)_g \hat{v} - (c_y)_g f \hat{u} & (c_y)_g b \hat{v} + \hat{q}_g & (c_z)_g \hat{v} - (c_y)_g f \hat{w} & (c_y)_g f \\
(c_z)_g \phi - \hat{w} \hat{q}_g & (c_x)_g \hat{w} - (c_z)_g f \hat{u} & (c_y)_g \hat{w} - (c_z)_g f \hat{v} & (c_z)_g b \hat{w} + \hat{q}_g & (c_z)_g f \\
(2\phi - \gamma \hat{E}) \hat{q}_g & \hat{C}_{42} & \hat{C}_{43} & \hat{C}_{44} & \gamma \hat{q}_g
\end{bmatrix} \tag{9.52}$$

where, for brevity,

$$\begin{aligned}
\hat{C}_{42} & \equiv (c_x)_g (\gamma \hat{E} - \phi) - f \hat{u} \hat{q}_g \\
\hat{C}_{43} & \equiv (c_y)_g (\gamma \hat{E} - \phi) - f \hat{v} \hat{q}_g \\
\hat{C}_{44} & \equiv (c_z)_g (\gamma \hat{E} - \phi) - f \hat{w} \hat{q}_g.
\end{aligned} \tag{9.53}$$

Also:

$$\begin{aligned}
 b &\equiv (2 - \gamma) \\
 f &\equiv (\gamma - 1) \\
 \phi &\equiv \frac{\gamma - 1}{2} (\hat{u}^2 + \hat{v}^2 + \hat{w}^2),
 \end{aligned} \tag{9.54}$$

and \hat{q}_g is defined by (9.28).

$|\hat{\mathbf{D}}|$ is the matrix that satisfies

$$|\hat{\mathbf{D}}| \Delta \mathbf{U} = \sum_k |\hat{\lambda}_k| \hat{\Omega}_k \hat{\mathbf{R}}_k. \tag{9.55}$$

For the 5-wave model in three dimensions, the elements of $|\hat{\mathbf{D}}|$ are given by:

$$\begin{aligned}
 |\hat{\mathbf{D}}|_{j1} &= |\hat{\lambda}_4| (\hat{\mathbf{R}}_4)_j + \phi \xi_1 - \xi_2 \hat{u} - \xi_3 \hat{v} - \xi_4 \hat{w} + \\
 &\quad |\hat{\lambda}_5| \{ (p_1)_j \hat{u} + (p_2)_j \hat{v} + (p_3)_j \hat{w} \} \\
 |\hat{\mathbf{D}}|_{j2} &= -(\gamma - 1) \hat{u} \xi_1 + \xi_2 - |\lambda_5| (p_1)_j \\
 |\hat{\mathbf{D}}|_{j3} &= -(\gamma - 1) \hat{v} \xi_1 + \xi_3 - |\lambda_5| (p_2)_j \\
 |\hat{\mathbf{D}}|_{j4} &= -(\gamma - 1) \hat{w} \xi_1 + \xi_4 - |\lambda_5| (p_3)_j \\
 |\hat{\mathbf{D}}|_{j5} &= (\gamma - 1) \xi_1,
 \end{aligned} \tag{9.56}$$

where

$$\begin{aligned}
 \xi_1 &= \frac{1}{2\hat{a}^2} \left\{ |\hat{\lambda}_1| (\hat{\mathbf{R}}_1)_j + |\hat{\lambda}_2| (\hat{\mathbf{R}}_2)_j - 2 |\hat{\lambda}_4| (\hat{\mathbf{R}}_4)_j \right\} \\
 \xi_2 &= \frac{\beta}{2\hat{a}} (c_x)'_d \left\{ |\hat{\lambda}_1| (\hat{\mathbf{R}}_1)_j - |\hat{\lambda}_2| (\hat{\mathbf{R}}_2)_j \right\} \\
 \xi_3 &= \frac{\beta}{2\hat{a}} (c_y)'_d \left\{ |\hat{\lambda}_1| (\hat{\mathbf{R}}_1)_j - |\hat{\lambda}_2| (\hat{\mathbf{R}}_2)_j \right\} \\
 \xi_4 &= \frac{\beta}{2\hat{a}} (c_z)'_d \left\{ |\hat{\lambda}_1| (\hat{\mathbf{R}}_1)_j - |\hat{\lambda}_2| (\hat{\mathbf{R}}_2)_j \right\}
 \end{aligned} \tag{9.57}$$

and

$$\begin{aligned}
 (p_k)_1 &= 0 \quad k = 1, 2, 3 \\
 (p_1)_2 &= (c_x)'_d{}^2 - 1 & (p_2)_2 &= (c_x)'_d (c_y)'_d & (p_3)_2 &= (c_x)'_d (c_z)'_d \\
 (p_1)_3 &= (c_y)'_d (c_x)'_d & (p_2)_3 &= (c_y)'_d{}^2 - 1 & (p_3)_3 &= (c_y)'_d (c_z)'_d \\
 (p_1)_4 &= (c_z)'_d (c_x)'_d & (p_2)_4 &= (c_z)'_d (c_y)'_d & (p_3)_4 &= (c_z)'_d{}^2 - 1 \\
 (p_k)_5 &= (p_1)_{k+1} \hat{u} + (p_2)_{k+1} \hat{v} + (p_3)_{k+1} \hat{w} \quad k = 1, 2, 3.
 \end{aligned} \tag{9.58}$$

In obtaining these elements of the $|\hat{\mathbf{D}}|$ matrix, it is assumed that the wavespeed of the $(\bar{n}'_d + \frac{\pi}{2})$ shear wave is zero.

Although no three-dimensional computations using explicit time-marching were done in this paper (only the modified implicit code CFL3D was used), a linearized stability analysis for the explicit scheme is included here for completeness. The analysis of the 4-stage time-marching scheme (6.18) is done in the same way in three dimensions as in two. However, since there are now three perturbation wavelengths $\zeta^{(i)}$, $\zeta^{(j)}$, and $\zeta^{(k)}$, each is cycled through 9 values from $-\pi$ to π inclusive, for a total of 729 conditions. Five eigenvalues are obtained at each condition. Since there are now more independent parameters to vary (the flow direction \bar{n}_f , the grid-normal direction \bar{n}_g , and the wave-propagation direction \bar{n}'_d each are defined by *two* angles θ and ψ), it is even more difficult to perform a thorough numerical analysis. Through extensive numerical experimentation, a “worst-case” Fourier footprint (of all variations tested) has been determined for first-order spatial differencing with the parameters $M=100$, $\theta_f = 0^\circ$, $\psi_f = 0^\circ$, $\beta = 0$, $\theta_g^{(i)} = 0^\circ$, $\psi_g^{(i)} = 0^\circ$, $\theta'_d = 22.5^\circ$, and $\psi'_d = 22.5^\circ$.

Plotting this “worst-case” Fourier footprint along with the stability boundary of (6.18) with $\eta = 0.15$ in figure 9.8, it is seen that the maximum ν that yields stability of the three-dimensional explicit scheme is about 1.55. This is slightly lower than the stability limit for two dimensions. For second-order spatial accuracy, the maximum ν is about 0.77, as shown in figure 9.9. It is expected that for lower Mach number flow these CFL number restrictions would be relaxed somewhat.

For three-dimensional implicit time-marching, the generalized eigenvalue problem

$$[\mathfrak{S}(\mathbf{M}) + \mathfrak{S}(-\mathbf{L})] \bar{x} = g [\mathfrak{S}(\mathbf{M})] \bar{x}, \quad (9.59)$$

arises, where g is any of the complex eigenvalues, and $[\mathfrak{S}(\mathbf{M}) + \mathfrak{S}(-\mathbf{L})]$ and $[\mathfrak{S}(\mathbf{M})]$

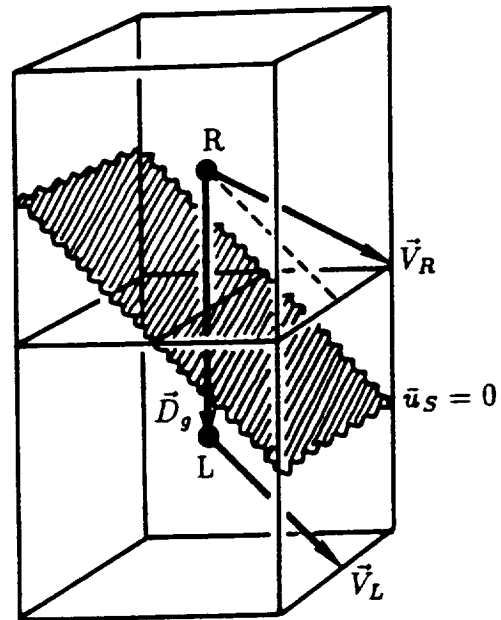


Figure 9.7: Steady Oblique Shear With Rotation Through the Wave

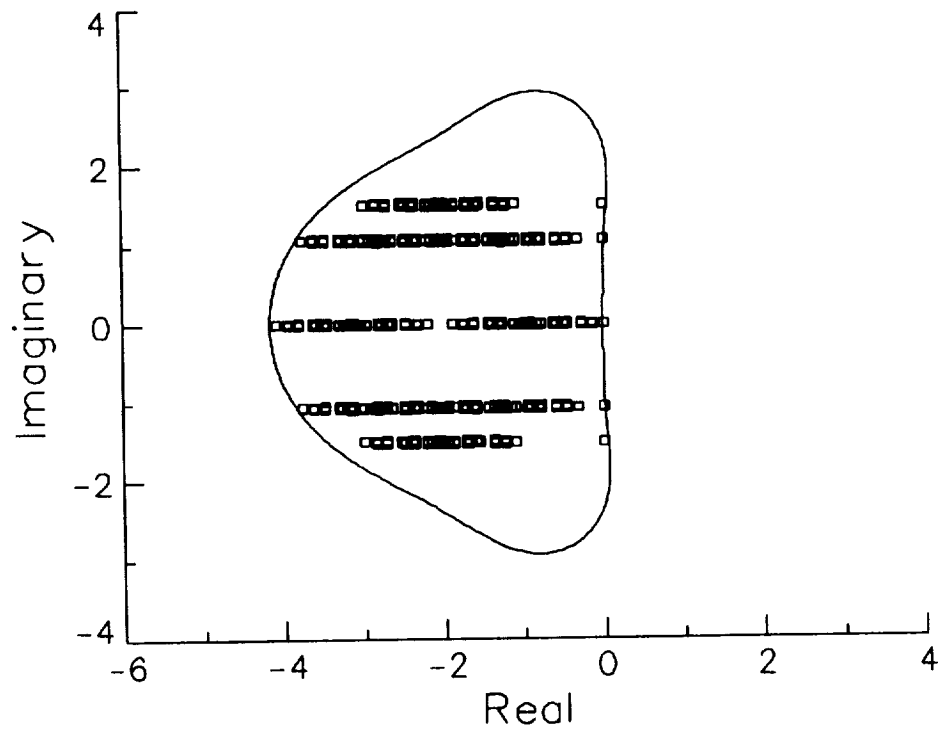


Figure 9.8: Stability Boundary of 4-Stage Time-Marching Scheme, and "Worst-Case" Fourier Footprint of First-Order Spatial Differencing Scheme for $\nu = 1.55$

are complex 5×5 matrices. For the three-factor approximately-factored left-hand side, (9.14), the Fourier transform of \mathbf{M} is given by:

$$\begin{aligned} \mathfrak{S}(\mathbf{M}) = & \left\{ \mathbf{I} + \frac{\nu}{\{\omega(\vec{n}_g^{(i)}) + \omega(\vec{n}_g^{(j)}) + \omega(\vec{n}_g^{(k)})\}} \left[\left| \frac{\partial \hat{\Phi}}{\partial \mathbf{U}}(\vec{n}_g^{(i)}) \right| (1 - \cos \zeta^{(i)}) + \right. \right. \\ & \left. \left. i \left(\frac{\partial \hat{\Phi}}{\partial \mathbf{U}}(\vec{n}_g^{(i)}) \right) \sin \zeta^{(i)} \right] \right\}^* \\ & \left\{ \mathbf{I} + \frac{\nu}{\{\omega(\vec{n}_g^{(i)}) + \omega(\vec{n}_g^{(j)}) + \omega(\vec{n}_g^{(k)})\}} \left[\left| \frac{\partial \hat{\Phi}}{\partial \mathbf{U}}(\vec{n}_g^{(j)}) \right| (1 - \cos \zeta^{(j)}) + \right. \right. \\ & \left. \left. i \left(\frac{\partial \hat{\Phi}}{\partial \mathbf{U}}(\vec{n}_g^{(j)}) \right) \sin \zeta^{(j)} \right] \right\}^* \\ & \left\{ \mathbf{I} + \frac{\nu}{\{\omega(\vec{n}_g^{(i)}) + \omega(\vec{n}_g^{(j)}) + \omega(\vec{n}_g^{(k)})\}} \left[\left| \frac{\partial \hat{\Phi}}{\partial \mathbf{U}}(\vec{n}_g^{(k)}) \right| (1 - \cos \zeta^{(k)}) + \right. \right. \\ & \left. \left. i \left(\frac{\partial \hat{\Phi}}{\partial \mathbf{U}}(\vec{n}_g^{(k)}) \right) \sin \zeta^{(k)} \right] \right\} \end{aligned} \quad (9.60)$$

when the approximate left-hand side Jacobians of the form given in Chapter 3 are employed.

The stability characteristics are determined by cycling through 9 of each of the frequencies $\zeta^{(i)}$, $\zeta^{(j)}$, and $\zeta^{(k)}$ from 0 to 2π . For first-order spatial differencing, the same “worst-case” parameters as those used for the explicit analysis were found to give the strictest stability limit out of the many variations tried. These parameters are: $M=100$, $\theta_f = 0^\circ$, $\psi_f = 0^\circ$, $\theta_g^{(i)} = 0^\circ$, $\psi_g^{(i)} = 0^\circ$, $\theta'_d = 22.5^\circ$, and $\psi'_d = 22.5^\circ$. Variations in β were found to make very little difference at these conditions. A plot of the maximum eigenvalue, average eigenvalue, and smoothing factor is given in figure 9.10. The maximum CFL number allowable turns out to be about 1.5.

For second-order spatial differencing, the same “worst-case” parameters were again used, but this time β was found to have an effect on the results. When $\beta = 0$, the analysis shows the scheme to be unstable except below $\nu = 0.005$. This is shown in figure 9.11(a). When $\beta = 0.05$, figure 9.11(b), the stability limit increases to about 0.3.

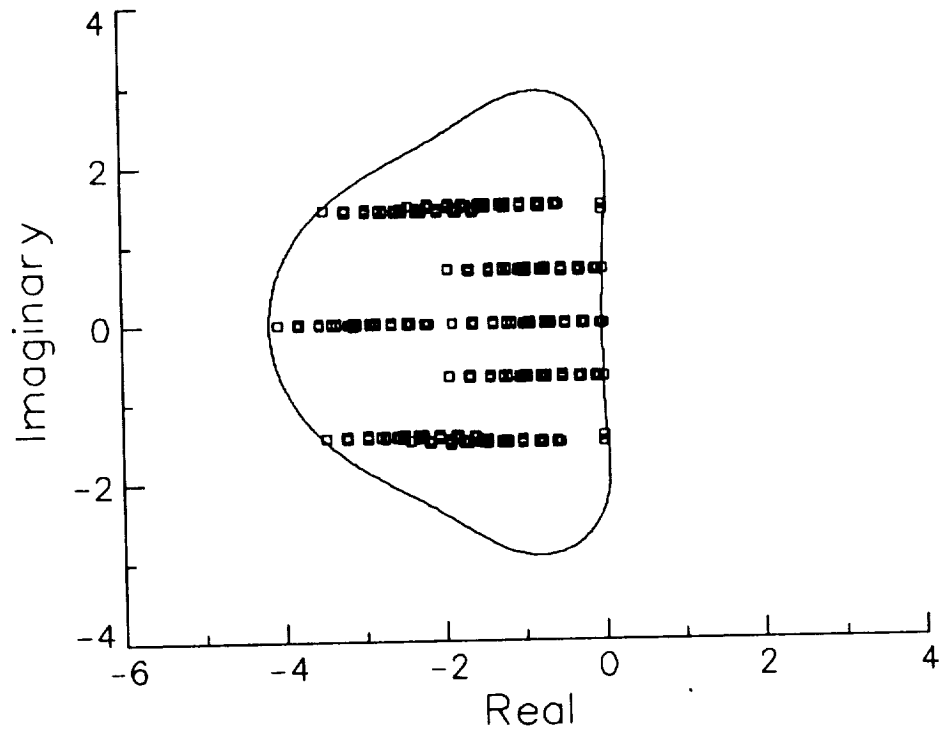


Figure 9.9: Stability Boundary of 4-Stage Time-Marching Scheme, and "Worst-Case" Fourier Footprint of Second-Order Spatial Differencing Scheme for $\nu = 0.77$

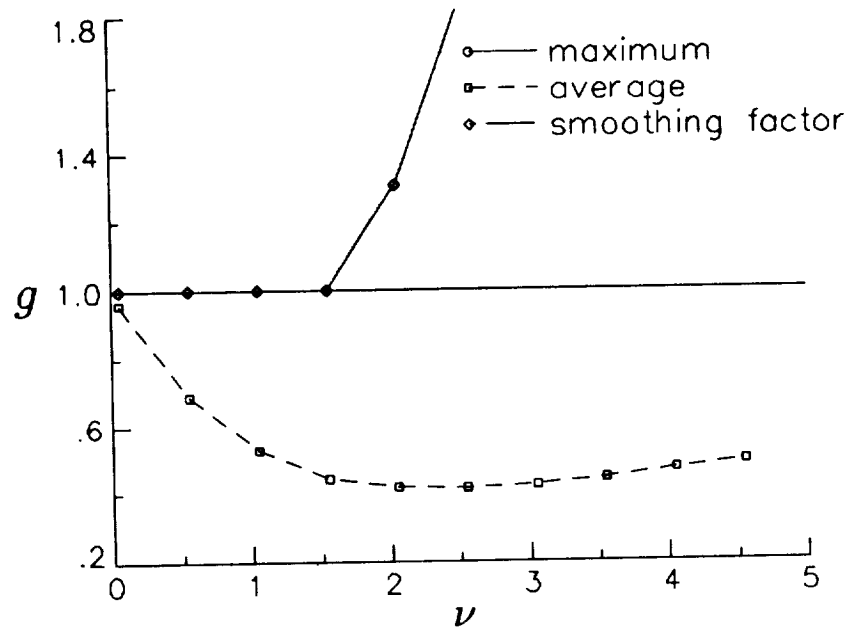


Figure 9.10: Eigenvalues as Function of CFL Number for Implicit Scheme, First-Order, "Worst-Case" Parameters

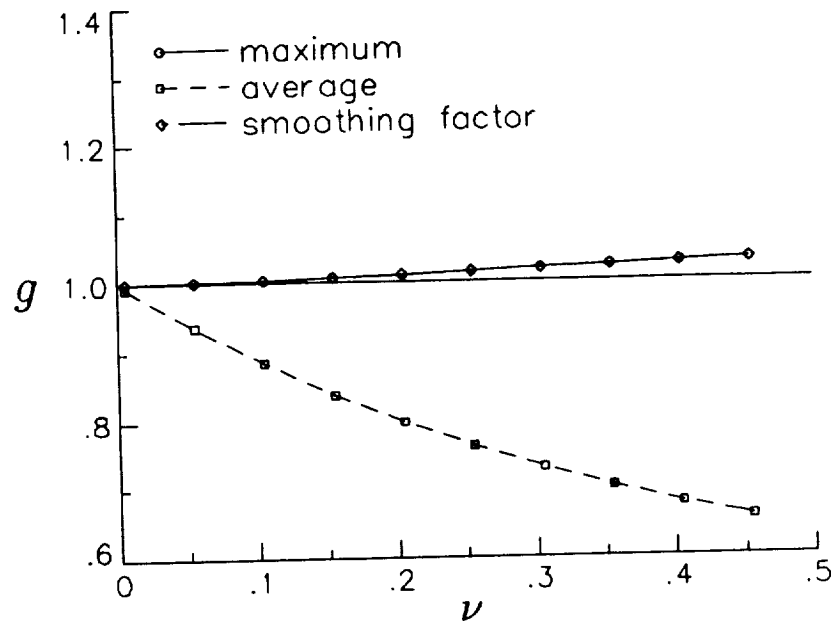
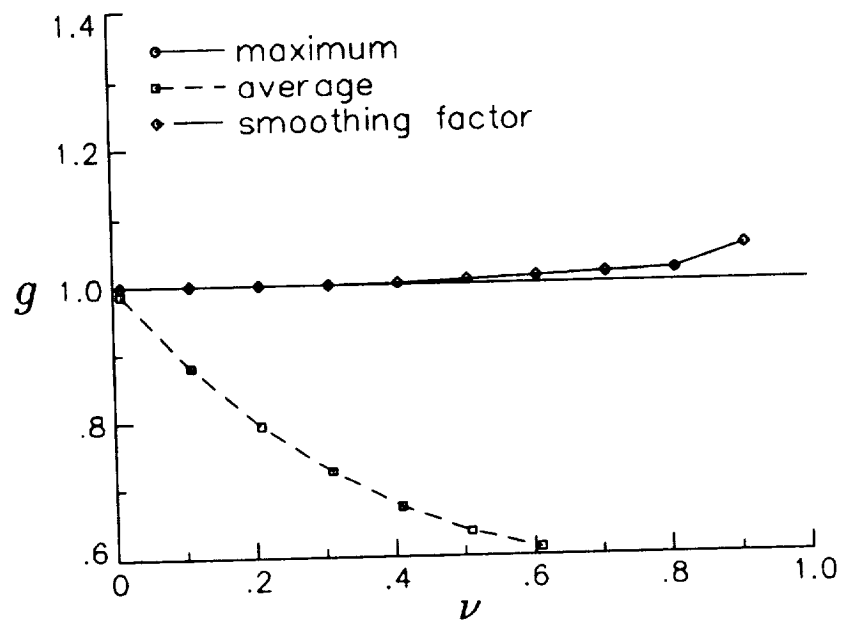
a) $\beta = 0$ b) $\beta = 0.05$

Figure 9.11: Eigenvalues as Function of CFL Number for Implicit Scheme, Second-Order, "Worst-Case" Parameters

Based on the results from two dimensions, it is believed that these stability restrictions for first and second-order can be relaxed somewhat for lower Mach number flows. It is also likely that the stability properties of the 5-wave model in three dimensions can be improved dramatically by modifying the left-hand side approximate Jacobians as described at the end of Chapter 6, as well as solving block-pentadiagonal systems for second-order computations. These modifications were not attempted in the current study.

9.6 Monotonicity Analysis

The monotonicity analysis for the three-dimensional Euler equations proceeds much the same way as for the two-dimensional equations. The monotonicity property is insured when

$$\text{e.v.} \left(\frac{\partial \Phi_{i+\frac{1}{2},j,k}}{\partial \mathbf{U}_{i+1,j,k}} \right) \leq 0 \quad \text{e.v.} \left(\frac{\partial \Phi_{i-\frac{1}{2},j,k}}{\partial \mathbf{U}_{i-1,j,k}} \right) \geq 0, \quad (9.61)$$

where $\text{e.v.}(\cdot)$ represents “the eigenvalues of (\cdot) ”, and the grid-normal \vec{n}_g , defined by the angles (θ_g, ψ_g) , is varied over the full range of possible angles. The 5-wave model can again be written in a form similar to (7.9), but it is assumed for this analysis that the wavespeed associated with the $(\vec{n}'_d + \frac{\pi}{2})$ shear wave is identically zero (which would be exactly true if the wave-propagation direction was never frozen). Therefore this shear wave is ignored in the analysis. All remaining waves travel in the \vec{n}'_d -direction, so the flux function per unit face-area can be written:

$$\Phi_{i+\frac{1}{2},j,k} = \frac{1}{2} (\Phi_{i+1,j,k} + \Phi_{i,j,k}) - \frac{1}{2} [\hat{\mathbf{R}}^*] |[\hat{\mathbf{\Lambda}}^*] \cos(\vec{n}'_d - \vec{n}_g) | \hat{\mathbf{\Omega}}^*. \quad (9.62)$$

There are only four waves which are assumed to travel in the \vec{n}'_d -direction, given by (9.34), (9.35), (9.37), and (9.38). However, in order for all the matrices in (9.62) to come out as 5×5 matrices, it is necessary to employ *five* waves in $\hat{\mathbf{R}}^*$.

Therefore the combined shear wave $\hat{\mathbf{R}}_5$ of (9.38) is broken back into two shear waves, chosen arbitrarily, which are perpendicular in $(\Delta u, \Delta v, \Delta w)$ -space:

$$\hat{\mathbf{R}}_{5a} = \begin{bmatrix} 0 \\ -\hat{a}\sin\theta'_d \\ \hat{a}\cos\theta'_d \\ 0 \\ \hat{a}(-\hat{u}\sin\theta'_d + \hat{v}\cos\theta'_d) \end{bmatrix} \quad (9.63)$$

$$\hat{\mathbf{R}}_{5b} = \begin{bmatrix} 0 \\ -\hat{a}\cos\theta'_d\sin\psi'_d \\ -\hat{a}\sin\theta'_d\sin\psi'_d \\ \hat{a}\cos\psi'_d \\ \hat{a}\hat{r}'_d \end{bmatrix}, \quad (9.64)$$

where

$$\hat{r}'_d \equiv -\hat{u}\cos\theta'_d\sin\psi'_d - \hat{v}\sin\theta'_d\sin\psi'_d + \hat{w}\cos\psi'_d. \quad (9.65)$$

The wavenumbers associated with each of these waves are:

$$\begin{aligned} \hat{\Omega}_{5a} &= \frac{\hat{\rho}}{\hat{a}}(-\Delta u\sin\theta'_d + \Delta v\cos\theta'_d) \\ \hat{\Omega}_{5b} &= \frac{\hat{\rho}}{\hat{a}}(-\Delta u\cos\theta'_d\sin\psi'_d - \Delta v\sin\theta'_d\sin\psi'_d + \Delta w\cos\psi'_d). \end{aligned} \quad (9.66)$$

Hence the $[\hat{\mathbf{R}}^*]$ matrix is made up of $\hat{\mathbf{R}}_{1,2,4}$ from (9.34), (9.35), and (9.37), as well as $\hat{\mathbf{R}}_{5a}$ and $\hat{\mathbf{R}}_{5b}$. The matrix of wavespeeds in the \hat{n}'_d -direction is $[\hat{\Lambda}^*] = \text{diag}(\hat{q}'_d + \hat{a}, \hat{q}'_d - \hat{a}, \hat{q}'_d, \hat{q}'_d, \hat{q}'_d)$, where \hat{q}'_d is defined by (9.39). Making the same assumptions as was done in Chapter 7, the linearized analysis gives

$$\frac{\partial \Phi_{i+\frac{1}{2},j,k}}{\partial \mathbf{U}_{i+1,j,k}} = \frac{1}{2} \frac{\partial \hat{\Phi}}{\partial \mathbf{U}}(\vec{n}_g) - \frac{1}{2} [\hat{\mathbf{R}}^*] | [\hat{\Lambda}^*] \cos(\vec{n}'_d - \vec{n}_g) | \frac{\partial \hat{\Omega}^*}{\partial \mathbf{U}_R} \quad (9.67)$$

$$\frac{\partial \Phi_{i-\frac{1}{2},j,k}}{\partial \mathbf{U}_{i-1,j,k}} = \frac{1}{2} \frac{\partial \hat{\Phi}}{\partial \mathbf{U}}(\vec{n}_g) - \frac{1}{2} [\hat{\mathbf{R}}^*] | [\hat{\Lambda}^*] \cos(\vec{n}'_d - \vec{n}_g) | \frac{\partial \hat{\Omega}^*}{\partial \mathbf{U}_L}. \quad (9.68)$$

The derivative matrix in (9.67) is given by $\partial \hat{\Omega}^* / \partial \mathbf{U}_R =$

$$\begin{bmatrix} \frac{\phi}{2\hat{a}^2} - \frac{\beta \hat{q}'_d}{2\hat{a}} & -\frac{f\hat{u}}{2\hat{a}^2} + \frac{\beta(c_x)'_d}{2\hat{a}} & -\frac{f\hat{v}}{2\hat{a}^2} + \frac{\beta(c_y)'_d}{2\hat{a}} & -\frac{f\hat{w}}{2\hat{a}^2} + \frac{\beta(c_z)'_d}{2\hat{a}} & \frac{f}{2\hat{a}^2} \\ \frac{\phi}{2\hat{a}^2} + \frac{\beta \hat{q}'_d}{2\hat{a}} & -\frac{f\hat{u}}{2\hat{a}^2} - \frac{\beta(c_x)'_d}{2\hat{a}} & -\frac{f\hat{v}}{2\hat{a}^2} - \frac{\beta(c_y)'_d}{2\hat{a}} & -\frac{f\hat{w}}{2\hat{a}^2} - \frac{\beta(c_z)'_d}{2\hat{a}} & \frac{f}{2\hat{a}^2} \\ 1 - \frac{\phi}{\hat{a}^2} & \frac{f\hat{u}}{\hat{a}^2} & \frac{f\hat{v}}{\hat{a}^2} & \frac{f\hat{w}}{\hat{a}^2} & -\frac{f}{\hat{a}^2} \\ -\frac{\hat{i}'_d}{\hat{a}} & -\frac{\sin\theta'_d}{\hat{a}} & \frac{\cos\theta'_d}{\hat{a}} & 0 & 0 \\ -\frac{\hat{r}'_d}{\hat{a}} & -\frac{\cos\theta'_d\sin\psi'_d}{\hat{a}} & -\frac{\sin\theta'_d\sin\psi'_d}{\hat{a}} & \frac{\cos\psi'_d}{\hat{a}} & 0 \end{bmatrix}, \quad (9.69)$$

where the variables f and ϕ are defined in (9.54), and:

$$\hat{t}'_d \equiv -\hat{u}\sin\theta'_d + \hat{v}\cos\theta'_d \quad (9.70)$$

The derivative matrix in (9.68) is given by $(\partial\hat{\Omega}^*/\partial\mathbf{U}_L) = -(\partial\hat{\Omega}^*/\partial\mathbf{U}_R)$.

For the three-dimensional monotonicity analysis, the Mach number M , flow angles (θ_f, ψ_f) , and β are chosen, then $\theta_g, \psi_g, \theta'_d$, and ψ'_d are each varied independently from -90° to 90° , with incremental change of $\pi/8$. Eigenvalues are computed for each condition. If they meet the criteria of equation (9.61), then monotonicity is preserved at that condition. The results are plotted as allowable $|\vec{n}'_d - \vec{n}_f|$ vs. $|\vec{n}_g - \vec{n}_f|$, for various ϕ_p , where ϕ_p is the angle between the plane defined by the vectors (\vec{n}_g, \vec{n}_f) and the plane defined by the vectors (\vec{n}'_d, \vec{n}_f) . The quantities within the absolute value signs indicate an angular difference between two vectors. When plotted this way, results are independent of the flow vector \vec{n}_f .

A result is given in figures 9.12(a) through (c) for $M = 3$, and $\beta = 1$. Figure 9.12(a) shows results for the case when $\phi_p < 15^\circ$. The allowable region for monotonicity looks very similar to the two-dimensional region at these same conditions (see figure 7.2(a)). It includes the grid-aligned wave model $\vec{n}'_d = \vec{n}_g$. Notice that for the three-dimensional case, in contrast to two dimensions, the absolute value of the angular differences are plotted so that only positive differences are given. This is done because of the difficulty associated with assigning a positive or negative angular difference in three dimensions. When $15^\circ < \phi_p < 30^\circ$, the plot of figure 9.12(b) results. Here, the monotone region is similar to that in figure 9.12(a) except that the grid-aligned model is no longer representable. When $30^\circ < \phi_p < 45^\circ$, the monotonicity region diminishes significantly in size, as shown in figure 9.12(c). Finally, when $45^\circ < \phi_p < 90^\circ$, then *no* region is monotone, according to this analysis.

A specific example is taken from this case. Referring to figures 9.12(a) through

(c), when $|\vec{n}_g - \vec{n}_f| \approx 75^\circ$, the allowable $|\vec{n}'_d - \vec{n}_f|$ goes from about 25° to 75° for $\phi_p < 15^\circ$, from about 25° to 65° for $15^\circ < \phi_p < 30^\circ$, and from about 35° to 45° for $30^\circ < \phi_p < 45^\circ$. A sketch is first drawn in figure 9.13(a) of the \vec{n}_f vector and the \vec{n}_g vector, separated by 75° , with the allowable \vec{n}'_d directions in the (\vec{n}_g, \vec{n}_f) -plane ($\phi_p = 0^\circ$) indicated by shading. Next, in figure 9.13(b), the allowable \vec{n}'_d directions in all three dimensions are indicated by including the results from the cases when the (\vec{n}'_d, \vec{n}_f) -plane differs significantly from the (\vec{n}_g, \vec{n}_f) -plane.

A second case using $M = 0.3, \beta = 1$ is shown in figure 9.14 for $\phi_p = 0^\circ$. When $\phi_p > 0^\circ$, there are no regions of monotonicity. This figure indicates (as did figure 7.2(b) for two dimensions) that only the grid-aligned method is monotone at these subsonic conditions. However, it is believed that this constraint, as well as the constraints imposed upon supersonic flows, can be relaxed somewhat in practice in an effort to reduce spurious oscillations near discontinuities while still maintaining much of the sharper resolution afforded by the 5-wave model. Although an empirical limiting method has not been devised for three-dimensional flow due to its inherent complexity, it is believed that a successful method could be patterned much the same as the method currently employed for two dimensions.

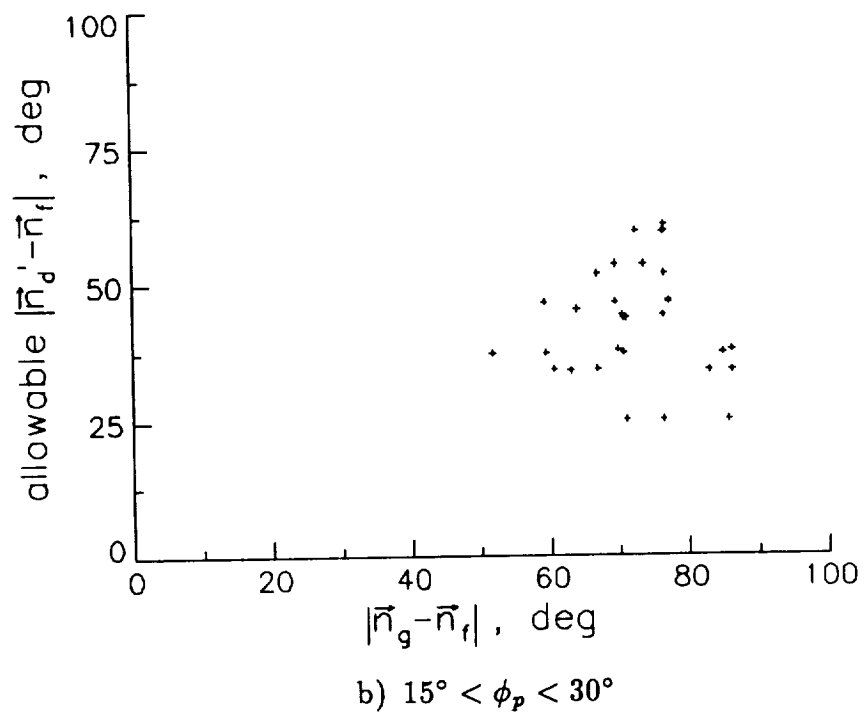
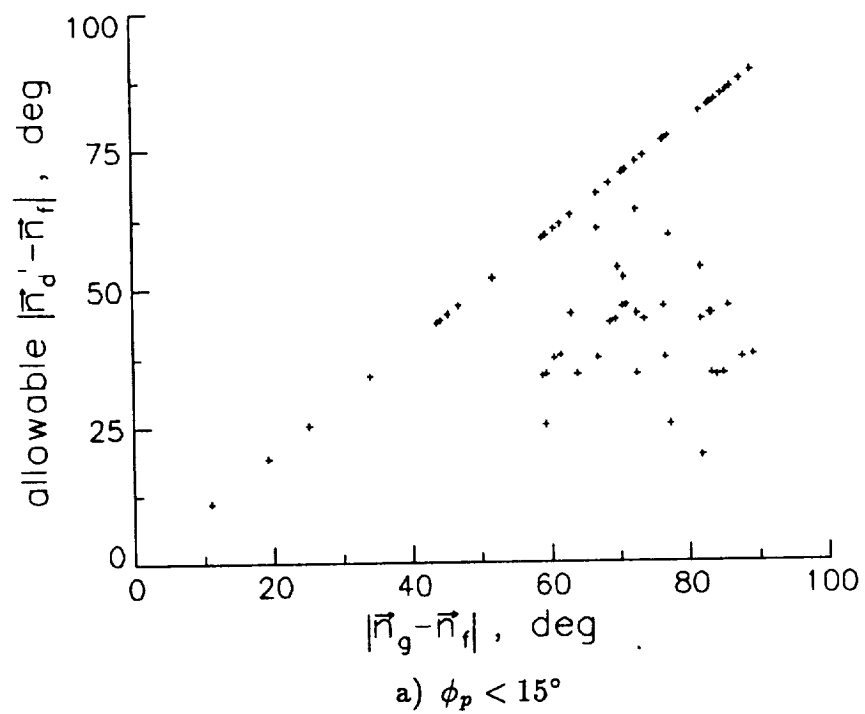
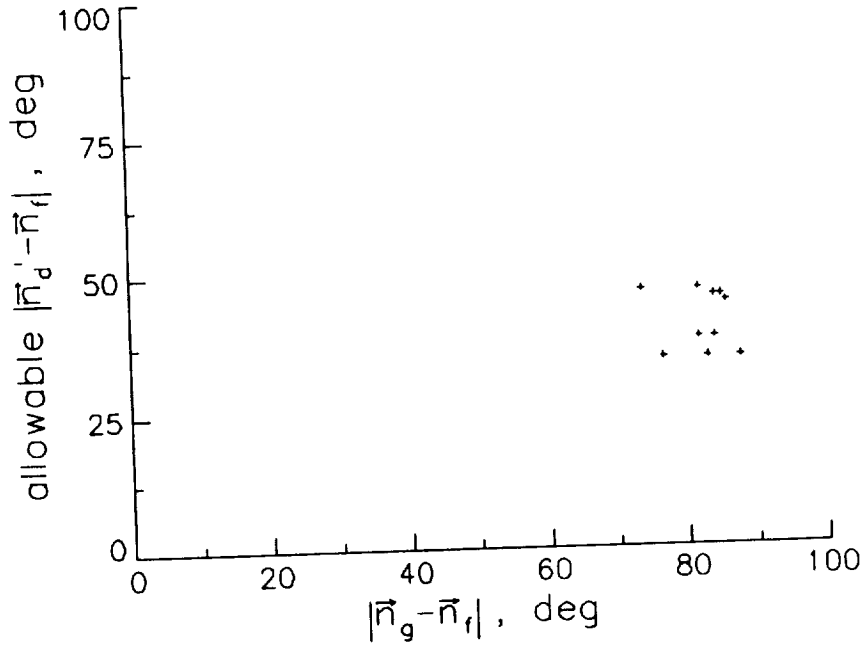
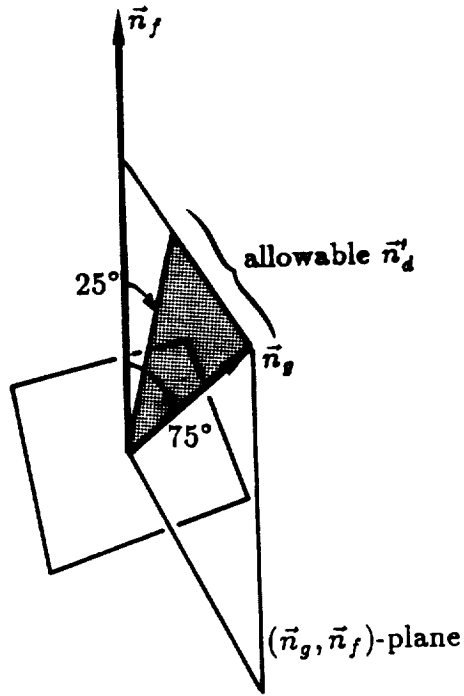


Figure 9.12: Monotonicity Regions, $M = 3$, $\beta = 1$



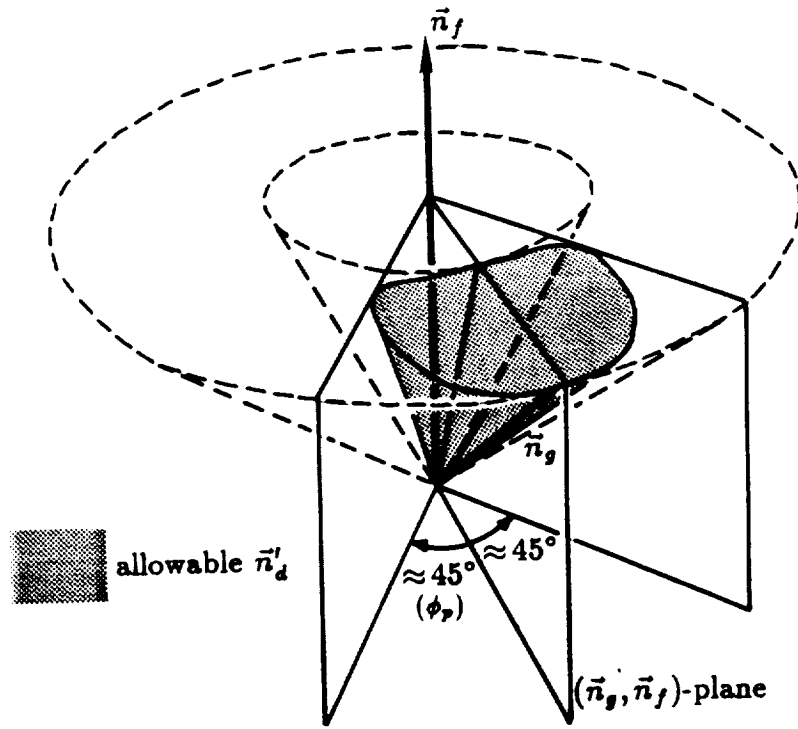
c) $30^\circ < \phi_p < 45^\circ$

Figure 9.12: Concluded



a) Approximate Allowable \vec{n}'_d in (\vec{n}_g, \vec{n}_f) -Plane

Figure 9.13: Monotonicity for $M = 3, \beta = 1$; Allowable \vec{n}'_d for $|\vec{n}_g - \vec{n}_f| = 75^\circ$



b) Approximate Allowable \vec{n}'_d in Three Dimensions

Figure 9.13: Concluded

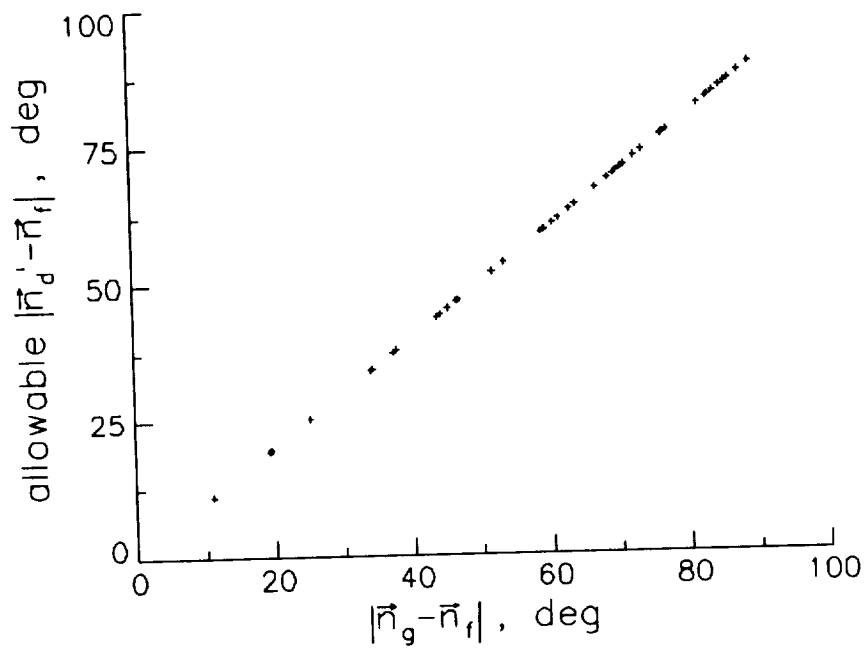


Figure 9.14: Monotonicity Region, $M = 0.3, \beta = 1, \phi_p = 0^\circ$

CHAPTER 10

THREE-DIMENSIONAL EULER RESULTS

All three-dimensional results are obtained using the implicit approximate-factorization algorithm CFL3D [32]. Only the flux function is varied in order to obtain either grid-aligned or grid-independent results. The CFL numbers chosen for stability for the 5-wave model are based on the theoretical analysis of Chapter 9. No wave-propagation-direction limiting procedure has been developed for the three-dimensional 5-wave model for improving its monotonicity properties.

10.1 Ramp Flow in a Channel

The geometry for the ramp flow in a channel with inflow Mach number of 2.8 is shown in figure 10.1. The domain is 1.8 units long by 0.72 units high by 0.5 units wide. An oblique ramp at the lower wall starts at 0.2 units with an angle of 12° at one side and at 0.5 units with an angle of 18° at the other side. This case was first computed by Parpia [33].

Computations are performed on a $41 \times 17 \times 17$ grid. Two $i = \text{constant}$ planes and one $k = \text{constant}$ plane from this grid are shown in figures 10.2(a) through (c). Simple reflection boundary conditions are applied at the four walls, inflow is taken as freestream, and outflow conditions are obtained from the interior of the grid using uniform first-order extrapolation.

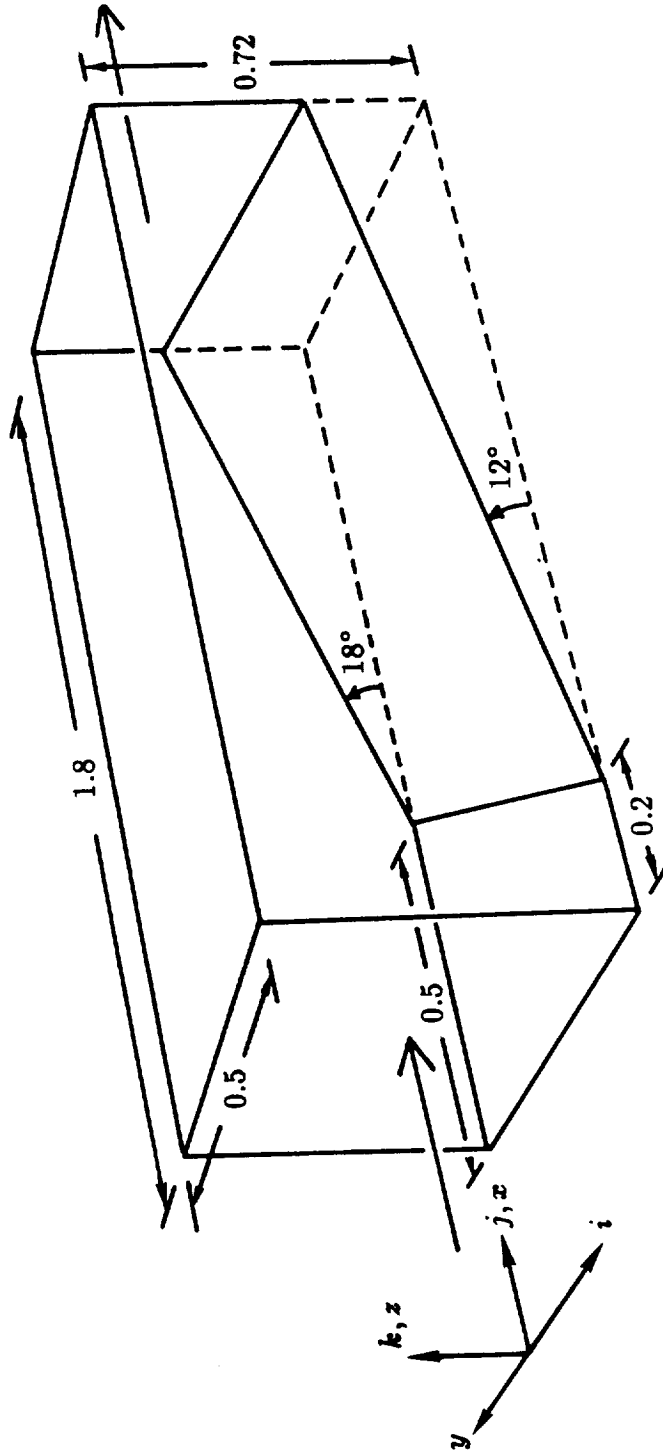
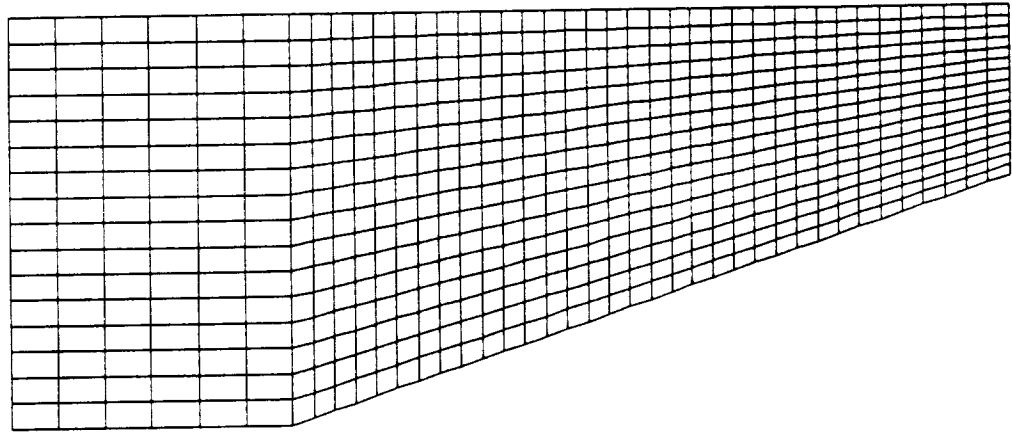
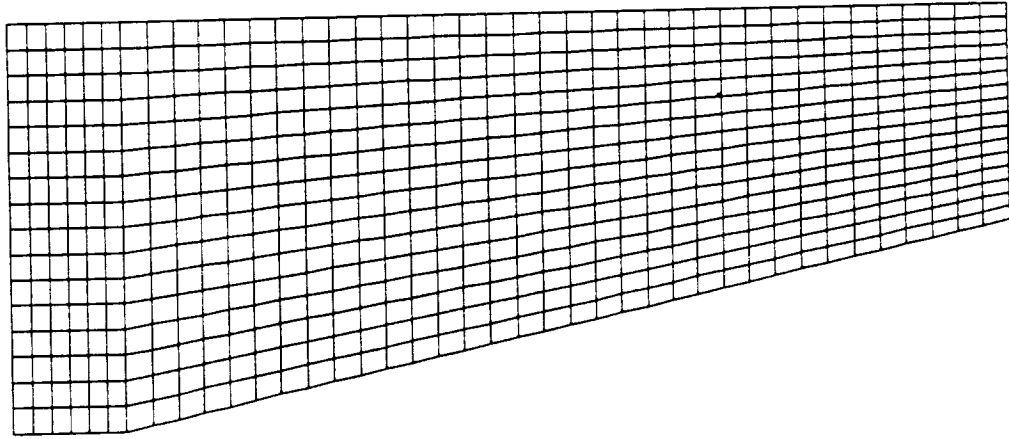
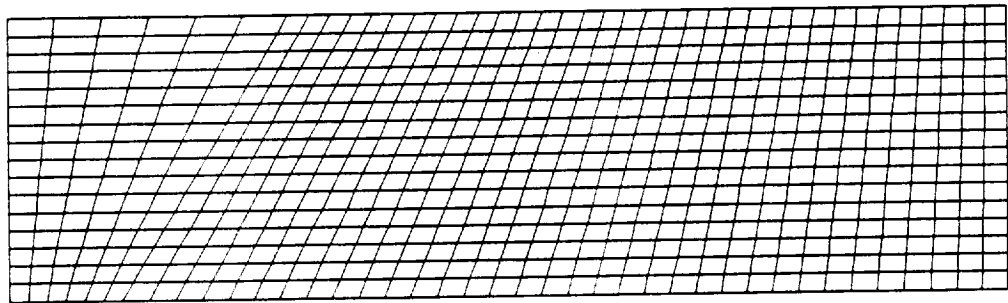


Figure 10.1: Geometry for Ramp Flow in Channel

a) $i = 1$ Planeb) $i = 17$ Planec) All $k = \text{Constant}$ PlanesFigure 10.2: 2-D Sections of $41 \times 17 \times 17$ Grid

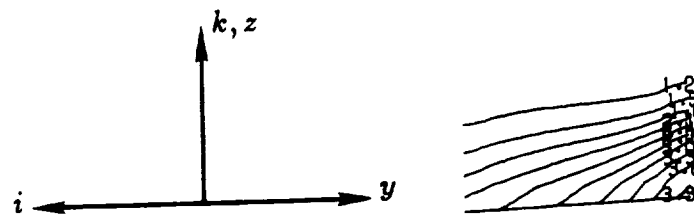
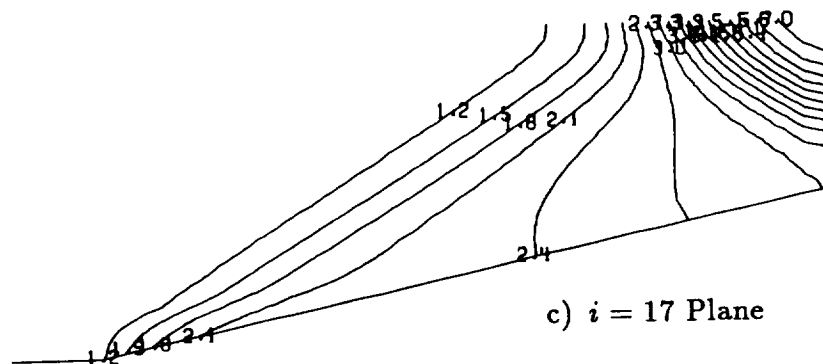
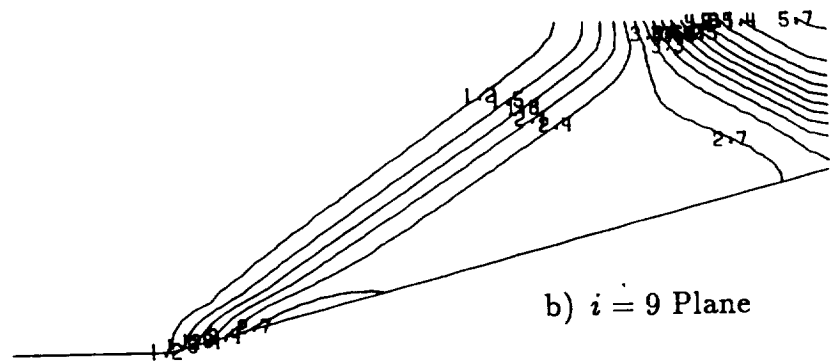
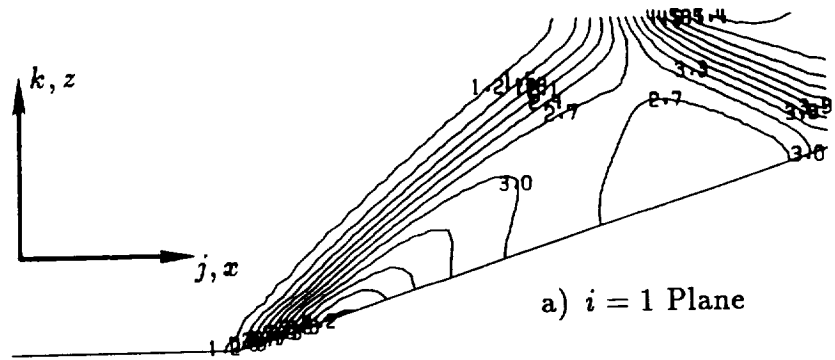
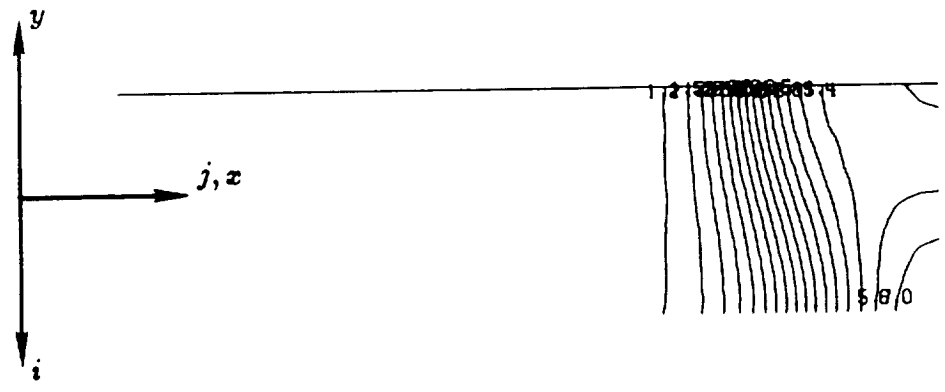
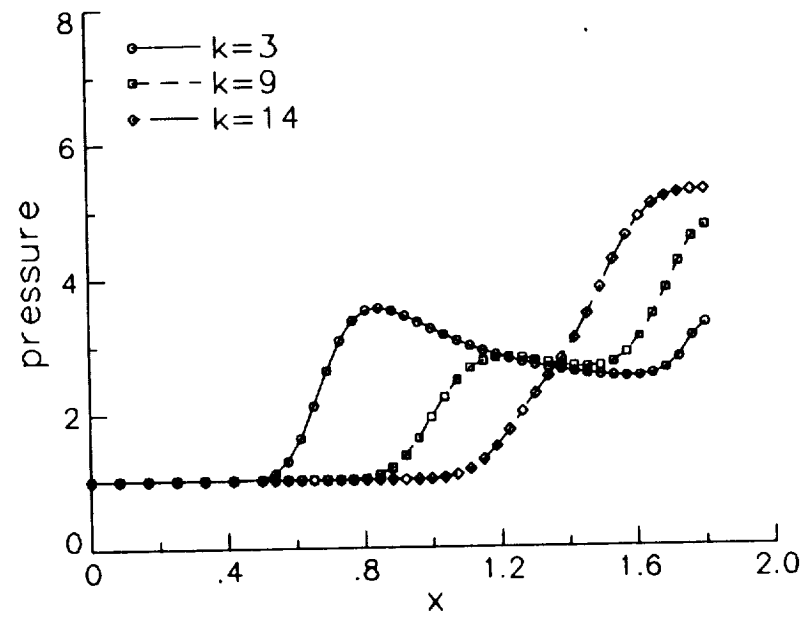


Figure 10.3: Ramp Flow, Pressure Contours, First-Order, Grid-Aligned



e) $k = 17$ Plane



f) Pressure Along $k = \text{Constant}$ Lines in $i = 1$ Plane

Figure 10.3: Concluded

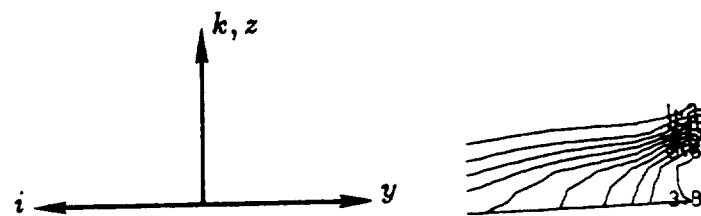
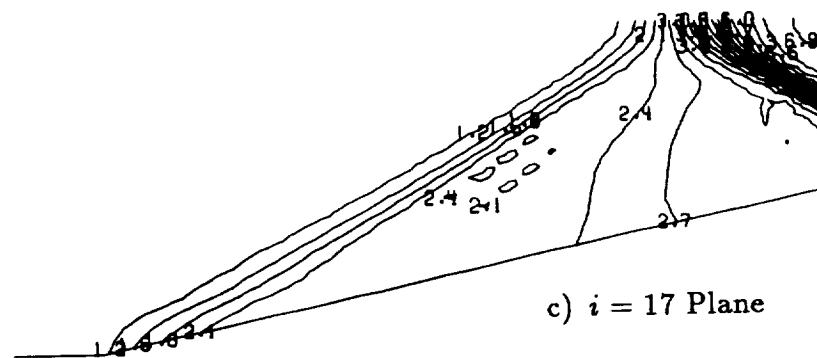
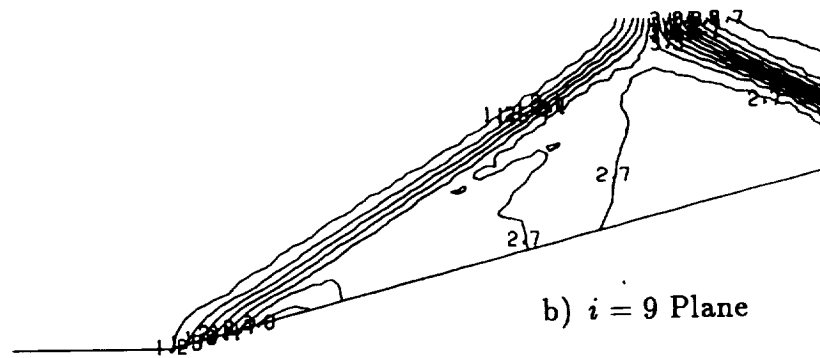
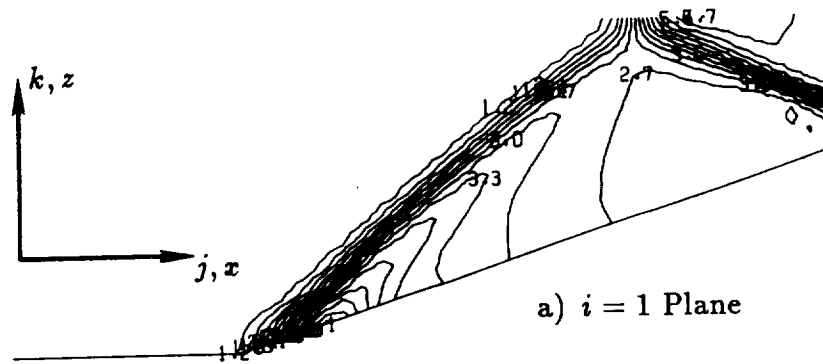


Figure 10.4: Ramp Flow, Pressure Contours, First-Order, 5-Wave

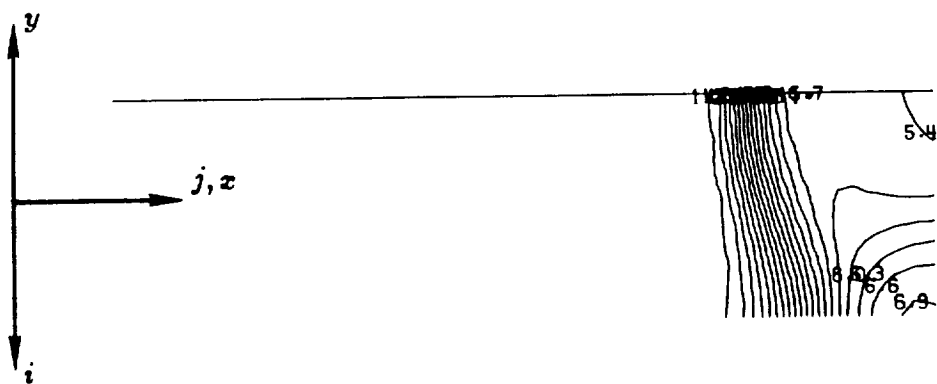
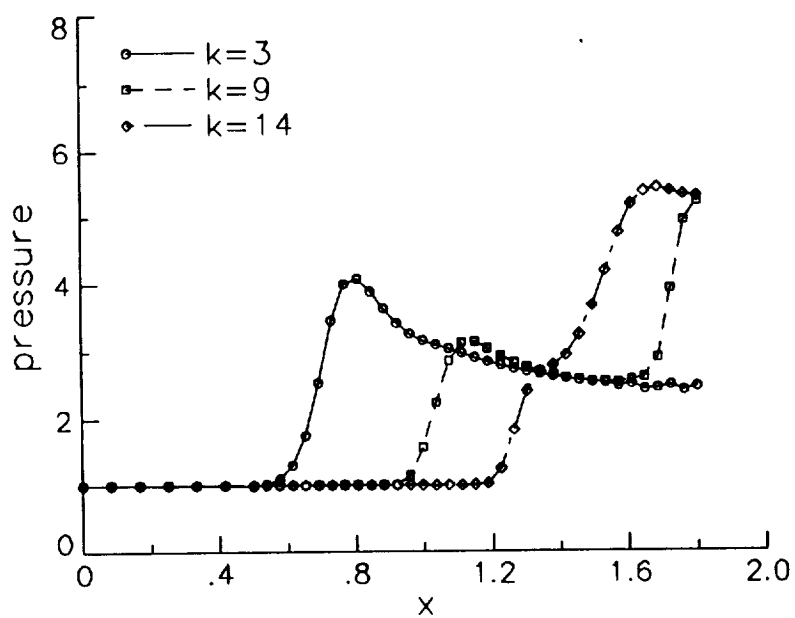
e) $k = 17$ Planef) Pressure Along $k = \text{Constant}$ Lines in $i = 1$ Plane

Figure 10.4: Concluded

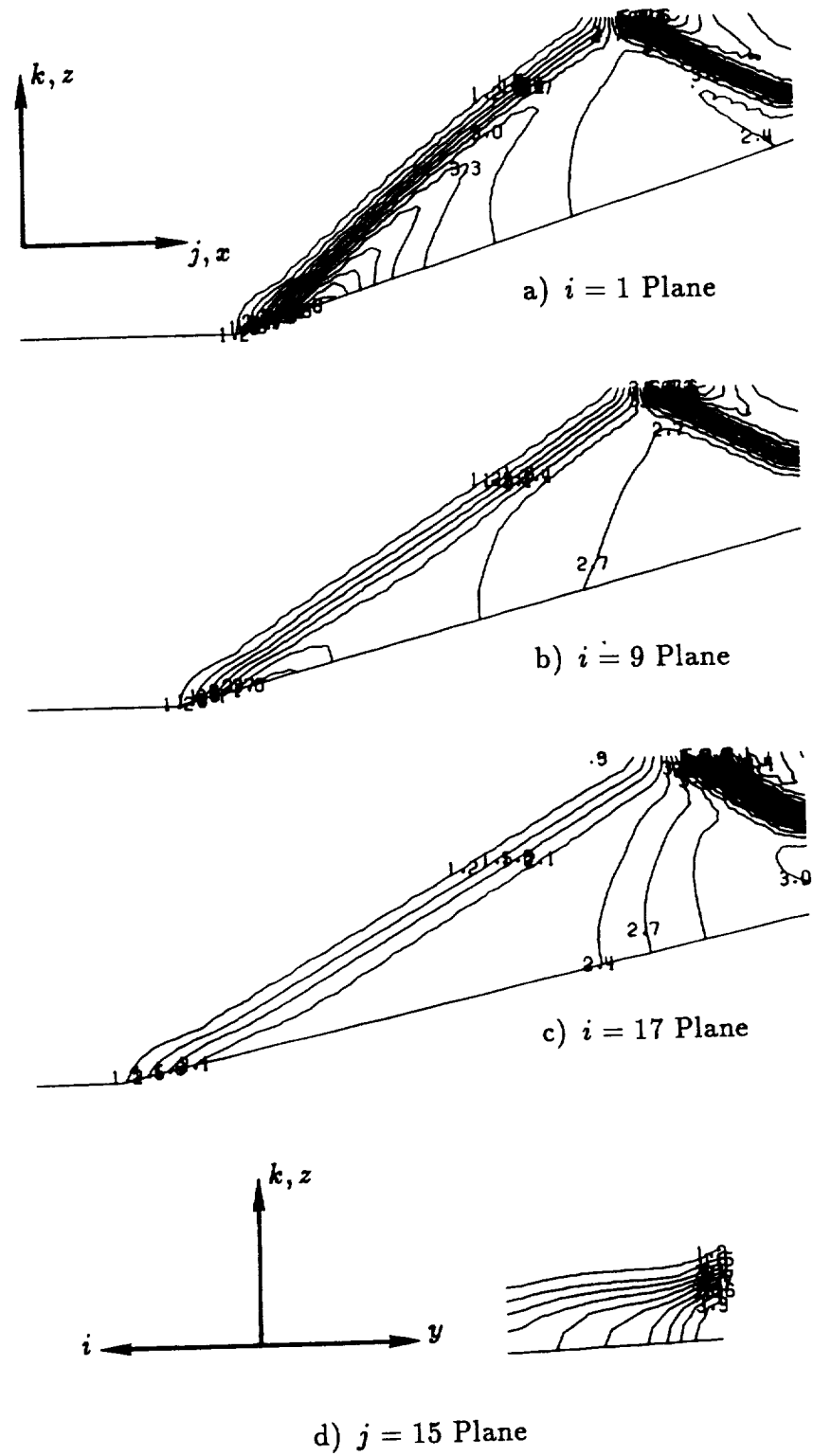
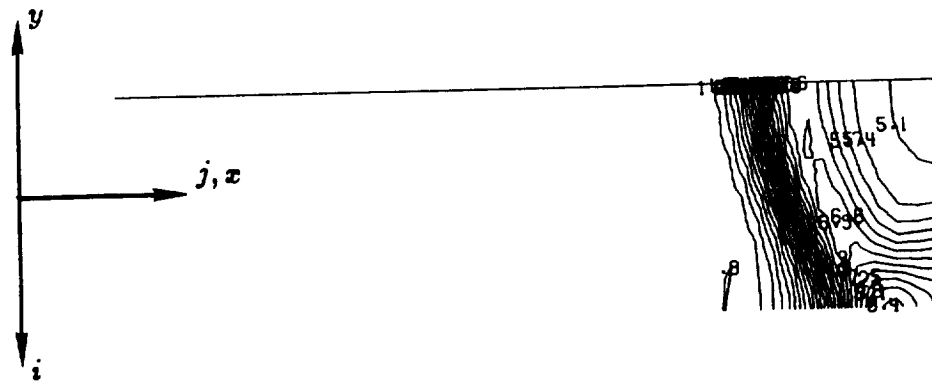


Figure 10.5: Ramp Flow, Pressure Contours, Second-Order, Grid-Aligned



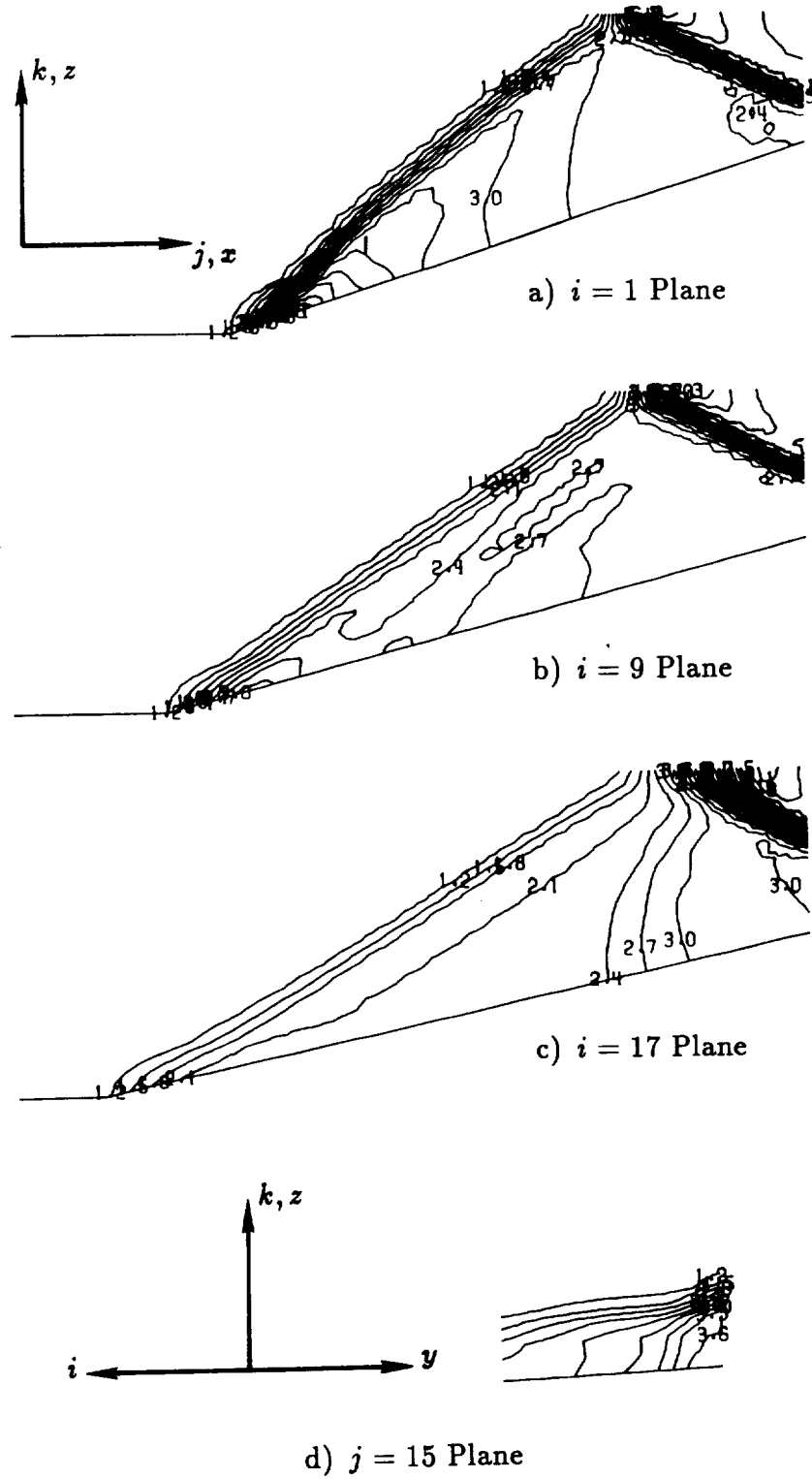
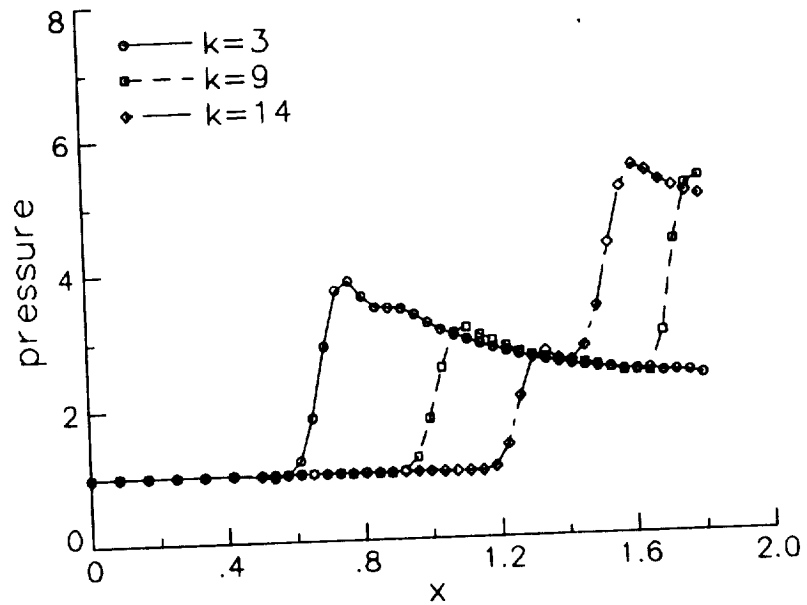


Figure 10.6: Ramp Flow, Pressure Contours, Second-Order, 5-Wave



e) $k = 17$ Plane



f) Pressure Along $k = \text{Constant}$ Lines in $i = 1$ Plane

Figure 10.6: Concluded

First-order computational results using the grid-aligned method are given in figure 10.3. Pressure contours are given in three $i = \text{constant}$ planes, one $j = \text{constant}$ plane, and one $k = \text{constant}$ plane. Also, nondimensional pressure values are given along three $k = \text{constant}$ lines in the $i = 1$ plane in figure 10.3(f). Results of the 5-wave model are obtained by restarting the grid-aligned results with the wave-propagation directions frozen. These 5-wave model results are given in figure 10.4. Shock waves are resolved with far fewer interior points using this method.

Second-order results using the grid-aligned model and the 5-wave model are given in figures 10.5 and 10.6, respectively. In this case, the 5-wave model does not improve the shock resolution to any noticeable extent over the grid-aligned model. Also, results are slightly more oscillatory. Hence for an oblique shock-type flow in three dimensions, as in two dimensions, the grid-independent model does not seem to be worth the additional effort when second-order spatial accuracy is employed.

10.2 Oblique Supersonic Shear

An oblique supersonic shear case is computed within a cube 1.8 units on a side using a Cartesian $17 \times 17 \times 17$ mesh. For the particular case considered, the velocity undergoes both an increase in magnitude as well as a rotation through the shear layer. The shear layer itself is assumed to lie along one diagonal of the cube, as shown in figure 10.7. Below the layer the velocity components are $u = 3$, $v = 3$, and $w = 3$, while above the layer they are $u = 4$, $v = 2$, and $w = 4$. There is one transition cell where $u = 3.5$, $v = 2.5$, and $w = 3.5$. There is no pressure or density change across the shear layer. The boundary conditions are applied as follows: at inflow the exact values are specified, and at outflow the variables are

obtained from the interior using uniform first-order extrapolation.

When β is not limited to be greater than 0.05, the 5-wave model preserves the exact solution when the initial condition is the exact solution. This exact solution is presented in figures 10.8 through 10.10 at an $i = \text{constant}$, a $j = \text{constant}$, and a $k = \text{constant}$ plane, respectively. Shown are in-plane Mach number contours and velocity vectors (the velocity component out-of-plane is ignored).

A first-order computation using the grid-aligned model gives the results shown in figures 10.11 through 10.13. The shear layer is seen to spread a significant amount through the domain. When restarted from the grid-aligned solution, the 5-wave model (with β now limited to be no less than 0.05 to improve stability) gives the results shown in figures 10.14 through 10.16. For this case the wave-propagation directions are computed once at restart, then remain frozen for the remainder of the computation. The shear layer is preserved with relatively few interior points using the 5-wave model. Although not shown, the pressure field is computed in error from the exact solution (of no pressure change at all through the shear layer) by about 23% using the grid-aligned model, while the 5-wave model solution is only about 5% in error.

In-plane Mach contours from a second-order computation using the grid-aligned model are given in figure 10.17, while second-order 5-wave model results, restarted from the first-order grid-aligned solution with the wave-propagation directions frozen, are given in figure 10.18. Even with second-order spatial accuracy the 5-wave model gives significantly higher shear-layer resolution than the grid-aligned model. The pressure field, not shown, is also computed more accurately. It is about 5% in error from the exact solution, while the grid-aligned result is about 10% in error.

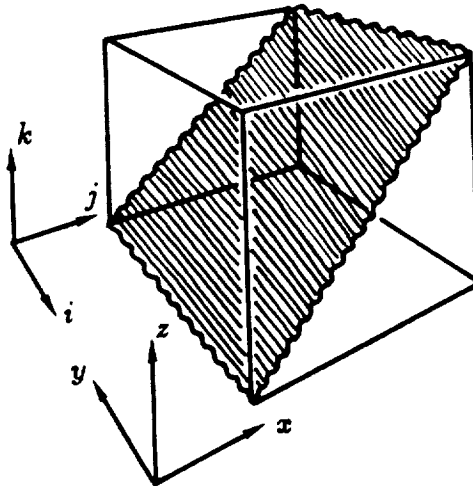
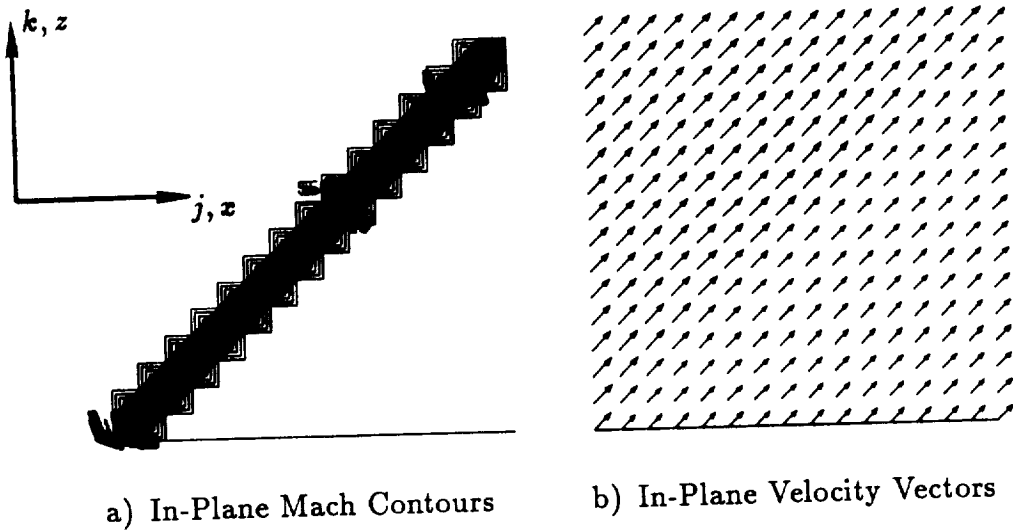


Figure 10.7: Shear Layer Orientation Within Cube



a) In-Plane Mach Contours

b) In-Plane Velocity Vectors

Figure 10.8: Oblique Shear, Exact Solution, $i = 9$ Plane

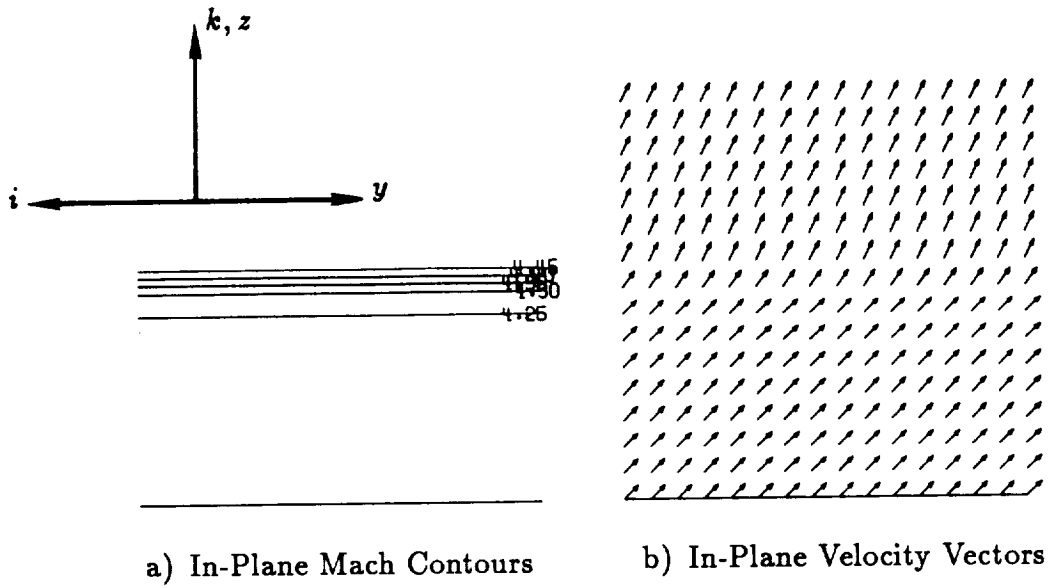


Figure 10.9: Oblique Shear, Exact Solution, $j = 9$ Plane

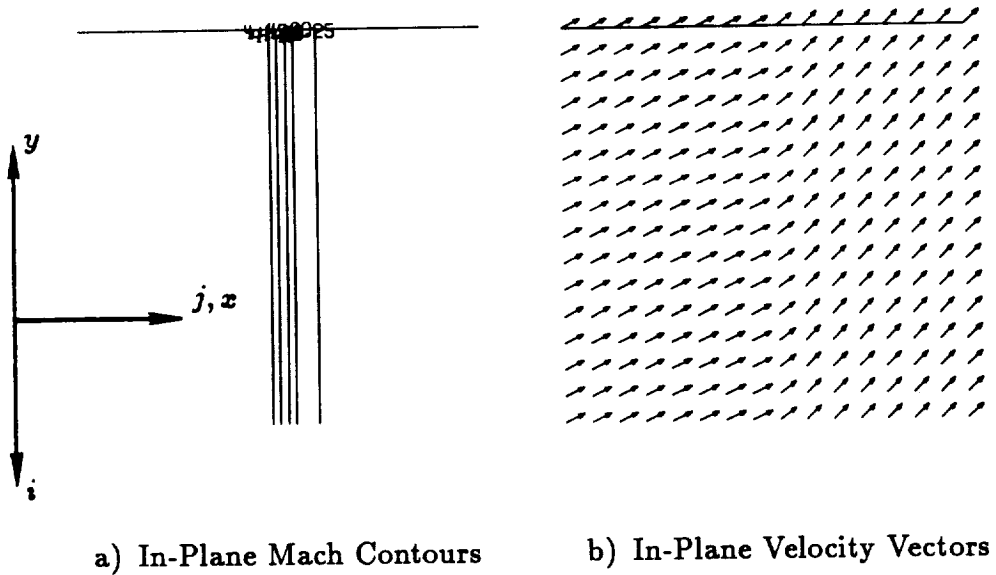
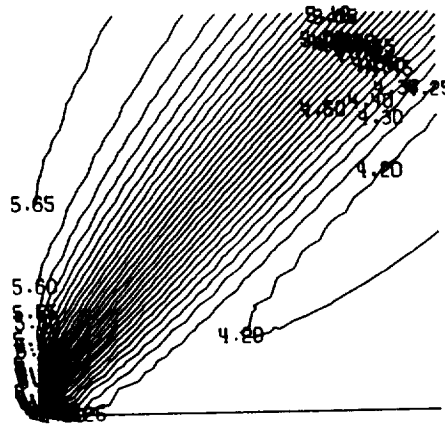
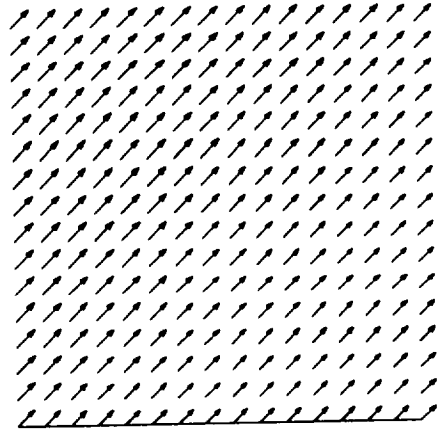


Figure 10.10: Oblique Shear, Exact Solution, $k = 9$ Plane

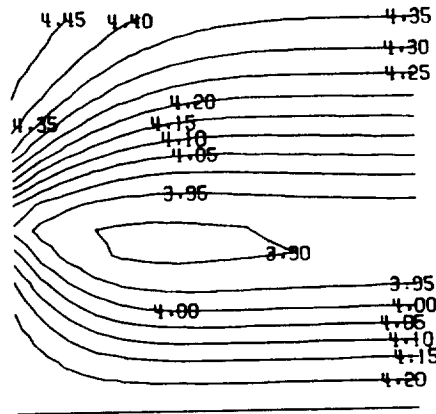


a) In-Plane Mach Contours

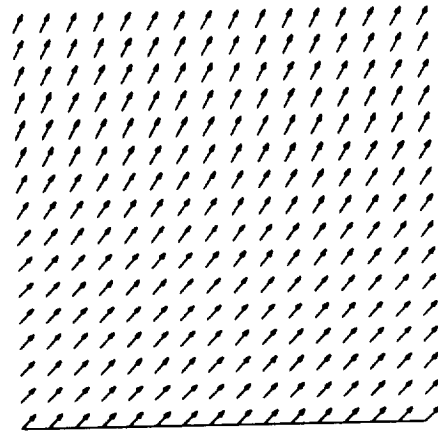


b) In-Plane Velocity Vectors

Figure 10.11: Oblique Shear, First-Order, Grid-Aligned, $i = 9$ Plane

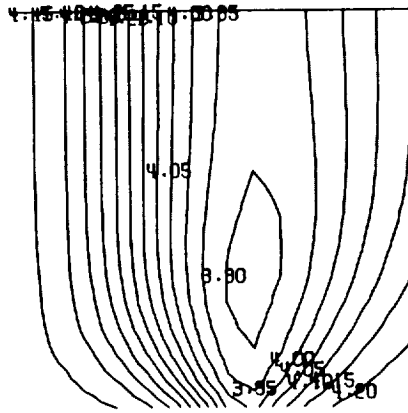


a) In-Plane Mach Contours

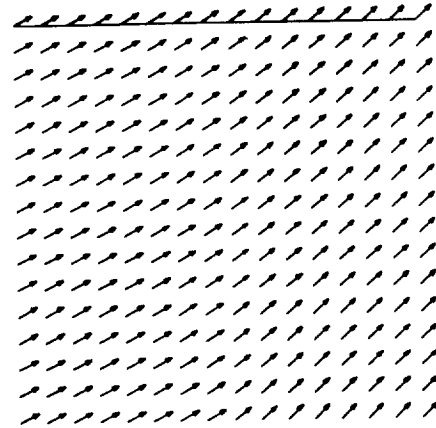


b) In-Plane Velocity Vectors

Figure 10.12: Oblique Shear, First-Order, Grid-Aligned, $j = 9$ Plane

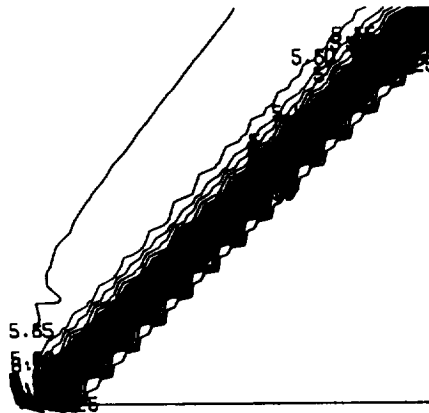


a) In-Plane Mach Contours

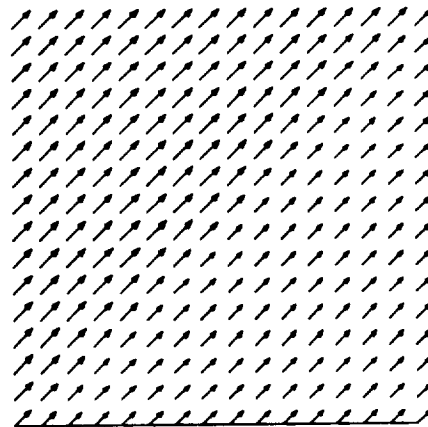


b) In-Plane Velocity Vectors

Figure 10.13: Oblique Shear, First-Order, Grid-Aligned, $k = 9$ Plane

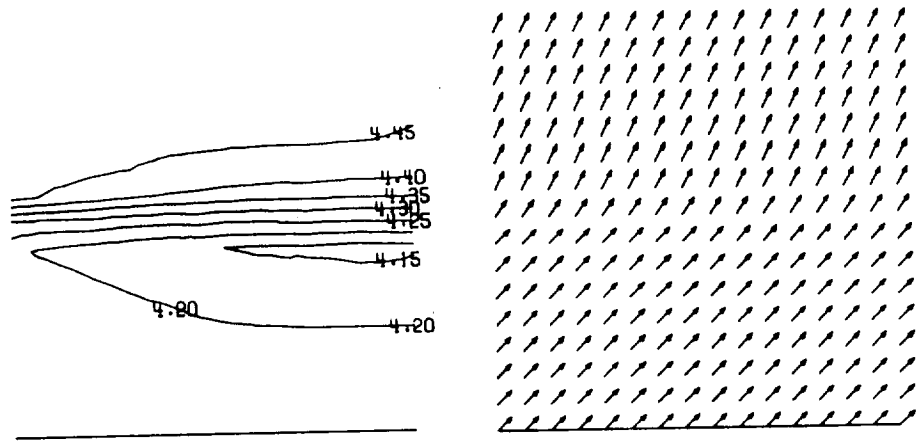


a) In-Plane Mach Contours



b) In-Plane Velocity Vectors

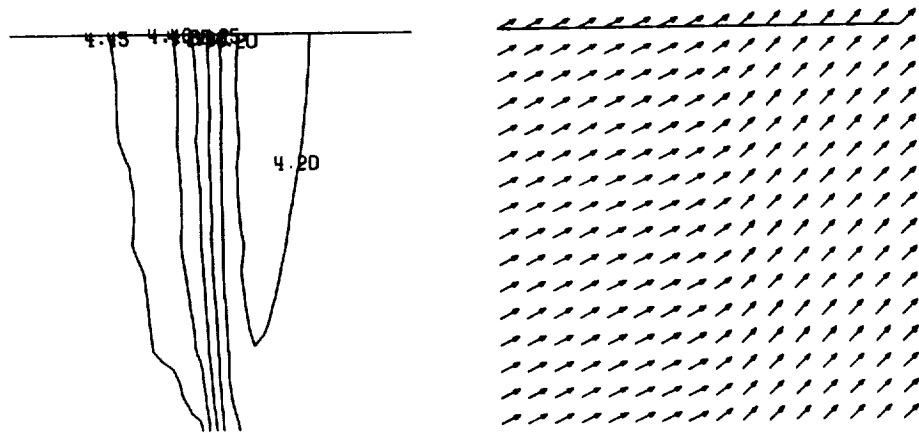
Figure 10.14: Oblique Shear, First-Order, 5-Wave, $i = 9$ Plane



a) In-Plane Mach Contours

b) In-Plane Velocity Vectors

Figure 10.15: Oblique Shear, First-Order, 5-Wave, $j = 9$ Plane



a) In-Plane Mach Contours

b) In-Plane Velocity Vectors

Figure 10.16: Oblique Shear, First-Order, 5-Wave, $k = 9$ Plane

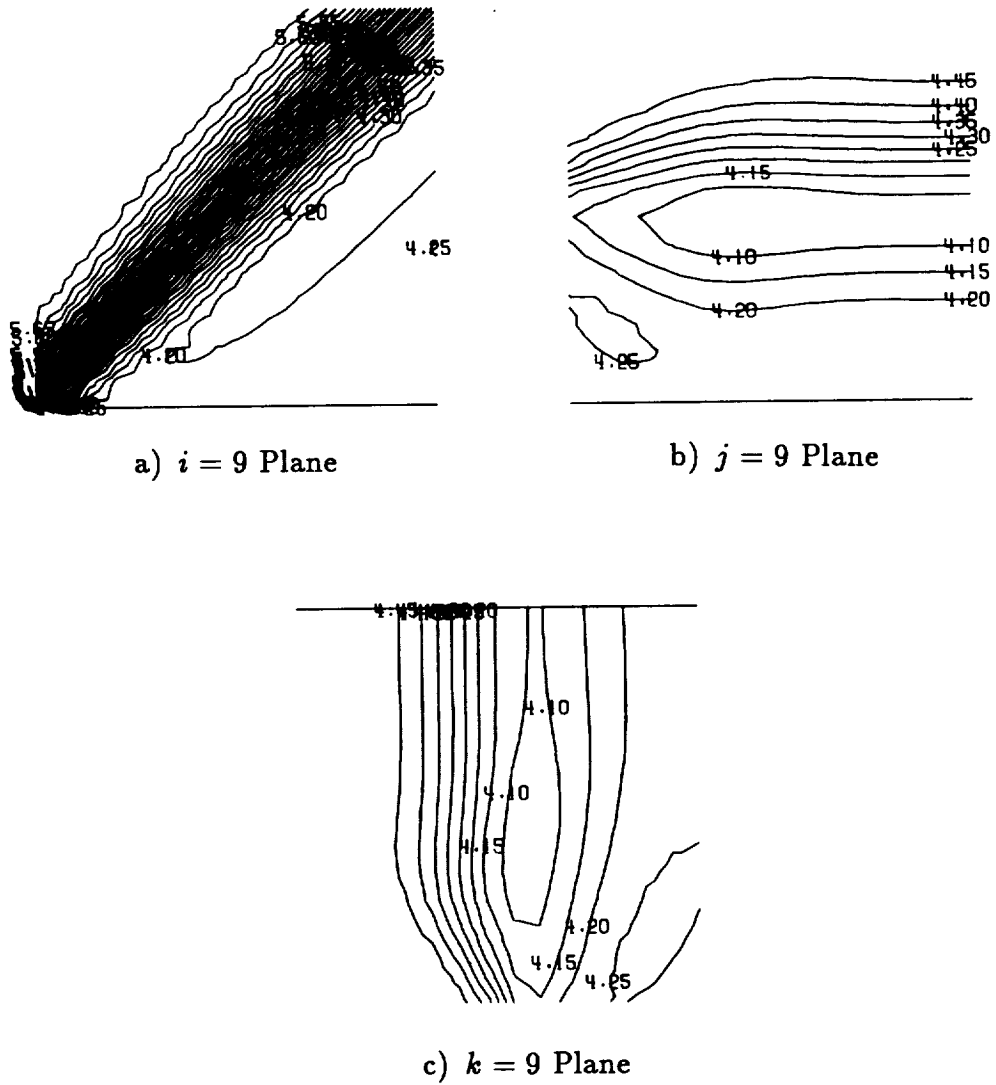


Figure 10.17: Oblique Shear, In-Plane Mach Contours, Second-Order, Grid-Aligned

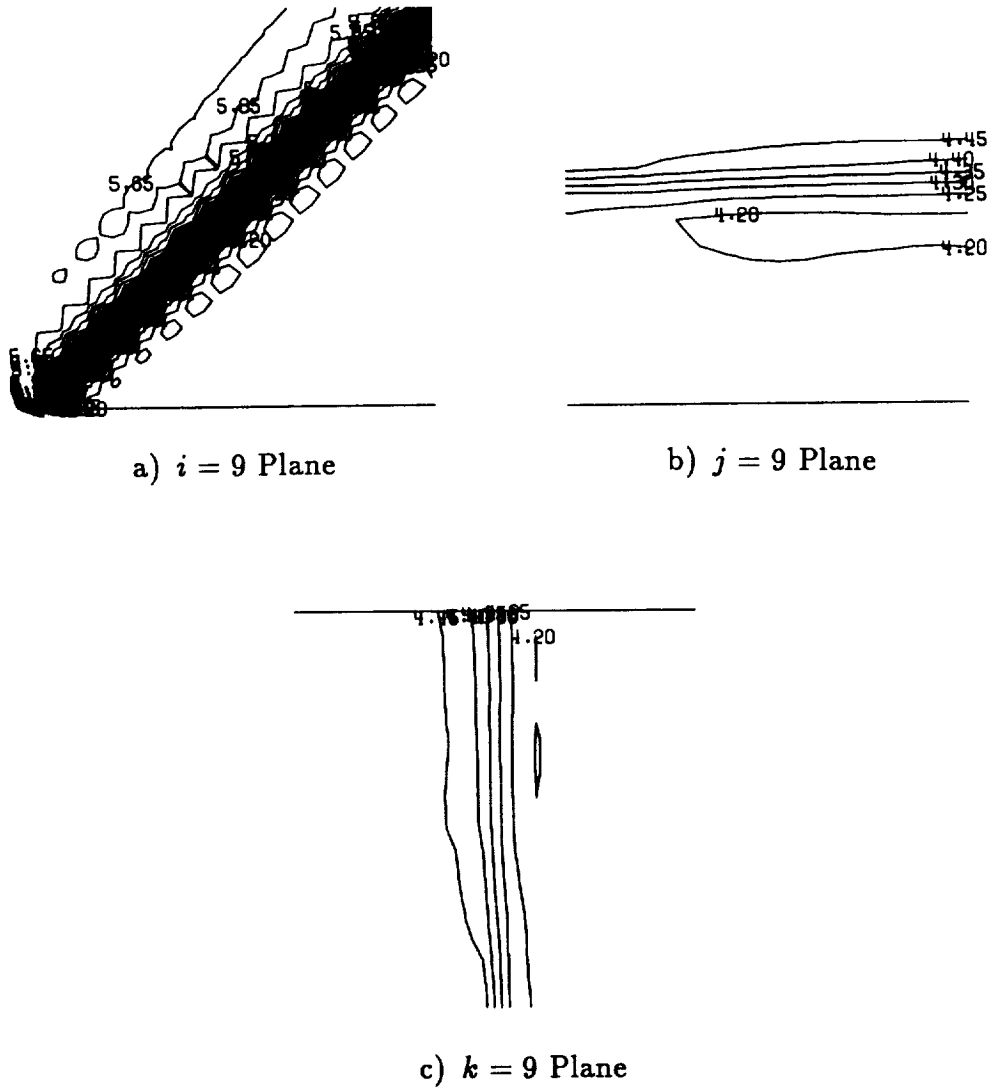


Figure 10.18: Oblique Shear, In-Plane Mach Contours, Second-Order, 5-Wave

10.3 Transonic Flow Over a Wing

Transonic flow is computed over the F-5 wing at the conditions $M = 0.95$, $\alpha = 0^\circ$. This wing has a root chord to tip chord to wing span ratio of $1.027 : 0.316 : 1.0$. A $97 \times 17 \times 17$ C-H grid is used, with maximum outer boundary extent of about 20 wing spans, and average normal spacing at the body of 0.0118 wing spans. The grid extends about one wing span past the wing tip, and there are 560 cells on the wing surface. A cut-a-way view of this grid, with the wing delineated by a heavy line, is shown in figure 10.19. Standard reflection boundary conditions are employed at the wing surface, and subsonic inflow/outflow boundary conditions (as described in section 8.1.5) are employed at the farfield boundaries.

Pressure contours at three $i = \text{constant}$ sections over the wing and pressure contours on the upper surface of the wing for a first-order computation using the grid-aligned model are shown in figure 10.20. Pressure values are plotted in increments of 0.02. Since the shock waves over the wing are more or less aligned with grid faces, the grid-aligned method captures these very sharply. Entropy contours at the same locations (plotted in increments of 0.002) are shown in figure 10.21.

The 5-wave model is run with first-order spatial accuracy by restarting the grid-aligned result with the wave-propagation directions frozen. Pressure contours are given in figure 10.22 and entropy contours are given in figure 10.23. The 5-wave model does not improve the shock resolution for this case. In fact, although the shock resolution is similar for both models over much of the wing, the 5-wave model actually shows worse resolution near the wing root. The reason for this is most likely due to the current strategy for freezing β and the propagation directions after the first iteration. Since the shocks are nearly aligned with the grid faces,

the grid-aligned model is already optimum for capturing them accurately. Any small difference in the wave-propagation direction and/or any numerical value of β lower than 1.0 near the shock waves contributes to a degradation of the result.

However, similar to the two-dimensional airfoil results, the 5-wave model also yields lower entropy generation over the wing than the grid-aligned model. (An "exact" solution would give no entropy generation except through the shocks.) The maximum values generated on the wing upper surface (figures 10.21(d) and 10.23(d)) are 0.0393 for grid-aligned and 0.0284 for 5-wave.

As this wing case demonstrates, the 5-wave model cannot give improved shock-resolution over the grid-aligned method when shock waves are aligned with grid-faces. However, as in two dimensions, it does produce lower numerically-generated entropy values near the body surface when first-order spatial accuracy is employed. Second-order computations are not performed for this case. However, it is expected that results would follow the trends exhibited for two-dimensional airfoil flow, and the 5-wave model would show no discernible advantage over the grid-aligned model.

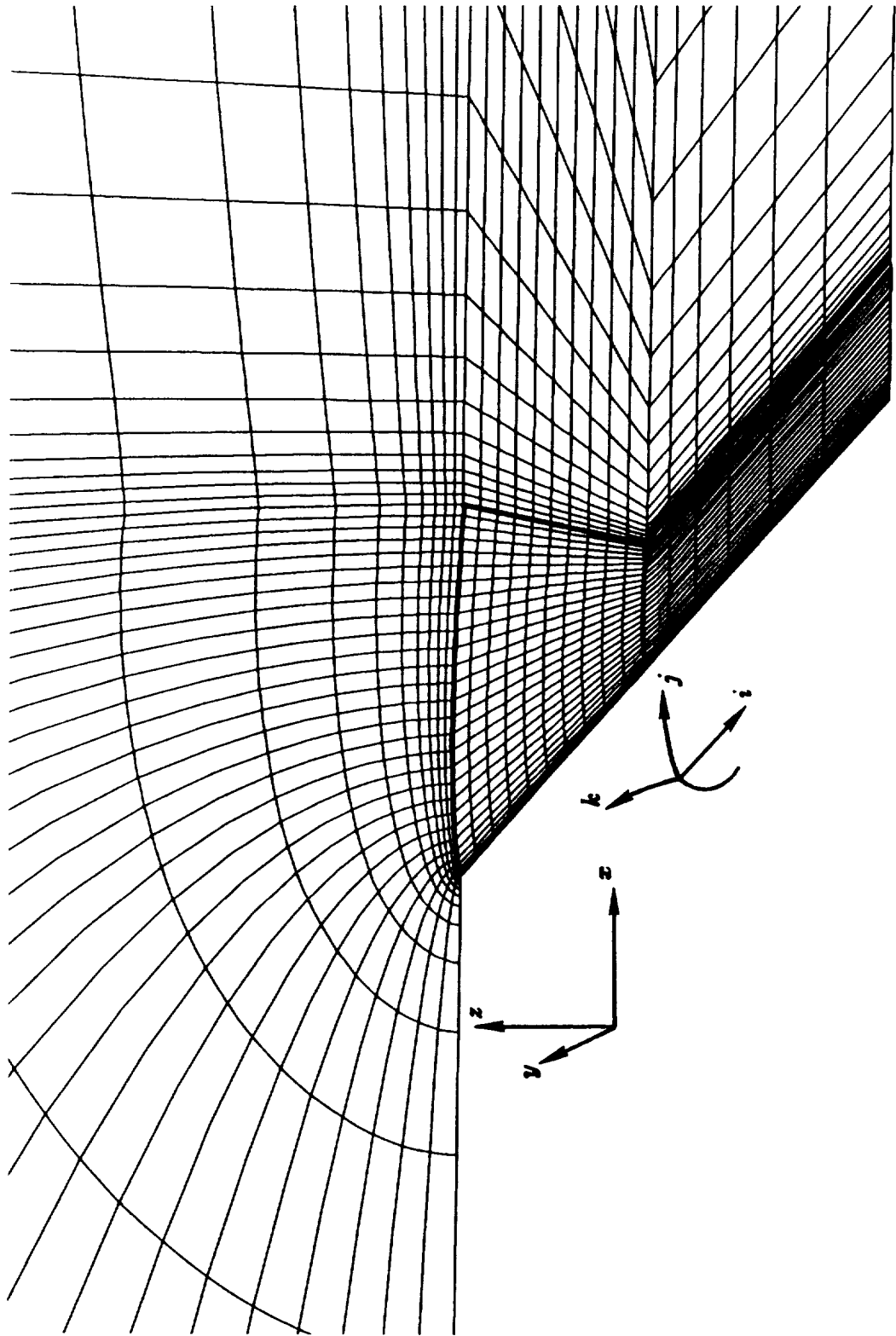


Figure 10.19: Cut-a-Way View of F-5 Wing $97 \times 17 \times 17$ C-H Grid

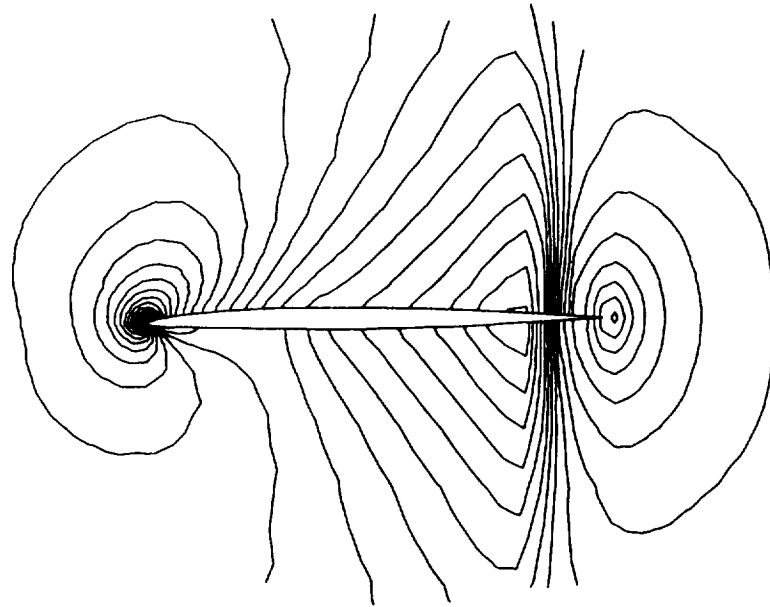
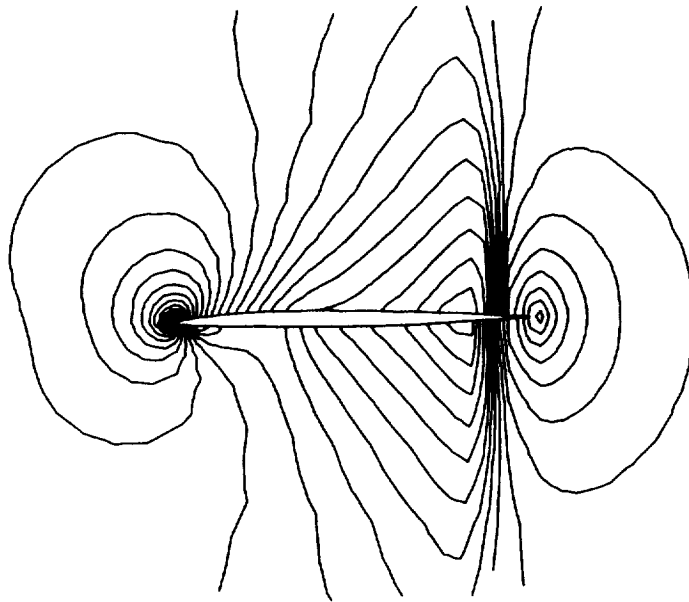
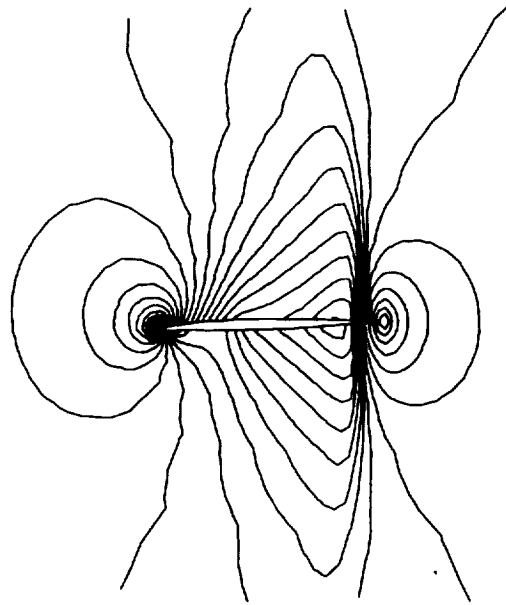
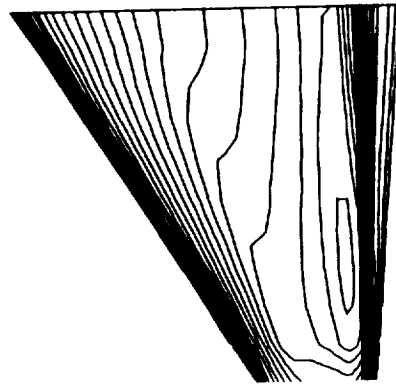
a) $i = 2$ Planeb) $i = 5$ Plane

Figure 10.20: F-5 Wing, Pressure Contours, First-Order, Grid-Aligned

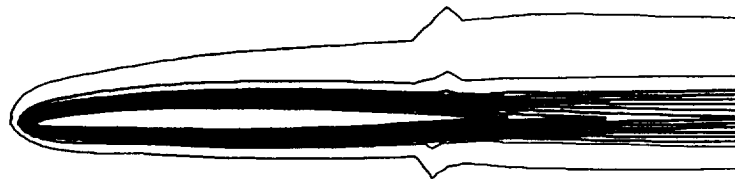
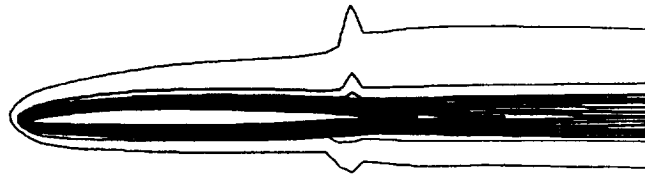
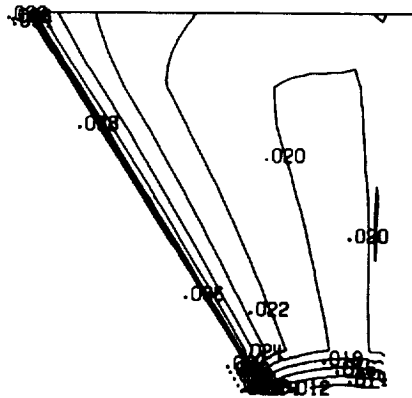


c) $i = 9$ Plane



d) Wing Upper Surface

Figure 10.20: Concluded

a) $i = 2$ Planeb) $i = 5$ Planec) $i = 9$ Plane

d) Wing Upper Surface

Figure 10.21: F-5 Wing, Entropy Contours, First-Order, Grid-Aligned

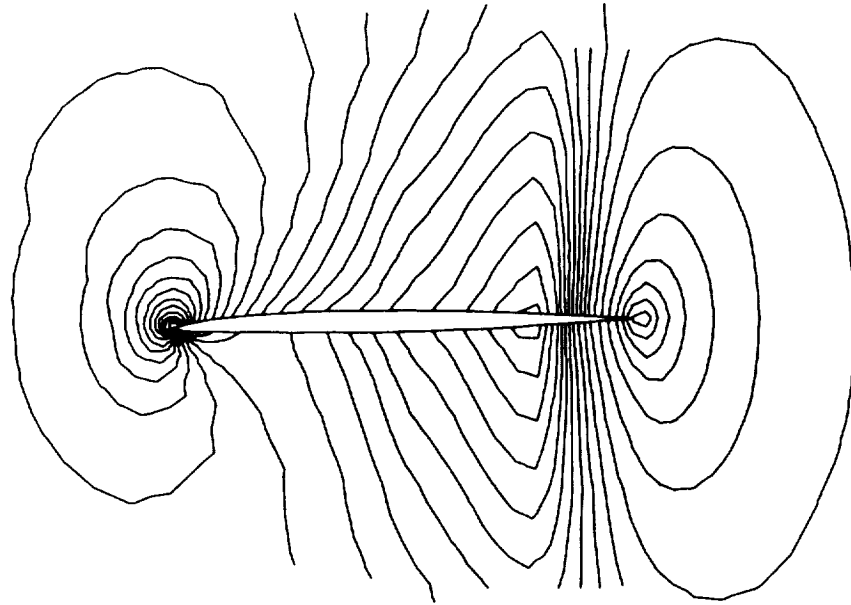
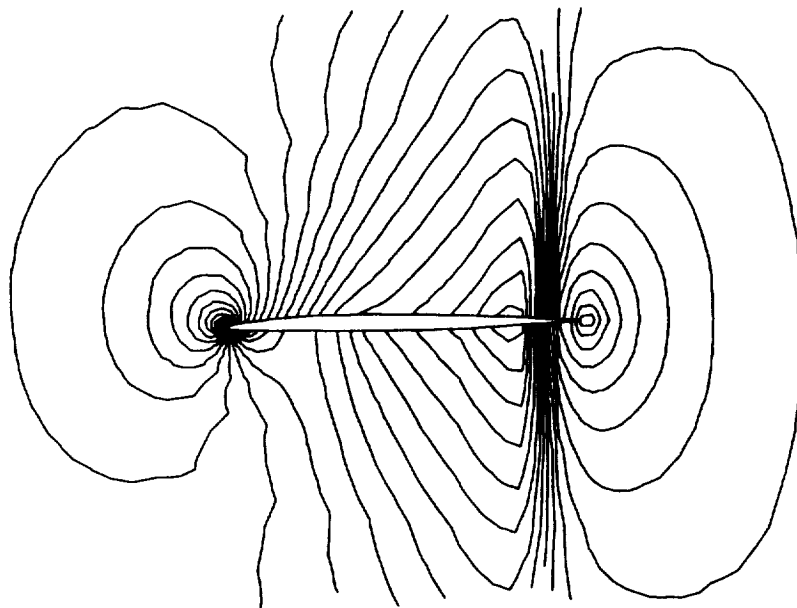
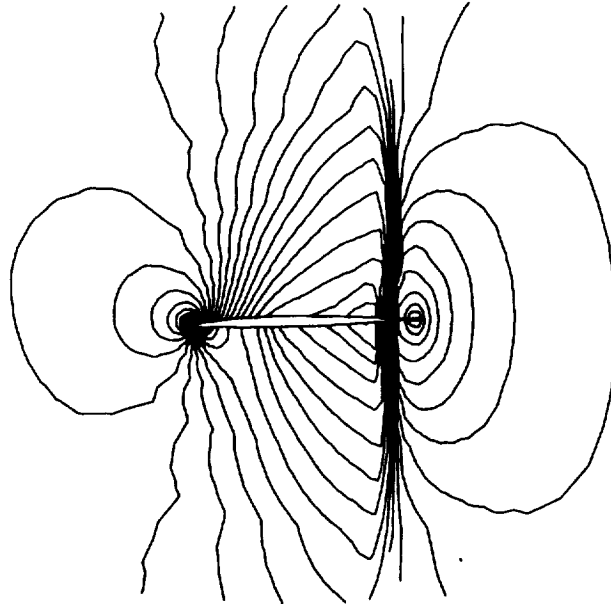
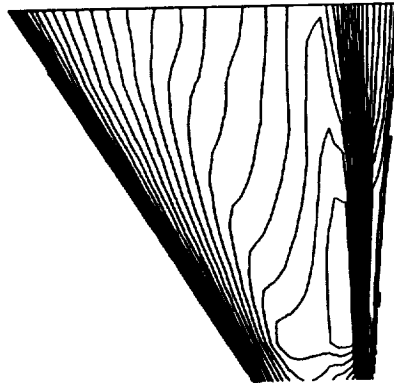
a) $i = 2$ Planeb) $i = 5$ Plane

Figure 10.22: F-5 Wing, Pressure Contours, First-Order, 5-Wave

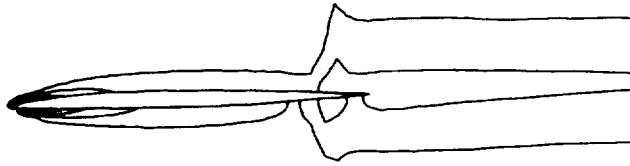
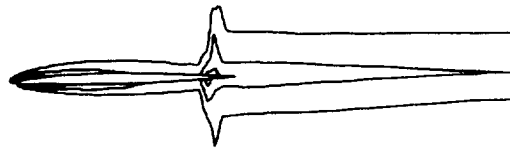
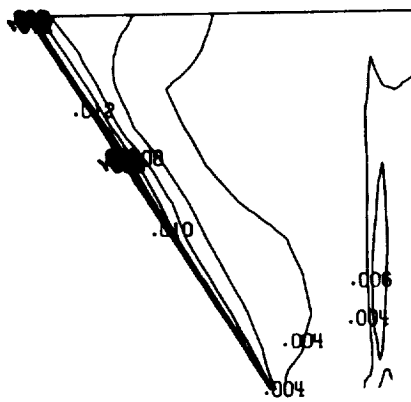


c) $i = 9$ Plane



d) Wing Upper Surface

Figure 10.22: Concluded

a) $i = 2$ Planeb) $i = 5$ Planec) $i = 9$ Plane

d) Wing Upper Surface

Figure 10.23: F-5 Wing, Entropy Contours, First-Order, 5-Wave

CHAPTER 11

CONCLUSIONS

The main object of the current research is to introduce and explore a grid-independent approximate Riemann solver for use with the Euler and Navier-Stokes equations. The primary reason for attempting a grid-independent method is to model the physics of the true two or three-dimensional flow more accurately. Most current multidimensional flow solvers that employ a Riemann solver implement it in a “direction-split” manner, *i.e.* one-dimensional theory is applied in each grid direction separately. In reality, however, the waves can travel in infinitely many directions. Constraining them to the grid directions is inconsistent with the physics of the flow and can result in improper interpretation of waves that are not aligned with the grid.

The current grid-independent model utilizes the velocity-difference direction as the direction of propagation of most of the waves, with an additional shear wave propagating 90° to this. Use of the velocity-difference direction as the dominant direction allows for more accurate interpretation of both shock and shear waves when they lie oblique to the grid. The direction is generally frozen during a computation to eliminate nonlinear feedback in the solution and aid convergence.

Simple left and right states obtained by interpolation along grid lines are used at each interface as the initial conditions for a Riemann problem. The difference in states is decomposed into a series of five waves, and the standard upwind flux

formula is employed to determine the flux at each face. It is shown in the derivation of the 5-wave model that the standard flux formula is the "best" within a certain class of formulas at reproducing the flux given by two rotated Riemann solvers.

A stability analysis of the 5-wave model in conjunction with the two-dimensional Euler equations, advanced in time using explicit time-marching, shows that some modes of the Fourier footprint contain eigenvalues that lie on the imaginary axis. Hence the stability boundary of the time-marching scheme must include a finite portion of the imaginary axis as well. Since only multistage schemes can satisfy this requirement, a four-stage scheme is chosen. It is stable up to CFL numbers of about 1.75 for first-order spatial accuracy and 0.87 for second-order, although in practice these restrictions can generally be relaxed somewhat.

An implicit approximate-factorization algorithm is shown to be stable only up to a CFL number of about 2.5 for first-order and 0.3 for second-order when the 5-wave model is employed on the right-hand side and first-order accurate grid-aligned approximate Jacobians are employed on the left-hand side. Again these CFL numbers are somewhat overrestrictive for most practical applications. When a grid-independent left-hand side approximate Jacobian is employed, first-order computations can be made unconditionally stable. Using a linearized analysis, second-order computations are shown to be unconditionally stable if block-pentadiagonal systems (as opposed to tridiagonal systems) are solved with appropriately chosen grid-independent approximate Jacobians. Maximum CFL numbers of about 100 can be attained in practice with this strategy, although the optimum CFL number for convergence generally lies between 2 and 6.

The monotonicity of the 5-wave model in conjunction with the two-dimensional Euler equations has also been investigated. Using a linearized analysis, it is shown that strictly only the grid-aligned first-order method is monotone. However, it is shown that the oscillations that occur near discontinuities can be reduced in

magnitude to acceptable levels for a wide variety of problems by limiting the wave-propagation directions of the 5-wave model according to a strategy suggested by the linearized analysis. This gain in monotonicity does result in the loss of some of the high resolution of oblique shock and shear waves, although the resolution is still generally greater than results using the grid-aligned scheme.

Two-dimensional results obtained using the 5-wave model indicate that the method is usually worthwhile for first-order computations. Flows with oblique shock or shear waves are captured more sharply than results using the grid-aligned method, even when the θ'_d -limiter is employed to reduce oscillations. Also, subsonic Euler airfoil flow computations show significantly reduced entropy generation over the airfoil surface, resulting in better drag prediction. The 5-wave model is about 1.2 times more costly per iteration than the grid-aligned model when no θ'_d -limiting is employed, and about 1.5 times more costly when it is. Hence the cost penalty is not severe considering the increased accuracy of the first-order solutions.

When second-order spatial accuracy is employed, the small increase in accuracy attained by the 5-wave model is generally not worth the added drawbacks. In particular, oblique shock waves are resolved only slightly more sharply than when using the grid-aligned method, and there is very little decrease in the numerical entropy generation for a subsonic airfoil computation. These facts, taken in combination with a propensity for increased oscillatory behavior near discontinuities, makes the 5-wave model an unattractive alternative to the grid-aligned model in general. The only notable exceptions to this conclusion are found in the pure supersonic oblique shear wave computation and the separated viscous airfoil flow computation. In the first case, the 5-wave model still gives significant improved resolution of the shear wave over results using the grid-aligned model. In the second case, numerical pressure oscillations evident in the separated region over

the airfoil upper surface using the grid-aligned model are dramatically reduced by the 5-wave model, which properly interprets the oblique shear waves present in the flowfield. Hence in specialized cases involving oblique shear waves, the 5-wave model in a second-order accurate computation can be worth the additional expense.

In the arena of second-order viscous flow computations, it should be noted that on very coarse grids the 5-wave model can do a much worse job than the grid-aligned model at resolving the boundary layer (for flat-plate flow) and predicting surface pressure values (for airfoil flow). The two models approach the same results as the mesh is refined, however, so as long as a fine enough grid is employed the 5-wave model will be accurate in these areas. This problem is particularly evident in the viscous separated airfoil flow case, where the 5-wave model result over the coarsest (65×25) grid *looks* better than the grid-aligned result, since the pressure distortions in the flowfield have been reduced. However, the lift predicted by the 5-wave model is about 120% too high due to its inaccurate surface pressure predictions. The grid-aligned model, plagued as it is with pressure deviations in the separated region above the airfoil, is only high in its lift prediction by about 8%.

The 5-wave model is also extended to three dimensions. The velocity-difference direction is again chosen as the primary wave propagation direction, and the difference in states can still be described by a series of five waves. One of these waves is a shear wave which is assumed to propagate normal to the plane spanned by \vec{V}_L and \vec{V}_R . Hence the velocity of this shear wave is identically zero when the wave propagation directions are not frozen. Oblique shear waves through which the velocity undergoes a change in magnitude and/or undergoes a rotation can be captured sharply by this method.

A stability analysis of the 5-wave model in three dimensions gives results

similar to those of the analysis in two dimensions, only with slightly lower stability limits. An explicit four-stage time marching scheme is stable up to CFL numbers of about 1.55 for first-order spatial accuracy and 0.77 for second-order. An implicit approximate-factorization algorithm with a first-order grid-aligned approximate left-hand side is stable up to a CFL number of about 1.5 for first-order and 0.3 for second-order.

The monotonicity properties in three dimensions are also investigated using a linearized analysis. Again, in a strict sense, only the grid-aligned first-order model turns out to be monotone. It is believed that a relaxation of this restriction on the wave-propagation direction similar to that in two dimensions can be employed in order to improve the monotonicity properties of the 5-wave model, but this has not been attempted in this study due to the complexity inherent in three dimensions. In any case, the extra degree of freedom in three dimensions seems to relieve some of the oscillation problems present in two dimensions when the 5-wave model is used.

Conclusions from three-dimensional Euler test cases run along similar lines to those from two dimensions. For a ramp flow with oblique shock waves, the 5-wave model improves the shock resolution considerably in a first-order computation, making the model worth the effort and additional expense. However, a second-order computation shows very little difference from a grid-aligned computation. This fact, taken in conjunction with the fact that the 5-wave model costs more and yields slightly increased oscillatory behavior over the grid-aligned method, makes the 5-wave model impractical for use with this type of problem using second-order spatial accuracy.

An oblique supersonic shear wave, on the other hand, is resolved better using the 5-wave model for both first and second-order accurate computations. This is similar to the result in two dimensions. Extrapolating from the two-dimensional

results, then, it is likely that the 5-wave model would also do well for a three-dimensional separated viscous flow computation similar to the NACA 0012 airfoil case. Three-dimensional viscous flow computations were not attempted in this study.

A first-order Euler computation performed over an F-5 wing using the 5-wave model produces lower entropy values over most of the the wing surface than the grid-aligned model. Since the shock waves for this case are aligned with grid faces for the most part, the 5-wave model does not improve their resolution over the grid-aligned model. Second-order computations on this configuration were not performed. However, results are expected to be similar in nature to the two-dimensional results, with little to no improvement in numerical entropy generation using the 5-wave model over the grid-aligned model.

Overall, for both two and three-dimensional computations, the 5-wave model is seen to be worth the additional effort only for first-order spatially-accurate computations, or computations involving only oblique shear waves. In general, inviscid flows with shock waves and/or flows with no shock or shear waves at all are better computed using the grid-aligned wave model when accuracy greater than first-order is desired. The additional expense and oscillation-prone nature of the 5-wave model makes it unattractive for use in such cases.

Despite its shortcomings, the 5-wave model can be thought of as a "step in the right direction" toward modeling the multidimensional flow physics of the Euler and Navier-Stokes equations more accurately than the grid-aligned model. Future work may best be focused on removing the inconsistency in the model (discussed in section 5.4) that does not allow it to reduce to the grid-aligned model when $\theta'_d = \theta_g$ unless $\beta = 1$. Although theoretically it seems that this would be a desirable property to meet, it is not known what the ramifications of *not* meeting it are. Possible avenues of investigation toward eliminating the inconsistency,

while still maintaining sharp resolution of oblique shear waves, might include experimentation with different types and directions of waves as well as varying the flux formula itself. Further efforts toward improving the grid-independent flux function might focus on a different type of limiting to improve the monotonicity properties of the method. Perhaps by limiting the left and right input states to the Riemann problem, rather than the wave-propagation directions, greater resolution of oblique waves might be maintained for both first and second-order accurate computations. Also, the extension to limiting in three dimensions might be more straightforward than the current angle-limiting procedure.

The current research has purposefully begun with the assumption that only the left and right states at each interface, obtained by interpolation along grid lines, are known at the beginning of the flux function computation. It is then up to the model to make the most of these input states, and infer from them the types and directions of waves likely to be present. This assumption was made to keep the cost of the grid-independent flux function as low as possible. By ignoring surrounding flowfield data, no complex interpolations are required to obtain gradients in non-grid-oriented directions. However, perhaps this initial assumption was unrealistic, and the inclusion of some multidimensional input states might be helpful or even necessary to improve the robustness of the model, particularly for second and higher-order accurate computations.

APPENDICES

APPENDIX A
DERIVATION OF β FOR THE MINIMUM-PATHLENGTH
AND MINIMUM-AREA MODELS

A.1 Minimum-Pathlength Model

As discussed in Chapter 5, the right state R lies inside the acoustic cone emanating from the origin when

$$(\Delta p)^2 \geq [\hat{\rho}\hat{a}(\Delta u \cos\theta_d + \Delta v \sin\theta_d)]^2, \quad (\text{A.1})$$

and the difference in states is described by two acoustic waves and an entropy wave. When θ_d is frozen as θ'_d , then the method is modified as follows. If the projection (R') of the right state R onto the θ'_d -plane lies inside the acoustic cone, then two θ'_d acoustic waves and an entropy wave are used, along with the necessary θ'_d shear wave to connect R with R'. The condition becomes:

$$(\Delta p)^2 \geq [\hat{\rho}\hat{a}\Delta q'_d]^2, \quad (\text{A.2})$$

where $\Delta q'_d$ is defined as

$$\Delta q'_d \equiv \Delta u \cos\theta'_d + \Delta v \sin\theta'_d. \quad (\text{A.3})$$

The wavenumbers $\hat{\Omega}_k$ must be determined which satisfy

$$\Delta \mathbf{W} = \sum_{k=1}^4 \hat{\Omega}_k \hat{\mathbf{P}}_k, \quad (\text{A.4})$$

where the $+\theta'_d$ acoustic, $-\theta'_d$ acoustic, entropy, and θ'_d shear are given by:

$$\begin{aligned}\hat{\mathbf{P}}_1 &= \left[1, \frac{\hat{a}}{\hat{\rho}} \cos\theta'_d, \frac{\hat{a}}{\hat{\rho}} \sin\theta'_d, \hat{a}^2 \right]^T \\ \hat{\mathbf{P}}_2 &= \left[1, -\frac{\hat{a}}{\hat{\rho}} \cos\theta'_d, -\frac{\hat{a}}{\hat{\rho}} \sin\theta'_d, \hat{a}^2 \right]^T \\ \mathbf{P}_3 &= [1, 0, 0, 0]^T \\ \hat{\mathbf{P}}_4 &= \left[0, -\frac{\hat{a}}{\hat{\rho}} \sin\theta'_d, \frac{\hat{a}}{\hat{\rho}} \cos\theta'_d, 0 \right]^T.\end{aligned}\tag{A.5}$$

These strengths turn out to be:

$$\hat{\Omega} = \begin{bmatrix} \frac{\Delta p}{2\hat{a}^2} + \frac{\hat{p}}{2\hat{a}} \Delta q'_d \\ \frac{\Delta p}{2\hat{a}^2} - \frac{\hat{p}}{2\hat{a}} \Delta q'_d \\ \frac{1}{\hat{a}^2} (\hat{a}^2 \Delta \rho - \Delta p) \\ \frac{\hat{p}}{\hat{a}} (-\Delta u \sin\theta'_d + \Delta v \cos\theta'_d) \end{bmatrix}.\tag{A.6}$$

Similarly, the condition for which one θ'_d acoustic, a $(\theta'_d + \frac{\pi}{2})$ shear, and an entropy wave (along with the necessary θ'_d shear wave) are used is

$$(\Delta p)^2 < [\hat{p}\hat{a}\Delta q'_d]^2.\tag{A.7}$$

This indicates that the projection of the right state R onto the θ'_d -plane lies outside the acoustic cone. Again wavestrengths must be determined such that (A.4) is satisfied, but this time the waves are

$$\begin{aligned}\hat{\mathbf{P}}_1 &= \left[1, \pm \frac{\hat{a}}{\hat{\rho}} \cos\theta'_d, \pm \frac{\hat{a}}{\hat{\rho}} \sin\theta'_d, \hat{a}^2 \right]^T \\ \hat{\mathbf{P}}_2 &= \left[0, -\frac{\hat{a}}{\hat{\rho}} \cos\theta'_d, -\frac{\hat{a}}{\hat{\rho}} \sin\theta'_d, 0 \right]^T \\ \mathbf{P}_3 &= [1, 0, 0, 0]^T \\ \hat{\mathbf{P}}_4 &= \left[0, -\frac{\hat{a}}{\hat{\rho}} \sin\theta'_d, \frac{\hat{a}}{\hat{\rho}} \cos\theta'_d, 0 \right]^T,\end{aligned}\tag{A.8}$$

where the + or - acoustic wave is chosen depending upon which minimizes the pathlength in $(\Delta u, \Delta v, \Delta p)$ -space. The strengths turn out to be:

$$\hat{\Omega} = \begin{bmatrix} \frac{\Delta p}{\hat{a}^2} \\ \pm \frac{\Delta p}{\hat{a}^2} - \frac{\hat{p}}{\hat{a}} \Delta q'_d \\ \frac{1}{\hat{a}^2} (\hat{a}^2 \Delta \rho - \Delta p) \\ \frac{\hat{p}}{\hat{a}} (-\Delta u \sin\theta'_d + \Delta v \cos\theta'_d) \end{bmatrix}.\tag{A.9}$$

The equations (A.6) and (A.9) can be combined as the 5-wave model described in Chapter 5, with strengths

$$\hat{\Omega} = \begin{bmatrix} \frac{\Delta p}{2\hat{a}^2} + \beta \frac{\hat{\rho}}{2\hat{a}} \Delta q'_d \\ \frac{\Delta p}{2\hat{a}^2} - \beta \frac{\hat{\rho}}{2\hat{a}} \Delta q'_d \\ (\beta - 1) \frac{\hat{\rho}}{\hat{a}} \Delta q'_d \\ \frac{1}{\hat{a}^2} (\hat{a}^2 \Delta \rho - \Delta p) \\ \frac{\hat{\rho}}{\hat{a}} (-\Delta u \sin \theta'_d + \Delta v \cos \theta'_d) \end{bmatrix} \quad (\text{A.10})$$

for the $+\theta'_d$ acoustic, $-\theta'_d$ acoustic, $(\theta'_d + \frac{\pi}{2})$ shear, entropy, and θ'_d shear, respectively. The variable β is given by

$$\beta = \min [|\zeta|, 1], \quad (\text{A.11})$$

where ζ is defined as

$$\zeta \equiv \frac{\Delta p / (\hat{\rho} \hat{a})}{\Delta q'_d}. \quad (\text{A.12})$$

When (A.2) is true,

$$|\zeta| \geq 1, \quad (\text{A.13})$$

so $\beta = 1$ and the strengths (A.6) are recovered. When (A.7) is true, β is assigned the value of ζ . If Δp and $\Delta q'_d$ both have the same sign:

$$\begin{aligned} \hat{\Omega}_1 &= \frac{\Delta p}{\hat{a}^2} \\ \hat{\Omega}_2 &= 0 \\ \hat{\Omega}_3 &= \frac{\Delta p}{\hat{a}^2} - \frac{\hat{\rho}}{\hat{a}} \Delta q'_d \end{aligned} \quad (\text{A.14})$$

and (A.9) with the +acoustic wave is recovered. If Δp and $\Delta q'_d$ have opposite signs:

$$\begin{aligned} \hat{\Omega}_1 &= 0 \\ \hat{\Omega}_2 &= \frac{\Delta p}{\hat{a}^2} \\ \hat{\Omega}_3 &= -\frac{\Delta p}{\hat{a}^2} - \frac{\hat{\rho}}{\hat{a}} \Delta q'_d \end{aligned} \quad (\text{A.15})$$

and (A.9) with the -acoustic wave is recovered. In both cases $\hat{\Omega}_4$ and $\hat{\Omega}_5$ are the same, as given by (A.10). With this method, the proper acoustic wave is always chosen such that the $(\theta'_d + \frac{\pi}{2})$ shear wavenumber $\hat{\Omega}_3$ is minimized.

Notice that the wave patterns change in a continuous fashion as ζ goes through 1.0, as shown in figure A.1.

A.2 Minimum-Area Model

As discussed in Chapter 5, the minimum-area model picks the path in $(\Delta u, \Delta v, \Delta p)$ -space that lies, in a sense, closest to the straight line connecting L and R. It does this by minimizing the area between the paths and the straight line. When θ_d is frozen as θ'_d , this criterion is modified slightly for simplicity. A θ'_d shear wave is used to connect the right state R with R', its projection onto the θ'_d -plane. Then $+\theta'_d$ acoustic, $-\theta'_d$ acoustic, and $(\theta'_d + \frac{\pi}{2})$ shear waves are chosen which minimize the area between the wave paths and the straight line connecting L and R' in $(\Delta u, \Delta v, \Delta p)$ -space. (The entropy wave, as always, is present but only contributes to changes in density. Its strength is always $\hat{\Omega}_5 = \Delta\rho - \Delta p/\hat{a}^2$.)

When inequality (A.2) is true, two acoustics and no $(\theta'_d + \frac{\pi}{2})$ shear wave minimize the area. This is identical to the minimum-pathlength model and hence corresponds to $\beta = 1$ in (A.10). When (A.7) is true, some combination of all three waves minimizes the area. The order in which the waves are taken makes a difference in the outcome. In the present derivation they are always taken such that the first wave (from L) is an acoustic that points *away* from R' in $(\Delta u, \Delta v, \Delta p)$ -space. The second wave is the $(\theta'_d + \frac{\pi}{2})$ shear, and the third wave is the remaining acoustic. This strategy is illustrated in figure A.2. The type of acoustic that leaves L depends on the sign of Δp and the sign of $\Delta q'_d$. If Δp and $\Delta q'_d$ have the same sign, a $-\theta'_d$ acoustic leaves L, while if Δp and $\Delta q'_d$ have opposite signs, a $+\theta'_d$ acoustic leaves L.

In this derivation it is assumed that the waves have strengths given by (A.10),

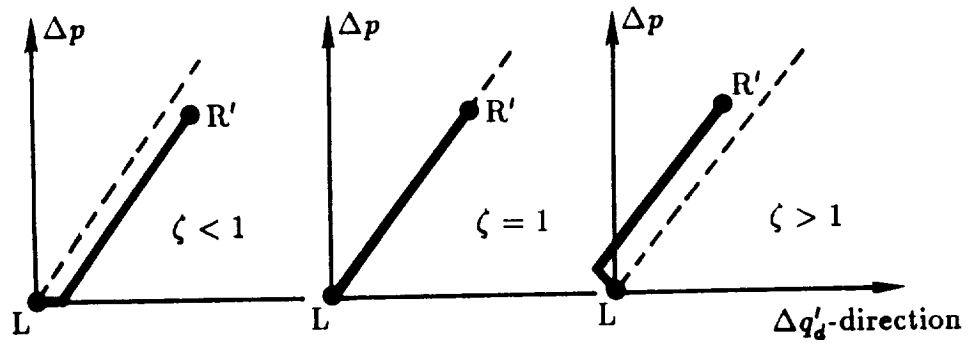


Figure A.1: Wave Patterns for Minimum-Pathlength Model

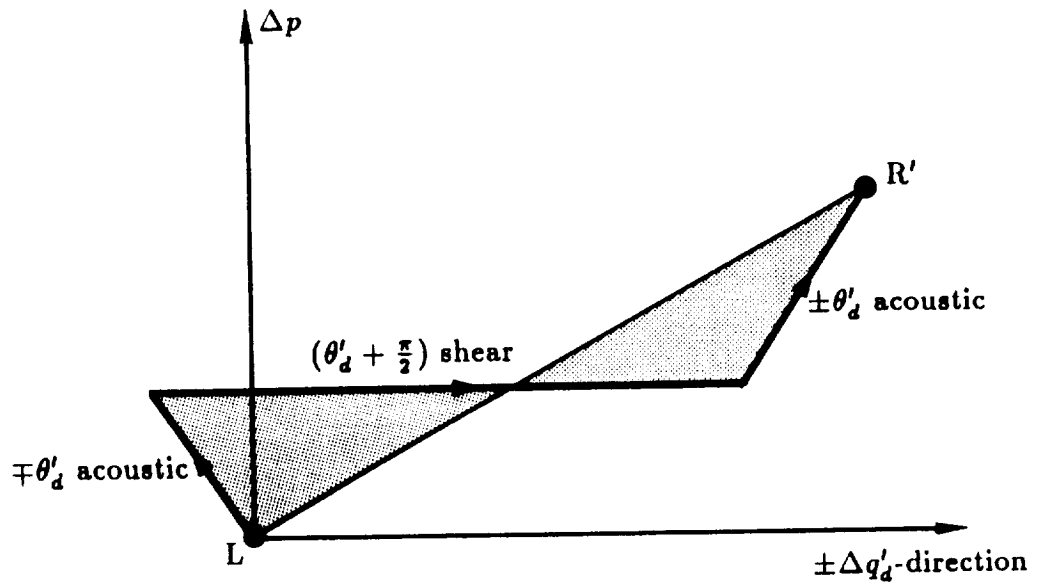


Figure A.2: Minimum-Area Model

where β is unknown. An expression for β is then determined that gives the minimum area. Figure A.3 is the same as figure A.2 with some relevant distances labeled. It is assumed for now that Δp and $\Delta q'_d$ are both positive. Hence the first wave to leave L is a $-\theta'_d$ acoustic. It turns out that the end result for β is the same regardless of the signs of Δp and $\Delta q'_d$.

From the geometry of figure A.3, the areas of the two triangles in the figure are

$$\begin{aligned} V_1 &= \frac{1}{2}(\Delta x_1 + \Delta x_3)\Delta p_1 \\ V_2 &= \frac{1}{2}\Delta x_4\Delta p_2. \end{aligned} \quad (\text{A.16})$$

Since it is known (from (A.9)) that an acoustic wave which causes a change in pressure Δp has an associated strength $\Delta p/\hat{a}^2$, Δp_1 can be found since the strength of the $-\theta'_d$ acoustic wave is known:

$$\hat{\Omega}_{-ac} = \frac{\Delta p}{2\hat{a}^2} - \beta \frac{\hat{\rho}}{2\hat{a}} \Delta q'_d. \quad (\text{A.17})$$

Therefore

$$\Delta p_1 = \frac{\Delta p}{2} - \frac{1}{2}\beta\hat{\rho}\hat{a}\Delta q'_d. \quad (\text{A.18})$$

The changes in primitive variables caused by a $\pm\theta'_d$ acoustic wave are:

$$\frac{\delta p}{\hat{\rho}\hat{a}^2} = \pm \frac{\delta u}{\hat{a}\cos\theta'_d} = \pm \frac{\delta v}{\hat{a}\sin\theta'_d}. \quad (\text{A.19})$$

From geometry, this can also be written as

$$\frac{\delta p}{\hat{\rho}\hat{a}} = \pm(\delta u\cos\theta'_d + \delta v\sin\theta'_d). \quad (\text{A.20})$$

This means that the distance Δx_1 is equal to $\Delta p_1/(\hat{\rho}\hat{a})$, or

$$\Delta x_1 = \frac{\Delta p}{2\hat{\rho}\hat{a}} - \frac{1}{2}\beta\Delta q'_d. \quad (\text{A.21})$$

Furthermore,

$$\Delta p_2 = \Delta p - \Delta p_1 = \frac{\Delta p}{2} + \frac{1}{2}\beta\hat{\rho}\hat{a}\Delta q'_d \quad (\text{A.22})$$

$$\Delta x_2 = \frac{\Delta p_2}{\hat{\rho}\hat{a}} = \frac{\Delta p}{2\hat{\rho}\hat{a}} + \frac{1}{2}\beta\Delta q'_d. \quad (\text{A.23})$$

The distance Δx_3 is found using the rule of similar triangles

$$\frac{\Delta x_3}{\Delta q'_d} = \frac{\Delta p_1}{\Delta p}, \quad (\text{A.24})$$

or

$$\Delta x_3 = \frac{1}{2}\Delta q'_d - \frac{1}{2\Delta p}\beta\hat{\rho}\hat{a}(\Delta q'_d)^2. \quad (\text{A.25})$$

Then Δx_4 is simply

$$\begin{aligned} \Delta x_4 &= \Delta q'_d - \Delta x_2 - \Delta x_3 \\ &= \frac{1}{2}\Delta q'_d - \frac{\Delta p}{2\hat{\rho}\hat{a}} + \beta \left\{ \frac{\hat{\rho}\hat{a}}{2\Delta p}(\Delta q'_d)^2 - \frac{1}{2}\Delta q'_d \right\}. \end{aligned} \quad (\text{A.26})$$

Now, the total area $V_T = V_1 + V_2$ is found by plugging in the appropriate expressions into (A.16). The final result is

$$V_T = \frac{1}{4}\Delta p\Delta q'_d - \beta \left\{ \frac{1}{2}\Delta p\Delta q'_d \right\} + \beta^2 \left\{ \frac{\hat{\rho}^2\hat{a}^2}{4\Delta p}(\Delta q'_d)^3 \right\}. \quad (\text{A.27})$$

To find the value of β for which V_T is minimized, solve for β when $\partial V_T/\partial\beta = 0$:

$$\beta = \left(\frac{\Delta p/(\hat{\rho}\hat{a})}{\Delta q'_d} \right)^2. \quad (\text{A.28})$$

Also, $\partial^2 V_T/\partial\beta^2 = \hat{\rho}^2\hat{a}^2(\Delta q'_d)^3/(2\Delta p) > 0$ for $\Delta p > 0$ and $\Delta q'_d > 0$, so this β indeed represents the minimum area.

It turns out that the expression for total area is given by (A.27) when Δp and $\Delta q'_d$ have the same sign, but is given by the negative of (A.27) when they have opposite signs. Therefore (A.28) is the correct expression for R' outside of the acoustic cone regardless of the sign of Δp and $\Delta q'_d$. It gives strengths of

$$\begin{aligned} \hat{\Omega}_1 &= \frac{\Delta p}{2\hat{a}^2} + \frac{\Delta p^2}{2\hat{\rho}\hat{a}^3\Delta q'_d} \\ \hat{\Omega}_2 &= \frac{\Delta p}{2\hat{a}^2} - \frac{\Delta p^2}{2\hat{\rho}\hat{a}^3\Delta q'_d} \\ \hat{\Omega}_3 &= \frac{\Delta p^2}{\hat{\rho}\hat{a}^3\Delta q'_d} - \frac{\hat{\rho}}{\hat{a}}\Delta q'_d \end{aligned} \quad (\text{A.29})$$

for the $+\theta'_d$ acoustic, $-\theta'_d$ acoustic, and $(\theta'_d + \frac{\pi}{2})$ shear, respectively.

The results for β for the two cases of R' outside or inside the acoustic cone can be combined as:

$$\beta = \min [\zeta^2, 1]. \quad (\text{A.30})$$

where again ζ is given by (A.12). The wave patterns represented by this model change in a continuous fashion as ζ goes through 1.0, as shown in figure A.4.

APPENDIX B

**DERIVATION OF THE COMBINED SHEAR-WAVE VECTOR
FOR THE 3-D EULER EQUATIONS**

The eigenvalues of the linearized system of three-dimensional Euler equations can be written as

$$\begin{aligned}\hat{\lambda}_1 &= \hat{q}_g + \hat{a} \\ \hat{\lambda}_2 &= \hat{q}_g - \hat{a} \\ \hat{\lambda}_3 &= \hat{\lambda}_4 = \hat{\lambda}_5 = \hat{q}_g,\end{aligned}\tag{B.1}$$

where \hat{q}_g is defined by (9.28). The eigenvector for the conserved-variable form of the equations associated with $\hat{\lambda}_1$ is given by $\hat{\mathbf{R}}_1$ in (9.23), while the eigenvector associated with $\hat{\lambda}_2$ is given by $\hat{\mathbf{R}}_2$ in (9.24).

There are three linearly independent eigenvectors associated with the eigenvalue \hat{q}_g that form a basis for its eigenspace. One, an entropy wave, is denoted by equation (9.26). The other two are shear waves that cause a change in the velocity with no change in density or pressure. Any two shear vectors that are orthogonal when written in primitive-variable form *and* cause a change in velocity normal to the \vec{n}_g -direction can be chosen. It turns out that the end result for the combined shear vectors is the same regardless of the choice. One set is

$$\hat{\mathbf{R}}_{\text{shear1}} = \begin{bmatrix} 0 \\ -\hat{a}\sin\theta_g \\ \hat{a}\cos\theta_g \\ 0 \\ \hat{a}(-\hat{u}\sin\theta_g + \hat{v}\cos\theta_g) \end{bmatrix}\tag{B.2}$$

$$\hat{\mathbf{R}}_{\text{shear2}} = \begin{bmatrix} 0 \\ -\hat{a}\cos\theta_g \sin\psi_g \\ -\hat{a}\sin\theta_g \sin\psi_g \\ \hat{a}\cos\psi_g \\ \hat{a}(-\hat{u}\cos\theta_g \sin\psi_g - \hat{v}\sin\theta_g \sin\psi_g + \hat{w}\cos\psi_g) \end{bmatrix}, \quad (\text{B.3})$$

where the angles θ_g and ψ_g define the grid-face normal direction as pictured in figure 9.1.

The strengths of each of the five waves can be obtained by solving

$$\Delta \mathbf{U} = \sum_k \hat{\Omega}_k \hat{\mathbf{R}}_k \quad (\text{B.4})$$

for the $\hat{\Omega}_k$. Only the shear-wave strengths are necessary in the present derivation.

They are given by:

$$\begin{aligned} \hat{\Omega}_{\text{shear1}} &= \frac{\hat{\rho}}{\hat{a}} (-\Delta u \sin\theta_g + \Delta v \cos\theta_g) \\ \hat{\Omega}_{\text{shear2}} &= \frac{\hat{\rho}}{\hat{a}} (-\Delta u \cos\theta_g \sin\psi_g - \Delta v \sin\theta_g \sin\psi_g + \Delta w \cos\psi_g). \end{aligned} \quad (\text{B.5})$$

The combined action of the two shear waves in the linearized system can be replaced by a single shear wave whose strength *and* direction are a function of the difference in states. An expression for this new shear vector can be found from:

$$\hat{\Omega}_{\text{new}} \hat{\mathbf{R}}_{\text{new}} = \hat{\Omega}_{\text{shear1}} \hat{\mathbf{R}}_{\text{shear1}} + \hat{\Omega}_{\text{shear2}} \hat{\mathbf{R}}_{\text{shear2}}. \quad (\text{B.6})$$

Combining terms, one obtains:

$$\hat{\Omega}_{\text{new}} \hat{\mathbf{R}}_{\text{new}} = \begin{bmatrix} 0 \\ -\hat{\rho}(\Delta r_1)_g \\ -\hat{\rho}(\Delta r_2)_g \\ -\hat{\rho}(\Delta r_3)_g \\ -\hat{\rho}\{\hat{u}(\Delta r_1)_g + \hat{v}(\Delta r_2)_g + \hat{w}(\Delta r_3)_g\} \end{bmatrix}, \quad (\text{B.7})$$

where the $(\Delta r_i)_g$'s are defined by

$$\begin{aligned} (\Delta r_1)_g &\equiv ((c_x)_g^2 - 1)\Delta u + (c_x)_g(c_y)_g\Delta v + (c_x)_g(c_z)_g\Delta w \\ (\Delta r_2)_g &\equiv (c_y)_g(c_x)_g\Delta u + ((c_y)_g^2 - 1)\Delta v + (c_y)_g(c_z)_g\Delta w \\ (\Delta r_3)_g &\equiv (c_z)_g(c_x)_g\Delta u + (c_z)_g(c_y)_g\Delta v + ((c_z)_g^2 - 1)\Delta w. \end{aligned} \quad (\text{B.8})$$

The c_x , c_y , and c_z are defined in spherical coordinates in (9.20). In order that the vector $\hat{\mathbf{R}}_{\text{new}}$ be somewhat similar in form to the two vectors from which it was derived, $\hat{\Omega}_{\text{new}}$ is taken to be $\hat{\rho}/\hat{a}$; the shear vector $\hat{\mathbf{R}}_{\text{new}}$ then becomes:

$$\hat{\mathbf{R}}_{\text{new}} = \begin{bmatrix} 0 \\ -\hat{a}(\Delta r_1)_g \\ -\hat{a}(\Delta r_2)_g \\ -\hat{a}(\Delta r_3)_g \\ -\hat{a}\{\hat{u}(\Delta r_1)_g + \hat{v}(\Delta r_2)_g + \hat{w}(\Delta r_3)_g\} \end{bmatrix}. \quad (\text{B.9})$$

Notice that $\Delta q_g \equiv (c_x)_g \Delta u + (c_y)_g \Delta v + (c_z)_g \Delta w$ represents the component of the velocity-difference $\Delta \vec{V}$ in the wave-propagation direction (normal to the grid face), so (B.8) can be rewritten as

$$\begin{aligned} (\Delta r_1)_g &= \Delta q_g (c_x)_g - \Delta u \\ (\Delta r_2)_g &= \Delta q_g (c_y)_g - \Delta v \\ (\Delta r_3)_g &= \Delta q_g (c_z)_g - \Delta w. \end{aligned} \quad (\text{B.10})$$

Hence each of these terms represents the difference between the x , y , or z component of the velocity difference along the grid-normal and the corresponding component of the whole velocity difference.

BIBLIOGRAPHY

BIBLIOGRAPHY

- [1] Van Leer, B., "On the Relation Between the Upwind-Differencing Schemes of Godunov, Engquist-Osher, and Roe," NASA Langley ICASE Rept. 81-11, 1981
- [2] Liepmann, H., Roshko, A., Elements of Gasdynamics, John Wiley and Sons, Inc., New York, 1957, pp. 79-83
- [3] Godunov, S., "Finite Difference Method for Numerical Computation of Discontinuous Solutions of the Equations of Fluid Dynamics," *Matematicheskii Sbornik* 47, No. 3, 1959, p. 271, Cornell Aeronautical Lab (CALSPAN) translation
- [4] Roe, P., "Approximate Riemann Solvers, Parameter Vectors, and Difference Schemes," *J. Comp. Phys.*, Vol. 43, 1981, pp. 357-372
- [5] Raithby, G., "Skew Upstream Differencing Schemes for Problems Involving Fluid Flow," *Comp. Meth. in Appl. Mech. and Eng.*, Vol. 9, 1976, pp. 153-164
- [6] Hassan, Y., Rice, J., Kim, J., "A Stable Mass-Flow-Weighted Two-Dimensional Skew Upwind Scheme," *Num. Heat Transfer*, Vol. 6, 1983, pp. 395-408
- [7] Lillington, J., "A Vector Upwind Differencing Scheme for Problems Involving Significant Source Terms in Steady-State Linear Systems," *Int. J. Numer. Methods Fluids*, Vol. 1, 1981, pp. 3-16
- [8] Jameson, A., "Iterative Solution of Transonic Flows Over Airfoils and Wings, Including Flows at Mach 1," *Comm. Pure and Appl. Math.*, Vol. 27, 1974, pp. 283-309
- [9] Jameson, A., "Transonic Potential Flow Calculations Using Conservation Form," *Proceedings of 2nd Computational Fluid Dynamics Conference*, June 1975, pp. 148-161
- [10] Moretti, G., "The λ -Scheme," *Computers and Fluids*, Vol. 7, 1979, pp. 191-205
- [11] Verhoff, A., O'Neil, P., "A Natural Formulation for Numerical Solution of the Euler Equations," *Tech. Rept MCAIR 83-031*, McDonnell Aircraft Company, 1983
- [12] Goorjian, P., "A New Algorithm for the Navier-Stokes Equations Applied to Transonic Flows Over Wings," *AIAA 87-1121-CP*, 1987
- [13] Obayashi, S., Goorjian, P., "Improvements and Applications of a Streamwise Upwind Algorithm," *AIAA 89-1957-CP*, 1989

- [14] Colella, P., "Multidimensional Upwind Methods for Hyperbolic Conservation Laws," J. Comp. Phys., Vol. 87, 1990, pp. 171-200; also: Lawrence Berkeley Laboratory Preprint LBL-17023, 1984
- [15] Van Leer, B., "Multidimensional Explicit Difference Schemes for Hyperbolic Conservation Laws," NASA CR 172254, 1983
- [16] Davis, S., "A Rotationally Biased Upwind Difference Scheme for the Euler Equations," J. Comp. Phys., Vol. 56, 1984, pp. 65-92; also: NASA CR 172179, 1983
- [17] Roe, P., "Discrete Models for the Numerical Analysis of Time-Dependent Multidimensional Gas Dynamics," J. Comp. Phys., Vol. 63, 1986, pp. 458-476; also: NASA CR 172574, 1985
- [18] Kroner, D., "Numerical Schemes for the Euler Equations in Two Space Dimensions Without Dimensional Splitting," Notes on Numerical Fluid Mechanics, Vol. 24, ed: Ballman & Jeltsch, Vieweg, 1988, pp. 342-352
- [19] Struijs, R., Deconinck, H., DePalma, P., Roe, P., Powell, K., "Progress on Multidimensional Upwind Euler Solvers for Unstructured Grids," AIAA 91-1550-CP, 1991 (to appear)
- [20] Hirsch, Ch., Lacor, C., "Upwind Algorithms Based on a Diagonalization of the Multidimensional Euler Equations," AIAA 89-1958, 1989
- [21] Powell, K., Van Leer, B., "A Genuinely Multi-Dimensional Upwind Cell-Vertex Scheme for the Euler Equations," AIAA 89-0095, 1989
- [22] Powell, K., "Towards a Genuinely Multi-Dimensional Upwind Scheme," presented at CFD Lecture Series at the Von Karman Institute, 1990
- [23] Giles, M., Anderson, W., Roberts, T., "The Upwind Control-Volume Scheme for Unstructured Triangular Grids," NASA TM 101664, 1989
- [24] Levy, D., Powell, K., Van Leer, B., "An Implementation of a Grid-Independent Upwind Scheme for the Euler Equations," AIAA 89-1931-CP, 1989
- [25] Parpia, I., Michalek, D., "A Shock Capturing Method for Multidimensional Flow," AIAA 90-3016-CP, 1990
- [26] Dadone, A., Grossman, B., "A Rotated Upwind Scheme for the Euler Equations," AIAA 91-0635, 1991
- [27] Parpia, I., "A Planar Oblique Wave Model for the Euler Equations," AIAA 91-1545-CP, 1991 (to appear)
- [28] Anderson, D., Tannehill, J., Pletcher, R., Computational Fluid Mechanics and Heat Transfer, McGraw-Hill Book Company, New York, 1984, p. 484
- [29] Barth, T., "Analysis of Implicit Local Linearization Techniques for Upwind and TVD Algorithms," AIAA 87-0595, 1987.

- [30] Anderson, W., Thomas, J., Van Leer, B., "Comparison of Finite Volume Flux Vector Splittings for the Euler Equations," AIAA Journal, Vol. 24, No. 9, 1986, pp. 1453-1460
- [31] Venkatakrisnan, V., "Viscous Computations Using a Direct Solver," Computers and Fluids, Vol. 18, No. 2, 1990, pp. 191-204
- [32] Thomas, J., Krist, S., Anderson, W., "Navier-Stokes Computations of Vortical Flows Over Low-Aspect-Ratio Wings," AIAA Journal, Vol. 28, No. 2, 1990, pp. 205-212
- [33] Parpia, I., private communication, 1990